

University of Warwick institutional repository: <http://go.warwick.ac.uk/wrap>

A Thesis Submitted for the Degree of PhD at the University of Warwick

<http://go.warwick.ac.uk/wrap/45411>

This thesis is made available online and is protected by original copyright.

Please scroll down to view the document itself.

Please refer to the repository record for this item for information to help you to cite it. Our policy information is available from the repository home page.

The design and synthesis of new molecule-based magnetic materials

by

Lihong Li

A thesis submitted in partial fulfillment of the requirements for the degree of
Doctor of Philosophy in Chemistry

University of Warwick, Department of Chemistry

December 2011

Table of Contents

1. Molecule-based magnetic materials: A review and prospect	1
1.1 Introduction	1
1.2 Simple paramagnetic compounds	3
1.3 Spin Crossover (SCO).....	4
1.4 Molecule-based magnets	6
1.4.1 High T_c metallo-organic magnets.....	7
1.4.2 Metallo-organic frameworks (MOFs).....	9
1.4.3 Interaction of ferromagnetism with optical, electrical or other properties.....	11
1.4.4 Organic magnets.....	12
1.5 Single-molecule magnets (SMMs).....	14
1.6 Conclusions and perspectives	15
1.7 References	15
2. Structural & Electronic Modulation of Magnetic Properties in a Family of Chiral Fe Coordination Polymers.....	20
2.1 Introduction	20
2.2 Synthesis	21
2.3 Crystal Structures of $\{\text{FeL}^n(\mu\text{-Z})\}_\infty$	24
2.3.1 $\{\text{FeL}^1_2(\mu\text{-pz})\}_\infty$	25
2.3.2 $\{\text{FeL}^1_2(\mu\text{-bpy})\}_\infty$	29
2.3.3 $\{\text{FeL}^2_2(\mu\text{-pz})\}_\infty$	31
2.3.4 $\{\text{FeL}^3_2(\mu\text{-pz})\}_\infty$	33

2.3.5	$\{\text{FeL}^3_2(\mu\text{-bpy})\}_\infty$	35
2.3.6	$\{\text{FeL}^5_2(\mu\text{-bpy})\}_\infty$	36
2.3.7	$\{\text{FeL}^6_2(\mu\text{-bpy})\}_\infty$	39
2.4	Magnetic measurements of $\{\text{FeL}^n_2(\mu\text{-Z})\}_\infty$	40
2.4.1	Magnetic data for $\{\text{FeL}^1_2(\mu\text{-pz})\}_\infty$	43
2.4.2	Magnetic data for $\{\text{FeL}^1_2(\mu\text{-bpy})\}_\infty$	45
2.4.3	Magnetic data for $\{\text{FeL}^2_2(\mu\text{-pz})\}_\infty$	47
2.4.4	Magnetic data for $\{\text{FeL}^2_2(\mu\text{-bpy})\}_\infty$	48
2.4.5	Magnetic data for $\{\text{FeL}^3_2(\mu\text{-pz})\}_\infty$ and $\{\text{FeL}^3_2(\mu\text{-bpy})\}_\infty$	50
2.4.6	Magnetic data for $\{\text{FeL}^4_2(\mu\text{-pz})\}_\infty$	52
2.4.7	Magnetic data for $\{\text{FeL}^4_2(\mu\text{-bpy})\}_\infty$	54
2.4.8	Magnetic data for $\{\text{FeL}^5_2(\mu\text{-pz})\}_\infty$	56
2.4.9	Magnetic data for $\{\text{FeL}^5_2(\mu\text{-bpy})\}_\infty$	58
2.4.10	Magnetic data for $\{\text{FeL}^5_2(\mu\text{-bpy})\}_\infty$	60
2.5	Conclusions	61
2.6	Summary	62
2.7	References	66
3.	Two pyridine containing Schiff base isomers as multidentate ligands to construct MOFs	68
3.1	Introduction	68
3.2	Synthesis	69
3.2.1	Synthesis of ligand precursors (HL^7 and HL^8)	69
3.2.2	Synthesis of $[\text{FeL}^7_2]_n$ and $[\text{FeL}^8_2]_n$	70
3.3	Magnetism of $[\text{FeL}^7_2]_n$ and $[\text{FeL}^8_2]_n$	75

3.4	Cu(II) complexes from HL^7 and HL^8	80
3.4.1	Synthesis of $[\text{CuL}^7_2]_n$	80
3.4.2	Magnetism of $[\text{CuL}^7_2]_n$	81
3.4.3	Synthesis of Cu(II) complexes from HL^8	83
	$[\text{CuL}^8_2]_n \cdot 2\text{THF}$ and $[\text{CuL}^8_2]_n \cdot \text{MeOH}$	84
	$[\text{Cu}_3\text{L}^8_4(\text{sal})_2]$	86
3.4.4	Magnetism of CuL^8_2 complexes	89
	$[\text{CuL}^8_2]_n \cdot 2\text{THF}$ and $[\text{CuL}^8_2]_n \cdot \text{MeOH}$	89
	$[\text{Cu}_3\text{L}^8_4(\text{sal})_2]_n$	93
3.5	Conclusions	97
3.6	References	98
4.	A family of transition metal complexes containing pyrrole-2-ketone derivatives	101
4.1	Introduction	101
4.2	Synthesis of proligands HL^n ($n = 9 - 11$)	102
4.3	Complexes made from Proligand HL^9	103
4.3.1	$[\text{FeL}^9_2]_n$	103
	Synthesis of FeL^9_2	103
	Magnetism of $[\text{FeL}^9_2]_n$	106
	Powder XRD of $[\text{FeL}^9_2]_n$	109
4.3.2	$[\text{CoL}^9_2]_n$	112
4.3.3	Mn(II) complexes	114
	$[\{\text{Na}_2\text{Mn}_2\text{L}^9_6(\text{THF})_4\}_\infty] \cdot 3\text{THF}$	114
	Magnetism of $[\{\text{Na}_2\text{Mn}_2\text{L}^9_6(\text{THF})_4\}_\infty] \cdot 3\text{THF}$	116

	$[\{\text{Na}_2\text{Mn}_2\text{L}^9(\text{MeCN})_2\}_\infty] \cdot \text{MeCN}$	119
	Magnetism of $[\{\text{Na}_2\text{Mn}_2\text{L}^9(\text{MeCN})_2\}_\infty] \cdot \text{MeCN}$	120
	Attempt to synthesis of complex Mn_3L^9	123
	A: LiOMe method	123
	Magnetism of MnL^9	124
	B: KH method	125
4.4	Complexes made from Proligand HL^{10}	128
4.4.1	$[\text{Na}_2\text{Fe}_2\text{L}^{10}_6(\text{THF})_6]$	128
	Magnetism of $[\text{Na}_2\text{Fe}_2\text{L}^{10}_6(\text{THF})_6]$	132
4.4.2	$[\text{Na}_2\text{Mn}_2\text{L}^{10}_6(\text{THF})_6]_{12}$	134
	Magnetism of $[\text{Na}_2\text{Mn}_2\text{L}^{10}_6(\text{THF})_6]_{12}$	136
4.5	Complexes made from Proligand HL^{11}	139
	Magnetism of $\{[\text{Na}_{10}\text{Co}_{16}\text{L}^{11}_{24}(\text{OH})_{18}] \cdot 3\text{THF}\}$	148
4.6	Conclusions	149
4.7	Reference.....	150
5.	Experimental details.....	152
5.1	General considerations	152
5.2	Experimental details for Chapter Two	154
5.2.1	$\text{Fe}_2\text{Cl}_4 \cdot 3\text{THF}$	154
5.2.2	5-tert-butyl-2-hydroxybenzaldehyde.....	154
5.2.3	3-formyl-4-hydroxybenzonitrile	156
5.2.4	General procedure for HL^n ($n = 1-6$) ligand precursors	157
	(R)-2-{(1-phenylethylimino)methyl}phenol (HL^1)	157

(R)-2-{(1-phenylethylimino)methyl}-4-tert-butylphenol (HL ²).	
.....	158
(R)-2-{(1-phenylethylimino)methyl}-4-nitrophenol (HL ³).....	
.....	159
(R)-2-{(1-phenylethylimino)methyl}-4-methoxyphenol (HL ⁴) .	
.....	159
(R)-3-{(1-phenylethylimino)methyl}-4-hydroxybenzonitrile	
(HL ⁵)	160
(R)-2-{(1-phenylethylimino)methyl}benzene-1,4-diol (HL ⁶)....	
.....	161
5.2.5 General Procedure for [FeL ⁿ ₂] complexes (n = 1-5)	162
[FeL ¹ ₂].....	162
[FeL ² ₂].....	162
[FeL ³ ₂].....	162
[FeL ⁴ ₂].....	163
[FeL ⁵ ₂].....	163
[FeL ⁶ ₂]·CH ₃ OH	163
5.2.6 [{FeL ¹ ₂ (μ-pz)} _∞]	164
5.2.7 [{FeL ¹ ₂ (μ -bpy)} _∞]·CH ₃ OH	165
5.2.8 [{FeL ² ₂ (μ-pz)} _∞]	166
5.2.9 [{FeL ² ₂ (μ -bpy)} _∞].....	167
5.2.10 [{FeL ³ ₂ (μ-pz)} _∞]	167
5.2.11 [{FeL ³ ₂ (μ -bpy)} _∞]·THF	168
5.2.12 [{FeL ⁴ ₂ (μ-pz)} _∞]	168

5.2.13	[{FeL ⁴ ₂ (μ -bpy)} _∞]	169
5.2.14	[{FeL ⁵ ₂ (μ-pz)} _∞].0.5CH ₃ OH	170
5.2.15	[{FeL ⁵ ₂ (μ -bpy)} _∞].THF	171
5.2.16	[{FeL ⁶ ₂ (μ-bpy)} _∞].2THF	172
5.3	Experimental details for Chapter Three	173
5.3.1	Synthesis of ligand precursors	173
	2-{(pyridin-4-yl)methyleneamino}phenol (HL ⁷)	173
	N-salicylidene-4-aminopyridine (HL ⁸)	174
5.3.2	Synthesis of [FeL ⁿ ₂] (n = 7, 8) MOFs complexes	175
	[FeL ⁷ ₂] _n	175
	[FeL ⁸ ₂] _n	176
	[CuL ⁷ ₂] _n	177
	[CuL ⁸ ₂ ·2THF] _n	178
	[CuL ⁸ ₂ ·MeOH] _n	179
	[CuL ⁸ ₄ (sal) ₂] _n	180
5.4	Experimental details for Chapter Four	182
5.4.1	Synthesis of ligand precursors	182
	Pyridin-4-yl(1H-pyrrol-2-yl)methanone (HL ⁹)	182
	1-Benzoylmorpholine	183
	Phenyl(1H-pyrrol-2-yl)methanone (HL ¹⁰)	184
	(1H-pyrrol-2-yl)(pyrrolidin-1-yl)methanone (HL ¹¹)	185
5.4.2	Synthesis of complexes from proligand HL ⁹	186
	[{Na ₂ Mn ₂ L ⁹ ₆ (THF) ₄ }·3THF] _∞	186
	[{Na ₂ Mn ₂ L ⁹ ₆ (MeCN) ₂ ·MeCN} _∞	187

	$[\{K_2Mn_2L^9_4(HL^9)_2(OH)_2(MeCN)_2\}_\infty] \cdot xMeCN \cdot yEt_2O$	189
	$[MnL^9_2]_n$	189
	$[FeL^9_2]_n$	190
	$[CoL^9_2]_n$	191
5.4.3	Synthesis of complexes from proligand HL^{10}	191
	$\{Na_2Mn_2L^{10}_6(THF)_6\}$	191
	$\{Na_2Fe_2L^{10}_6(THF)_6\}$	192
5.4.4	Synthesis of complexes from proligand HL^{11}	193
	$[Mn(III)L^{11}_3]$	193
	$[Fe(III)L^{11}_3]$	194
	$[Na_9Co_{14}L^{11}_{18}(OH)_{18}]^+[Co_2NaL^{11}_6]^-$	195
5.5	References	196

List of Figures

Figure 1.1 Spin crossover complex $[\text{Fe}(\text{NH}_2\text{trz})_3](\text{NO}_3)_{1.7}(\text{BF}_4)_{0.3}$ with a reproducible thermal hysteresis.....	1
Figure 1.2 Typical ligands used to make N_6 , N_5O and N_4O_2 coordinated systems	6
Figure 1.3 Two earliest molecule-base magnets discovered in 1967 and 1987 ...	7
Figure 1.4 The design of MOFs by using multidentate ligands and metal ions.	11
Figure 1.5 Face-to-face stacking of DMe-DCNQI species in solid state of $\text{Cu}(\text{Me}_2\text{DCNQI})_2$	12
Figure 1.6 Two organic radical magnets	13
Figure 1.7 First discovered SMM Mn_{12} -acetate	15
Figure 2.1 (a) Derivation of the clockwise <i>C</i> and anticlockwise <i>A</i> descriptors of the enantiotopic faces of planar region of the <i>trans</i> - FeL_2 units; (b) how the phenyl substituents surround the <i>A</i> face in the more commonly observed orientation; (c) the less frequently observed, more sterically compressed orientation; (d) a hybrid structure observed only in $\{\text{FeL}^1_2(\mu\text{-pz})\}_\infty$	25
Figure 2.2 $\{\text{FeL}^1_2(\mu\text{-pz})\}_\infty$ showing triple π - π stacking (green dashed lines) and edge-face stacking (brown dashed lines)	27
Figure 2.3 Two symmetry-related chains in crystals of $\{\text{FeL}^1_2(\mu\text{-pz})\}_\infty$: (a) showing the angle between the planes of the zigzag chains (<i>ca</i> 49°). Red spheres represent Fe atoms and smaller blue spheres represent pyrazine N atoms; (b) with chains projecting into the page and in the plane of the page.....	28

Figure 2.4	(a) Structure of asymmetric unit in $[\{\text{FeL}^1_2(\mu\text{-bpy})\}\cdot\text{CH}_3\text{OH}]_\infty$, showing edge-face interactions (brown dashed line) between two benzyl groups from two adjacent chains; (b) viewed along the chains showing shortest interchain Fe-Fe distance	30
Figure 2.5	Polymeric chain structure for $\{\text{FeL}^2_2(\mu\text{-pz})\}_\infty$	32
Figure 2.6	Asymmetric unit for $\{\text{FeL}^2_2(\mu\text{-pz})\}_\infty$ with two t-butyl groups (in rectangles) slightly rotating and complex units are slightly rotated to avoid steric interactions	32
Figure 2.7	Structure of $\{\text{FeL}^3_2(\mu\text{-pz})\}_\infty$; (a) Asymmetric unit; (b) Unidirectional chains showing π - π stacking between benzyl ring and bridging pyrazine ligand	34
Figure 2.8	Crystal packing of $\{\text{FeL}^3_2(\mu\text{-pz})\}_\infty$ showing the shortest inter-distance of 10.33 Å	35
Figure 2.9	Alternating directions of neighbouring chains in $[\{\text{FeL}^3_2(\mu\text{-bpy})\}\cdot\text{THF}]_\infty$ showing edge-face interactions	36
Figure 2.10	Asymmetric unit for $[\{\text{FeL}^5_2(\mu\text{-bpy})\}\cdot\text{THF}]_\infty$ showing triple π - π stacking (green dash lines) and edge-face contact (brown dash lines)	38
Figure 2.11	Showing the longer inter-chain distance and lateral shift between Fe atoms in adjacent chains in $[\{\text{FeL}^5_2(\mu\text{-bpy})\}\cdot\text{THF}]_\infty$	38
Figure 2.12	(a) The asymmetric unit of $[\{\text{FeL}^6_2(\mu\text{-bpy})\}\cdot 2\text{THF}]_\infty$; (b) Interchain hydrogen bonds and edge-face CH... π contacts in $\{\text{FeL}^6_2(\mu\text{-bpy})\}_\infty$	40
Figure 2.13	χ_M and $\chi_M T$ vs. T for $\{\text{FeL}^1_2(\mu\text{-pz})\}_\infty$ with fitting to the Bonner-Fisher	

Equation	44
Figure 2.14 χ_M^{-1} vs. T for $\{\text{FeL}^1_2(\mu\text{-pz})\}_\infty$ with fitting to the Curie-Weiss Law ...	44
Figure 2.15 χ_M and $\chi_M T$ vs. T for $\{\text{FeL}^1_2(\mu\text{-bpy})\}_\infty$ with fitting to the ZFS model	46
Figure 2.16 χ_M^{-1} vs. T for $\{\text{FeL}^1_2(\mu\text{-bpy})\}_\infty$ with fitting to the Curie-Weiss Law	46
Figure 2.17 χ_M and $\chi_M T$ vs. temperature for $\{\text{FeL}^2_2(\mu\text{-pz})\}_\infty$ with fitting to ZFS model.....	47
Figure 2.18 χ_M^{-1} vs. temperature for $\{\text{FeL}^2_2(\mu\text{-pz})\}_\infty$ with fitting to χ_M^{-1}	48
Figure 2.19 χ_M and $\chi_M T$ vs. temperature for $\{\text{FeL}^2_2(\mu\text{-bpy})\}_\infty$ with fitting to ZFS model.....	49
Figure 2.20 χ_M^{-1} vs. temperature for $\{\text{FeL}^2_2(\mu\text{-bpy})\}_\infty$ with fitting to χ_M^{-1}	49
Figure 2.21 χ_M , $\chi_M T$ vs. Temperature for $\{\text{FeL}^3_2(\mu\text{-pz})\}_\infty$	50
Figure 2.22 χ_M^{-1} vs. temperature for $\{\text{FeL}^3_2(\mu\text{-pz})\}_\infty$ with fitting to χ_M^{-1}	51
Figure 2.23 χ_M , $\chi_M T$ vs. Temperature for $\{\text{FeL}^3_2(\mu\text{-bpy})\}_\infty$	51
Figure 2.24 χ_M^{-1} vs. temperature for $\{\text{FeL}^3_2(\mu\text{-bpy})\}_\infty$ with fitting to χ_M^{-1}	52
Figure 2.26 χ_M , $\chi_M T$ vs. temperature for $\{\text{FeL}^4_2(\mu\text{-pz})\}_\infty$ with fitting to the Bonner- Fisher equation	53
Figure 2.27 χ_M^{-1} vs. temperature for $\{\text{FeL}^4_2(\mu\text{-pz})\}_\infty$ with fitting to χ_M^{-1}	54
Figure 2.28 χ_M , $\chi_M T$ vs. temperature for $\{\text{FeL}^4_2(\mu\text{-4,4'-bipyridine})\}_\infty$	55
Figure 2.29 χ_M^{-1} vs. temperature for $\{\text{FeL}^4_2(\mu\text{-bpy})\}_\infty$ with fitting to χ_M^{-1}	56
Figure 2.30 χ_M , $\chi_M T$ vs. temperature for $\{\text{FeL}^5_2(\mu\text{-pz})\}_\infty$ with fitting to the Bonner-Fisher equation	57
Figure 2.31 χ_M^{-1} vs. Temperature for $\{\text{FeL}^5_2(\mu\text{-pz})\}_\infty$ with fitting to χ_M^{-1}	58
Figure 2.32 χ_M , $\chi_M T$ vs. temperature for $\{\text{FeL}^5_2(\mu\text{-bpy})\}_\infty$ with fitting to ZFS Model	59

Figure 2.33 χ_M^{-1} vs. Temperature for $\{\text{FeL}^5_2(\mu\text{-bpy})\}_\infty$ with fitting to χ_M^{-1}	59
Figure 2.34 χ_M and $\chi_M T$ vs. T for $\{\text{FeL}^6_2(\mu\text{-bpy})\}_\infty$ with fitting to the ZFS model.....	60
Figure 2.35 χ_M^{-1} vs. Temperature for $\{\text{FeL}^6_2(\mu\text{-bpy})\}_\infty$ with fitting to the Curie- Weiss Law	61
Figure 3.1 X-ray structure of $[\text{FeL}^7_2] \cdot 1\frac{1}{4}(\text{H}_2\text{O}) \cdot \frac{1}{2}(\text{MeOH})$: (a) the complex unit at Fe(1) [Fe(2) is similar]; (b) the corresponding diamond-like network with Fe-Fe distances of 7.93 Å (turquoise) and 7.58 Å (green)	71
Figure 3.2 X-ray structure of $[\text{FeL}^7_2] \cdot 1\frac{1}{4}(\text{H}_2\text{O}) \cdot \frac{1}{2}(\text{MeOH})$ showing a diamond- like topology, with Fe-Fe distances of 7.93 Å (turquoise) and 7.58 Å (green)	72
Figure 3.3 X-ray structure of $[\text{FeL}^8_2]$: (a) the asymmetric unit; (b) 2 D array of orthogonal complexes	74
Figure 3.4 Two adjacent layers in $[\text{FeL}^8_2]$ viewed along the c axis	75
Figure 3.5 $\chi_M T$ vs. T curve of $[\text{FeL}^7_2]$ measured at 1000 Oe.....	76
Figure 3.6 Mössbauer spectrum of complex 1 at 80 K showing high spin (HS) and low spin (LS) centers. δ = isomer shift, ΔE_Q = quadrupole splitting, Γ = half width at half maximum height, % shows relative amount of the two spin centers. Errors 0.01 mms ⁻¹ unless shown otherwise	77
Figure 3.7 χ_M vs. T for $[\text{FeL}^8_2]$ measured at 1000 Oe.....	78
Figure 3.8 $\chi_M T$ and χ_M^{-1} vs. T for complex $[\text{FeL}^8_2]$ measured at 1000 Oe.....	79
Figure 3.9 ZFCW and FCC M vs. T curves for $[\text{FeL}^8_2]$ measured at 1000 Oe...	79

Figure 3.10 M vs. H curve at 1.8 K for complex $[\text{FeL}^8_2]$ showing ferromagnetic Hysteresis	80
Figure 3.11 $\chi_M, \chi_M T$ vs. T for $[\text{CuL}^7_2]$ measured at 1000 Oe.....	82
Figure 3.12 Proligand HL^8 , a possible coordination environment $[\text{ML}^8_2]_n$ and a related Cu(II) system.....	83
Figure 3.13 Asymmetric unit of complex $[\text{CuL}^8_2]_n \cdot 2\text{THF}$	84
Figure 3.14 Asymmetric unit of complex $[\text{CuL}^8_2]_n \cdot 2\text{THF}$	85
Figure 3.15 Representative of crystal packing of (a) $[\text{CuL}^8_2]_n \cdot 2\text{THF}$ and (b) $[\text{CuL}^8_2]_n \cdot \text{MeOH}$ viewed along a axis.....	86
Figure 3.16 Asymmetric unit of $[\{\text{Cu}_3\text{L}^8_4(\text{sal})_2\} \cdot 2\text{MeOH}]_\infty$	87
Figure 3.17 The formation of 2 D mat from zigzag chains.....	88
Figure 3.18 The wave-like mat arrangement of chains (dark blue lines) cross-linked by $\text{Cu}(\text{sal})_2$ units.....	89
Figure 3.19 $\chi_M T$ vs. T for $[\text{CuL}^8_2]_n \cdot 2\text{THF}$ measured at 1000 Oe	91
Figure 3.20 χ_M, χ_M^{-1} vs. T for $[\text{CuL}^8_2]_n \cdot 2\text{THF}$ with fitting to the Bonner-Fisher equation	92
Figure 3.21 χ_M, χ_M^{-1} vs. T for $[\text{CuL}^8_2]_n \cdot \text{MeOH}$ with fitting to the Bonner-Fisher equation	92
Figure 3.22 $\chi_M T$ vs. T for $[\text{CuL}^8_2]_n \cdot \text{MeOH}$ measured at 1000 Oe	93
Figure 3.23 $\chi_M T$ vs. T for $[\text{Cu}_3\text{L}^8_4(\text{sal})_2]$	95
Figure 3.24 $\chi_M T$ vs. T for $[\text{Cu}_3\text{L}^8_4(\text{sal})_2]$ with fitting to a mean-field corrected high temperature Heisenberg model and modifies Curie-Weiss law ($\chi = C/(T - \Theta) + \chi_{\text{TIP}}$)	95
Figure 3.25 Magnetization of complex $[\text{CuL}^8_2]_n \cdot 2\text{THF}$, $[\text{CuL}^8_2]_n \cdot \text{MeOH}$ and $[\text{Cu}_3\text{L}^8_4(\text{sal})_2]$ at 1.8 K.....	96
Figure 4.1 The repeated unit of complex $[\text{FeL}^9_2]_n$	105
Figure 4.2 2 D array of orthogonal complexes	105
Figure 4.3 Two adjacent layers in $[\text{FeL}^9_2]_n$	106
Figure 4.4 χ_M vs T curve of $[\text{FeL}^9_2]_n$ measured at 1000 Oe	107

Figure 4.5	$\chi_M T$ vs T of $[\text{FeL}^9_2]_n$ measured at 1000 Oe.....	108
Figure 4.6	ZFCW and FCC M vs. T curves for $[\text{FeL}^9_2]_n$ measured at 100 Oe.	108
Figure 4.7	Magnetization of material $[\text{FeL}^9_2]_n$ measured at 2 K (---) and 10 K (---).....	109
Figure 4.8	Powder XRD at 50 K, 250 K	110
Figure 4.9	Powder XRD at 30 K, 50 K.....	110
Figure 4.10	Powder XRD at 30 K, 250 K.....	111
Figure 4.11	$\chi_M T$ vs. T for material $[\text{CoL}^9_2]_n$ measured at 1000 Oe.....	113
Figure 4.12	M vs. H for material $[\text{CoL}^9_2]_n$ measured at 2 K.....	114
Figure 4.13	The repeated unit of chain complex $[\{\text{Na}_2\text{Mn}_2\text{L}^9_6(\text{THF})_4\} \cdot 3\text{THF}]_\infty$	115
Figure 4.14	Zigzag chain complex bridged by a tetra THF sodium complex....	116
Figure 4.15	$\chi_M T$ vs. T for material $[\{\text{Na}_2\text{Mn}_2\text{L}^9_6(\text{THF})_4\} \cdot 3\text{THF}]_\infty$ measured at 1000 Oe	117
Figure 4.16	χ_M, χ_M^{-1} vs. T for material $[\{\text{Na}_2\text{Mn}_2\text{L}^9_6(\text{THF})_4\} \cdot 3\text{THF}]_\infty$ measured at 1000 Oe	118
Figure 4.17	The repeated unit for complex $[\{\text{Na}_2\text{Mn}_2\text{L}^9_6(\text{MeCN})_2\} \cdot \text{MeCN}]_\infty$..	119
Figure 4.18	2 D grid topology of $[\{\text{Na}_2\text{Mn}_2\text{L}^9_6(\text{MeCN})_2\} \cdot \text{MeCN}]_\infty$	120
Figure 4.19	Size of solvents being crucial in determination of topology of product	121
Figure 4.20	$\chi_M T$ vs. T for material $[\{\text{Na}_2\text{Mn}_2\text{L}^9_6(\text{MeCN})_2\} \cdot \text{MeCN}]_\infty$ measured at 1000 Oe	122
Figure 4.21	M vs. H for $[\{\text{Na}_2\text{Mn}_2\text{L}^9_6(\text{MeCN})_2\} \cdot \text{MeCN}]_\infty$ measured at 2 K.....	122
Figure 4.22	Representation of a ideal sandwich-like model	123

Figure 4.23 a possible 2 D molecular structure of MnL^9_2	124
Figure 4.24 χ_M^{-1} , $\chi_M T$ vs. T for $[\text{MnL}^9_2]_n$ measured at 1000 Oe	125
Figure 4.25 The asymmetric unit of complex $[\{\text{K}_4\text{Mn}_2\text{L}^9_4(\text{HL}^9)_2(\text{OH})_2(\text{MeCN})_2\}]_\infty \cdot x\text{MeCN} \cdot y\text{Et}_2\text{O}$	126
Figure 4.26 The coordination environment of Mn^{2+} and K^+ ion in the asymmetric unit of $[\{\text{K}_4\text{Mn}_2\text{L}^9_4(\text{HL}^9)_2(\text{OH})_2(\text{MeCN})_2\}]_\infty \cdot x\text{MeCN} \cdot y\text{Et}_2\text{O}$	127
Figure 4.27 The topology of complex $[\{\text{K}_4\text{Mn}_2\text{L}^9_4(\text{HL}^9)_2(\text{OH})_2(\text{MeCN})_2\}]_\infty \cdot$ $x\text{MeCN} \cdot y\text{Et}_2\text{O}$	127
Figure 4.28 Crystal structure of $[\text{Na}_2\text{Fe}_2\text{L}^{10}_6(\text{THF})_6]$ showing the complex cation and anion with minor disorder removed for clarity.....	129
Figure 4.29 The arrangement of ligands L^{10} in complex $[\text{Na}_2\text{Fe}_2\text{L}^{10}_6(\text{THF})_6]$ seen from the top of view	129
Figure 4.30 A picture showing the two disordered orientations of the ligand L^{10} about Fe(1) and Na(1).N1 is common to both orientations of the ligand.....	130
Figure 4.31 Another view looking out from the three fold inversion axis at the two orientations of the ligand in the asymmetric unit of $[\text{Na}_2\text{Fe}_2\text{L}^{10}_6(\text{THF})_6]$ (54 : 46 major: minor)	131
Figure 4.32 A picture of the three different orientations of the THF coordinated to the sodium in the complex cation.....	131
Figure 4.33 $\chi_M T$ vs T for complex $[\text{Na}_2\text{Fe}_2\text{L}^{10}_6(\text{THF})_6]$ measured at 1000 Oe..	133
Figure 4.34 $\chi_M \chi_M^{-1}$ vs T for complex $[\text{Na}_2\text{Fe}_2\text{L}^{10}_6(\text{THF})_6]$ measured at 1000 Oe	134
Figure 4.35 The repeated unit of complex $[\text{Na}_2\text{Mn}_2\text{L}^{10}_6(\text{THF})_6]_{12}$	136

Figure 4.36 $\chi_M T$ vs. T curves for complex $[\text{Na}_2\text{Mn}_2\text{L}^{10}(\text{THF})_6]_{12}$ measured at 1000 Oe	137
Figure 4.37 ZFCW and FCC M vs. T curves for complex $[\text{Na}_2\text{Mn}_2\text{L}^{10}(\text{THF})_6]_{12}$ measured at 1000 Oe	138
Figure 4.38 χ_M, χ_M^{-1} vs. T curves for complex $[\text{Na}_2\text{Mn}_2\text{L}^{10}(\text{THF})_6]_{12}$	138
Figure 4.39 M vs. H curve for complex $[\text{Na}_2\text{Mn}_2\text{L}^{10}(\text{THF})_6]_{12}$ measured at 2 K	139
Figure 4.40 Crystal structure of Mn(III) complex (a) and Fe(III) complex (b) made from Ligand HL^1	141
Figure 4.41 Crystal structure of complex $\{[\text{Na}_{10}\text{Co}_{16}\text{L}^{11}_{24}(\text{OH})_{18}]\cdot 3\text{THF}\}$	143
Figure 4.42 The complex anion of $\{[\text{Na}_{10}\text{Co}_{16}\text{L}^{11}_{24}(\text{OH})_{18}]\cdot 3\text{THF}\}$	144
Figure 4.43 (a) Representation of orientation of oxygen atoms and Co(II) ion in the dimer cation; (b) Representation of the top part of the dimer cation, with a triangular pyramid sit on a crown.....	146
Figure 4.44 Top (a) and bottom (b) view of half part of cation cluster; Grey: Na; Red: O; each polyhedral contains a Co(II) metal centre, dashed line represent a bidentate ligand.....	147
Figure 4.45 $\chi_M T$ vs. T for complex $\{[\text{Na}_{10}\text{Co}_{16}\text{L}^{11}_{24}(\text{OH})_{18}]\cdot 3\text{THF}\}$, measured at 1000 Oe	149

List of Schemes

Scheme 2.1	Synthesis of coordination polymers	22
Scheme 2.2	Schematic representation of the intrachain coupling where J is the antiferromagnetic coupling constant, R is the substituent on ligand L^n . Circles represent the paramagnetic metal complex units FeL^n_2	41
Scheme 3.1	Schiff-base proligands; HL^7 and HL^8 are isomeric	69
Scheme 3.2	Synthesis of Schiff bases of HL^7 and HL^8	70
Scheme 4.1	Synthesis of proligand HL^9 , HL^{10} and HL^{11}	103

List of Tables

Table 2.1	Properties of the coordination polymers $\{\text{FeL}^n(\mu\text{-Z})\}_\infty$	23
Table 2.2	Crystallographic data, collection parameters, and refinement parameters for $\{\text{FeL}^n_2(\mu\text{-Z})\}_\infty$	64
Table 4.1	Selected bond length and angles of crystal structure of MnL^{11}_3 and FeL^{11}_3	142

List of Charts

Chart 1.1	A list of interests in molecule-based magnetic materials.....	2
Chart 1.2	Fe(II) ion in O_h Crystal Field	5
Chart 1.3	DDQ, TCNQ and TCNE	8
Chart 4.1	Pyrrolyl ketone and amide ligands used in the Chapter 4	102

List of Equations

Eqn 2.1	Bonner-Fisher equation.....	42
Eqn 2.2	ZFS model for d^6 high spin octahedral species.....	43
Eqn 3.1	Heisenberg chain model.....	83
Eqn 3.2	Mean-field correction to the high temperature Heisenberg model	94
Eqn 4.1	Molecule-based magnets isotropic Heisenberg magnetic model (HDVV) ($S_A = S_B = 5/2$)	117
Eqn 4.2	Molecule-based magnets isotropic Heisenberg magnetic model (HDVV) ($S_A = S_B = 2$)	132

Acknowledgements

Firstly, I would like to thank my supervisor, Professor Peter Scott for giving me the opportunity to work on such an interesting and challenging project in his group, and all his guidance, supports, patience and encouragements during my PhD. I would also like to thank the Overseas Research Students Awards Scheme and the University of Warwick for financial support of my doctoral study.

I would like to thank the colleagues of the department of Chemistry for their support with measurements and helpful discussions, they are Professor Richard Walton (PXRD), Dr Ivan Prokes (NMR) and Philip Aston (ICP), and particular thanks to Dr. Guy Clarkson for spending a massive amount of time to collect crystal data of my complexes. Collaborators from other institutions, in particular Dr Scott Turner for SQUID training and showing me the most sparkling part of the field of molecular magnetism.

I also want to thank the Scott group members, Giles, Suzanne, Nikola, Chris, Alan and Becky for their help in the lab and language, Cynthia who was such a generous friend and was always ready to help, and Jan for his sagely advice on the project. My Chinese friends, who got me updated everyday by sharing daily news world wide at lunch time.

I would have never got this far without the support of my family. I would like to thank my parents, for their constant encouragement, support and love. My son, Huangzhang, always cheers me up every time I felt stressed but I was unable to make more time for him. Finally, many thanks to my wife, Juan, who has always been there for me and has been so understanding and caring.

Publications

The following publications have arisen from the work in this thesis:

Chapter 2

Structural & Electronic Modulation of Magnetic Properties in a Family of Chiral Fe Coordination Polymers, Lihong Li, Jan M Becker, Laura E N Allan, Guy J Clarkson, Scott S Turner and Peter Scott, *Inorganic Chemistry*, **2011**, 50(13), 5925-5935.

Chapter 3

Isomeric Fe(II) MOFs: from a diamond-like SCO material to a 2D hard magnet, Lihong Li, Guy J Clarkson, David J Evans, Martin R Lees, Scott S Turner, Peter Scott, *Chem. Commun.*, 2011, **47**, 12646-12648.

Declaration

The work performed in this thesis was carried out in the Department of Chemistry, University of Warwick between October 2008 and October 2011. Unless otherwise stated, it is the work of the author and has not been submitted in whole or in part for any other degree at this or any other university.

Summary

Chapter One gives an overview of molecule-based magnetic materials, and a summary of topics of current interest in this field such as spin crossover (SCO), molecule-based magnets (particularly three room temperature metallo-organic magnets), Metallo-organic frameworks (MOFs), free radical magnets and single molecule magnets (SMMs). There is a brief introduction of key examples and developments in the specific topics, and a perspective at the end.

Chapter Two introduces a family of optically pure Fe(II) polymeric chain complexes of formula $\{\text{FeL}_2(\mu\text{-pz})\}_\infty$ and $\{\text{FeL}_2(\mu\text{-bpy})\}_\infty$. [**L** = bidentate Schiff base ligands obtained from (*R*)-(+)- α -phenylethanamine and 4-substituted salicylaldehydes]. The structural and magnetic properties of the polymeric products are determined by single crystal X-ray diffraction and SQUID magnetometry. By fitting magnetic data of these complexes with the Bonner-Fisher 1-D chain model, the magnitudes of their magnetic exchanges are rationalised on the basis of substituent electronic properties and bridging ligand identity.

Chapter Three describes two Fe(II) coordination polymers containing pyridine-conjugated Schiff base isomer ligands. The isomerism of the two ligands leads to a change from *trans* to *cis* coordination in the $[\text{FeL}_2]$ SBU and thus from a tetrahedral diamond-like 3 D network exhibiting a gradual SCO to a 2 D hard magnet. Furthermore, we have also synthesised another four Cu(II) complexes

based on these two ligands. Crystallographic studies reveal their structures ranging from 1 D zigzag chains and 2 D mat while their magnetic properties are transformed from ferro- to ferrimagnetic behavior.

Chapter Four focuses on three pyrrole-2-ketone bidentate ligands. Three transition metal ions Mn^{2+} , Fe^{2+} and Co^{2+} were studied, based on which twelve complexes have been made. The system is structurally diverse, with 1 D, 2 D, monometallic, trimetallic “sandwich” structures and a high nuclearity cluster being observed depending on the use of cations and solvents. Unusual magnetic phenomena are discovered, including a system in which SCO and ferromagnetic coupling are present.

Chapter Five details the experimental procedures used to carry out the work in this thesis.

Symbols and Abbreviations

Most of the abbreviations and symbols used in this thesis are in common use within the scientific community, a list of non-standard abbreviations used in this thesis:

ICP-MS	Inductively Coupled Plasma Mass Spectrometry
SQUID	Superconducting Quantum Interference Device
QTM	Quantum Tunnelling of Magnetization
SMMs	Single Molecule Magnets
SCO	Spin Crossover
MChD	Magneto-chiral Dichroism
ZFS	Zero Field Splitting
HDVV	Heisenberg-Dirac-VanVleck
MOFs	Metallo-organic Frameworks
SBU	Secondary Building block Units
dp _{ya} -triz	2,4,6-(di-pyridin-2-yl-amino)-[1,3,5]triazine
TCNE	Tetracyanoethylene
DDQ	2,3-dichloro-5,6-dicyano-1,4-benzoquinone
TCNQ	7,7,8,8-tetracyano-quinodimethane
<i>D</i>	Zero-field splitting parameter
<i>T_c</i>	Curie temperature

1. Molecule-based magnetic materials: A review and prospect

1.1 Introduction

The significance of magnetic materials to mankind can be traced back to *ca.* 1200 AD, when a floating compass was created in China using a naturally magnetic variety of magnetite (Fe_3O_4).¹ Man's fascination with magnets continued, and in the early 16th century, William Gilbert created a new artificial magnet from iron.² In the 19th century, a number of advances in electromagnetism were announced, and most significantly, low-cost electricity was produced by use of magnets in 1886.³⁻⁴ In contrast to these practical matters, advances in fundamental understanding of magnetism was still quite limited until Bohr's introduction of quantum mechanics in 1913; through this, magnetic phenomena were explained and the era of modern magnetism began.⁵

Magnetic materials are ubiquitous in modern society. Metallurgically or ceramically processed inorganic materials dominate the market. Over time, these conventional magnets have, however, exhibited some disadvantages such as the need for harsh manufacturing processes, weight and cost. The great demand for advanced magnetic materials for high-technology applications has resulted in a new field of research – molecule-based magnetic materials.

Compared with conventional magnetic materials which are comprised of metals or metal oxides, molecule-based magnetic materials can be either

metallo-organic or purely organic compounds. Undoubtedly, the use of molecules (or molecular ions) presents an exciting prospect since it may be possible to: (i) synthesize materials close to ambient temperature or from solution; (ii) make magnets with other properties such as mesomorphism or chirality which are only found in the molecule-based systems; (iii) improve commercially useful magnetic properties *via* synthetic methodologies.⁶

Alongside all the common magnetic properties (para-, ferro-, ferri- and antiferromagnetism)⁷ associated with conventional magnetic materials, numerous new magnetic phenomena are found in molecule-based magnetic materials, such as single molecule magnetism (SMMs),⁸ magnetochiral dichroism (MChD),⁹⁻¹⁰ and spin crossover (SCO).¹¹⁻¹² A summary of current interest of molecule-based magnetic materials is listed (Chart 1.1).

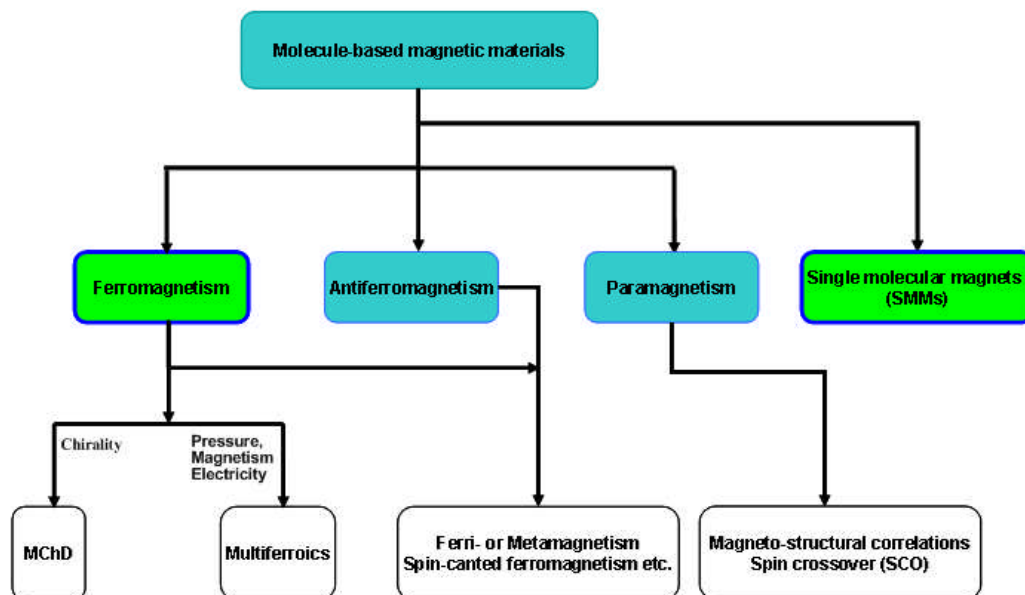


Chart 1.1: A list of interests in molecule-based magnetic materials

1.2 Simple paramagnetic compounds

Except for relatively few occasions where some molecular compounds have shown to be molecular magnets or SMMs, most molecule-based magnetic materials are unfortunately found to be simple paramagnets. This is not surprising since one of the crucial factors in the achievement of simultaneous magnetization is magnetic exchange between spin carriers. The study of these paramagnetic materials is nevertheless important since it allows us to understand fundamental magnetic exchange behaviours and thus approach the rational design of molecule-based magnets.

The flexibility of synthetic chemistry enables us to produce innumerable paramagnetic compounds. A simple modification of ligand, the use of a metal salt with different anions or changing of solvents could result in a significant difference of molecular structures in solid state materials. This may be good news if we desire a large molecule database for the study of magnetostructural relationships.¹³⁻¹⁶ On the other hand, this diversity and attendant magnetic materials creates a problem if we wish to create a unified magnetic model. Nevertheless, progress has been made by physicists, and for example, the 1 D Fisher chain model and Heisenberg-Dirac-VanVleck (HDVV) Hamiltonian are readily applied to many isotropic simple molecular system.¹¹

Apart from this, spin crossover compounds, as a special type of paramagnetic complex, have attracted much attention.

1.3 Spin crossover (SCO)

SCO materials are an interesting class of switchable molecules first discovered by Cambi *et al.* 60 years ago.¹⁷ Under the external stimuli such as pressure, temperature, light and so on, the spin status of metal ions in molecules were changed in solid state materials. Sometimes this transition is associated with a thermal hysteresis (Figure 1.1) during the process that gives rise to molecular bistability. This switchable magnetic property is of importance from the perspective of producing molecular switches, data storage and other devices.¹⁸

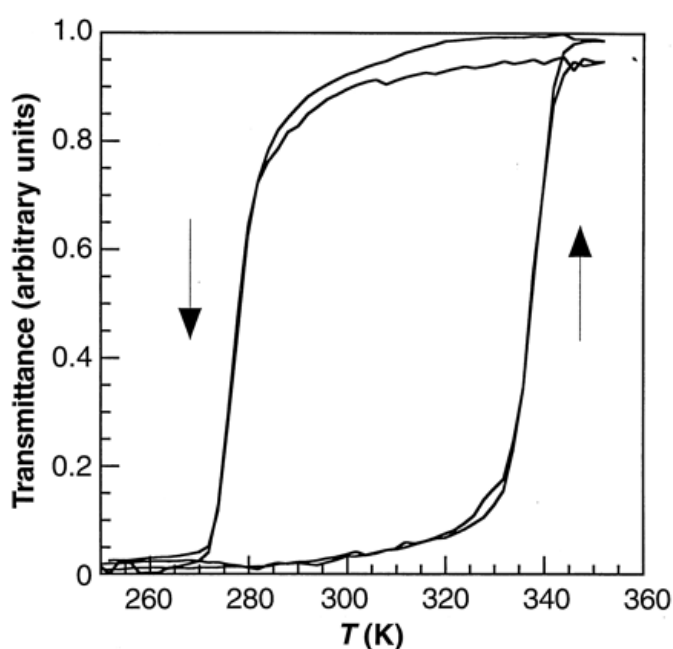


Figure 1.1: Spin crossover complex $[\text{Fe}(\text{NH}_2\text{trz})_3](\text{NO}_3)_{1.7}(\text{BF}_4)_{0.3}$ with a reproducible thermal hysteresis¹⁹

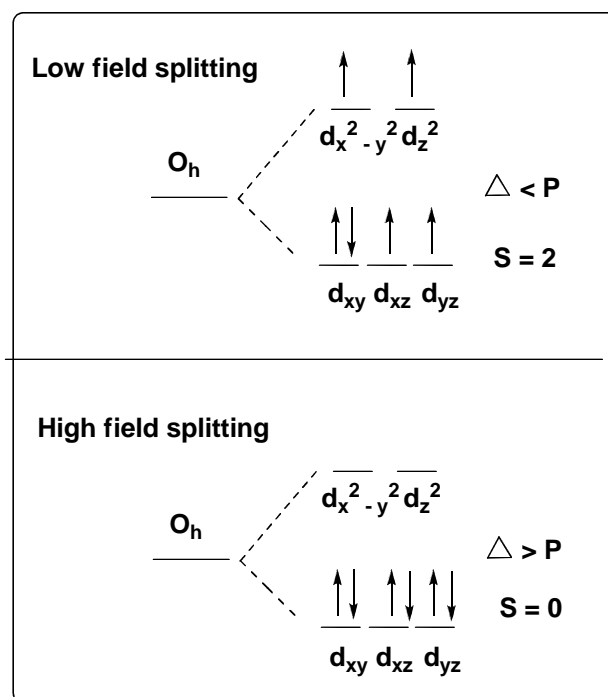


Chart 1.2: Fe(II) ion in O_h Crystal Field; Δ , crystal field splitting energy; S , spin quantum; P , electron pairing energy

The best known example involving a change in the magnetic properties is the low-spin to high-spin transition of some d^4 to d^7 complexes.¹¹⁻¹² The most common spin crossover compounds are octahedral Fe(II) complexes with an all-nitrogen donor environment (N_6 type), made up of pyridine or related heterocyclic rings. Among the various ligands employed in constituent complexes (Figure 1.2), the salicylaldimines are attractive targets since they are easy to prepare and synthetically versatile, and accordingly, have been popular ligands for the synthesis of transition metal complexes.²⁰ Recently N_5O and N_4O_2 coordinated systems have been investigated, developing new classes of compounds.²¹⁻²⁷

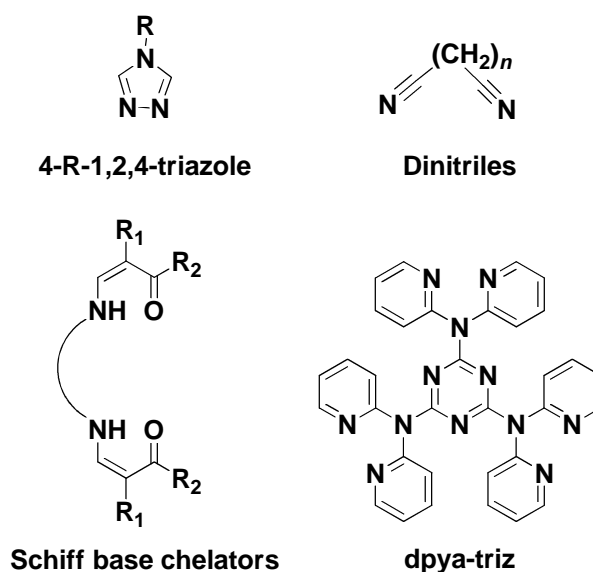


Figure 1.2: Typical ligands used to make N_6 , N_5O and N_4O_2 coordinated systems²²

In the interest of applications, compounds with a thermal transition occurring at room temperature are preferable and a wide thermal hysteresis is also necessary for the sake of the reliable read-record process of devices.¹⁸⁻¹⁹ It has been postulated that joining SCO centres together by use of covalent bridges will, in comparison to the weak intermolecular van der Waals and hydrogen bonding interactions in mononuclear complexes, enhance cooperativity because of a more efficient distribution of molecular distortions occurring during HS to LS conversions.^{20,28-30}

1.4 Molecule-based magnets

Molecule-based magnets are a class of molecular compounds capable of exhibiting spontaneous magnetization at a finite temperature (T_c). The first genuine molecule-based magnet, chloro-bis(diethyldithiocarbamate) iron(III) [$\text{Fe}(\text{dtc})_2\text{Cl}$], was reported by Wickman *et al.* as early as 1967, with an ordering

temperature of 2.46 K.³¹ Since then, an increasing number of research groups became involved until in 1987, Miller *et al.* characterized another metallo-organic salt, $[\text{Fe}(\text{Me}_5\text{C}_5)_2]^+[\text{TCNE}]^-$,³² showing a huge coercive field (1000 Oe) at 2 K. This discovery provoked a substantial amount of activity in this area. Soon after, many new molecule-based magnets were characterized.³³⁻³⁸ In most cases, the paramagnetic metal centres in these materials are transition metal ions although a growing number are being reported which contain rare earth metal ions.³⁹⁻⁴⁹ A few cases are pure organic radicals⁵⁰⁻⁵⁴ where the magnetism entirely arises from 2p electrons. Additionally, the magnetic properties may also result from a combination of both metallo-organic and organic radical contributions.⁵⁵⁻⁵⁶

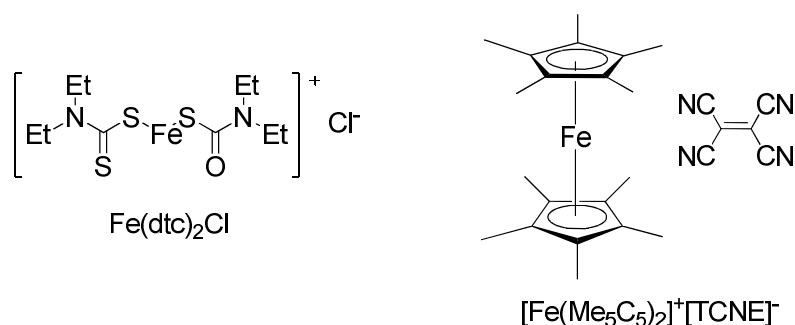


Figure 1.3: Two earliest molecule-based magnets discovered in 1967 and 1987.

1.4.1 High T_c metallo-organic magnets

Among all the metallo-organic complexes, the Prussian-blue analogues $[\text{M}^{\text{x}+}]_A[\text{M}^{\text{y}+}(\text{CN})_z] \cdot n \text{ solvent}$ ⁵⁷ - with regular structures and short bridging ligands as metal-to-metal electronic pathways - have been the preferred targets in the investigation of molecular magnets, not least because many have a high Curie temperature (T_c).⁵⁸⁻⁵⁹ One of the most striking examples is

$\text{V}[\text{Cr}(\text{CN})_6]0.86 \cdot 2.8\text{H}_2\text{O}$,⁴⁰ reported in 1995 as a room temperature magnet ($T_c = 315 \text{ K}$). However, these Prussian blue compounds are typically amorphous and characterization is challenging. Other room temperature molecular magnets include metallo-organic donor-acceptor salt $\text{V}(\text{TCNE})_x \cdot y(\text{CH}_2\text{Cl}_2)$ ($x \sim 2$ and $y \sim 1/2$)³⁹ and $[\text{Ni}_2\text{A} \cdot (\text{O})_x \cdot (\text{H}_2\text{O})_y \cdot (\text{OH})_z]$ ($\text{A} = \text{DDQ}$, TCNQ or TCNE).⁶⁰ These materials are unfortunately amorphous and fragile, and consequently the molecular interactions responsible for their striking properties are not well understood.

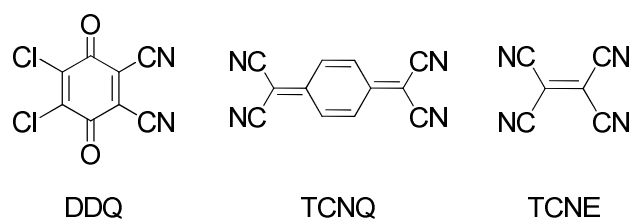


Chart 1.3: DDQ, TCNQ and TCNE.

The discovery of these three room temperature molecule-based magnets indicated potential for applications. However, the rational design and synthesis of such magnets, particularly with the sought-after high T_c , is still in its infancy, and many other fascinating aspects of molecule-based magnetic materials remain unexplained.⁶¹ On the other hand, as material scientists begin to map out the field, several orbital models describing the nature of magnetic interactions have become available.¹¹ Kahn for example suggested that a strict orthogonality of the magnetic orbitals of a A-B type of compound (A and B are two different metals) favors the ferromagnetic interaction between two nearest magnetic centres (A and B).⁶² As for Curie Temperature (T_c), a higher T_c for a molecular magnet is promoted in

multi-dimensional coordination systems (such as MOFs) with short M-M pathways.¹¹

1.4.2 Metallo-organic frameworks (MOFs)

Metallo-organic frameworks (MOFs) are a recently named class of coordination polymeric materials, consisting of metal ions linked together by organic bridging ligands.⁶³ In the early days these hybrid organic-inorganic assemblies were referred to as coordination polymers, due to the fact that preparation of these materials uses traditional coordination chemistry. As the number of examples increased and a wide range of 2 D and 3 D coordination polymers emerged, systematic descriptions were made and applications were identified.⁶³⁻⁶⁴

The advantages of MOFs as magnetic materials are in that many of them show a long-range magnetic ordering behaviour³⁹⁻⁴⁹ providing that some interaction pathways are present in two or three directions in solid states of materials. The complexity of molecular architectures and topologies of MOFs also brought diversity into molecular magnetism. Some unusual magnetic properties are observed such as canted ferromagnetism, metamagnetism and ferrimagnetism.^{45, 49, 65-67} However, some major disadvantages have also been recognised such as comparatively weak magnetic exchange due to the longer distance between the two nearest magnetic centres, leading to low T_c for many MOF magnets so far reported. Poor solubility is a common property for this type of material, and characterisation is often challenging.

MOFs have traditionally been synthesised by the use of solvothermal methods under autoclave conditions. However, due to the complexity and

unpredictability of reactions, products are commonly not pure. Other techniques based on coordination chemistry methodologies have also been developed, such as self-assembly, which only gives the lowest thermodynamically stable species.

A more rational approach to MOFs is the use of Secondary Building block Units (SBUs) which was first introduced by Yagi *et al.* in 2003.⁶⁸ The idea is based on a set of rigid, well-defined starting materials in the interest of making porous molecular solids for gas storage. Apart from this, many multidentate ligands have been explored to make MOFs, such as oxalate ion $\text{C}_2\text{O}_4^{2-}$, well known to be an ligand because its ambidentate coordination ability enables the construction of a diversity of transition metal frameworks (Figure 1.4).⁶³ Compared with the SBUs based method, the use of multidentate ligands has yielded some very good magnetically interesting examples.⁶⁹⁻⁷⁰ The use of pyridine-conjugated Schiff base ligands in the synthesis of 2 D and 3 D MOFs will be introduced in Chapter 3.

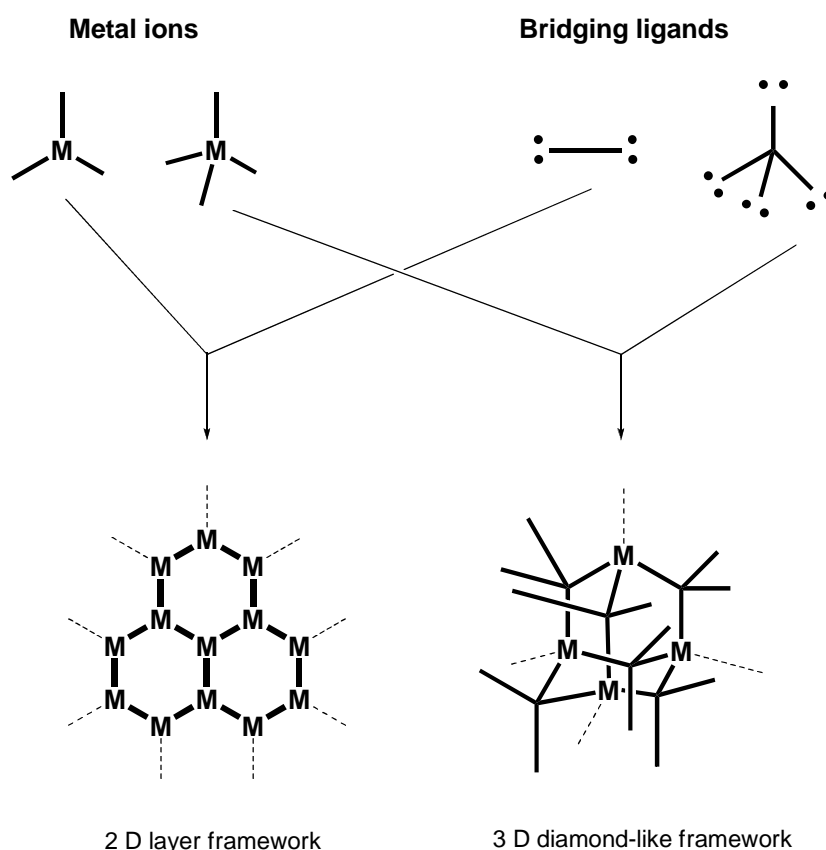


Figure 1.4: The design of MOFs by using multidentate ligands and metal ions

Numerous extended three-dimensional network structures have been identified. It is the elusiveness and diversity of molecular structure of these networks that brings more and more new features to molecular magnetism. In some rare cases such as network structures with a second or even several equivalent lattices interpenetrating in a primary lattice⁷¹, due to their high symmetry and intertwining nature, they could exhibit some exotic physical properties with respect to magnetic, electrical, and optical properties.

1.4.3 Interaction of ferromagnetism with optical, electrical or other properties

One of the potential advantages of molecule-based materials is the ability to create systems which display more than one physical phenomenon. A notable example is metal-like electrical conductivity observed for $\text{Cu}(\text{Me}_2\text{DCNQI})_2$ ⁷² due to an overlap of adjacent Me_2DCNQI groups, providing evidence of a direct structural consequence of the interpenetrating structure (Figure 1.5). Additionally, MChD,⁹⁻¹⁰ as was mentioned before, is an interesting second-order effect which might only be observed in chiral ferromagnets. Multiferroic phenomena, previously the reserve of some conventional perovskite magnetic materials, have recently been observed in MOF systems.⁷³⁻⁷⁵

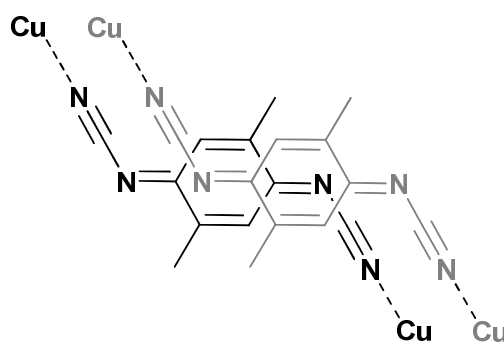


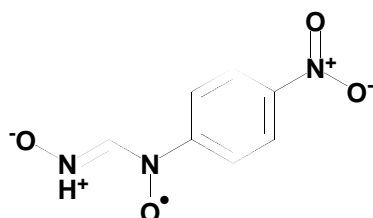
Figure 1.5: Face-to-face stacking of DMe-DCNQI species in solid state of $\text{Cu}(\text{Me}_2\text{DCNQI})_2$.

1.4.4 Organic magnets

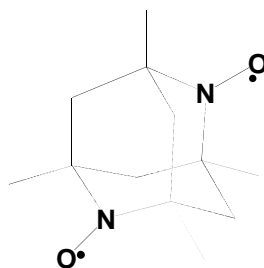
Heisenberg concluded earlier last century that ferromagnetism could not exist in compounds consisting only of light elements. This was believed to be true until ferromagnetic interactions were first observed at low temperatures on a few well defined purely organic materials (polymers).⁷⁶⁻⁷⁸ In principle, the magnetic

moments of this type of material are due to the presence of “free electrons” on a stable free radical species.

Interest in organic magnets arises from properties such as low density, transparency, photo-responsiveness, electrical insulation and biocompatibility. However, because there are not very many readily accessible and stable free radicals,⁷⁹ the development of organic magnets is obstructed. Furthermore, owing to ferromagnetic interactions of organic radical magnets entirely resulting from 2p electrons, most of these materials have been found to have a very low T_c . For instance, the *p*-nitrophenyl nitronyl nitroxide radical (Figure 1.6, top) has a T_c of 0.60 K⁵² while another organic nitroxide N, N'-dioxy-1,3,5,7-tetramethyl-2,6 diazaadamantane (Figure 1.6, bottom) has a T_c of 1.48 K.⁵³



p-nitrophenyl nitronyl nitroxide



N, N'-dioxy-1,3,5,7-tetramethyl-2,6 diazaadamantane

Figure 1.6: Two organic radical magnets

1.5 Single-molecule magnets (SMMs)

SMMs are a class of molecules, below a certain blocking temperature, exhibiting superparamagnetic behaviour normally seen in mesoscale magnetic particles. The existence of this phenomenon was first noted in the complex Mn₁₂-acetate [Mn₁₂O₁₂(O₂CMe)₁₆(H₂O)₄].⁸⁰⁻⁸¹ SMMs have attracted considerable interest in recent times.⁸² Since each of the molecules may respond to an external magnetic field like a small magnet, they may thus function as a data-storage domain in magnetic media. Furthermore, the Quantum Tunnelling of Magnetization (QTM) effect⁸³⁻⁸⁴ has led to the proposal that SMMs could be exploited as qubits in quantum computing.⁸⁵

The unusual properties of SMMs arise from a combination of a large ground-state spin (S) and large, easy-axis-type anisotropy due to a negative axial zero-field splitting (ZFS), D .⁸² Hence maximization of S and $|D|$ is the primary goal in this area. Based on this rule, a large number of scientific studies have been carried out recently.^{82, 86} The most appealing systems for SMM study are the metallo-organic clusters due to their high aggregation and large S .

In chapter 4, we report our accidental synthesis of a Co₁₆ cluster which unfortunately is not SMM.

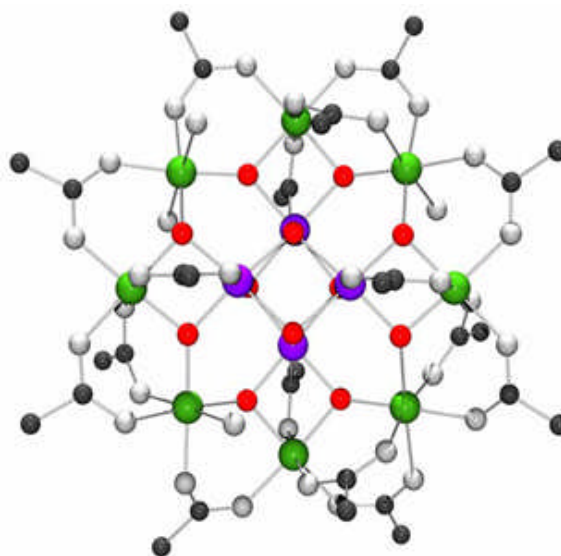


Figure 1.7: First discovered SMM Mn₁₂-acetate

1.6 Conclusions and perspectives

Among the enormous number of magnetic solids prepared, characterized and exploited in the last century, molecule-based magnetic materials have brought many new features. Although there may be a long way to go before we see molecule-based magnets in many applications, it is hopeful that the research is aiming for new applications and complementing rather than replacing of existing magnetic materials. Additionally, as a very new research area, there is huge scope for the synthesis of new molecular materials. In doing so, this undoubtedly will give new impetus to those relevant fields such as supramolecular and coordination chemistry, or even purely organic synthetic chemistry.

1.7 References

1. R. T. Merrill and M. W. McElhiny, *The earth's magnetic field: its history, origin, and planetary perspective*, Academic press, New York, 1983.
2. E. N. D. C. Andrade, *Endeavour*, 1958, **17**, 65, (Reformatted and updated references, August 2009).
3. E. W. Lee, *Magnetism: An Introductory Survey*, Dover Publications, Houston, USA, 1984.
4. L. R. Moskowitz, *Permanent magnet design and application handbook*, Krieger, 1976.
5. S. Miller Joel and J. Epstein Arthur, *Molecule-Based Magnetic Materials*, 1996, **644**, 1-13.
6. P. Day, ed., *Metal-Organic and Organic Molecular Magnets*, The Royal Society, London, 1999.
7. N. A. Spaldin, *Magnetic materials: Fundamental and Applications*, Cambridge, 2003.
8. R. Winpenny, ed., *Single-Molecule Magnets and Related Phenomena*, Springer-Verlag, Berlin Heidelberg, 2006.
9. C. Train, R. Gheorghe, V. Krstic, L.-M. Chamoreau, N. S. Ovanesyan, G. L. J. A. Rikken, M. Gruselle and M. Verdaguer, *Nature Mater.*, 2008, **7**, 729-734.
10. L. D. Barron, *Nat. Mater.*, 2008, **7**, 691-692.
11. O. Kahn, *Molecular Magnetism*, WILEY-VCH, New York, 1993.
12. P. Gütlich and H. A. Goodwin, in *Spin Crossover in Transition Metal Compounds*, Springer-Verlag, Berlin Heidelberg, 2004, vol. 233,234,235.
13. S. Tancharakorn, F. P. A. Fabbiani, D. R. Allan, K. V. Kamenev and N. Robertson, *J. Am. Chem. Soc.*, 2006, **128**, 9205-9210.
14. E. Coronado, J. R. Galán-Mascarós, C. J. Gómez-García and A. Murcia-Martínez, *Chem. Eur. J.*, 2006, **12**, 3484-3492.
15. A. Beghidja, P. Rabu, G. Rogez and R. Welter, *Chem. Eur. J.*, 2006, **12**, 7627-7638.
16. A. Beghidja, G. Rogez, R. Welter and M. Drillon, *J. Mater. Chem.*, 2006, **16**, 2715-2728.
17. L. Cambi and L. Szegő, *Chem. Ber.*, 1931, **64**, 2591-2598.
18. D. Gatteschi, A. Caneschi, R. Sessoli and A. Cornia, *Chem. Soc. Rev.*, 1996, **25**, 101-112.
19. O. Kahn and C. J. Martinez, *Science*, 1998, **279**, 44-48.
20. G. W. E. R. H. Holm, Jr., A. Chakavorty, *Prog. Inorg. Chem.*, 1966, **7**, 83.
21. S. Imatomi, T. Sato, T. Hamamatsu, R. Kitashima and N. Matsumoto, *Bull. Chem. Soc. Jpn*, 2007, **80**, 2375-2377.
22. K. S. Murray, *Eur. J. Inorg. Chem.*, 2008, **2008**, 3101-3121.
23. M. Quesada, P. de Hoog, P. Gamez, O. Roubeau, G. Aromí, B. Donnadieu, C. Massera, M. Lutz, A. L. Spek and J. Reedijk, *Eur. J. Inorg. Chem.*, 2006, **2006**, 1353-1361.
24. J. Wagner, H. Görls and H. Keutel, *Inorg. Chim. Acta.*, 2005, **358**, 808-813.
25. P. A. Anderson, T. Astley, M. A. Hitchman, F. R. Keene, B. Moubaraki, K. S. Murray, B. W. Skelton, E. R. T. Tiekink, H. Toftlund and A. H. White, *J. Chem Soc., Dalton Trans.*, 2000, 3505-3512.

-
26. J. A. Real, H. Bolvin, A. Bousseksou, A. Dworkin, O. Kahn, F. Varret and J. Zarembowitch, *J. Am. Chem. Soc.*, 1992, **114**, 4650-4658.
 27. J. A. Real, A. B. Gaspar, V. Niel and M. C. Muñoz, *Coord. Chem. Rev.*, 2003, **236**, 121-141.
 28. H. Hagiwara, S. Hashimoto, N. Matsumoto and S. Iijima, *Inorg. Chem.*, 2007, **46**, 3136-3143.
 29. M. Seredyuk, A. B. Gaspar, M. C. Muñoz, M. Verdaguer, F. Villain and P. Gütlich, *Eur. J. Inorg. Chem.*, 2007, **2007**, 4481-4491.
 30. V. Niel, J. M. Martinez-Agudo, M. C. Muñoz, A. B. Gaspar and J. A. Real, *Inorg. Chem.*, 2001, **40**, 3838-3839.
 31. H. H. Wickman, A. M. Trozzolo, H. J. Williams, G. W. Hull and F. R. Merritt, *Phys. Rev.*, 1967, **155**, 563.
 32. J. S. Miller, J. C. Calabrese, H. Rommelmann, S. R. Chittipeddi, J. H. Zhang, W. M. Reiff and A. J. Epstein, *J. Am. Chem. Soc.*, 1987, **109**, 769-781.
 33. V. Laget, C. Hornick, P. Rabu, M. Drillon and R. Ziessel, *Coord. Chem. Rev.*, 1998, **178-180**, 1533-1553.
 34. A. Y. Robin and K. M. Fromm, *Coord. Chem. Rev.*, 2006, **250**, 2127-2157.
 35. V. A. Friesse and D. G. Kurth, *Coord. Chem. Rev.*, 2008, **252**, 199-211.
 36. G. Ferey, *Chem. Soc. Rev.*, 2008, **37**, 191-214.
 37. L. Ouahab, *Coord. Chem. Rev.*, 1998, **178-180**, 1501-1531.
 38. J. Mrozinski, *Coord. Chem. Rev.*, 2005, **249**, 2534-2548.
 39. J. M. Manriquez, G. T. Yee, R. S. Mclean, A. J. Epstein and J. S. Miller, *Science*, 1991, **252**, 1415-1417.
 40. S. Ferlay, T. Mallah, R. Ouahes, P. Veillet and M. Verdaguer, *Nature*, 1995, **378**, 701-703.
 41. R. Jain, K. Kabir, J. B. Gilroy, K. A. R. Mitchell, K.-c. Wong and R. G. Hicks, *Nature*, 2007, **445**, 291-294.
 42. J. Zhang, J. Ensling, V. Ksenofontov, P. Gütlich, A. J. Epstein and J. S. Miller, *Angew. Chem. Int. Ed.*, 1998, **37**, 657-660.
 43. K. Fegy, D. Luneau, T. Ohm, C. Paulsen and P. Rey, *Angew. Chem. Int. Ed.*, 1998, **37**, 1270-1273.
 44. H. Kumagai and K. Inoue, *Angew. Chem. Int. Ed.*, 1999, **38**, 1601-1603.
 45. M. Ohba, N. Usuki, N. Fukita and H. Ōkawa, *Angew. Chem. Int. Ed.*, 1999, **38**, 1795-1798.
 46. K. Inoue, H. Imai, P. S. Ghalsasi, K. Kikuchi, M. Ohba, H. Ōkawa and J. V. Yakhmi, *Angew. Chem. Int. Ed.*, 2001, **40**, 4242-4245.
 47. M. Minguet, D. Luneau, E. Lhotel, V. Villar, C. Paulsen, D. B. Amabilino and J. Veciana, *Angew. Chem. Int. Ed.*, 2002, **41**, 586-589.
 48. J. R. Galán-Mascarós and K. R. Dunbar, *Angew. Chem. Int. Ed.*, 2003, **42**, 2289-2293.
 49. K. Inoue, K. Kikuchi, M. Ohba and H. Ōkawa, *Angew. Chem. Int. Ed.*, 2003, **42**, 4810-4813.
 50. A. A. Ovchinnikov and V. N. Spector, *Synth. Met.*, 1988, **27**, 615-624.
-

-
51. M. Tamura, Y. Nakazawa, D. Shiomi, K. Nozawa, Y. Hosokoshi, M. Ishikawa, M. Takahashi and M. Kinoshita, *Chem. Phys. Lett.*, 1991, **186**, 401-404.
 52. Y. Nakazawa, M. Tamura, N. Shirakawa, D. Shiomi, M. Takahashi, M. Kinoshita and M. Ishikawa, *Phys. Rev. B*, 1992, **46**, 8906.
 53. R. Chiarelli, M. A. Novak, A. Rassat and J. L. Tholence, *Nature*, 1993, **363**, 147-149.
 54. F. Palacio, G. Antorrena, M. Castro, R. Burriel, J. Rawson, J. N. B. Smith, N. Bricklebank, J. Novoa and C. Ritter, *Phys. Rev. Lett.*, 1997, **79**, 2336.
 55. D. Maspoch, D. Ruiz-Molina, K. Wurst, N. Domingo, M. Cavallini, F. Biscarini, J. Tejada, C. Rovira and J. Veciana, *Nat. Mater.*, 2003, **2**, 190-195.
 56. H. O. Stumpf, L. Ouahab, Y. Pei, D. Grandjean and O. Kahn, *Science*, 1993, **261**, 447-449.
 57. J. M. Becker, *PhD Degree Thesis, The University of Warwick*, 2009.
 58. W. R. Entley and G. S. Girolami, *Science*, 1995, **268**, 397-400.
 59. S. M. Holmes and G. S. Girolami, *J. Am. Chem. Soc.*, 1999, **121**, 5593-5594.
 60. R. Jain, K. Kabir, J. B. Gilroy, K. A. R. Mitchell, K. C. Wong and R. G. Hicks, *Nature*, 2007, **445**, 291-294.
 61. M. Joel S, *Polyhedron*, 2001, **20**, 1723-1725.
 62. O. Kahn, Y. Pei and Y. Journaux, *Mol. Cryst. Liq. Cryst.*, 1989, **176**, 163.
 63. S. L. James, *Chem. Soc. Rev.*, 2003, **32**, 276-288.
 64. J. L. C. Rowsell and O. M. Yaghi, *Micropor. Mesopor. Mat.*, 2004, **73**, 3-14.
 65. J. S. Miller, T. E. Vos and W. W. Shum, *Adv. Mater.*, 2005, **17**, 2251-2254.
 66. A. Escuer, F. A. Mautner, M. A. S. Goher, M. A. M. Abu-Youssef and R. Vicente, *Chem. Comm.*, 2005, 605-607.
 67. O. Kahn, *Acc. Chem. Res.*, 2000, **33**, 647-657.
 68. O. M. Yaghi, M. O'Keeffe, N. W. Ockwig, H. K. Chae, M. Eddaoudi and J. Kim, *Nature*, 2003, **423**, 705-714.
 69. H. Tamaki, Z. J. Zhong, N. Matsumoto, S. Kida, M. Koikawa, N. Achiwa, Y. Hashimoto and H. Okawa, *J. Am. Chem. Soc.*, 1992, **114**, 6974-6979.
 70. S. Decurtins, H. W. Schmalle, P. Schneuwly, J. Ensling and P. Guetlich, *J. Am. Chem. Soc.*, 1994, **116**, 9521-9528.
 71. S. R. Batten and R. Robson, *Angew. Chem. Int. Ed.*, 1998, **37**, 1460-1494.
 72. R. Kato, H. Kobayashi and A. Kobayashi, *J. Am. Chem. Soc.*, 1989, **111**, 5224-5232.
 73. S. Ohkoshi, H. Tokoro, T. Matsuda, H. Takahashi, H. Irie and K. Hashimoto, *Angew. Chem. Int. Ed.*, 2007, **46**, 3238-3241.
 74. G.-C. Xu, X.-M. Ma, L. Zhang, Z.-M. Wang and S. Gao, *J. Am. Chem. Soc.*, 2010, **132**, 9588-9590.
 75. P. Jain, V. Ramachandran, R. J. Clark, H. D. Zhou, B. H. Toby, N. S. Dalal, H. W. Kroto and A. K. Cheetham, *J. Am. Chem. Soc.*, 2009, **131**, 13625-13627.
-

- 76. I. Hiizu, in *Advances in Physical Organic Chemistry*, ed. D. Bethell, Elsevier, New York, 1991, vol. 26.
- 77. A. L. Buchachenko, *Mol. Cryst. Liq. Cryst.*, 1989, **176**, 307-319.
- 78. A. Rassat, *Pure & Appl. Chem.*, 1990, **62**, 223-227.
- 79. M. T. Lemaire, *Pure & Appl. Chem.*, 2004, **76**, 277-293.
- 80. R. Sessoli, H. L. Tsai, A. R. Schake, S. Wang, J. B. Vincent, K. Folting, D. Gatteschi, G. Christou and D. N. Hendrickson, *J. Am. Chem. Soc.*, 1993, **115**, 1804-1816.
- 81. R. Sessoli, D. Gatteschi, A. Caneschi and M. A. Novak, *Nature*, 1993, **365**, 141-143.
- 82. D. Gatteschi and R. Sessoli, *Angew. Chem. Int. Ed.*, 2003, **42**, 268-297.
- 83. L. Thomas, F. Lioni, R. Ballou, D. Gatteschi, R. Sessoli and B. Barbara, *Nature*, 1996, **383**, 145-147.
- 84. J. R. Friedman, M. P. Sarachik, J. Tejada and R. Ziolo, *Phys. Rev. Lett.*, 1996, **76**, 3830.
- 85. M. N. Leuenberger and D. Loss, *Nature*, 2001, **410**, 789-793.
- 86. A. K. Boudalis, B. Donnadieu, V. Nastopoulos, J. M. Clemente-Juan, A. Mari, Y. Sanakis, J.-P. Tuchagues and S. P. Perlepes, *Angew. Chem. Int. Ed.*, 2004, **43**, 2266-2270.

2. Structural & Electronic Modulation of Magnetic Properties in a Family of Chiral Fe Coordination Polymers

2.1 Introduction

There has been intense interest in molecule-based coordination polymers with one or multiple-dimensional structures¹. These may be of use in understanding the fundamental magnetic interactions and magnetostructural correlations in molecular systems, and also as new multifunctional molecule-based materials.² For instance, applications of coordination polymers have been sought in the areas of nonlinear optical,³ electrochromic⁴ and multiferroic materials.⁵⁻⁷

In the approach toward molecule-based magnets, various intermolecular interactions (π -stacking, hydrogen bonding, van der Waals) are thought to play a role as information transmitters and, therefore, have an important impact on the intermolecular magnetic exchange. The design and characterisation of new molecular extended architectures using non-covalent interactions to give predictable physical properties is challenging. In contrast, Olivier Kahn first introduced the idea that direct covalent linking of the active metal sites could increase cooperativity in polymeric compounds in regard to mononuclear ones.^{8,9}

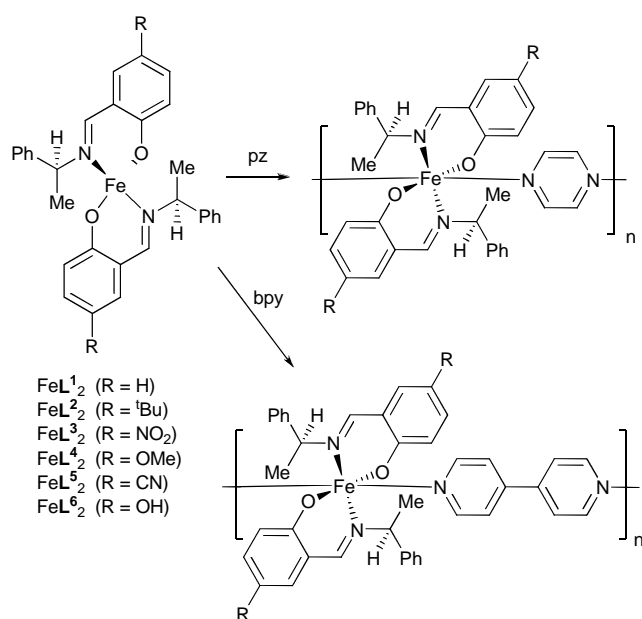
In this way, small ligands that offer a pathway for magnetic exchange e.g. cyanide (CN^-)¹⁰⁻¹¹, oxalate ($\text{C}_2\text{O}_4^{2-}$),¹²⁻¹⁶ azido (N_3^-),¹⁷⁻²¹ pyrazine (pz)²²⁻²³ and 4,4'-bipyridine (bpy)²⁴⁻²⁵ are responsible for many molecule-based magnets in the literature. These have allowed the engineering of numbers of metal-containing polymers with a large diversity of network topologies, such as one-dimensional molecular chains and ladders, two-dimensional grids and brick-wall structures, and three-dimensional frameworks.^{11, 19, 26-33}

The extension of these concepts to the synthesis of optically pure chiral systems is of current interest because of the possibility of observation of phenomena such as Magneto-Chiral Dichroism (MChD)³⁴ and/or electrical Magneto-Chiral Anisotropy (MCA).³⁵ With this in mind, and with the paucity of opportunities to synthesise a range of systematically related materials, we focused our attention on the reaction of the readily available chiral building blocks FeL_2 (Scheme 2.1) which we expected to form new coordination polymer systems with bridging ligands such as pz and bpy. The number of comparable systems is rather limited.³⁶⁻³⁸ We were particularly interested in being able to make magnetostructural correlations for a family of complexes since general trends and indications for future directions are likely to be a result.

In this Chapter, we report the synthesis, structure and magnetic properties of eleven Fe(II) chain complexes with general formula $\{\text{FeL}_2(\mu\text{-pz})\}$ and $\{\text{FeL}_2(\mu\text{-bpy})\}$ prepared in this way (Table 2.1).

2.2 Syntheses

Tetrahedral Fe(II) complexes $[\text{FeL}^n_2]$ were synthesized according to previously reported procedures.³⁹ The complexes $[\text{FeL}^n_2]$, ($n = 1, 2, 4$) are soluble in diethyl ether, and treatment of them with pz or bpy in this solvent gave moderate to high yields of highly crystalline and slightly air sensitive coordination polymers (Scheme 2.1). The complexes of L^3 , L^5 and L^6 are relatively insoluble, and their reactions with the bridging ligands in THF gave correspondingly less soluble but crystalline and air stable materials. We could not isolate a reaction product between $[\text{FeL}^6_2]$ and pz. The structural and magnetic properties of the polymeric products, as determined by single crystal X-ray diffraction and SQUID magnetometry are summarized in Table 2.1. The materials were also characterized by IR, UV/vis and microanalysis.



Scheme 2.1: Synthesis of coordination polymers. The structures shown represent stoichiometry and the actual crystal structures vary considerably (*vide infra*).

Lⁿ	R	Bridge	Structure	Space group	Intrachain Fe-Fe distance d₁ /Å	Shortest interchain distance d₂ /Å	Weiss constant Θ [K]	Intrachain J [cm⁻¹]	C [cm³ K mol⁻¹]	T_N [K]	D [cm⁻¹]	g-factor
L¹	H	pz	Figure 2, 3	C2	7.3229(10)	12.40	-13.72	-2.44	3.600	14		2.20
		bpy	Figure 4	C2	11.5749(2)	7.45	-0.06	-	3.231	-	10.2	2.10
L²	^tBu	pz	Figure 5	C2	7.3012(23)	12.40	-16.06	-	3.773	-	38.5	2.14
		bpy	-	-	-	-	-0.23	-	3.207	-	11.5	2.10
L³	NO₂	pz	Figure 6	P2(1)	7.3694(6)	10.33	-5.67	-	3.453	-	21.0	2.10
		bpy	Figure 7	P2	11.6027 (2)	9.08	-7.55	-	3.602	-	10.2	2.06
L⁴	OMe	pz	-	-	-	-	-18.72	-3.85	3.056	19		2.14
		bpy	-	-	-	-	-3.33	-0.72	3.610	3		2.16
L⁵	CN	pz	-	-	-	-	-7.59	-1.66	3.317	7		2.20
		bpy	Figure 8-9	P2(1)2(1))2	11.5590(1)	8.06	-5.88	-	3.680	-	10.5	2.15
L⁶	OH	bpy	Figure 10	P1	11.6927(3)	6.58	-0.81	-	3.423	-	12.9	2.12

Table **2.1**: Properties of the coordination polymers {FeLⁿ₂(μ-Z)}_∞ [Z = 1,4-pyrazine (pz), 4,4'-bipyridine (bpy)]

2.3 Crystal Structures of $\{\text{FeL}^n_2(\mu\text{-Z})\}_\infty$

The Fe containing units in the following structures usually contain planar *trans*- FeL_2 moieties, and as a result the faces presented to incoming ligands are enantiotopic, as was described recently.³⁹ However, all such planar centres in this study are symmetrically substituted by bridging ligands and so – ignoring the inherent lack of mirror symmetry implied by the chiral side chains – no new stereogenic centre is created on formation of the polymer. It remains however that we need to define directionality (*i.e.* the relative directions of these enantiotopic faces in the polymer). We will thus refer to the ‘clockwise’ and ‘anticlockwise’ (*C* and *A*) faces with respect to the order of chelating donors (N, O atoms) as shown in Figure 2.1a. Notably the phenyl substituents are usually arranged about the *A* face (Figure 2.1(b)) whereas the *C* face is relatively unencumbered.

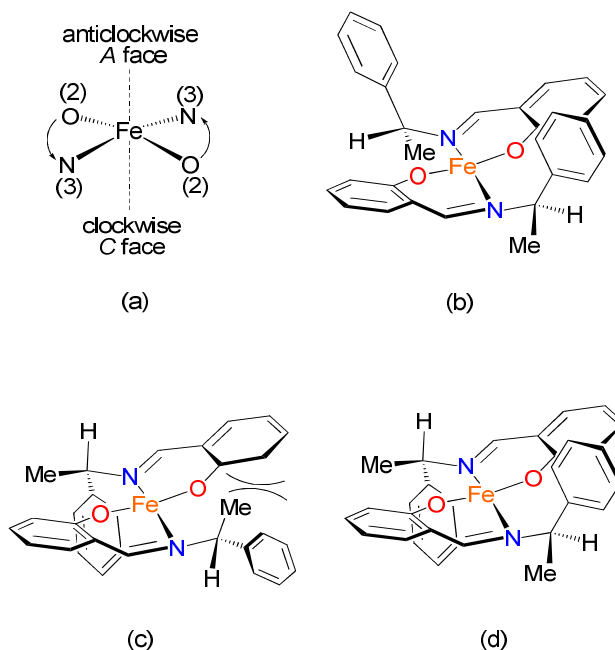


Figure 2.1: (a) Derivation of the clockwise *C* and anticlockwise *A* descriptors of the enantiotopic faces of planar region of the *trans*-FeL₂ units; (b) how the phenyl substituents surround the *A* face in the more commonly observed orientation; (c) the less frequently observed, more sterically compressed orientation; (d) a hybrid structure observed only in {FeL¹₂(μ-pz)}_∞.

2.3.1 {FeL¹₂(μ-pz)}_∞

The asymmetric unit of {FeL¹₂(μ-pz)}_∞ contains a trimer with three independent FeL¹₂ units and three pyrazine ligands (Figure 2.2). The unit at Fe(2) has the conventional all *trans* structure with two bidentate salicyaldiminato ligands occupying the meridional plane. The rotational orientations of the phenethyl groups in this monomer unit are unique in this study (vide infra) in that they point in opposite directions along the chain (as shown in Figure 1.1(d)). Nevertheless, the *A* face of the Fe(2) unit is pointing to the right in Figure 2.2. The axial

positions of Fe(2) are occupied by coordinated pyrazines with an angle N(9)-Fe(2)-N(6) of *ca* 179.1°. In contrast to this *trans* Fe(2) which generates a local linear architecture, the Fe(1) and Fe(3) centres produce “corners” via their chiral *cis-α* configurations [N(10)-Fe(3)-N(1) and N(5)-Fe(1)-N(2) of 86.1° and 87.1° respectively. Interestingly they are of opposite helicity (absolute configuration); Λ for Fe(3) and Δ for Fe(1). As we have previously noted, this type of ligand is poorly effective in determining diastereoselection at octahedral centres,³⁹ although this is the first time we have observed the presence of two absolute configurations at Fe in the same crystal.

The rotational orientations of the Fe(3) and Fe(1) units about the notional Fe(1)-Fe(2)-Fe(3) axis facilitate the formation of two triple π - π stacks in the asymmetric unit (the centroid-centroid distance is 3.527 Å), which direct the N(1) and N(2) pyrazine bridges “down” and “up” as shown in Figure 2.2. The torsional angle N(1)-Fe(3)-Fe(1)-N(2) thus created is *ca* 180° so that the extended structure of this single chain describes an achiral (*i.e.* planar 2-D) zigzag. Additionally, there are edge-face contacts showing as brown dashed lines. The unit cell however contains two symmetry-related chains (Figure 2.3(a)) and the angle between the planes of these zigzag chains is *ca* 49° (Figure 2.3(b)).

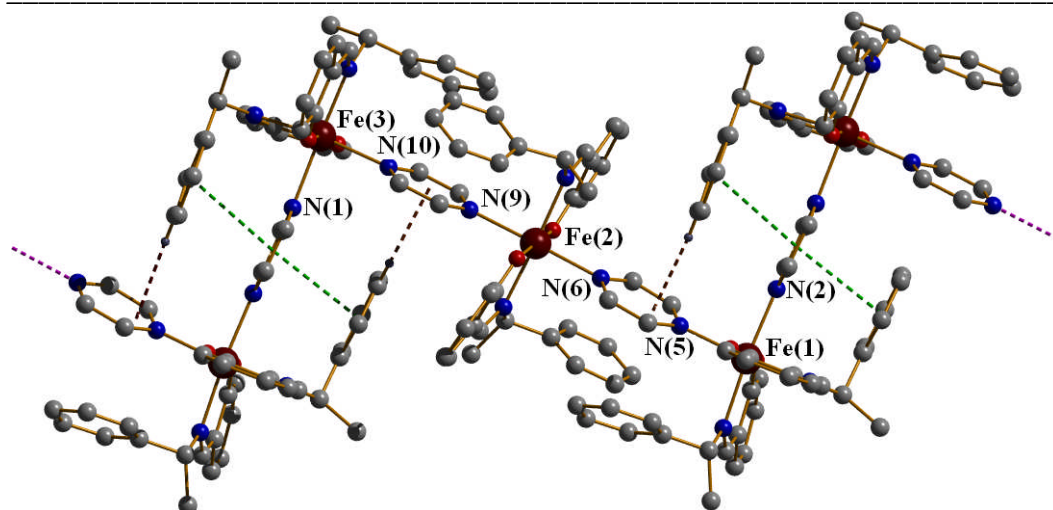
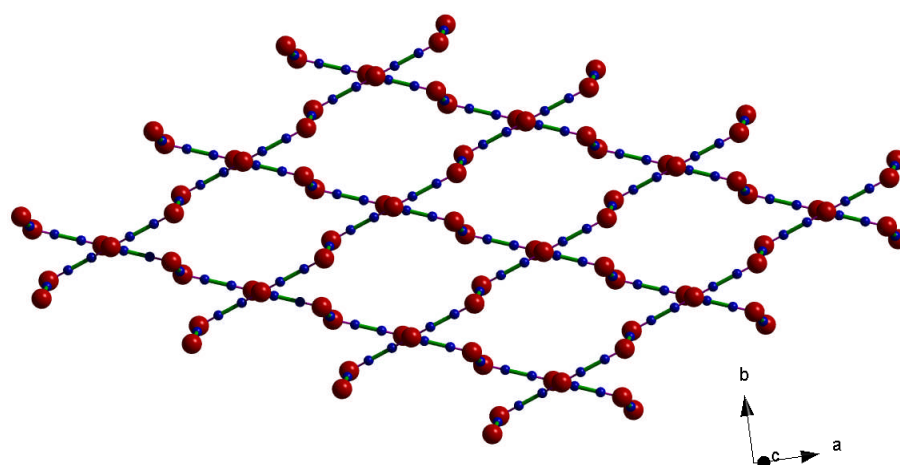
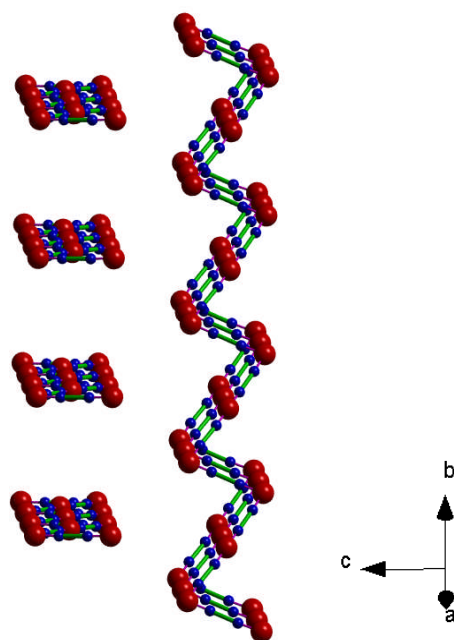


Figure 2.2: $\{\text{FeL}^1_2(\mu\text{-pz})\}_\infty$ showing triple π - π stacking (green dashed lines) and edge-face stacking (brown dashed lines)



(a)

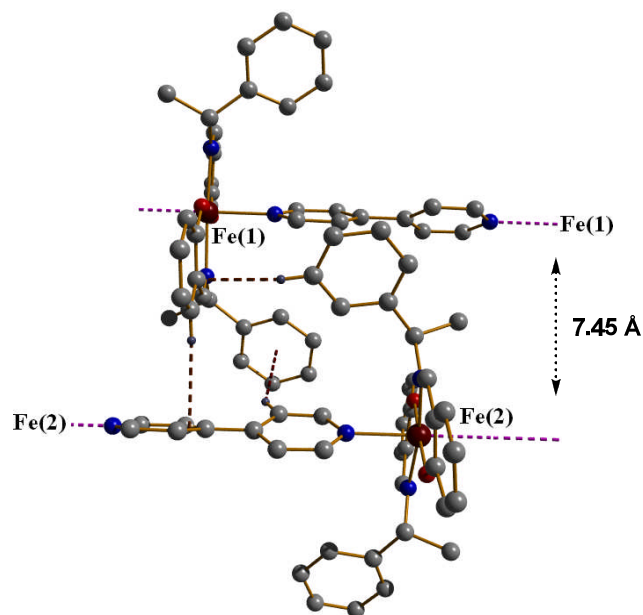


(b)

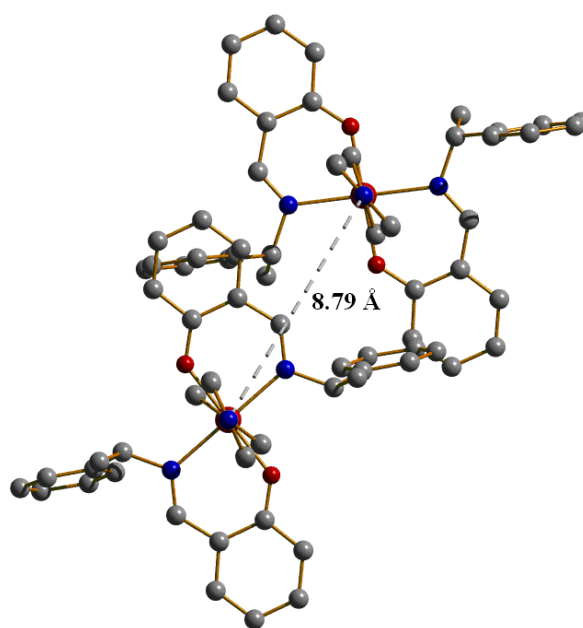
Figure 2.3: Two symmetry-related chains in crystals of $\{\text{FeL}^1_2(\mu\text{-pz})\}_\infty$: (a) showing the angle between the planes of the zigzag chains (*ca* 49°). Red spheres represent Fe atoms and smaller blue spheres represent pyrazine N atoms; (b) with chains projecting into the page and in the plane of the page.

2.3.2 $[\{\text{FeL}^1_2(\mu\text{-bpy})\}\cdot\text{CH}_3\text{OH}]_\infty$

For $[\{\text{FeL}^1_2(\mu\text{-bpy})\}\cdot\text{CH}_3\text{OH}]_\infty$ there are two crystallographically independent six-coordinate Fe complex units Fe(1) and Fe(2) (Figure 2.4(a)). The Fe atoms and bpy N atoms of each polymer lie on the two-fold axis on special positions *a* and *b*.⁴⁰ The salicyaldiminato ligands are again observed to have the *trans* arrangement and the angles subtended by bpy N donor atoms are all close to 180°. The difference in the two polymer chains arises in the directionality of the enantiotopic faces of the planar *trans* FeL^1_2 moieties in relation to the *b* axis of the crystal. In the Fe(2) chain travelling along the two-fold axis on special position *a*, the *A* face (vide supra) points up the *b* axis of the cell (i.e. to the left in Figure 2.4(a)). In the Fe(1) chain running along the two-fold axis on special position *b*, the *A* face points down the *b* axis of the cell (i.e. to the right). The orientations of the imine phenethyl groups are all conventional (Figure 2.1(b)) and thus the two phenyls of each *trans* FeL^1_2 unit surround the pyridyl ring at the enantiotopic *A* face and the methyls align themselves around the *C* face. There are edge-face interactions between a bpy bridging ligand from one chain and a benzyl group from another chain in the asymmetric unit (brown dash lines) so that the side-chains are interdigitated. This allows close approach of the main chains at 7.45 Å (Figure 2.4(b)).



(a)



(b)

Figure 2.4: (a) Structure of asymmetric unit in $[\{\text{FeL}^1_2(\mu\text{-bpy})\}\cdot\text{CH}_3\text{OH}]_\infty$, showing edge-face interactions (brown dashed line) between two benzyl groups from two adjacent chains; (b) viewed along the chains showing shortest interchain Fe-Fe distance. (Hydrogens and solvent have been removed for clarity)

2.3.3 $\{\text{FeL}_2(\mu\text{-pz})\}_\infty$

As shown in Figure 2.5, in $\{\text{FeL}_2(\mu\text{-pz})\}_\infty$ there are also two crystallographically independent chains in the asymmetric unit (inter-chain distance is 12.40 Å, see Figure 2.6); one with repeat unit Fe(1)-Fe(2)-Fe(3) and one Fe(4)-Fe(5)-Fe(6). The chains lie on the two-fold axes with the 4-*t*-butylsalicyaldiminato ligands adopting a *trans* orientation and the Fe and pyrazine N atoms lying on the two-fold axis. The three complexes that form the repeat unit of each polymeric chain do not have the same directionalities; for example the *C* faces of Fe(1) and Fe(3) are oriented in the positive direction of the *b* axis (right-left in Figure 2.5) whereas for Fe(2) it is the *A* face. At the same time, the orientation of the phenethyl units in Fe(1) is the more sterically compressed type of Figure 1(c) with the phenyl groups surrounding the *C* face. Overall this leads to substantial differences in the environments of the bridges. Pyrazine N(8)-N(7) is surrounded by four phenyl groups from neighbouring complex units, pyrazine N(5)-N(4) is surrounded by two phenyl groups while pyrazine N(2)-N(1) has only neighbouring acetonitrile solvent.

In the Fe(4)-Fe(5)-Fe(6) chain no solvent was located in this region. This sterically unencumbered pyrazine bridge is also unique in that it is tilted out of the near co-planar arrangement of the other pyrazine bridges. The *t*-butyl groups of the ligands on alternate complexes of the polymer chain are roughly orthogonal except on either side of the sterically unencumbered pyrazine bridges where they are eclipsed (torsion angle N(3)-Fe(1)-Fe(3)-N(9) is 1.3°).

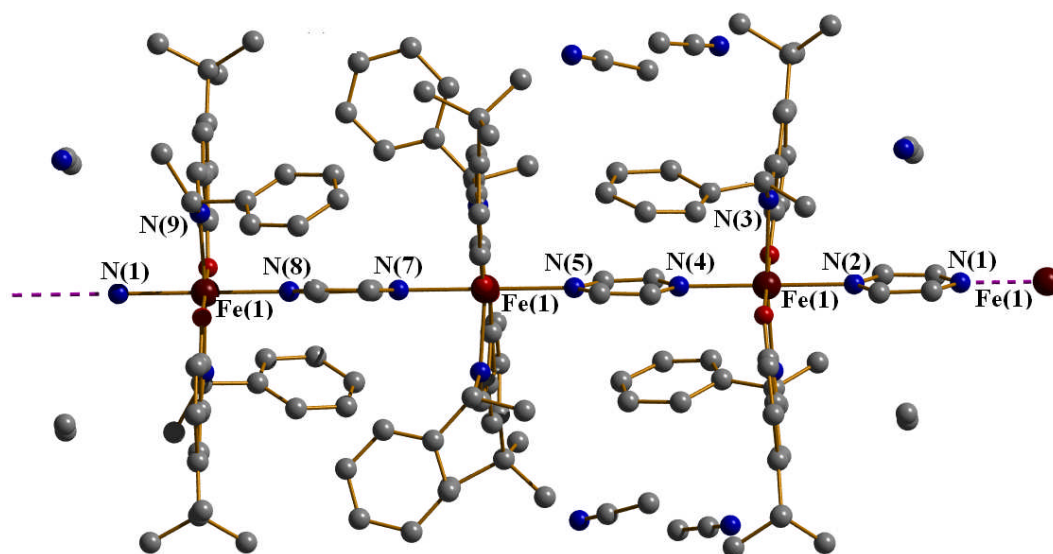


Figure 2.5: Polymeric chain structure for $\{\text{FeL}_2(\mu\text{-pz})\}_\infty$. (Hydrogens have been removed for clarity)

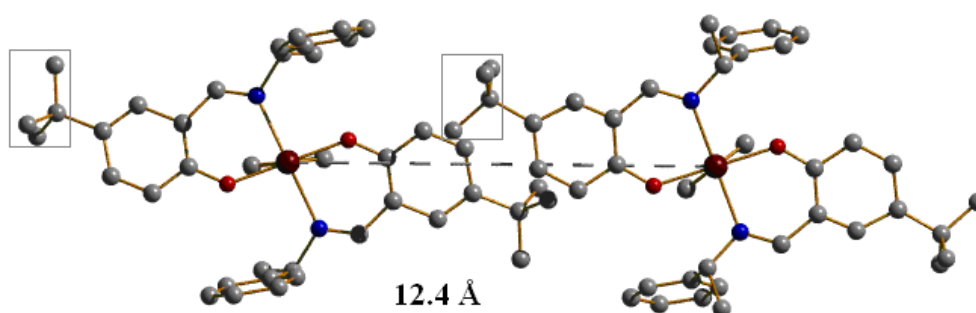


Figure 2.6: Asymmetric unit for $\{\text{FeL}_2(\mu\text{-pz})\}_\infty$ with two t-butyl groups (in rectangles) slightly rotating and complex units are slightly rotated to avoid steric interactions. (Hydrogens and solvent acetonitrile have been removed for clarity)

2.3.4 $\{\text{FeL}^3_2(\mu\text{-pz})\}_\infty$

The asymmetric unit of complex $\{\text{FeL}^3_2(\mu\text{-pz})\}_\infty$ contains the FeL^3_2 complex and a pz bridging ligand (Figure 2.7(a)). The complex forms a simple 1 D chain travelling parallel to the *a* axis of the cell. The *C* enantiotopic face of each FeL^3_2 complex points the same way along the polymer backbone. There is a symmetry related chain facing the opposite direction in the unit cell related by the 2(1) screw axis (Figure 2.8) and this results in the shortest inter-chain axis distance of 10.33 Å for this particular material (Table 2.1).

The 4-nitrosalicyaldiminato ligands are all aligned (eclipsed) along the polymer backbone and the pz bridges all lie in the same plane (Figure 2.7(b)). There is a π - π stacking interaction between one of the benzyl groups of the ligands and the bridging pyrazine with the centroid-centroid distance of ca. 3.607 Å and an angle between planes of interacting π -systems of ca. 9.67° (Figure 2.7(b)). Additionally, each nitro group is sandwiched between the aromatic rings of the nitrophenyls of a neighbouring chain so that the chains are interdigitated. The NO₂ groups extend far enough into the sandwich to have a relatively close contact with the H atoms of the pyrazine bridges (the closest contact = 2.59 Å).

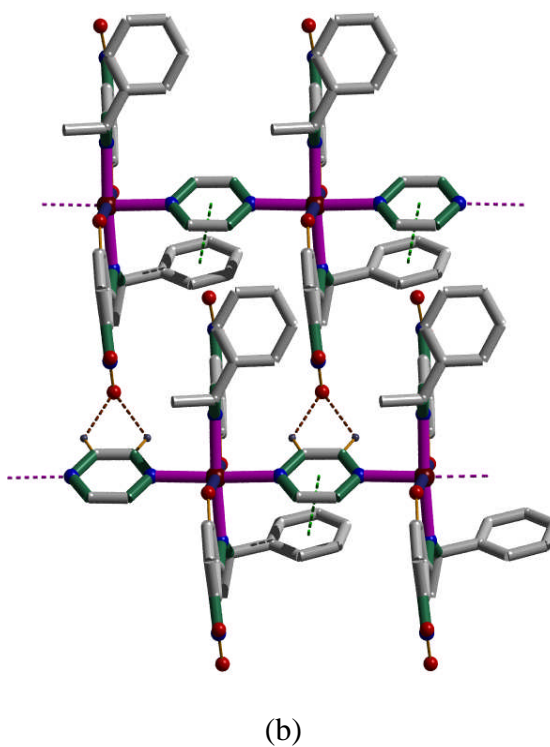
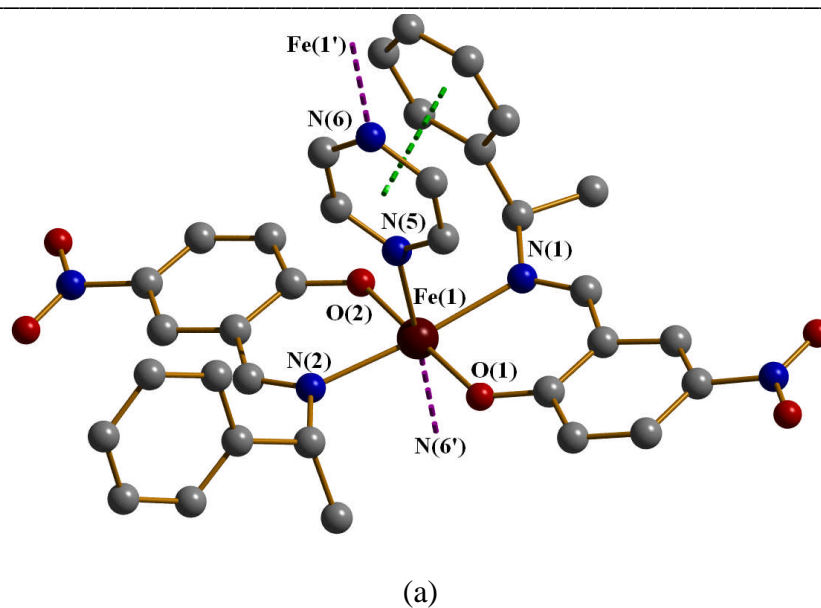


Figure 2.7: Structure of $\{\text{FeL}^3_2(\mu\text{-pz})\}_\infty$; (a) Asymmetric unit; (b) Unidirectional chains showing π - π stacking between benzyl ring and bridging pyrazine ligand. (Hydrogen atoms and solvent acetonitrile have been removed for clarity).

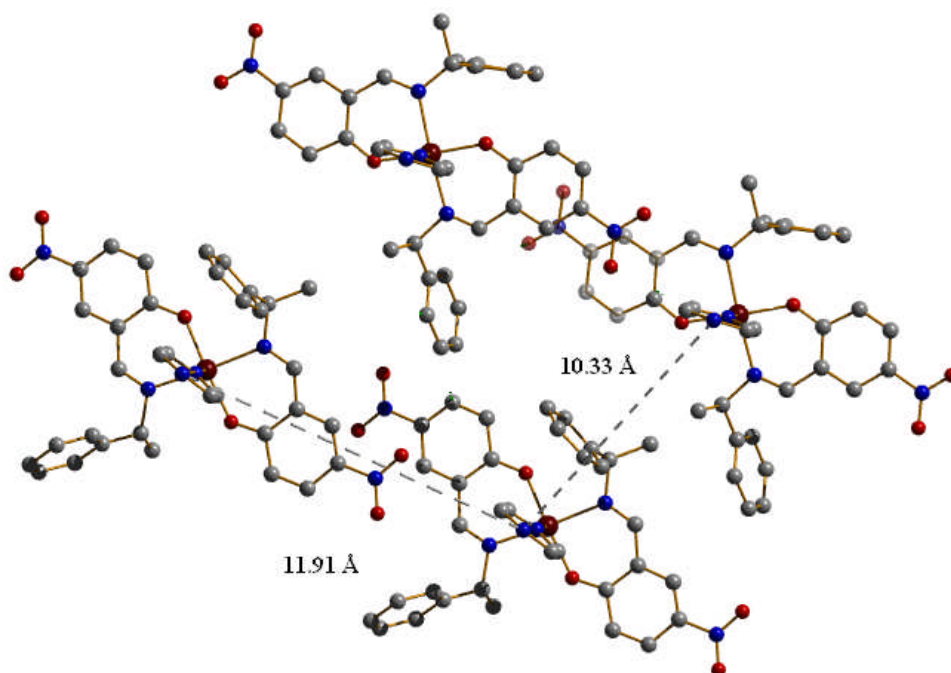


Figure **2.8**: Crystal packing of $\{\text{FeL}^3_2(\mu\text{-pz})\}_\infty$ showing the shortest inter-distance of 10.33 Å (hydrogen atoms and solvent methanol have been removed for clarity)

2.3.5 $[\{\text{FeL}^3_2(\mu\text{-bpy})\}\cdot\text{THF}]_\infty$

The asymmetric unit of $[\{\text{FeL}^3_2(\mu\text{-bpy})\}\cdot\text{THF}]_\infty$ contains two polymeric complexes that lie on the two-fold axis (Figure **2.9**) and several molecules of THF. The Fe(1) complex lies on the two-fold axis on special position d^{40} running through the centre of the cell and the Fe(2) polymer lies on the special position a where the two-fold axis runs along the b axis of the cell. The *trans* 4-nitrosalicyaldiminato ligands of each FeL^3_2 unit are aligned along the polymer backbone. Each bridging bpy ligand has an identical orientation with a dihedral angle between the pyridine rings of 26.6 ° in the Fe(1) polymer and 39.0 ° in the Fe(2) polymer. The *A* enantiotopic faces of the Fe(1) chain face up the b cell axis whereas for Fe(2) it is the *C* face.

In both polymers, the pyridinyl unit at the A face of the FeL^3_2 unit is surrounded by the two aromatic rings of the phenethyl substituents of that complex (Figure 2.9). In the Fe(2) chain, the angle between the phenethyl rings and the pyridine ring of the bipy bridge is 64.9° with a CH- π interaction between a phenethyl aromatic CH and the pyridine ring (CH-pyridine ring centroid ca. 2.852 Å). In the Fe(1) polymer, the angle between the phenethyl aromatics and the bridging pyridine is much more acute at 29.2° but with little overlap that could indicate π stacking. Accompanying this is however an edge-face short contact between the nitroarene from the Fe(2) chain and pyrazine ring from the Fe(1) chain. The distance between these two chains is 9.08 Å.

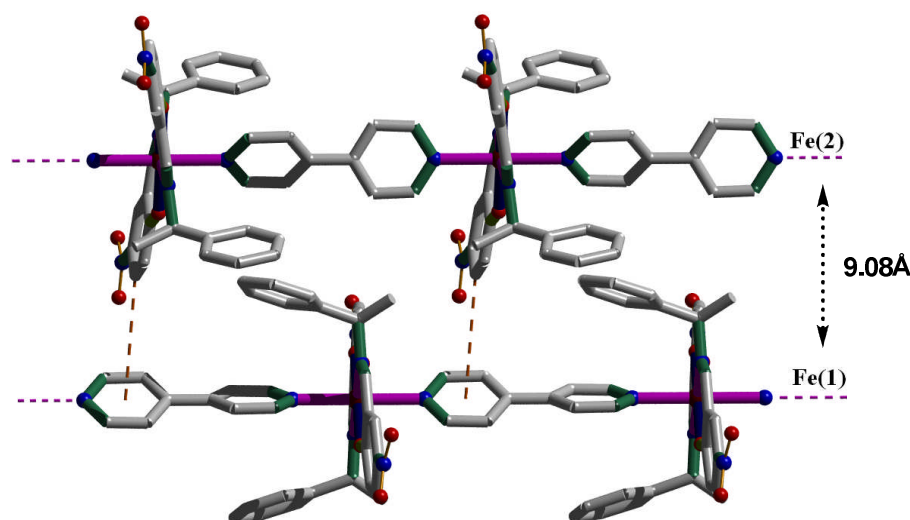


Figure 2.9: Alternating directions of neighbouring chains in $[\{\text{FeL}^3_2(\mu\text{-bpy})\}\cdot\text{THF}]_\infty$ showing edge-face interactions (brown dash lines). (Hydrogen atoms and solvent THF removed for clarity).

2.3.6 $[\{\text{FeL}^5_2(\mu\text{-bpy})\}\cdot 0.5\text{MeOH}]_\infty$

The asymmetric unit of $[\{\text{FeL}^5_2(\mu\text{-bpy})\}\cdot 0.5\text{MeOH}]_\infty$ contains two independent monomer units at Fe(1) and Fe(2) which form chains running in opposite directions (Figure 2.10). In the structures described earlier the mean planes of the salicyl arene units are close to orthogonal to the polymer axis, and the angles between these planes are usually $<10^\circ$. In the Fe(2) chain here there is a substantial distortion creating a bowl around the *C* enantiomeric face of the complex unit; the angle between the two salicyl arene planes (i.e. at the base of the bowl) is *ca* 112° . This is accompanied by a unusually large distortion from octahedral in the first coordination sphere at Fe(2) [with the angle N(5)-Fe(2)-N(5') rather low at $171.8(10)^\circ$] and the formation of a triple π - π stack between the two phenethyl groups and the bpy ring at N(8) outside the bottom of the bowl. The angle between mean planes defined by the two symmetry-related phenethyl aromatic rings and the pyridinyl unit is 9.25° with the shortest interatomic contact 3.32 \AA . At the Fe(1) centres there is also a significant bowl distortion with the same orientation as at Fe(2) but it is less pronounced, and the angle between salicyl arene planes is 153° .

Figure 2.10 also indicates short edge-face interactions formed between the chains. Nearest neighbour chain axes are *ca* 8.06 \AA apart with a more distant approach of 10.53 \AA . The longer inter-chain distance is also indicated in Figure 2.11 which shows how the relative orientations of the chains and in particular the lateral “shift” between chains positions in the crystal.

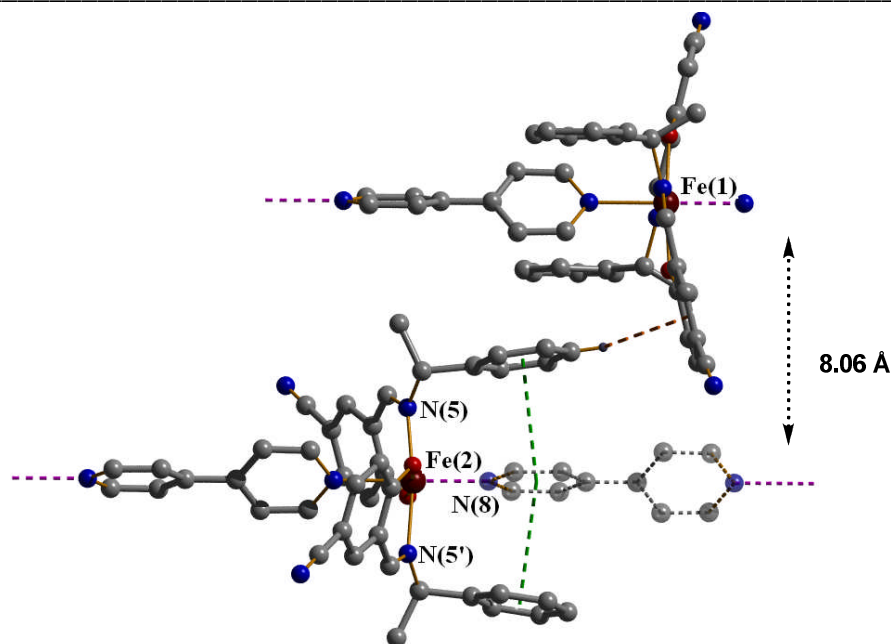


Figure 2.10: Asymmetric unit for $[\{\text{FeL}^5_2(\mu\text{-bpy})\} \cdot 0.5\text{MeOH}]_\infty$ showing triple π - π stacking (green dash lines) and edge-face contact (brown dash lines). Hydrogen atoms and solvent CHCl_3 have been removed for clarity.

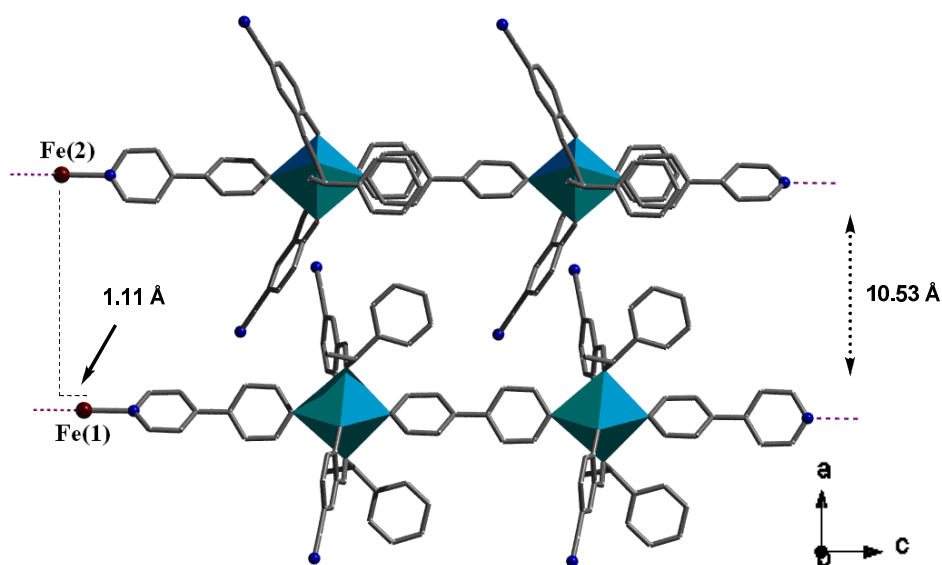


Figure 2.11: Showing the longer inter-chain distance and lateral shift between Fe atoms in adjacent chains in $[\{\text{FeL}^5_2(\mu\text{-bpy})\} \cdot 0.5\text{MeOH}]_\infty$

2.3.7 $[\{\text{FeL}^6_2(\mu\text{-bpy})\}\cdot\text{THF}]_\infty$

The compound $[\{\text{FeL}^6_2(\mu\text{-bpy})\}\cdot\text{THF}]_\infty$ comprises linear chains all oriented in the same direction. The dihedral angle between mean planes through the pyridinyl units of the bridging ligand is ca 31.6°. The aromatic rings of the phenethyl substituents have no strong intramonomer interactions with the bridge but there are many contacts with neighbouring polymer chains. The monomers lie in the plane of a hydrogen bonded network formed by the OH groups Figure 2.12(b)). These hydrogen bonded contacts are complemented by several CH *pi* interactions between the neighbouring chains involving the phenethyl aromatic rings, the salicyl rings and the bpy ligand, and range from 2.4 to 3.4 Å in the CH to ring centroid distance. Although the intra-chain Fe-Fe distances are governed by the length of the bridging bpy ligand, this compound has the shortest inter-chain Fe-Fe distance at 8.7967(2) Å (inter-chain axis distance d_2 of 6.58 Å). Additionally, there is a much longer inter-chain distance of 14.89 Å between pairs connected by hydrogen bonds.

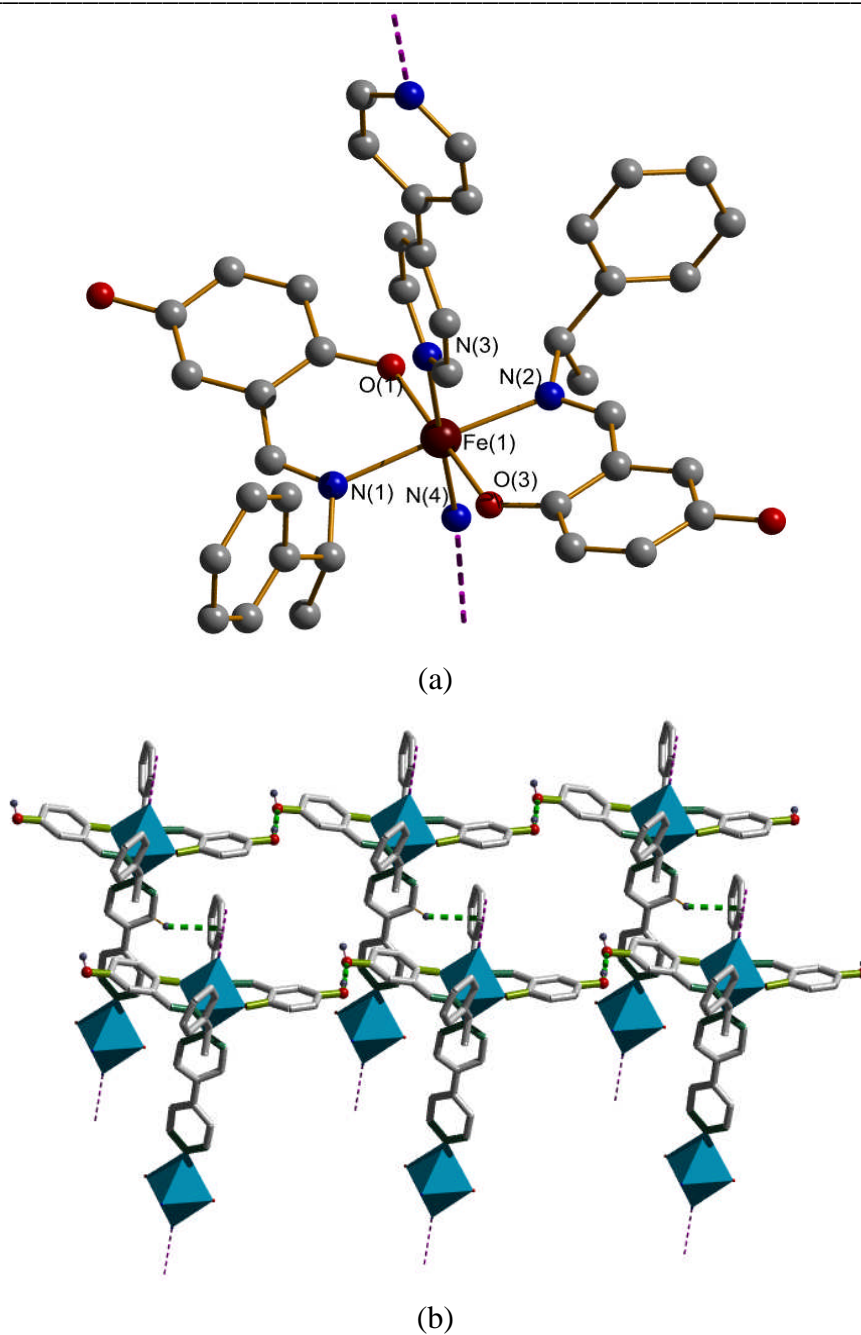
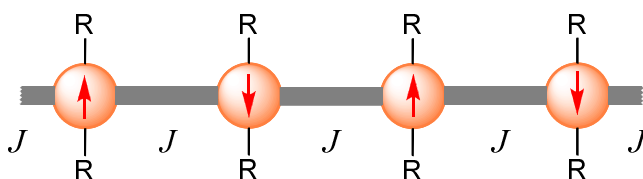


Figure 2.12: (a) The asymmetric unit of $[FeL^6_2(\mu-bpy)] \cdot THF$; (b) Interchain hydrogen bonds and edge-face CH... π contacts in $\{FeL^6_2(\mu-bpy)\}_\infty$. (Hydrogens and solvent molecules have been removed for clarity)

2.4 Magnetic measurements

In this section we will describe trends in the magnetic properties that relate to the nature of the bridging group, inter-chain distances and electronic properties of the Fe complex units arising from the ligand substituents.

For mononuclear iron(II) complexes with a regular octahedral crystal field, the $^5T_{2g}$ ground term has a first-order spin-orbit coupling contribution (with a spin-orbit parameter λ of about -100 cm^{-1}) which removes the degeneracy of the electronic ground states and may cause magnetic anisotropy. In this case, the average susceptibility may not follow the Curie-Weiss law, particularly at low temperatures.² The presence of four unpaired electrons ($S = 2$), together with the imposed distortion from O_h symmetry, results in the $^5T_{2g}$ term splitting into the 5B_2 and 5E multiplets, or a zero-field splitting (ZFS).² For an isolated Fe(II) ion, a spin only $\chi_M T$ value of $3.001\text{ cm}^3\text{ K mol}^{-1}$ (when $g = 2$, χ_M is molar magnetic susceptibility) would be expected at room temperature, which should remain constant as temperature is lowered. However, due to the presence of either ZFS, antiferromagnetic interactions or spin crossover (SCO),⁴¹ the experimental magnetic moments can be lower than this value.⁴²



Scheme 2.2: Schematic representation of the intrachain coupling where J is the antiferromagnetic coupling constant, R is the substituent on ligand L^n (Scheme 2.1). Circles represent the paramagnetic metal complex units FeL^n_2 .

As spin-orbit coupling contributes significantly for regular octahedral complexes and ZFS contributes more when there is a strong distortion in the regular geometry, the magnetic behavior for mononuclear Fe(II) complexes will depend on the geometry. Further complication arises when there is the possibility of exchange-coupled transition-metal ions, as in the coordination polymers we present here (Scheme 2.2). When the Fe(II) magnetic centres are bridged with either pz or bpy, the magnetic coupling between the two nearest spin carriers is expected to be antiferromagnetic. To study these systems we have modelled the high temperature data ($> ca. 50K$) with the Curie-Weiss law, in order to determine the magnitude of short range coupling. For some compounds a slightly modified Curie-Weiss equation has been used which takes into consideration a small temperature independent paramagnetic term. In addition we have applied a model covering the whole temperature range, which depends on the form of the data. Some compounds show antiferromagnetic order, with a maximum in χ_M vs T at T_N . For these we have assumed a 1 D chain structure and applied the Bonner-Fisher equation (Eqn. 2.1) for a $S = 2$ system in order to extract J and g values.⁴³

$$\mathbf{H} = -J \sum_{i=1}^{n-1} \mathbf{S}_{A_i} \cdot \mathbf{S}_{A_{i+1}} + D \sum_{i=1}^n [S^2_{A_i(z)} - S_A(S_A + 1)/3]$$

$$\chi_M = \frac{Ng^2\beta^2 S(S+1)}{3kT} \frac{1+u}{1-u} \quad \dots\dots\dots \text{Eqn. 2.1}$$

$$\text{where } u = \coth \left[\frac{JS(S+1)}{kT} \right] - \left[\frac{kT}{JS(S+1)} \right]$$

The remaining compounds do not have a maximum in χ_M , but do have a sharp downturn in $\chi_M T$, at low temperature, and we have assumed the effect is a result of

ZFS. For these cases we have applied a ZFS model for d^6 high spin octahedral species (Eqn. 2.2), to extract g and D , the axial ZFS parameter.⁴⁴

$$\mathbf{H} = D \left[S_z^2 - \frac{1}{3} S(S+1) \right] + E (S_x^2 - S_y^2)$$

$$\chi_m = (\chi_{\parallel} + \chi_{\perp})/3$$

$$\text{where } \chi_{\perp} = \frac{Ng^2\beta^2}{kT} \left(\frac{2\exp(-A) + 8\exp(-4A)}{1 + 2\exp(-A) + 2\exp(-4A)} \right)$$

$$\chi_{\parallel} = \frac{Ng^2\beta^2}{kT} \left(\frac{(6A^{-1})(1 - \exp(-A)) + \left(\frac{4}{3}A^{-1}\right)(\exp(-A) + \exp(-4A))}{1 + 2\exp(-A) + 2\exp(-4A)} \right) \text{ and}$$

$$A = \frac{D}{kT}$$

.....Eqn. 2.2

Table 2.1 summarizes the parameters obtained from least squares fitting to the above equations.

2.4.1 Magnetic data for $\{\text{FeL}^1_2(\mu\text{-pz})\}_{\infty}$

Figure 2.13 shows curves of χ_M , and $\chi_M T$ vs. T for $\{\text{FeL}^1_2(\mu\text{-pz})\}_{\infty}$. From 350 K, the molar susceptibility χ_M increases smoothly with decreasing temperature, passing through a rounded maximum at 14 K, and then decreases down to the base temperature. The value of $\chi_M T$ decreases gradually from room temperature ($3.438 \text{ cm}^3 \text{ K mol}^{-1}$) to 70 K ($3.016 \text{ cm}^3 \text{ K mol}^{-1}$) and then drops rapidly to $0.512 \text{ cm}^3 \text{ K mol}^{-1}$. This indicates an antiferromagnetic ordered behaviour. A least squares fit to the Bonner-Fisher equation gives $J = -2.44 \text{ cm}^{-1}$ and $g = 2.20$ (solid line in Figure 2.13). The inverse molar susceptibility χ_M^{-1} vs. T for $\{\text{FeL}^1_2(\mu\text{-pz})\}_{\infty}$

is given in Figure 2.14, and fitting to the Curie-Weiss law (solid line) gives a Curie constant of 3.60 and a Weiss constant of -13.72 K.

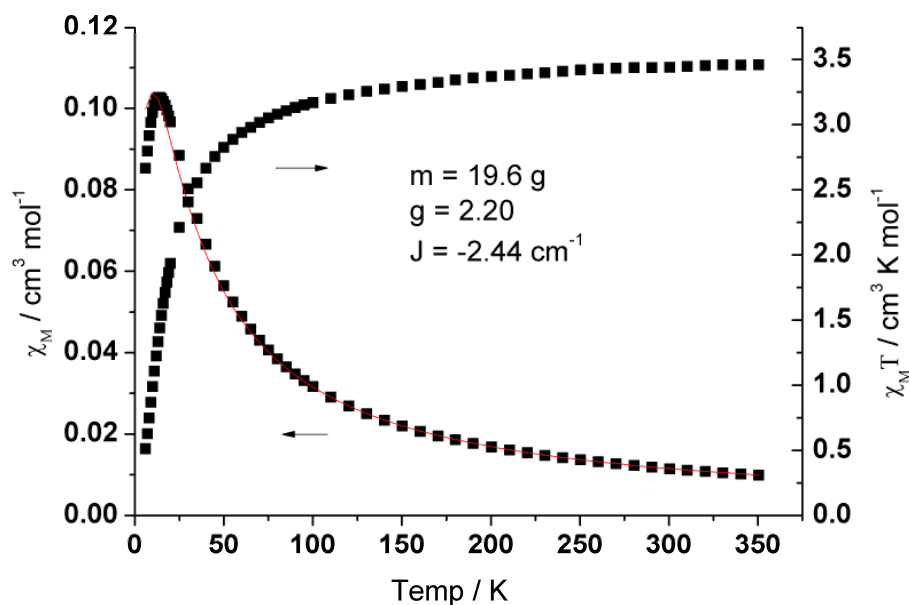


Figure 2.13: χ_M and $\chi_M T$ vs. T for $\{\text{FeL}^1_2(\mu\text{-pz})\}_\infty$ with fitting to the Bonner-Fisher equation

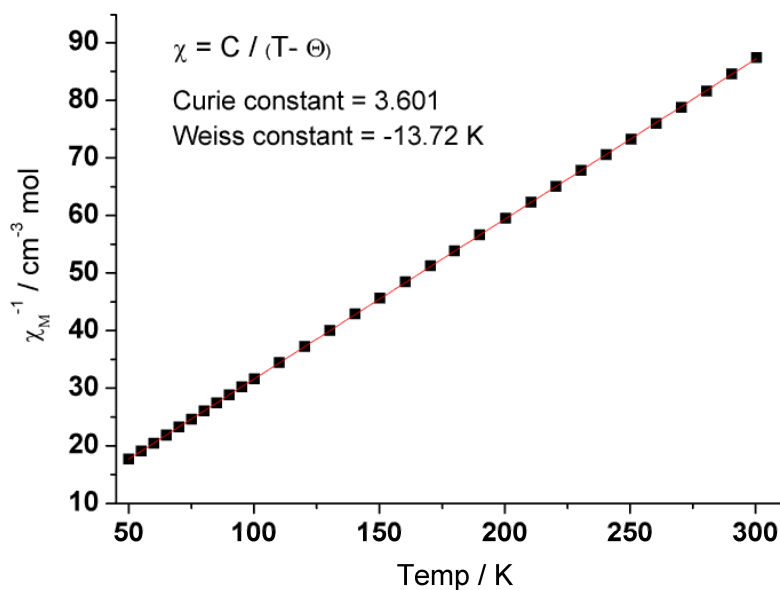


Figure 2.14: χ_M^{-1} vs. T for $\{\text{FeL}^1_2(\mu\text{-pz})\}_\infty$ with fitting to the Curie-Weiss Law

2.4.2 Magnetic data for $\{\text{FeL}^1_2(\mu\text{-bpy})\}_\infty$

Curves of χ_M and $\chi_M T$ vs. T for $\{\text{FeL}^1_2(\mu\text{-bpy})\}_\infty$ are shown in Figure 2.15. The room temperature $\chi_M T$ value per Fe(II) ion is $3.521 \text{ cm}^3 \text{ K mol}^{-1}$, which is comparable to the expected spin only value of $3.372 \text{ cm}^3 \text{ K mol}^{-1}$, when $S = 2$ and $g = 2.10$ (g is obtained from fitting the data to the ZFS model). The fitting to the ZFS model also gives a value of $D = 10.2 \text{ cm}^{-1}$. A plot of the inverse molar susceptibility χ_M^{-1} vs. T (Figure 2.16) shows a slight deviation from Curie-Weiss behaviour, which was modeled by a modified Curies-Weiss law ($\chi_M = C / (T - \Theta) + \chi_{\text{TIP}}$). This gave a Curie constant of 3.23, a Weiss constant of -0.48 K and a temperature independent paramagnetic term, χ_{TIP} , of $1.0 \times 10^{-5} \text{ cm}^3 \text{ mol}^{-1}$. Compared to $\{\text{FeL}^1_2(\mu\text{-pz})\}_\infty$, the intrachain Fe(II)-Fe(II) distance is longer, at $11.5749(2) \text{ \AA}$, and there is consequently no observed antiferromagnetic ordering.

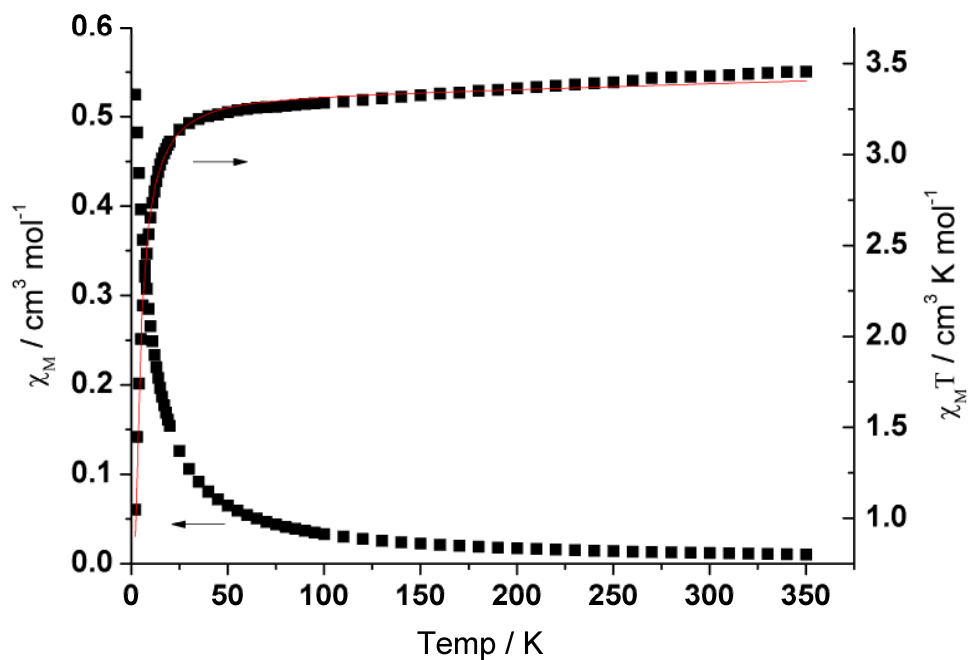


Figure 2.15: χ_M and $\chi_M T$ vs. T for $\{\text{FeL}^1_2(\mu\text{-bpy})\}_\infty$ with fitting to the ZFS model.

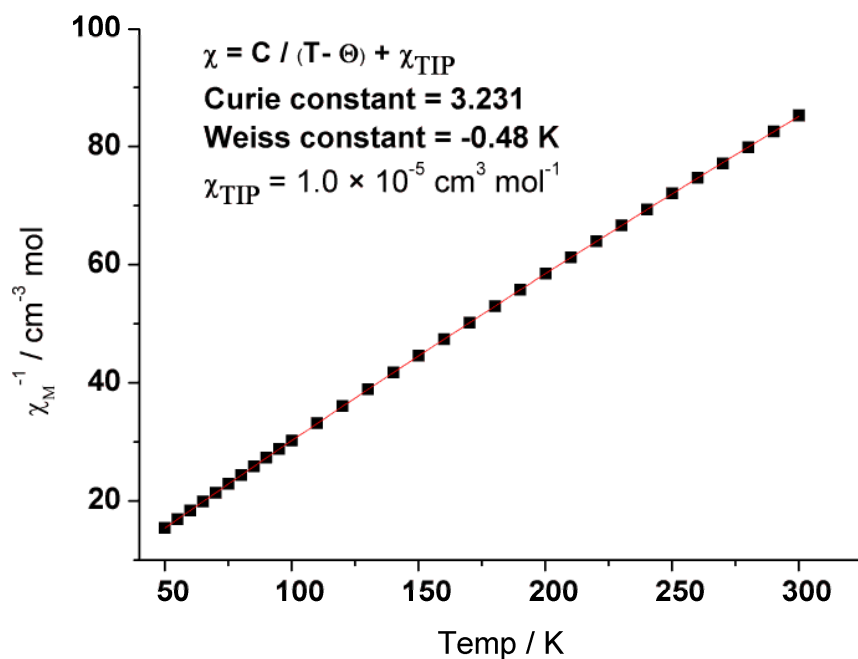


Figure 2.16: χ_M^{-1} vs. T for $\{\text{FeL}^1_2(\mu\text{-bpy})\}_\infty$ with fitting to the Curie-Weiss Law

2.4.3 Magnetic data for $\{\text{FeL}_2(\mu\text{-pz})\}_\infty$

The χ_M and $\chi_M T$ vs. temperature plots for $\{\text{FeL}_2(\mu\text{-pz})\}_\infty$ are shown in Figure 2.17. The $\chi_M T$ values in the higher temperature region of 300-100 K range from $3.569 \text{ cm}^3 \text{ K mol}^{-1}$ (at 300 K) to $3.277 \text{ cm}^3 \text{ K mol}^{-1}$ (100 K). This is the expected spin-only value for a HS Fe(II) species ($3.533 \text{ cm}^3 \text{ K mol}^{-1}$, $S = 2$, $g = 2.14$). After this point, a steady decrease in $\chi_M T$ continues until the low temperature region (30-2 K). A plot of the inverse molar susceptibility vs. temperature can be fitted to the Curie-Weiss law giving $C = 3.77 \text{ cm}^3 \text{ K mol}^{-1}$, Weiss constant of -16.06 K (Figure 2.18). The negative Weiss constant indicates that the dominant coupling is antiferromagnetic. The fitting to the ZFS model also gives a value of $D = 38.5 \text{ cm}^2$

1.

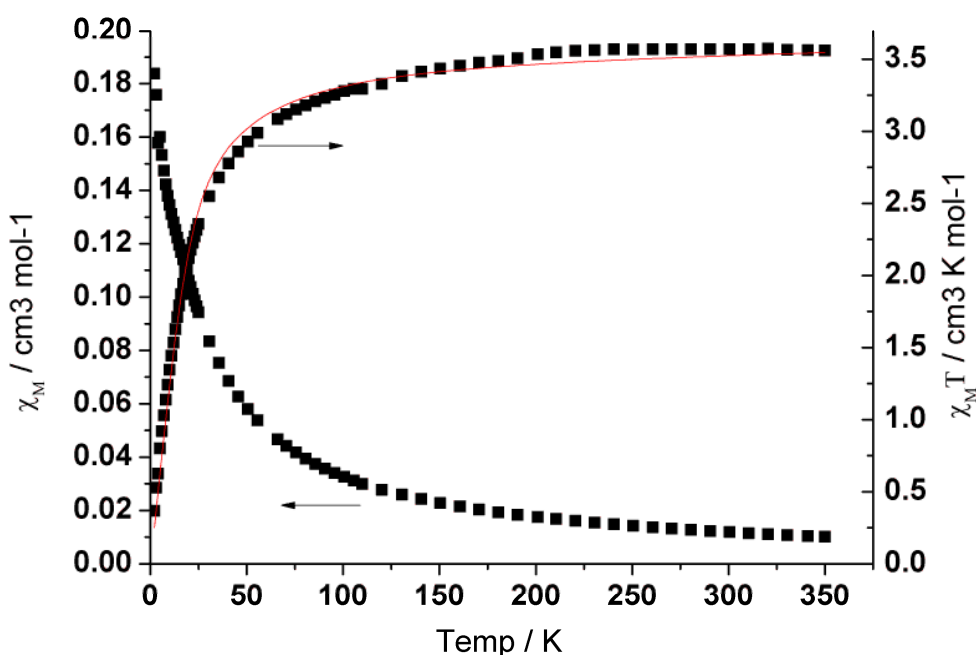


Figure 2.17: χ_M and $\chi_M T$ vs. temperature for $\{\text{FeL}_2(\mu\text{-pz})\}_\infty$ with fitting to ZFS model

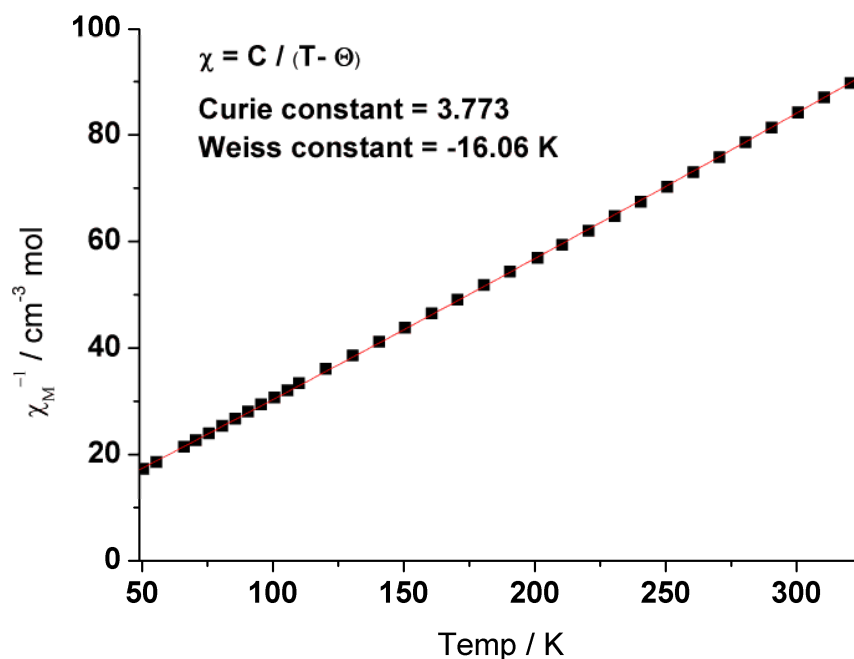


Figure 2.18: χ_M^{-1} vs. temperature for $\{\text{FeL}^2_2(\mu\text{-pz})\}_\infty$ with fitting to χ_M^{-1}

2.4.4 Magnetic data for $\{\text{FeL}^2_2(\mu\text{-bpy})\}_\infty$

The molar susceptibility, χ_M , and $\chi_M T$ for $\{\text{FeL}^2_2(\mu\text{-bpy})\}_\infty$ in the temperature range 2-350 K is shown in Figure 2.19. At 300 K, the $\chi_M T$ value of $3.629 \text{ cm}^3 \text{ K mol}^{-1}$ is slightly higher than expected for non-coupled spin only Fe(II) ions $3.404 \text{ cm}^3 \text{ K mol}^{-1}$, $S = 2$, $g = 2.10$). A plot of χ_M^{-1} vs. temperature for $\{\text{FeL}^2_2(\mu\text{-4,4'-bipyridine})\}_\infty$ is shown in Figure 2.20. The average susceptibility can be fitted to the modified Curie-Weiss law as above to give a $C = 3.21 \text{ cm}^3 \text{ K mol}^{-1}$, Weiss constant of -0.23 K and χ_{TIP} of $1.4 \times 10^{-3} \text{ cm}^3 \text{ mol}^{-1}$. The fitting to the ZFS model also gives a $D = 11.5 \text{ cm}^{-1}$.

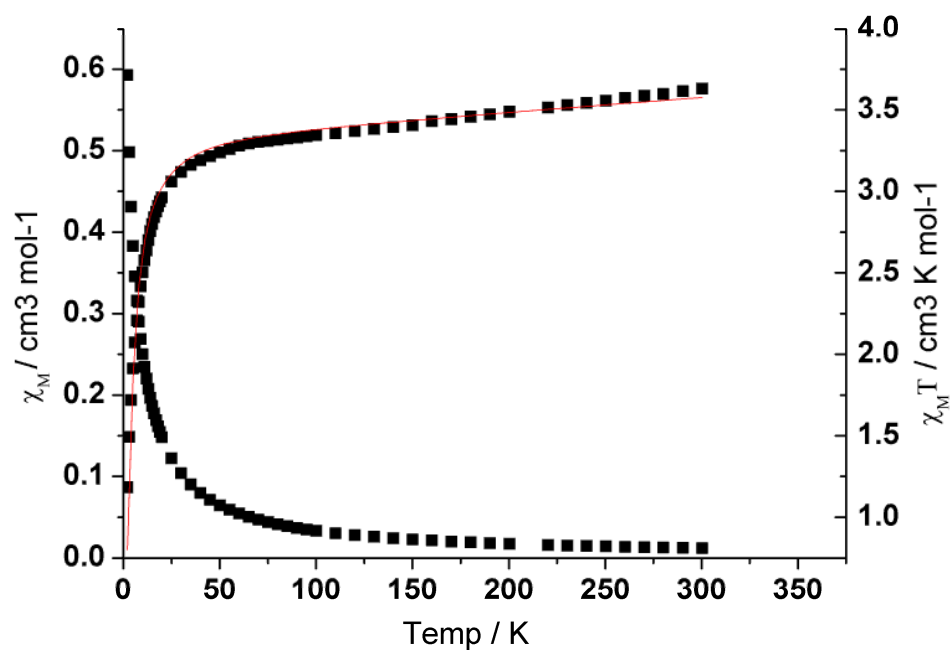


Figure 2.19. χ_M and $\chi_M T$ vs. temperature for $\{\text{FeL}^2_2(\mu\text{-bpy})\}_\infty$ with fitting to ZFS model

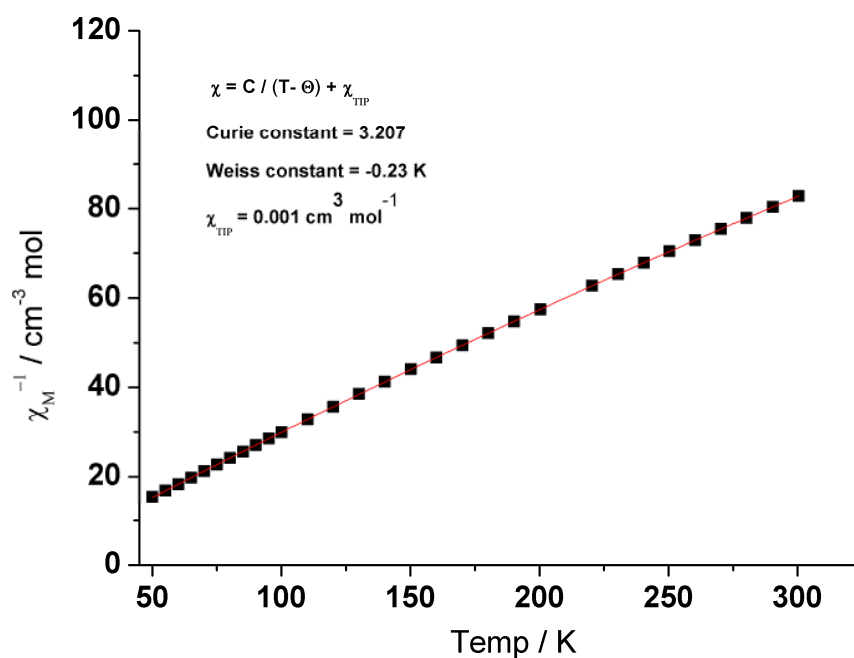


Figure 2.20: χ_M^{-1} vs. temperature for $\{\text{FeL}^2_2(\mu\text{-bpy})\}_\infty$ with fitting to χ_M^{-1}

2.4.5 Magnetic data for $\{\text{FeL}^3_2(\mu\text{-pz})\}_\infty$ and $\{\text{FeL}^3_2(\mu\text{-bpy})\}_\infty$

Curves of χ_M and $\chi_M T$ vs. temperature for $\{\text{FeL}^3_2(\mu\text{-pz})\}_\infty$, $\{\text{FeL}^3_2(\mu\text{-bpy})\}_\infty$ are shown in Figure 2.21 and Figure 2.23. The values of $\chi_M T$ for the two complexes are $3.352 \text{ cm}^3 \text{ K mol}^{-1}$ and $3.513 \text{ cm}^3 \text{ K mol}^{-1}$ at 300 K. Both of them show a slightly decrease from 300K to 80 K, indicating a short range of antiferromagnetic coupling; the fits (Figure 2.22, 2.24) for two complexes are performed using Curie-Weiss law to obtain $\Theta = -5.67 \text{ K}$ and -7.55 K respectively. The fitting to the ZFS model also gives $D = 21.0 \text{ cm}^{-1}$ and 10.2 cm^{-1} for these two complexes.

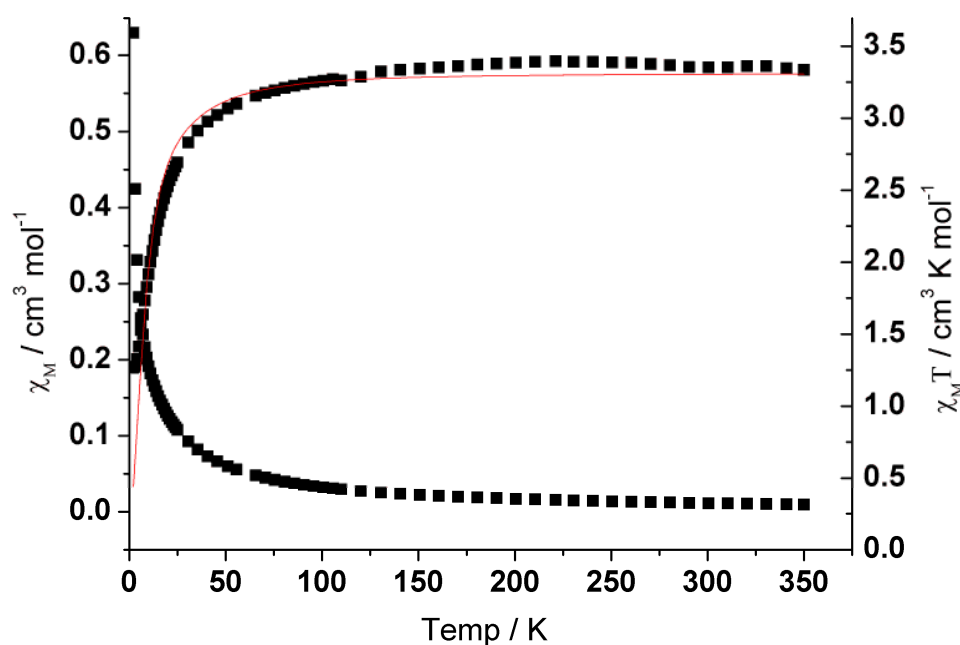


Figure 2.21: χ_M , $\chi_M T$ vs. Temperature for $\{\text{FeL}^3_2(\mu\text{-pz})\}_\infty$

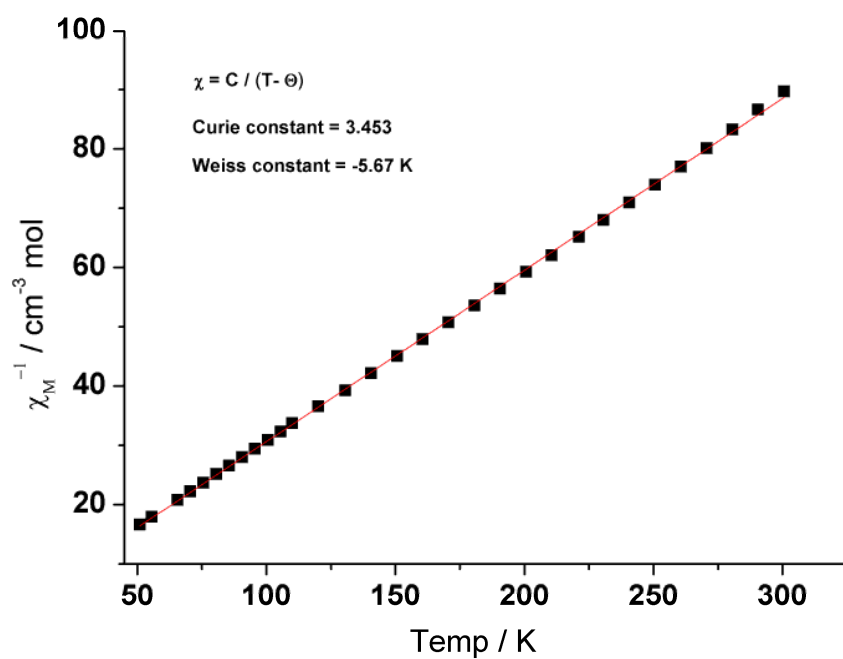


Figure 2.22: χ_M^{-1} vs. temperature for $\{\text{FeL}^3(\mu\text{-pz})\}_\infty$ with fitting to χ_M^{-1}

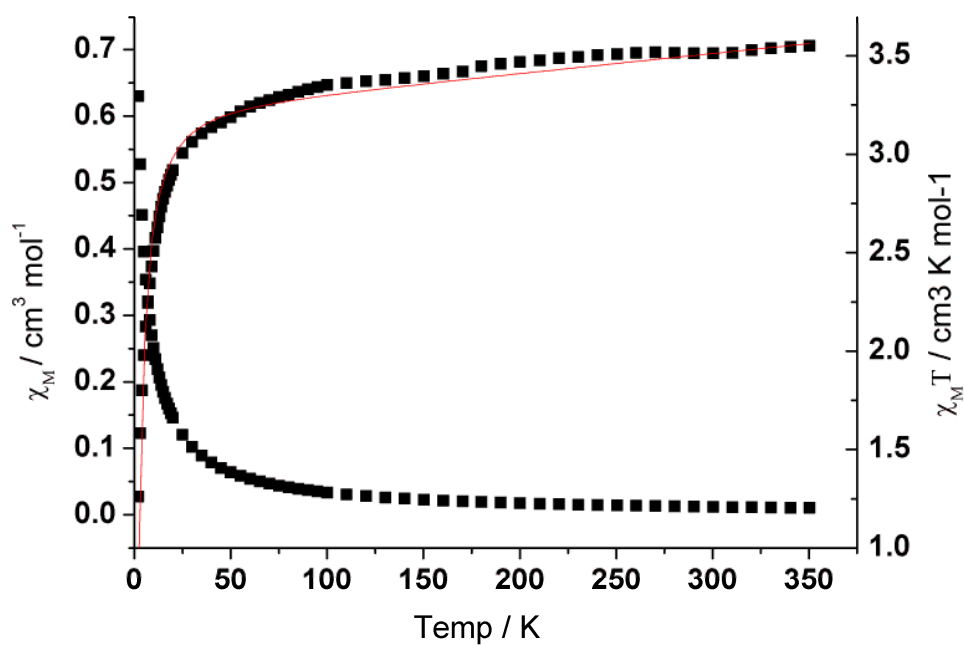


Figure 2.23: χ_M , $\chi_M T$ vs. Temperature for $\{\text{FeL}^3(\mu\text{-bpy})\}_\infty$

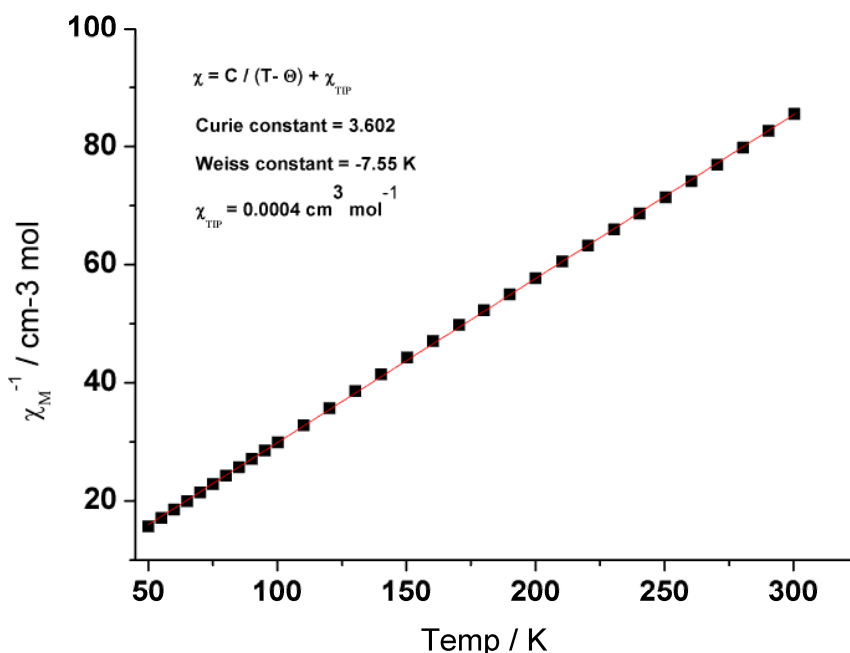


Figure 2.24: χ_M^{-1} vs. temperature for $\{\text{FeL}^3_2(\mu\text{-bpy})\}_\infty$ with fitting to χ_M^{-1}

2.4.6 Magnetic data for $\{\text{FeL}^4_2(\mu\text{-pz})\}_\infty$

The χ_M and $\chi_M T$ vs. temperature plot for $\{\text{FeL}^4_2(\mu\text{-pz})\}_\infty$ is shown in Figure 2.26. The χ_M value in the temperature region of 300-19 K range from $0.010 \text{ cm}^3 \text{ K mol}^{-1}$ (at 300 K) to $0.068 \text{ cm}^3 \text{ K mol}^{-1}$ (19 K). A sharp maximum is observed in the χ_M vs. temperature curve, which indicates an antiferromagnetic coupling at $T_N = 19 \text{ K}$ mediated by the pyrazine bridging ligand. The same approach has been used approximately as that adopted for $\{\text{FeL}^1_2(\mu\text{-pz})\}_\infty$. The best agreement between experimental and calculated data corresponds to $J = -3.85 \text{ cm}^{-1}$ and $g = 2.14$. The red solid lines represent the best fit obtained.

The inverse χ_M vs. temperature plot for $\{\text{FeL}^4_2(\mu\text{-pz})\}_\infty$ is shown in Figure 2.27. The data were fitted by a modified Curie-Weiss law [$\chi_M = C / (T - \Theta)$]

+ χ_{TIP} , from which the Curie and Weiss constants have been obtained as 3.056 and -18.72 K respectively, with a $\chi_{\text{TIP}} = 5.11 \times 10^{-4} \text{ cm}^3 \text{ mol}^{-1}$.

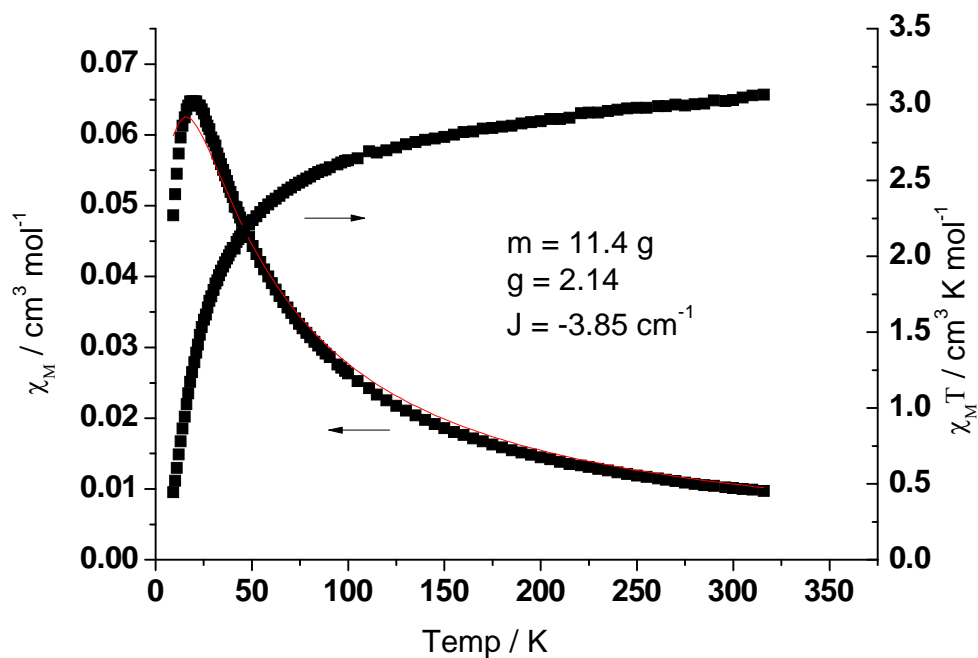


Figure 2.26: χ_M , $\chi_M T$ vs. temperature for $\{\text{FeL}^4_2(\mu\text{-pz})\}_\infty$ with fitting to the Bonner-Fisher equation

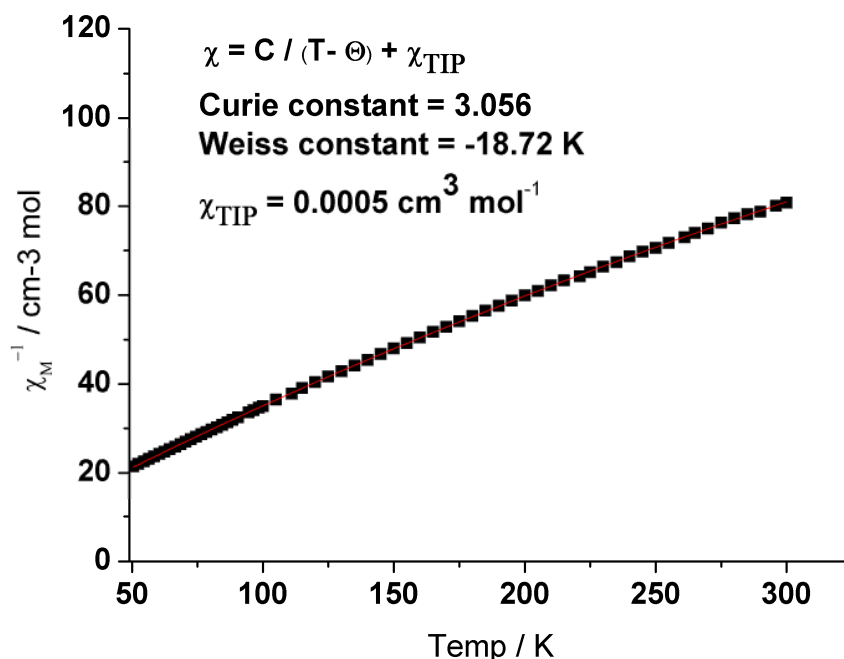


Figure 2.27: χ_{M}^{-1} vs. temperature for $\{\text{FeL}^4_2(\mu\text{-pz})\}_\infty$ with fitting to χ_{M}^{-1}

2.4.7 Magnetic data for $\{\text{FeL}^4_2(\mu\text{-bpy})\}_\infty$

The χ_{M} , $\chi_{\text{M}}T$ vs. temperature plot for $\{\text{FeL}^4_2(\mu\text{-4,4'-bipyridine})\}_\infty$ is shown in Figure 2.28. The room temperature $\chi_{\text{M}}T$ value per Fe(II) ion is $3.526 \text{ cm}^3 \text{ K mol}^{-1}$, which is slightly higher than the expected value ($3.001 \text{ cm}^3 \text{ K mol}^{-1}$ assuming $g = 2.00$, $S = 2$) as a result of a significant orbital contribution. A sharp maximum is also observed in the χ_{M} vs. temperature curve, which indicates an antiferromagnetic coupling with $T_{\text{N}} = 3 \text{ K}$ mediated by the pyrazine bridging ligand. The same approach has been used approximately as that adopted for $\{\text{FeL}^1_2(\mu\text{-pz})\}_\infty$. The best agreement between experimental and calculated data corresponds to $J = -0.72 \text{ cm}^{-1}$ and $g = 2.16$. The red solid lines represent the best fit obtained.

Above 50 K, the inverse χ_M vs. temperature plot for $\{\text{FeL}^4_2(\mu\text{-4,4'}$ -bipyridine) $\}_\infty$ is shown in Figure 2.29. The data were fitted by Curie-Weiss law [$\chi_M = C / (T - \Theta)$], from which the Curie and Weiss constants have been obtained as 3.610 and -3.326 K respectively.

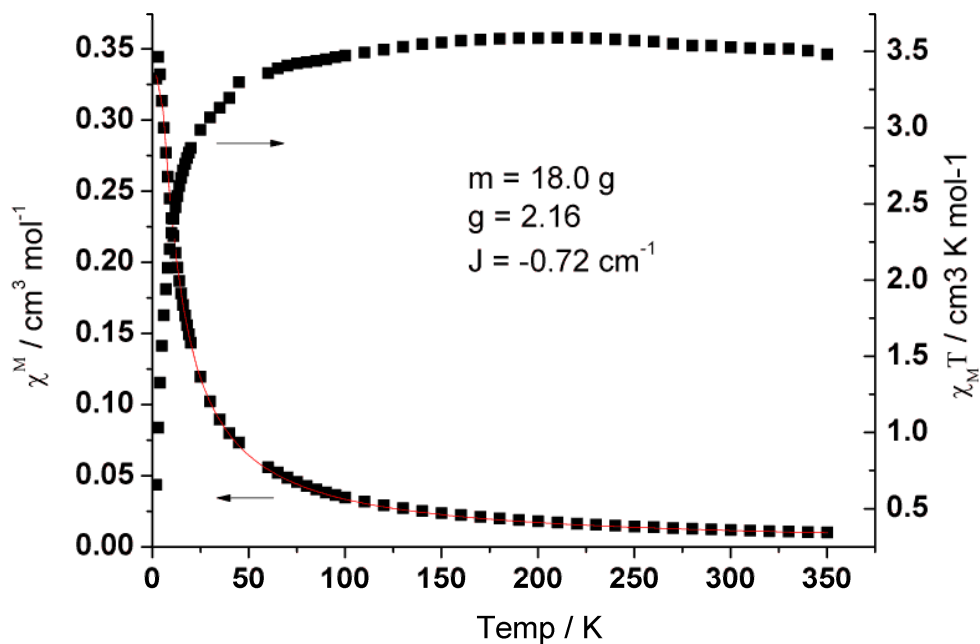


Figure 2.28: χ_M , $\chi_M T$ vs. temperature for $\{\text{FeL}^4_2(\mu\text{-4,4'}$ -bipyridine) $\}_\infty$

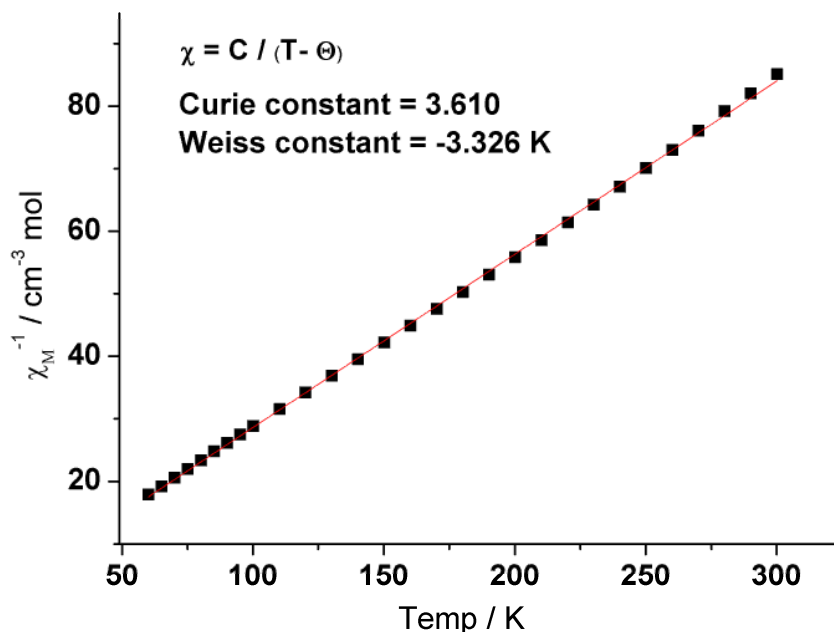


Figure 2.29: χ_M^{-1} vs. temperature for $\{\text{FeL}^4(\mu\text{-bpy})\}_\infty$ with fitting to χ_M^{-1}

2.4.8 Magnetic data for $\{\text{FeL}^5_2(\mu\text{-pz})\}_\infty$

The χ_M , $\chi_M T$ vs. temperature plot for $\{\text{FeL}^5_2(\mu\text{-pz})\}_\infty$ is shown in Figure 2.30. The χ_M value in the temperature region of 300-7 K ranges from $0.011 \text{ cm}^3 \text{ K mol}^{-1}$ (at 300 K) to $0.151 \text{ cm}^3 \text{ K mol}^{-1}$ (7 K). A sharp maximum is observed in the χ_M vs. T curve, which indicates an antiferromagnetic coupling at $T_N = 7 \text{ K}$ mediated by the pyrazine bridging ligand. This was fitted to χ_M using the method explained for $\{\text{FeL}^1_2(\mu\text{-pz})\}_\infty$. The best agreement between experimental and calculated data corresponds to $J = -1.66 \text{ cm}^{-1}$ and $g = 2.20$. The red solid lines represent the best fit obtained.

The temperature dependence of $\chi_M T$ (Figure 2.30) decreases gradually from $3.492 \text{ cm}^3 \text{ K mol}^{-1}$ at 300 K (higher than expected value of $3.00 \text{ cm}^3 \text{ K mol}^{-1}$ for free Fe(II), $S = 2$) to $3.172 \text{ cm}^3 \text{ K mol}^{-1}$ at 100 K. The inverse χ_M vs.

temperature plot for $\{\text{FeL}^5_2(\mu\text{-pz})\}_\infty$ is shown in Figure 2.31. The data were fitted by modified Curie-Weiss law $[\chi_M = C / (T - \Theta) + \chi_{\text{TIP}}]$, from which Curie and Weiss constants have been obtained as $3.317 \text{ cm}^3 \text{ K mol}^{-1}$ and -7.59 K respectively, with a $\chi_{\text{TIP}} = -8.96 \times 10^{-4} \text{ cm}^3 \text{ mol}^{-1}$.

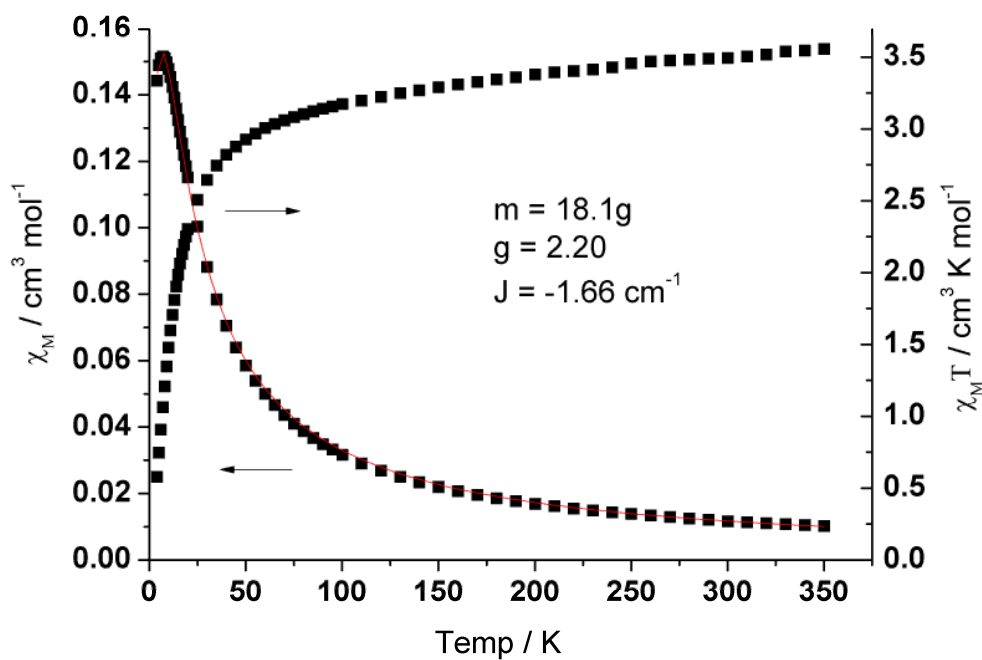


Figure 2.30: χ_M , $\chi_M T$ vs. temperature for $\{\text{FeL}^5_2(\mu\text{-pz})\}_\infty$ with fitting to the Bonner-Fisher equation

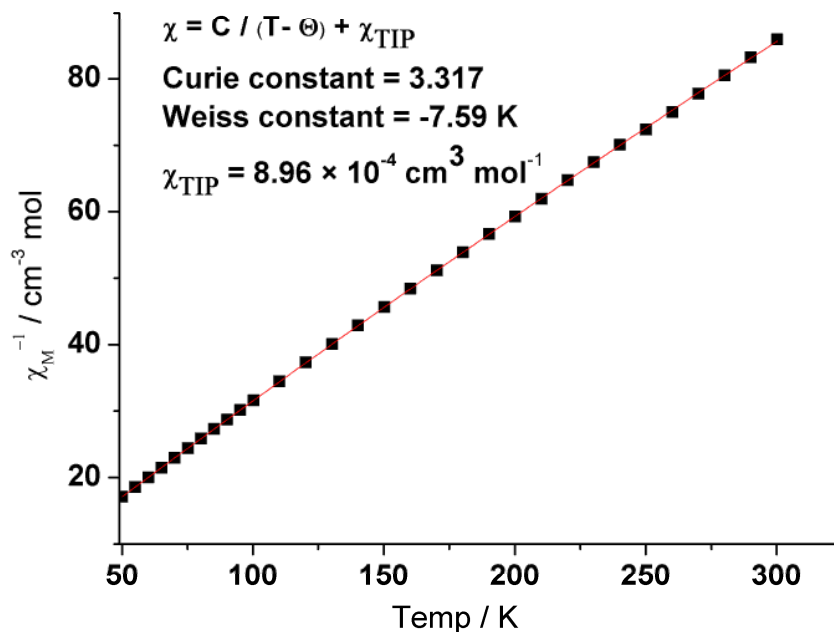


Figure 2.31: χ_M^{-1} vs. Temperature for $\{\text{FeL}^5_2(\mu\text{-pz})\}_\infty$ with fitting to χ_M^{-1}

2.4.9 Magnetic data for $\{\text{FeL}^5_2(\mu\text{-bpy})\}_\infty$

The χ_M , $\chi_M T$ vs. temperature plot for $\{\text{FeL}^5_2(\mu\text{-bpy})\}_\infty$ is shown in Figure 2.32. At 300 K, the $\chi_M T$ value ($3.598 \text{ cm}^3 \text{ K mol}^{-1}$) is slightly higher than the expected value ($3.468 \text{ cm}^3 \text{ K mol}^{-1}$ for free Fe(II) ion with $S = 2$, $g = 2.15$) and then decreases gradually to about $3.505 \text{ cm}^3 \text{ K mol}^{-1}$ at 120 K. Above 50 K, by fitting with Curie-Weiss law on the plot of χ_M^{-1} , χ_M^{-1} vs. temperature (Figure 2.33) Curie and Weiss constants have been obtained as 3.680 and -5.88 K. The negative Weiss constant indicates an antiferromagnetic coupling of the material.

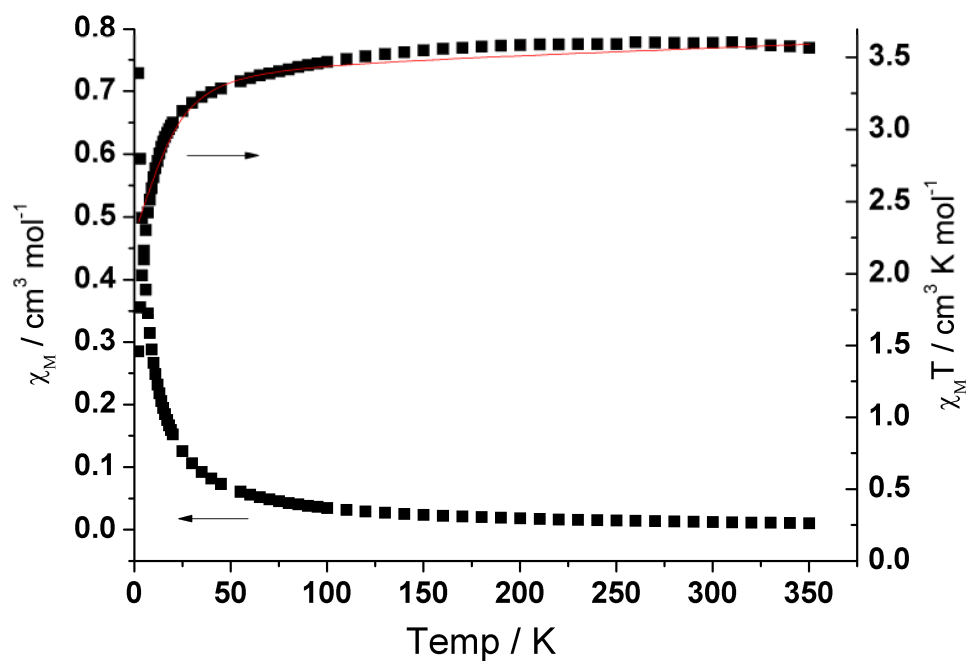


Figure 2.32: χ_M , $\chi_M T$ vs. temperature for $\{\text{FeL}^5_2(\mu\text{-bpy})\}_\infty$ with fitting to ZFS model

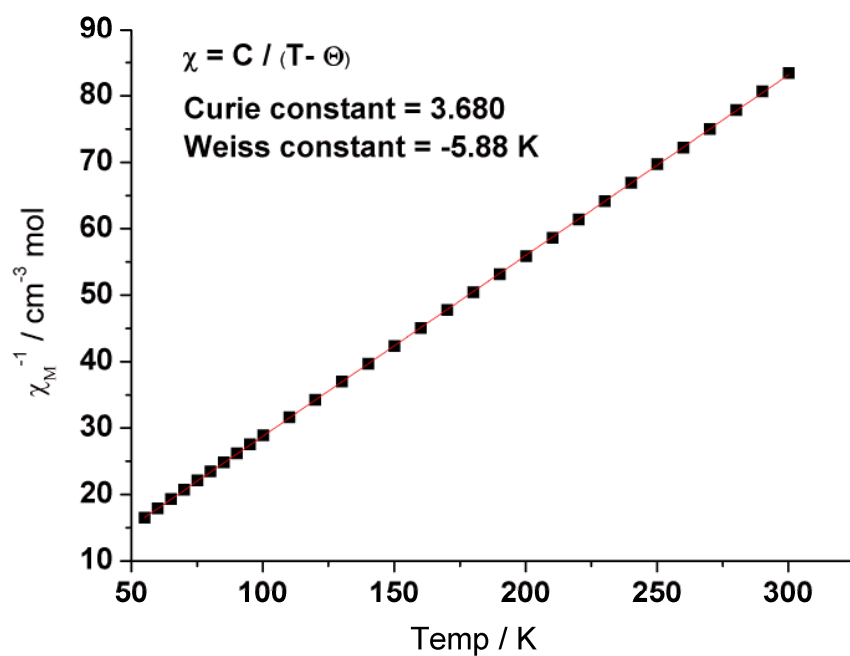


Figure 2.33: χ_M^{-1} vs. Temperature for $\{\text{FeL}^5_2(\mu\text{-bpy})\}_\infty$ with fitting to χ_M^{-1}

2.4.10 Magnetic data for $\{\text{FeL}^5_2(\mu\text{-bpy})\}_\infty$

Curves of χ_M and $\chi_M T$ vs T for the single material based on L^6 i.e. $\{\text{FeL}^6_2(\mu\text{-bpy})\}_\infty$ are shown in Figure 2.34. As the temperature is decreased from 350 to 105 K, the value of $\chi_M T$ is nearly a constant of $3.360 \text{ cm}^3 \text{ K mol}^{-1}$, and then shows a slightly increase of the $\chi_M T$. After passing through a maximum of $3.446 \text{ cm}^3 \text{ K mol}^{-1}$ at 80 K, $\chi_M T$ then drops sharply to $0.894 \text{ cm}^3 \text{ K mol}^{-1}$ at 2 K, indicating the presence of ZFS. While we do not have the analogous pz compound for comparison, the Weiss constant is small, presumably as a result of the relatively large Fe-Fe distance and the electron-releasing effect of the OH group.

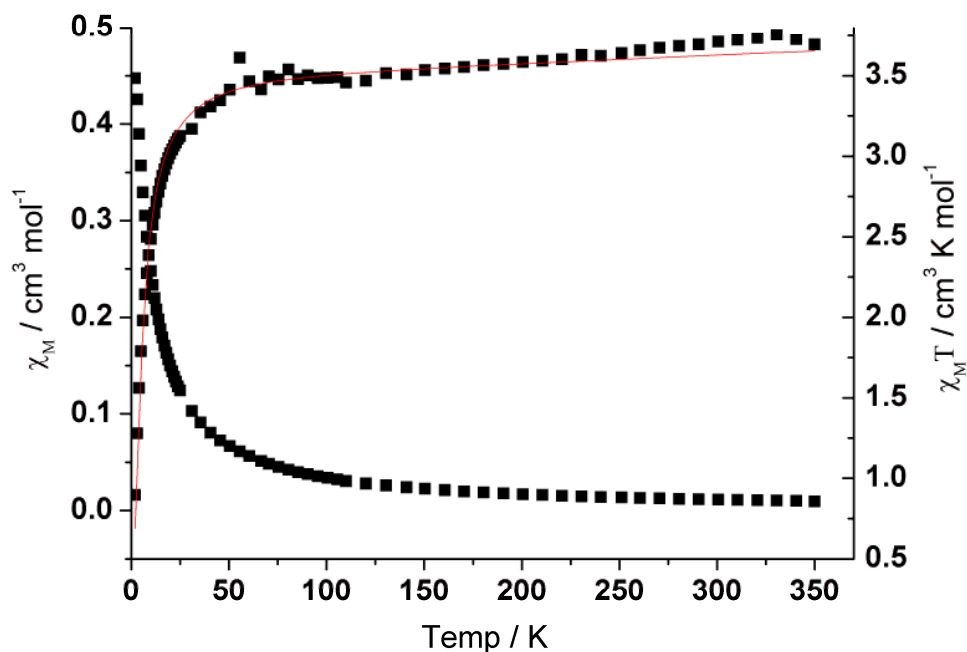


Figure 2.34: χ_M and $\chi_M T$ vs. T for $\{\text{FeL}^6_2(\mu\text{-bpy})\}_\infty$ with fitting to the ZFS model

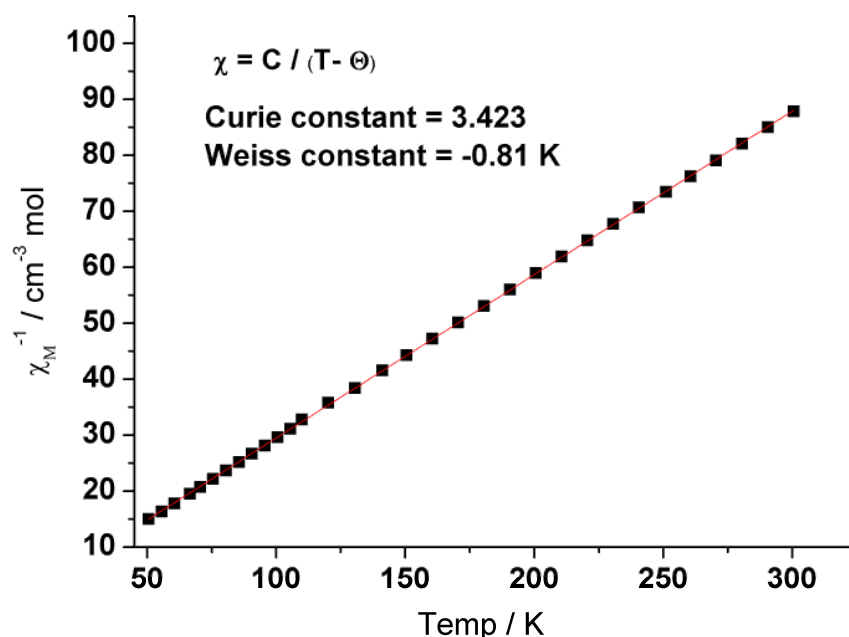


Figure 2.35: χ_M^{-1} vs. Temperature for $\{\text{FeL}^6(\mu\text{-bpy})\}_\infty$ with fitting to the Curie-Weiss Law

2.5 Conclusions

For the pz series there is a clear trend in the magnetic data that as the electron releasing power of the substituent R increases ($L^3 < L^5 < L^1 < L^2 < L^6 < L^4$), the magnitude of Weiss constant Θ increases, consistent with stronger short range antiferromagnetic interaction between spin centres. While there are some structural differences between compounds in this series – perhaps most importantly the zig-zag structure of the L^1 complex – the inter-chain distances are all relatively large (Table 2.1) and the intra-chain interactions are expected to dominate. In this respect it is noteworthy that the Fe...Fe distances d_1 fall off in the same order as above i.e. $L^3 > L^1 > L^2$ from ca 7.37 Å to 7.30 Å. While this change will contribute to an increase in magnetic coupling we consider that it is

insufficient to explain alone the substantial change in Θ . If however we consider the Fe(II) centre to be a charge donor and the neutral pz to be a charge acceptor, as we increase the energy of occupied metal orbitals (by increasing the electron-releasing power of the substituent) we expect to improve the energy match between these orbitals and the acceptor orbitals on the pz ligand, and thus facilitate intrachain magnetic coupling.

For the bpy series the Weiss constants are generally lower in magnitude and there is no consistent trend in the magnetic data with the electronic properties of substituent of R. This might be expected on the basis of the longer distances d_1 compared with the pz series, and indeed corresponds with our expectation that if the intra-chain Fe...Fe distances are too large to facilitate substantial magnetic coupling we do not expect a remote electronic property in substituent R to have a significant modulating effect. We note however that while the pz materials have isolated chains (with some inter-chain secondary interactions) the bpy systems are characterized by interdigitation of planar FeL_2 units (e.g. Figure 2.4). This leads to substantially shorter inter-chain distances d_2 . For the four structures available, d_2 falls from ca 9.1 Å to 6.6 Å in the order $\text{L}^3 > \text{L}^5 > \text{L}^1 > \text{L}^6$ and Θ increases from -7.6 to -0.8 in the same order. There does therefore seem to be a correspondence between this structural parameter d_2 and the magnetic properties, although of course the effects are weak. It is nevertheless reasonable, given that the inter-chain distances are becoming rather short, to ascribe this to the onset of inter-chain magnetic interactions.

2.6 Summary

We have synthesized eleven new polymeric chain complexes. For seven of these materials we have obtained single crystal structural data. As a result of the presence of stereogenic centres on the ligands and/or at the metal atoms, a range of structural types and features was observed; simple 1 D chains, zigzags, directionality of the enantiotopic faces (Figure 2.1(a)) and interchain interactions such as H-bonding and arene-arene contacts. We have also investigated their magnetism: for the complexes bridged with 1,4-pyrazine, relatively short intrachain distances between nearest spin carriers generally leads to strong antiferromagnetic behaviour via coupling along the chain. Electronic effects also play a role and electron releasing groups promote this antiferromagnetic interaction in part via the accompanying shortening of intrachain distances but probably also as a result of the increased reducing power of the Fe(II) centres as R becomes more electron-releasing. For complexes with the longer bpy bridge this electronic effect is unimportant, but since there is a trend in the magnetic data with inter-chain distance we suggest that structural effects including secondary interactions (π -interactions and H-bonding) may be beginning to play a role.

Overall this study clearly shows how the electronic properties of substituents and the crystal structure can affect magnetism in such extended molecular systems.

Table 2.2: Crystallographic data, collection parameters, and refinement parameters for $\{\text{FeL}^n(\mu\text{-Z})\}_\infty$

	$[\{\text{FeL}^1_2(\mu\text{-pz})\}_\infty]_3(\text{Et}_2\text{O})_2$	$[\{\text{FeL}^1_2(\mu\text{-bpy})\}_\infty]_2(\text{MeCN})_2$	$[\{\text{FeL}^2_2(\mu\text{-pz})\}_\infty]_3(\text{MeCN})_{2.25}$	$[\{\text{FeL}^3_2(\mu\text{-pz})\}_\infty](\text{MeCN})_{0.75}$	$[\{\text{FeL}^3_2(\mu\text{-bpy})\}_\infty](\text{THF})_{2.5}$	$\{\text{FeL}^5_2(\mu\text{-bpy})\}_\infty\text{CHCl}_3$	$[\{\text{FeL}^6_2(\mu\text{-bpy})\}_\infty](\text{THF})_2$
empirical formula	$\text{C}_{110}\text{H}_{116}\text{Fe}_3\text{N}_{12}\text{O}_8$	$\text{C}_{44}\text{H}_{42}\text{FeN}_6\text{O}_2$	$\text{C}_{130}\text{H}_{150.75}\text{Fe}_3\text{N}_{14.25}\text{O}_6$	$\text{C}_{35.50}\text{H}_{32.25}\text{FeN}_{6.75}\text{O}_6$	$\text{C}_{50}\text{H}_{54}\text{FeN}_6\text{O}_{8.50}$	$\text{C}_{43}\text{H}_{35}\text{Cl}_3\text{FeN}_6\text{O}_2$	$\text{C}_{48}\text{H}_{52}\text{FeN}_4\text{O}_6$
Fw	1901.70	742.69	2182.45	705.28	930.84	829.97	836.79
crystal size (mm)	0.30 x 0.12 x 0.12	0.20 x 0.10 x 0.08	0.20 x 0.10 x 0.06	0.25 x 0.03 x 0.01	0.40 x 0.18 x 0.02	0.20 x 0.10 x 0.06	0.30 x 0.20 x 0.10
crystal system	Monoclinic	Monoclinic	Monoclinic	Monoclinic	Monoclinic	orthorhombic	Triclinic
space group	C2	C2	C2	P2(1)	P2	P2(1)2(1)2	P1
<i>a</i> (Å)	28.9533(7)	26.8700(6)	25.4871 (8)	7.3694 (6)	13.3100(3)	21.05493(13)	8.7967 (2)
<i>b</i> (Å)	13.0045(3)	11.5749(2)	21.9537 (8)	19.797 (3)	11.6027(2)	16.11390(10)	8.9245 (2)
<i>c</i> (Å)	26.7340(8)	14.8955(3)	24.8107 (11)	12.13478 (18)	15.9378(4)	11.55863(8)	14.7428(4)
α (deg)	90	90	90	90	90	90	102.135
β (deg)	90.526(2)	121	116.882	102.388 (12)	103.807(2)	90	106.334
γ (deg)	90	90	90	90	90	90	97.4319
<i>V</i> (Å ³)	10065.5(5)	3964.96(16)	12382.3 (8)	1729.1 (4)	2390.19(9)	3921.58(4)	1063.73(4)
<i>D</i> _{calcd} (mg/m ³)	1.255	1.244	1.171	1.355	1.293	1.406	1.306
μ (mm ⁻¹)	0.489	3.393	0.405	0.491	0.376	5.330	0.409
<i>F</i> ₀₀₀	4008	1560	4638	733	980	1712	442
total reflections	24234	6483	74329	34948	23230	23665	25207
Independent reflns	16354	4934	40956	6087	11055	6066	13952
<i>R</i> _{int}	0.0369	0.0169	0.1277	0.1937	0.0381	0.0276	0.0239
Data/restraints/param.	16354/ 1192/ 1208	4934/1/485	40956/ 1818/ 1430	6087/ 37/ 453	11.055/ 14/ 590	6066/6/520	13952/ 249/ 580
<i>R</i> 1, [<i>I</i> > 2σ(<i>I</i>)]	0.0582	0.0367	0.0740	0.0487	0.0561	0.0290	0.0492

CHAPTER TWO

<i>wR</i> ²	0.1542	0.0951	0.1691	0.0990	0.1413	0.0784	0.1329
GoF on F ²	0.977	0.985	0.693	0.689	0.975	1.080	1.065
Z	4	4	4	2	2	4	1
T(K)	100(2)	100(2)	100(2)	293(2)	100(2)	100(2)	100(2)
Flack parameter	0.018(16)	0.005(4)	0.02(2)	0.05(3)	0.016(15)	0.006(3)	0.020(10)

2.7 Reference

1. W. L. Leong and J. J. Vittal, *Chem. Rev.*, 2010, **111**, 688-764.
2. O. Kahn, *Molecular Magnetism*, WILEY-VCH, New York, 1993.
3. C. Janiak, *Dalton Trans.*, 2003, 2781-2804.
4. J. Slinker, D. Bernards, P. L. Houston, H. D. Abruna, S. Bernhard and G. G. Malliaras, *Chem. Commun.*, 2003, 2392-2399.
5. S. Ohkoshi, H. Tokoro, T. Matsuda, H. Takahashi, H. Irie and K. Hashimoto, *Angew. Chem. Int. Ed.*, 2007, **46**, 3238-3241.
6. G.-C. Xu, X.-M. Ma, L. Zhang, Z.-M. Wang and S. Gao, *J. Am. Chem. Soc.*, 2010, **132**, 9588-9590.
7. P. Jain, V. Ramachandran, R. J. Clark, H. D. Zhou, B. H. Toby, N. S. Dalal, H. W. Kroto and A. K. Cheetham, *J. Am. Chem. Soc.*, 2009, **131**, 13625-13627.
8. P. O. Kahn and E. Codjovi, *Trans. R. Soc. London, Ser. A*, 1996, **354**, 359.
9. Y. G. O. Kahn, J. -F. Létard and C. Mathonière, 1998, **518**, 127.
10. D. Zhang, H. Wang, L. Tian, H.-Z. Kou, J. Jiang and Z.-H. Ni, *Cryst. Growth Des.*, 2009, **9**, 3989-3996.
11. E. Colacio, M. Ghazi, H. Stoeckli-Evans, F. Lloret, J. M. Moreno and C. Pérez, *Inorg. Chem.*, 2001, **40**, 4876-4883.
12. M. B. Hursthouse, M. E. Light and D. J. Price, *Angew. Chem. Int. Ed.*, 2004, **43**, 472-475.
13. T. Keene, H. Ogilvie, M. Hursthouse and D. Price, *European Journal of Inorg. Chem.*, 2004, **2004**, 1007-1013.
14. H. Tamaki, Z. J. Zhong, N. Matsumoto, S. Kida, M. Koikawa, N. Achiwa, Y. Hashimoto and H. Okawa, *J. Am. Chem. Soc.*, 1992, **114**, 6974-6979.
15. W. Li, H. P. Jia, Z. F. Ju and J. Zhang, *Dalton Trans.*, 2008, 5350-5357.
16. Y.-Z. Zheng, W. Xue, M.-L. Tong, X.-M. Chen, F. Grandjean and G. J. Long, *Inorg. Chem.*, 2008, **47**, 4077-4087.
17. S. Konar, E. Zangrando, M. G. B. Drew, T. Mallah, J. Ribas and N. R. Chaudhuri, *Inorg. Chem.*, 2003, **42**, 5966-5973.
18. Z.-G. Gu, Y.-F. Xu, X.-J. Yin, X.-H. Zhou, J.-L. Zuo and X.-Z. You, *Dalton Trans.*, 2008, 5593-5602.
19. L.-F. Tang, L. Zhang, Li, P. Cheng, Z.-H. Wang and J.-T. Wang, *Inorg. Chem.*, 1999, **38**, 6326-6328.
20. E.-Q. Gao, S.-Q. Bai, Y.-F. Yue, Z.-M. Wang and C.-H. Yan, *Inorg. Chem.*, 2003, **42**, 3642-3649.
21. H.-R. Wen, C.-F. Wang, Y. Song, J.-L. Zuo and X.-Z. You, *Inorg. Chem.*, 2005, **44**, 9039-9045.
22. M. Wriedt, I. Jeß and C. Näther, *European Journal of Inorg. Chem.*, 2009, **2009**, 1406-1413.
23. H. N. Bordallo, L. Chapon, J. L. Manson, C. D. Ling, J. S. Qualls, D. Hall and D. N. Argyriou, *Polyhedron*, 2003, **22**, 2045-2049.

-
24. N. Moliner, M. C. Muñoz, S. Létard, L. Salmon, J.-P. Tuchagues, A. Bousseksou and J. A. Real, *Inorg. Chem.*, 2002, **41**, 6997-7005.
 25. C. Genre, G. S. Matouzenko, E. Jeanneau and D. Luneau, *New J. Chem.*, 2006, **30**, 1669-1674.
 26. S. Tancharakorn, F. P. A. Fabbiani, D. R. Allan, K. V. Kamenev and N. Robertson, *J. Am. Chem. Soc.*, 2006, **128**, 9205-9210.
 27. M. Manoli, R. D. L. Johnstone, S. Parsons, M. Murrie, M. Affronte, M. Evangelisti and E. K. Brechin, *Angew. Chem. Int. Ed.*, 2007, **46**, 4456-4460.
 28. N. Roques, D. Maspoch, I. Imaz, A. Datcu, J.-P. Sutter, C. Rovira and J. Veciana, *Chem. Commun.*, 2008, 3160-3162.
 29. H. W. Roesky and M. Andruh, *Coord. Chem. Rev.*, 2003, **236**, 91-119.
 30. H. Xiang, S.-J. Wang, L. Jiang, X.-L. Feng and T.-B. Lu, *European Journal of Inorg. Chem.*, 2009, **2009**, 2074-2082.
 31. H.-L. Sun, Z.-M. Wang and S. Gao, *Inorg. Chem.*, 2005, **44**, 2169-2176.
 32. S. Triki, F. Bérézovsky, J. Sala Pala, C. J. Gómez-García, E. Coronado, K. Costuas and J.-F. Halet, *Inorg. Chem.*, 2001, **40**, 5127-5132.
 33. J. L. Manson, J. Gu, J. A. Schlueter and H. H. Wang, *Inorg. Chem.*, 2003, **42**, 3950-3955.
 34. C. Train, R. Gheorghe, V. Krstic, L.-M. Chamoreau, N. S. Ovanesyan, G. L. J. A. Rikken, M. Gruselle and M. Verdaguer, *Nature Mater.*, 2008, **7**, 729-734.
 35. G. L. J. A. Rikken, J. Fölling and P. Wyder, *Phys. Rev. Lett.*, 2001, **87**, 236602.
 36. E. Coronado, J. R. Galán-Mascarós, C. J. Gómez-García and A. Murcia-Martínez, *Chem. Eur. J.*, 2006, **12**, 3484-3492.
 37. A. Beghidja, P. Rabu, G. Rogez and R. Welter, *Chem. Eur. J.*, 2006, **12**, 7627-7638.
 38. A. Beghidja, G. Rogez, R. Welter and M. Drillon, *J. Mater. Chem.*, 2006, **16**, 2715-2728.
 39. J. M. Becker, J. Barker, G. J. Clarkson, R. v. Gorkum, G. K. Johal, R. I. Walton and P. Scott, *Dalton Trans.*, 2010, **39**, 2309-2326.
 40. C. Norman F. M. Henpy, K, *International Tables for X-Ray Crystallography*, Kynoch Press, Birmingham, 1965.
 41. P. Gutlich, Y. Garcia and H. A. Goodwin, *Chem. Soc. Rev.*, 2000, **29**, 419-427.
 42. S. C. Manna, E. Zangrando, J. Ribas and N. Ray Chaudhuri, *Inorg. Chim. Acta.*, 2005, **358**, 4497-4504.
 43. M. E. Fisher, *J. Phys.*, 1964, **32**, 343.
 44. *For the family of Fe(II) chains, it is important to note that D and J are strongly correlated, and neither fitting to the Fisher model (antiferromagnetic ordered) or the ZFS model (weak magnetic exchange between magnetic anisotropic Fe(II) centres) is perfect. However, given that the values of D are usually large, D is probably more reliable than J.*
-

3. Two pyridine containing Schiff base isomers as multidentate ligands to construct MOFs

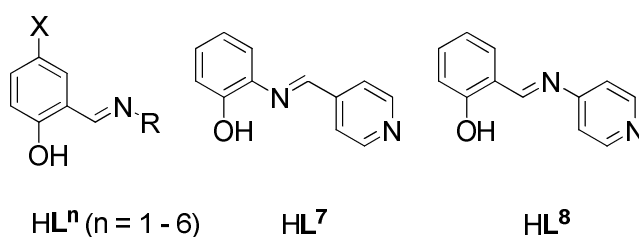
3.1 Introduction

Molecule-based magnetic materials are being investigated for potential applications in fields such as molecular switches, magnetic refrigeration, data storage, and quantum computing.¹⁻⁸ They have many potential advantages over conventional magnets, such as processability, structural diversity and relative ease of magneto-structural correlation. In addition, a number of unusual properties such as spin-crossover,⁸⁻⁹ magnetochiral dichroism (MChD),¹⁰⁻¹¹ and magnetic semiconductivity¹²⁻¹⁵ are available. While preparations of M-M couplings are rarely if ever fully under the control of the synthetic chemist, a great deal of research in this area has provided us with structural targets to attain in order that the interactions between local spin carriers lead to useful properties. For example, ferromagnetic coupling is favoured where neighbouring “magnetic orbitals” are oriented orthogonally, and long-range ordering is promoted by metal-to-metal electronic pathways in multi-dimensional architectures.⁸

In Chapter 2, we introduced a family of chiral 1 D chains comprised of Fe(II) complexes of salicylaldimines **Lⁿ** (n = 1 - 6) linked by pyrazine and bipyridine bridges. The magnitude and nature of M-M coupling was limited by our complex design, and we thus looked to ligand systems which incorporate a

bridging group, and particularly those which would promote orthogonal arrangement of neighbouring units.

We consider the pyridine-conjugated Schiff-base systems HL^7 or HL^8 (Scheme 3.1) to be prototypical in this role, but to our great surprise no complexes of these ligands have been reported. The deceptively simple imine HL^8 has been inaccessible until just recently.¹⁶



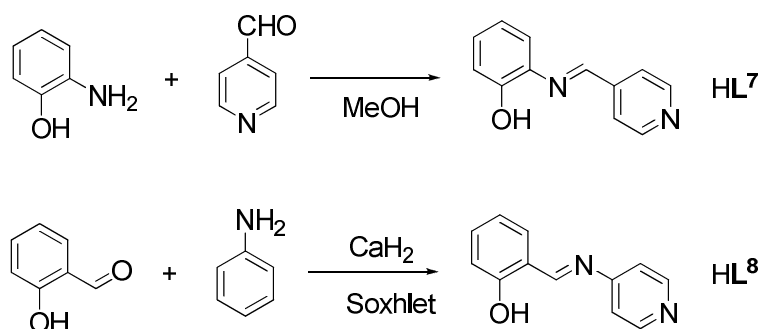
Scheme 3.1: Schiff-base proligands; HL^7 and HL^8 are isomeric.

3.2 Synthesis

3.2.1 Synthesis of ligand precursors (HL^7 and HL^8)

Condensation of 2-aminophenol and isonicotinaldehyde in methanol gave HL^7 in high purity (Scheme 3.2).¹⁷ There have been various mentions of the unstable Schiff-base HL^8 in the literature^{16, 18}. Attempted synthesis of this compound *via* standard conditions from salicylaldehyde and 4-aminopyridine (which has a very poorly nucleophilic NH_2 group) was unsuccessful. Solvent free reactions at 140°C , and refluxing in toluene with a Dean & Stark trap¹⁹ were unproductive. During the course of this work a new synthesis was presented,¹⁶ and while characterising data were presented for the first time, we could not reproduce the synthesis. In our hands this compound could be reliably accessed in high yield by heating

salicylaldehyde and 4-aminopyridine to reflux in dry toluene under an inert atmosphere in a Soxhlet extractor fitted with a CaH_2 filled thimble.

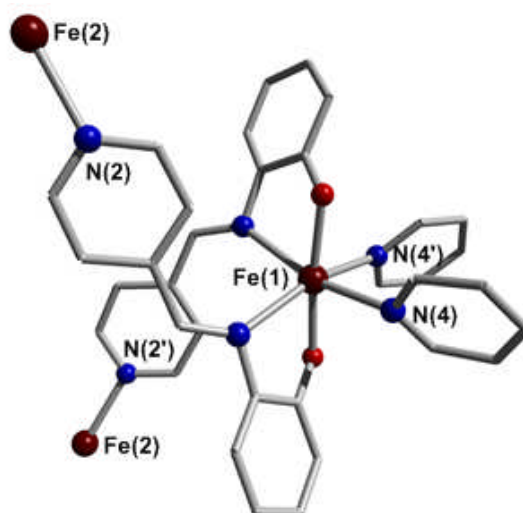


Scheme 3.2: Synthesis of Schiff bases of HL⁷ and HL⁸

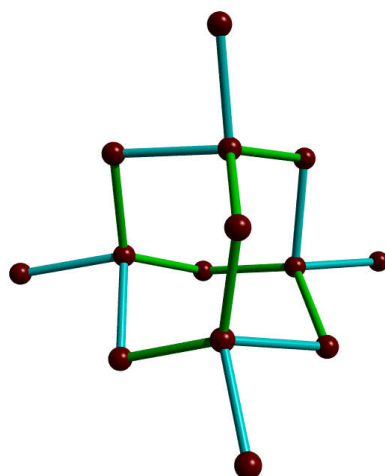
3.2.2 Synthesis of $[\text{FeL}^7_2]_n$ and $[\text{FeL}^8_2]_n$

Deprotonation of proligand HL⁷ with sodium hydride in THF followed by salt metathesis with $[\text{FeCl}_2(\text{THF})_{1.5}]^{20}$ yielded a brown solid $[\text{FeL}^7_2]_n$. Recrystallisation from methanol produced single crystals of $[\text{FeL}^7_2] \cdot 1\frac{1}{4}(\text{H}_2\text{O}) \cdot \frac{1}{2}(\text{MeOH})$. This is the first reported complex of L⁷.

The crystal contains two independent Fe(II) centres each of which are coordinated by two phenoxyimine N-O chelates and two pyridine N atoms from adjacent units [Figure 3.1(a)]. The latter occupy *cis* coordination sites with N(4)-Fe(1)-N(4') and N(2)-Fe(2)-N(2') of 84.5(2) and 89.7(2)° respectively. As a result each Fe centre has four nearest neighbours at *ca* 7.58 and 7.93 Å arranged in a distorted tetrahedron and the extended network is diamond-like [Figures 3.1(b) and 3.2].



(a)



(b)

Figure 3.1: X-ray structure of $[\text{FeL}^7_2] \cdot 1\frac{1}{4}(\text{H}_2\text{O}) \cdot \frac{1}{2}(\text{MeOH})$: (a) the complex unit at Fe(1) [Fe(2) is similar]; (b) the corresponding diamond-like network with Fe-Fe distances of 7.93 Å (turquoise) and 7.58 Å (green).

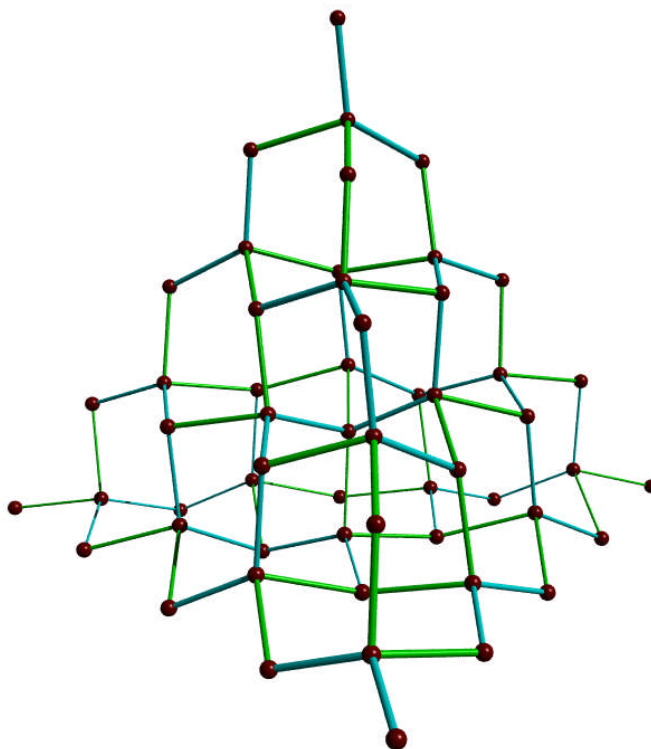
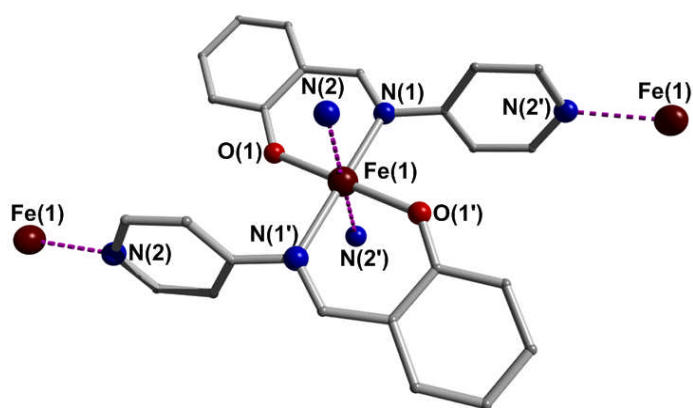


Figure 3.2: X-ray structure of $[\text{FeL}^7_2] \cdot 1\frac{1}{4}(\text{H}_2\text{O}) \cdot \frac{1}{2}(\text{MeOH})$ showing a diamond-like topology, with Fe-Fe distances of 7.93 Å (turquoise) and 7.58 Å (green).

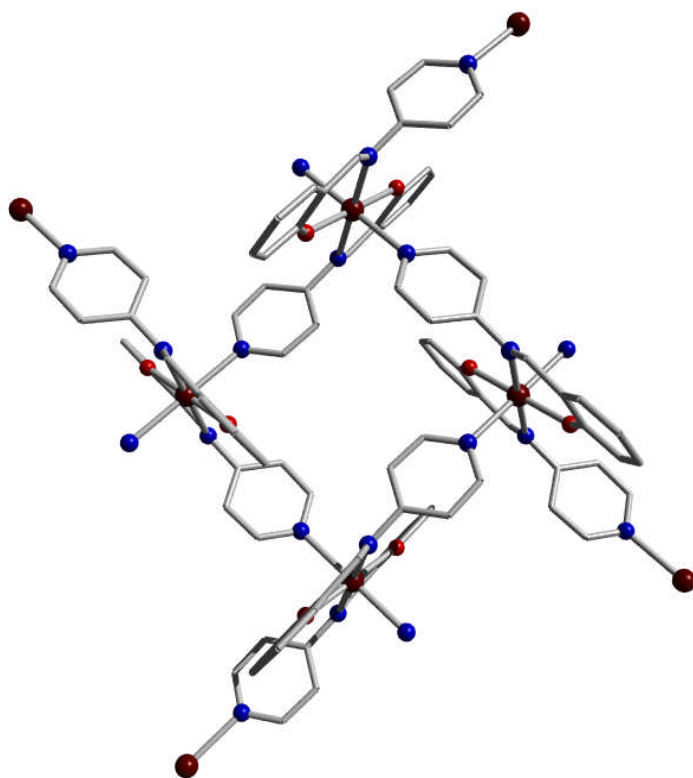
The treatment of the sodium salt of L^8 with $[\text{FeCl}_2(\text{THF})_{1.5}]$ in THF afforded a brown solid, but we could not separate the co-product NaCl. Subsequently we carried out a similar reaction with the lithium salt in dry methanol. This gave analytically pure and air stable $[\text{FeL}^8_2]$ in high yield, the LiCl remaining dissolved. This is the first complex reported of L^8 or of any similar 4-aminopyridine Schiff-base. Single crystals were grown from MeOH/THF (1:1).

Figure 3.3(a) shows the asymmetric unit of $[\text{FeL}^8_2]$ which contains one Fe centre. Similar to the situation for $[\text{FeL}^7_2]$ each Fe(II) is coordinated by two bidentate N-O ligands and two pyridines of adjacent units, but in contrast the

configuration in $[\text{FeL}^8_2]$ is all-*trans*. The geometry is close to octahedral with chelate N(1)-Fe(1)-O(1) angle of $85.24(14)^\circ$ and other *cis* angles close to 90° . These molecular units are assembled via pyridine coordination to give a planar rhombic array of Fe atoms [Figure 3.3(b)] with Fe-Fe-Fe angles of 83.93 and 97.07° . The ligand structure dictates that nearest neighbour coordination units (Fe...Fe distance 7.44 \AA) are arranged almost orthogonally; the angle between *xy* planes [i.e. Fe(1), N(1,1'), O(2,2')] of adjacent coordination units is *ca* 86.0° . These *xy* planes all form an angle of *ca* 72.0° to the Fe atom plane. Figure 3.4 depicts the mutual arrangement of the layers which are related by an *a* glide orthogonal to the *c* axis with the overall effect of reflecting and off-setting alternate layers in the stack. The undulations of the organic ligands are accommodated efficiently by interdigitation and no solvent is included (as confirmed by microanalysis). The Fe(1)-Fe(1) inter-plane distances are *ca* 11.2 \AA and 10.9 \AA .



(a)



(b)

Figure 3.3: X-ray structure of $[\text{FeL}^8_2]$: (a) the asymmetric unit; (b) 2 D array of orthogonal complexes.

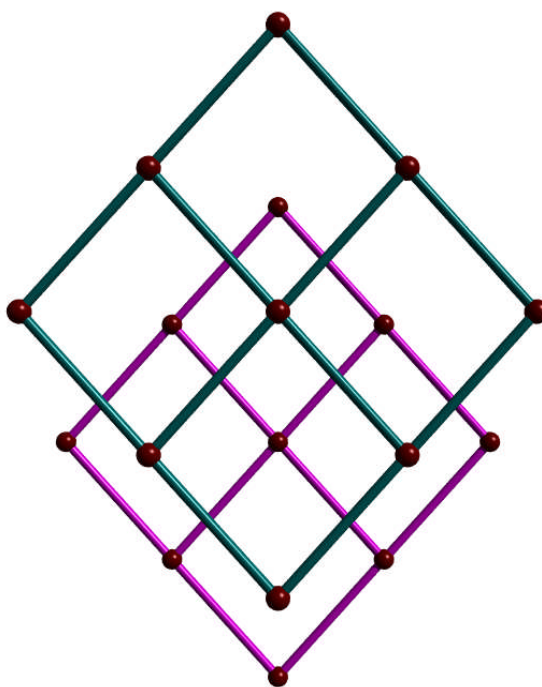


Figure 3.4: Two adjacent layers in $[\text{FeL}^8_2]$ viewed along the c axis.

3.4 Magnetism of $[\text{FeL}^7_2]_n$ and $[\text{FeL}^8_2]_n$

The curve of molar magnetic susceptibility (χ_M) \times temperature (T) against T for diamond-like $[\text{FeL}^7_2]_n$ is shown in Figure 3.5. The general form of the data indicates that $[\text{FeL}^7_2]_n$ undergoes a gradual spin state transition as the temperature changes. The $\chi_M T$ value increases sharply from 2 K to 25 K, likely due to a zero field splitting, but then rises more gradually to a value of *ca.* $2.90 \text{ cm}^3 \text{ K mol}^{-1}$ at 320 K. This value is lower than expected if all the Fe(II) centres were in the high spin state ($> 3.0 \text{ cm}^3 \text{ K mol}^{-1}$ since Fe(II) typically has g values significantly greater than 2). Therefore, some of the Fe(II) centres must remain in the low spin state at this temperature. Therefore the spin transition is incomplete. While this behaviour could result from antiferromagnetic interactions, the Mössbauer

spectrum is consistent with a mixture of spin states, with low spin ($S = 0$, 65%) and high spin ($S = 2$, 35%) Fe(II) at 80 K (Figure 3.6).²¹⁻²² As the bulk magnetic data give a value for $\chi_M T$ of $2.16 \text{ cm}^3 \text{ K mol}^{-1}$ at 80 K, this would correspond to an average g value of 2.87, which is certainly high but not unreasonable for Fe(II) in distorted octahedral environments.²³⁻²⁶

Spin crossover Fe(II) systems in imine N -rich environments are well known, and sharp transitions are frequently observed in mononuclear complexes and some 1D chains.^{9, 22, 27-28} Here the gradual nature of the spin state change is probably due in the main to the coexistence of two slightly different Fe(II) environments.

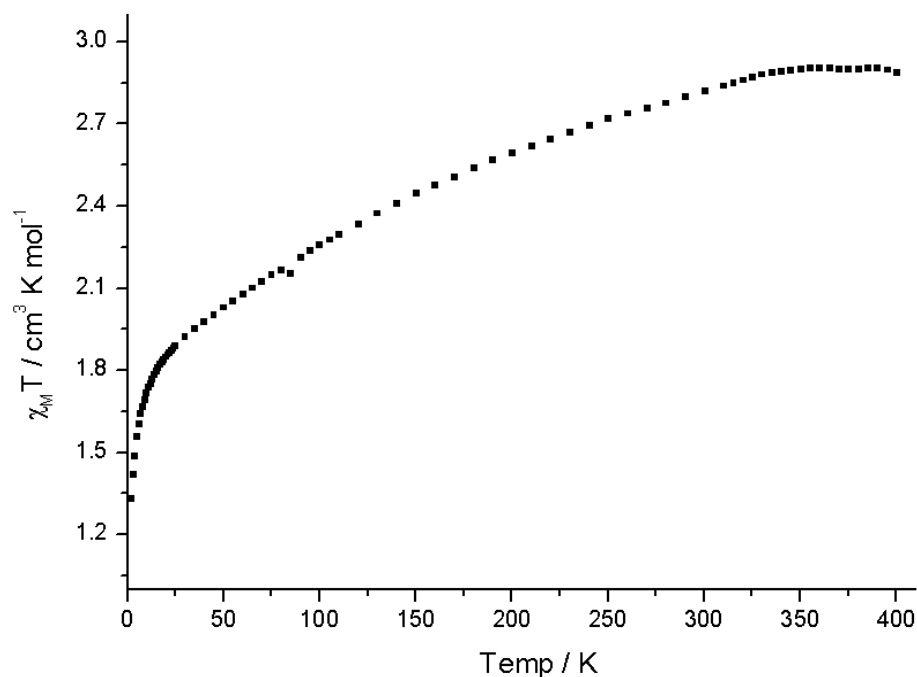
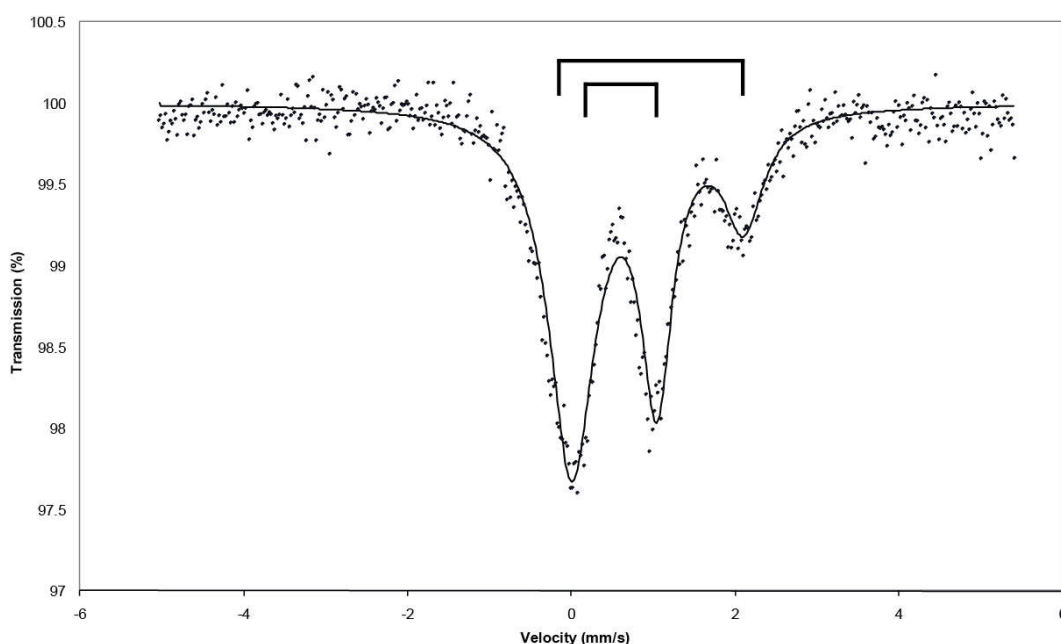


Figure 3.5: $\chi_M T$ vs. T curve of $[\text{FeL}_2^7]$ measured at 1000 Oe.



Assignment	δ	ΔE_Q	Γ	%
HS Fe(II)	0.92	2.36(2)	0.32(2)	35(2)
LS Fe(II)	0.54	0.95	0.26	65(2)

Figure 3.6: Mössbauer spectrum of complex 1 at 80 K showing high spin (HS) and low spin (LS) centers. δ = isomer shift, ΔE_Q = quadrupole splitting, Γ = half width at half maximum height, % shows relative amount of the two spin centers.

Errors 0.01 mms^{-1} unless shown otherwise.

The magnetic properties of $[\text{FeL}^8_2]_n$ are strikingly different, as shown in the plots of χ_M vs. T (Figure 3.7) and $\chi_M T$ vs. T (Figure 3.8). In the high temperature regime the magnetic susceptibility data obey the Curie-Weiss law with $C = 2.93 \text{ cm}^3 \text{ K mol}^{-1}$ and $\Theta = +9.9 \text{ K}$. The $\chi_M T$ vs. T plot also indicates magnetic ordering with $\chi_M T$ of *ca.* $3.17 \text{ cm}^3 \text{ K mol}^{-1}$ at 300 K, which is consistent for an isolated high spin Fe(II) centre with $g > 2.0$. This $\chi_M T$ value rises dramatically from *ca.* 10 K and reaches a maximum of $44.4 \text{ cm}^3 \text{ K mol}^{-1}$ at *ca.* 5 K. This suggests that

$[\text{FeL}^8_2]_n$ undergoes long range magnetic ordering at that temperature. This was confirmed by measurements on warming the sample after cooling in zero field (ZFCW), followed by measuring on cooling in a field (FCC) from 2 - 25 K using a field of 1000 Oe. These two curves diverge at a T_C of 5.3 K (Figure 3.9).

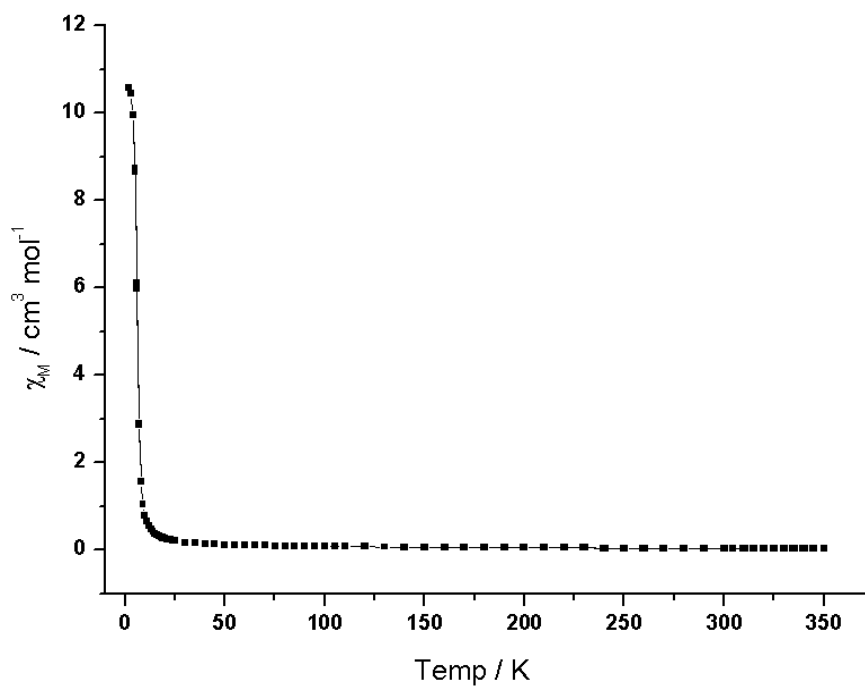


Figure 3.7: χ_M vs. T for $[\text{FeL}^8_2]_n$ measured at 1000 Oe

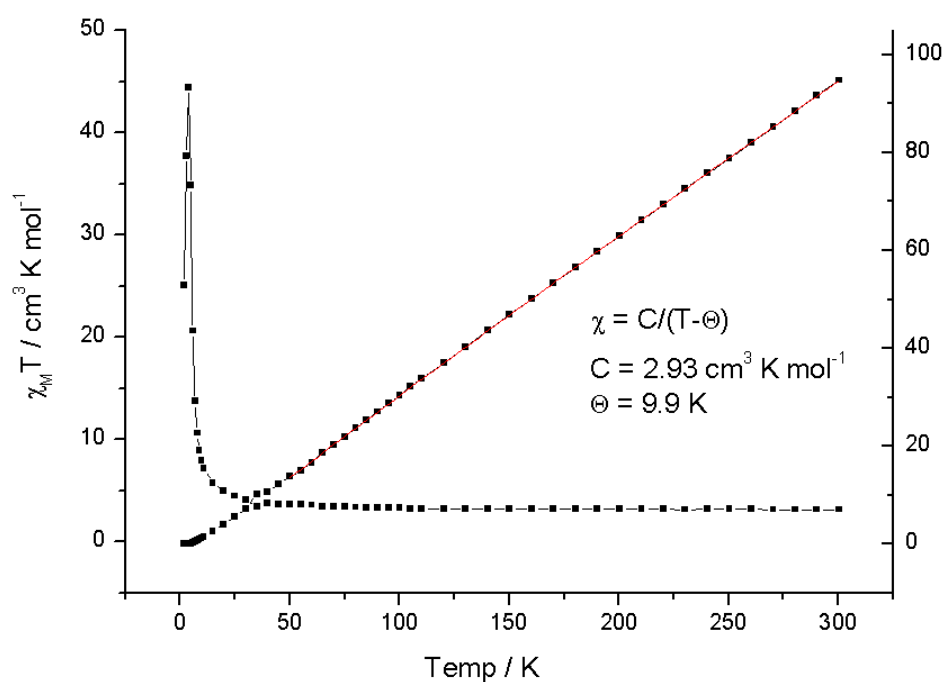


Figure 3.8: $\chi_M T$ and χ_M^{-1} vs. T for complex $[\text{FeL}^8_2]_n$ measured at 1000 Oe

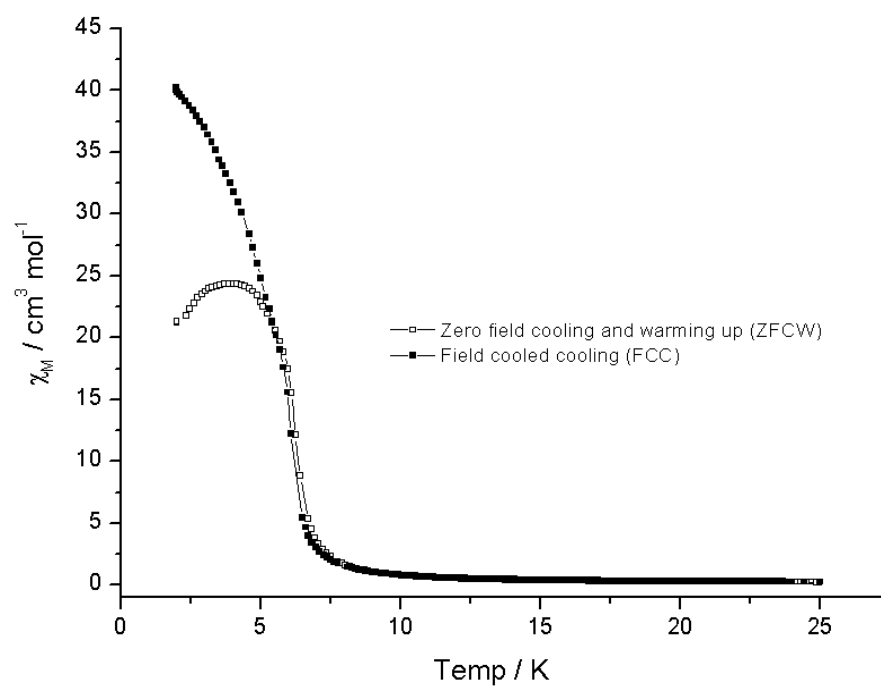


Figure 3.9: ZFCW and FCC M vs. T curves for $[\text{FeL}^8_2]_n$ measured at 1000 Oe.

The hysteresis curve for $[\text{FeL}^8_2]_n$ (Figure 3.10) at 1.8 K indicates magnetic saturation at *ca.* 2000 Oe. While the coercive field for the compound of 467 Oe is smaller than for some room temperature permanent magnets²⁹ such as SmCo_5 (44 kOe) and $\text{Nd}_2\text{Fe}_{14}\text{B}$ (19 kOe), such hard magnetism even at low temperatures is unusual in molecular systems where a few examples of very large coercivities have been observed.³⁰⁻³²

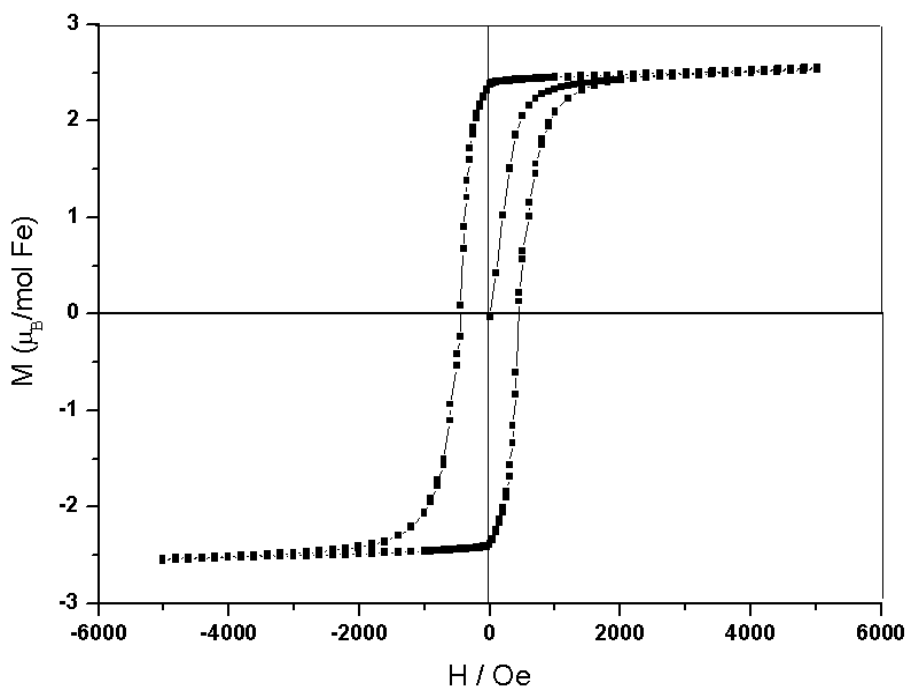


Figure 3.10: *M* vs. *H* curve at 1.8 K for complex $[\text{FeL}^8_2]_n$ showing ferromagnetic hysteresis.

3.4 Cu(II) complexes from HL^7 and HL^8

3.4.1 Synthesis of $[\text{CuL}^7_2]_n$

The reaction of CuCl_2 with in situ generated NaL^7_2 in MeOH led to precipitation of a deep red solid. Attempts to grow single crystals failed due to its insolubility in common solvents. Elemental analysis corresponding to $[\text{CuL}^7_2]$ is consistent with the presence of a chain complex when Cu(II) is five-coordinated with a pyramidal geometry or a 2 or 3 D MOF when Cu(II) has an octahedral geometry as we have seen on the previous two Fe(II) complexes. However, based on its poor solubility, we assume that the $[\text{CuL}^7_2]_n$ is more likely to be a MOF architecture than a simple 1 D chain compound.

3.4.2 Magnetism of $[\text{CuL}^7_2]_n$

Magnetic data were collected from 2 K to 300K as shown in Figure 3.11. At room temperature, the χT value is $0.62 \text{ cm}^3 \text{ K mol}^{-1}$ which is much higher than a $0.375 \text{ cm}^3 \text{ K mol}^{-1}$ expected for a Cu(II) free ion system ($S = 1/2$, $g = 2.00$). As temperature decreases, the χT value decreases steadily due to an antiferromagnetic exchange, which commonly occurs in Cu(II) complexes.

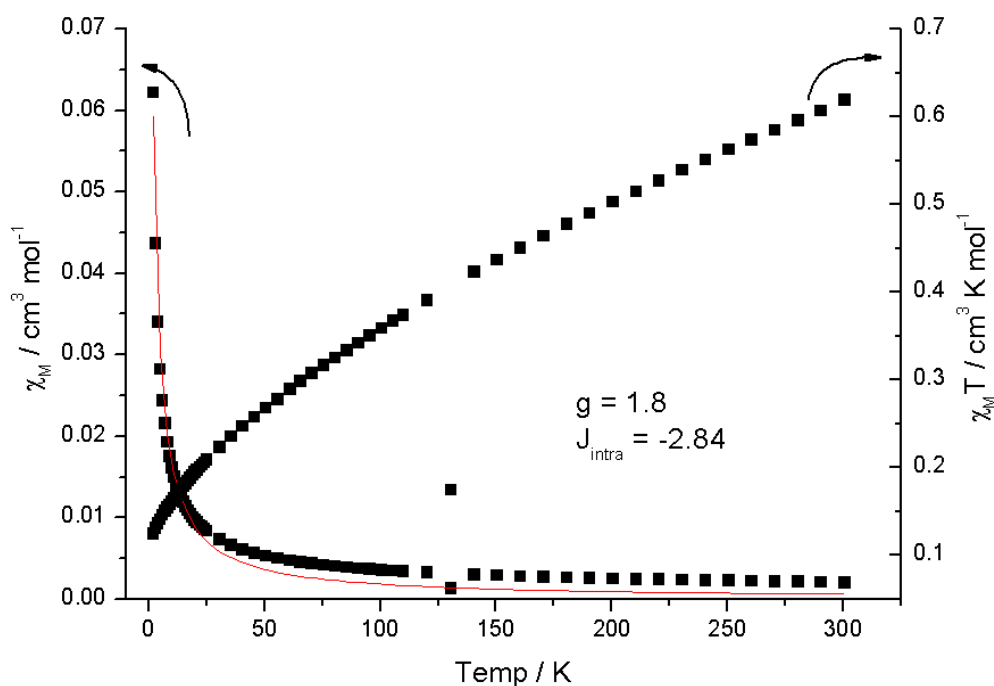


Figure 3.11: χ_M , $\chi_M T$ vs. T for $[\text{CuL}^7_2]_n$ measured at 1000 Oe

In order to interpret experimental data quantitatively, we have assumed a 1 D antiferromagnetic chain structure. The data were fitted to a high-temperature (> 50

K) Heisenberg chain model ($\hat{H} = -J \sum_{i=1}^{n-1} S_i S_{i+1}$)³³ (Eqn. 3.1) for an $S = 1/2$ system.

The least squares fit gives $g = 1.8$, $J_{\text{intra}} = -2.84$ K. The values confirm the weak intrachain antiferromagnetic exchanges for $[\text{CuL}^7_2]_n$. However, given that the material is probably a 3 D MOF, it is not surprising that this magnetic model did not fit well at higher temperature.

$$\chi_M = \frac{Ng^2\beta^2}{4kT} \left[\frac{N}{D} \right]^{\frac{2}{3}} \dots\dots\dots \text{Eqn. 3.1}$$

$$N = 1.0 + 5.7979916y + 16.902653y^2 + 29.376885y^3 + 29.832959y^4 + 4.036918y^5$$

$$D = 1.0 + 2.79799y + 7.0086780y^2 + 8.6538644y^3 + 4.5743114y^4$$

$$\text{where } y = \frac{J}{2kT}$$

3.4.3 Synthesis of Cu(II) complexes from HL⁸

Using the proligand HL⁸, we made a Fe(II) MOF hard magnet, as a result of this ligand favouring an orthogonal arrangement of ML⁸₂ entities (Figure 3.12). A few other ligand systems are known also to promote this feature.^{8, 34-38}

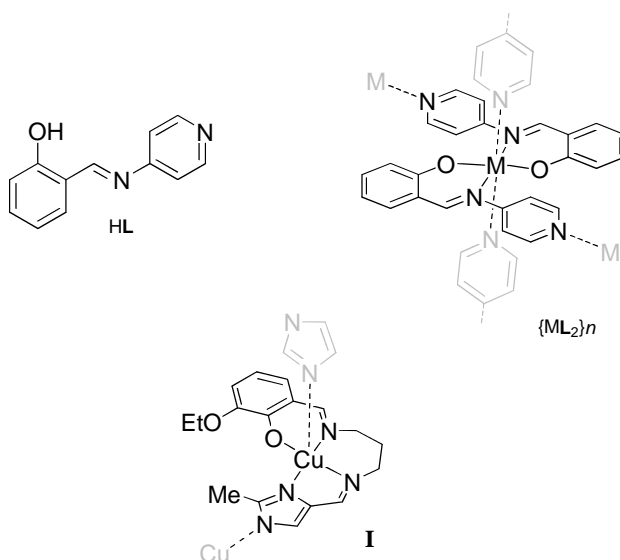


Figure 3.12: Proligand HL⁸, a possible coordination environment [ML⁸₂]_n and a related Cu(II) system

$[\text{CuL}^8_2]_n \cdot 2\text{THF}$ and $[\text{CuL}^8_2]_n \cdot \text{MeOH}$

The treatment of the ligand HL^8 with NaH and copper(II) chloride in THF gave a green solution from which crystals of the chain compound $[\text{CuL}^8_2]_n \cdot 2\text{THF}$ were readily grown. This material has convenient solubility, and recrystallisation from methanol gave large crystals of $[\text{CuL}_2]_n \cdot \text{MeOH}$.

The basic five-coordinate structural units CuL^8_2 of these two compounds are similar (Figure 3.13 and 3.140) although while $[\text{CuL}^8_2]_n \cdot 2\text{THF}$ is close to square-pyramidal geometry ($\tau = 0.22$),³⁹ $[\text{CuL}^8_2]_n \cdot \text{MeOH}$ is more substantially distorted towards trigonal-bipyramidal ($\tau = 0.47$). Only one of the pyridine units of each unit N(2) is coordinated to a neighbouring Cu atom and these bonds are also significantly elongated at *ca* 2.25 Å

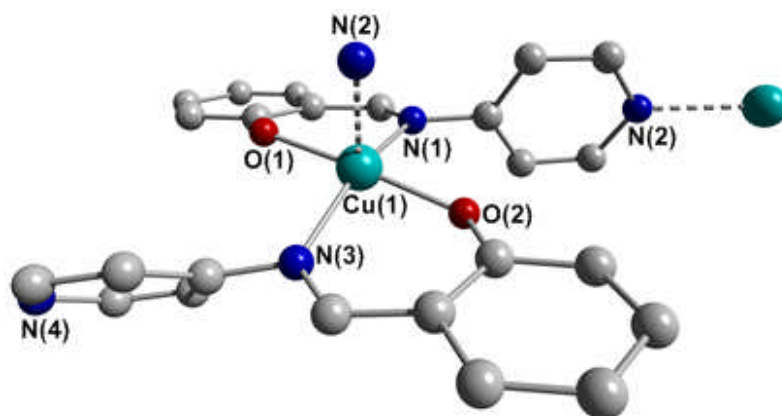


Figure 3.13: Asymmetric unit of complex $[\text{CuL}^8_2]_n \cdot 2\text{THF}$. Selected bond length (Å): Cu(1)-O(2) 1.9049(15), Cu(1)-O(1) 1.9102(15), Cu(1)-N(1) 2.0242(18), Cu(1)-N(3) 2.0497(17), Cu(1)-N(2) 2.2682(17);

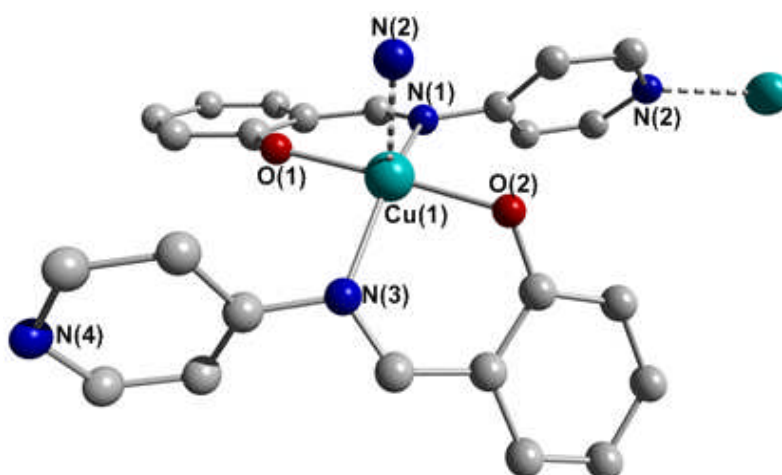


Figure 3.14: Asymmetric unit of complex $[\text{CuL}^8_2]_n \cdot \text{MeOH}$. Selected bond length (Å): Cu(1)-O(1) 1.9055(8), Cu(1)-O(2) 1.9102(8), Cu(1)-N(1) 2.0735(9), Cu(1)-N(3) 2.0478(9), Cu(1)-N(2) 2.2425(9)

The consequent zig-zag chain structures shown in Figure 3.15 are related to that of Matsumoto's Cu complex **I** (Figure 3.12, $\tau = 0.03$)³⁶. The geometry of these chains, and in particular the relative orientations of the adjacent complex units, is of relevance to an interpretation of their magnetic properties (*vide infra*) but a comparison between distorted five-coordinate complexes such as $[\text{CuL}^8_2]_n \cdot 2\text{THF}$ and $[\text{CuL}^8_2]_n \cdot \text{MeOH}$ is more challenging than it would be in an octahedral system or where more simple linkers such as O^{2-} and N_3^- are concerned. Nevertheless we note that the angles between the mean "equatorial" N_2O_2 planes of adjacent Cu atoms in $[\text{CuL}^8_2]_n \cdot 2\text{THF}$ and $[\text{CuL}^8_2]_n \cdot \text{MeOH}$ are 77.3° and 89.7° respectively, compared to 75.2° for **I**. The differences in solvation between $[\text{CuL}^8_2]_n \cdot 2\text{THF}$ and $[\text{CuL}^8_2]_n \cdot \text{MeOH}$ result then in minor structural variations in the chain, although interestingly the shortest interchain Cu...Cu distance of 9.24 \AA in **1** falls to 7.41 \AA in $[\text{CuL}^8_2]_n \cdot \text{MeOH}$ which contains less solvent.

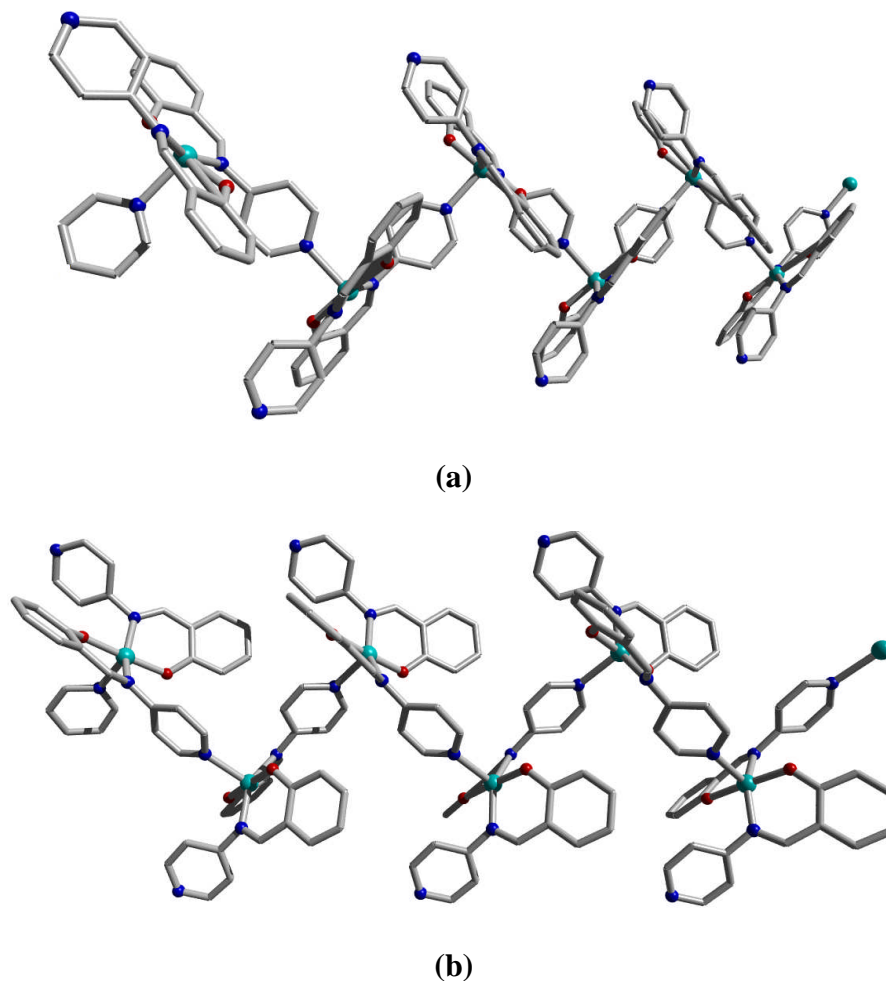


Figure 3.15: Orientation of 1D zigzag chain structure: (a) $[\text{CuL}_2^8]_n \cdot 2\text{THF}$ and (b) $[\text{CuL}_2^8]_n \cdot \text{MeOH}$ viewed along a axis.

$[\text{Cu}_3\text{L}_4^8(\text{sal})_2]$

Although proligand HL^8 is highly sensitive to water the above complexes are air stable so the synthesis of the chain system was also attempted from a mixture of salicylaldehyde, 4-aminopyridine and copper(II) chloride in methanol. However, this resulted in a different material $[\text{Cu}_3\text{L}_4(\text{sal})_2]$ which has the same CuL_2^8 chain

system as in $[\text{CuL}^8_2]n \cdot 2\text{THF}$ and $[\text{CuL}^8_2]_n \cdot \text{MeOH}$ “crosslinked” by $\text{Cu}(\text{sal})_2$ units to form a 2 D mat.

As shown in Figure 3.16, the asymmetric unit has three crystallographically independent $\text{Cu}(\text{II})$ ions. Two of these $\text{Cu}(1)$ and $\text{Cu}(2)$ have a distorted square-pyramidal structure ($\tau = 0.24$ and 0.31 respectively) with elongated “apical” Cu-N bonds as for $[\text{CuL}^8_2]n \cdot 2\text{THF}$ and $[\text{CuL}^8_2]_n \cdot \text{MeOH}$. The six-coordinated $\text{Cu}(3)$ centre is all-*trans* with the carbonyl O atom in the Jahn-Teller elongated axis [$\text{Cu}(3)\text{-O}(2\text{E})$ of $2.260(2)$ Å and $\text{Cu}(3)\text{-O}(2\text{F})$ of $2.311(2)$ Å].

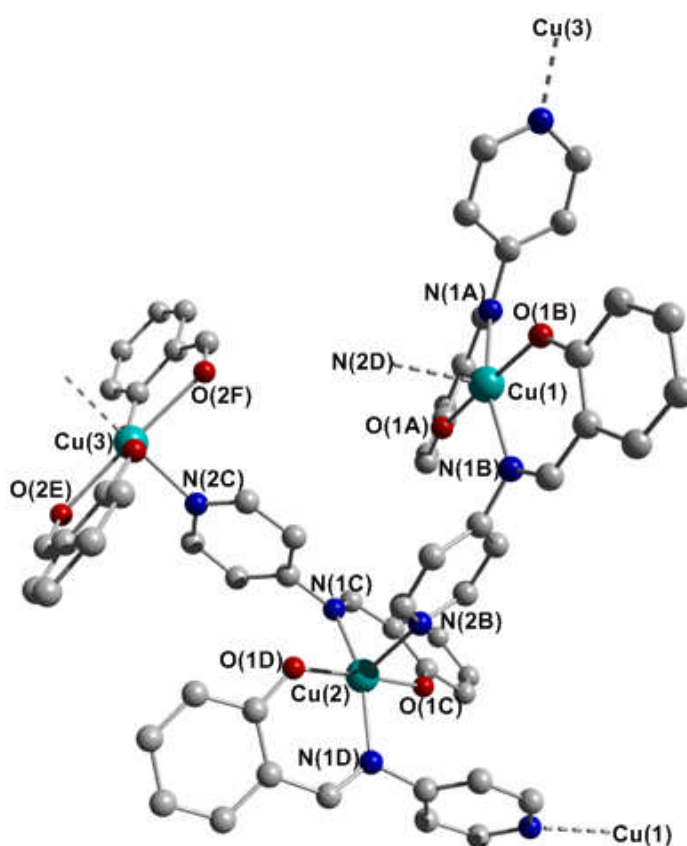


Figure 3.16: Asymmetric unit of $[\{\text{Cu}_3\text{L}^8_4(\text{sal})_2\}, \text{So} \cdot 2\text{MeOH}]_\infty$, hydrogen atoms and solvents were removed for clarity.

As shown in Figure 3.17, these Cu atoms are linked in the crystal to form chair-conformation octanuclear rings which are tiled to form a herringbone structure. This Figure also shows the relationship between the zig-zag of five-coordinated Cu(1) and Cu(2) atoms with the bridging six-coordinate Cu(3). The 2 D mat thus formed presents a wavelike pattern as shown in Figure 3.18.

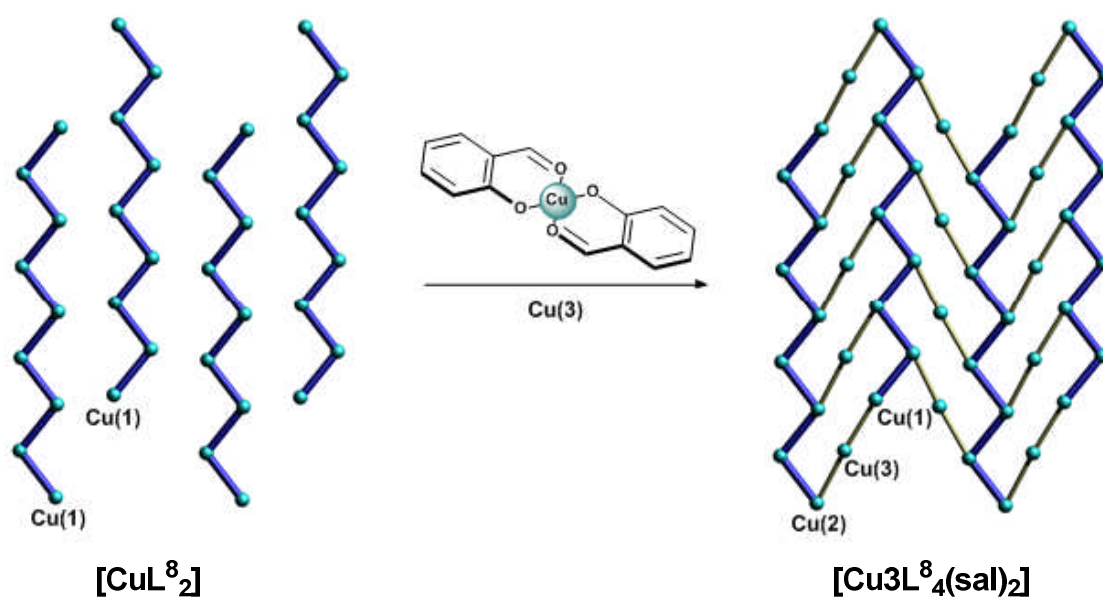


Figure 3.17: The formation of 2 D mat from zigzag chains.

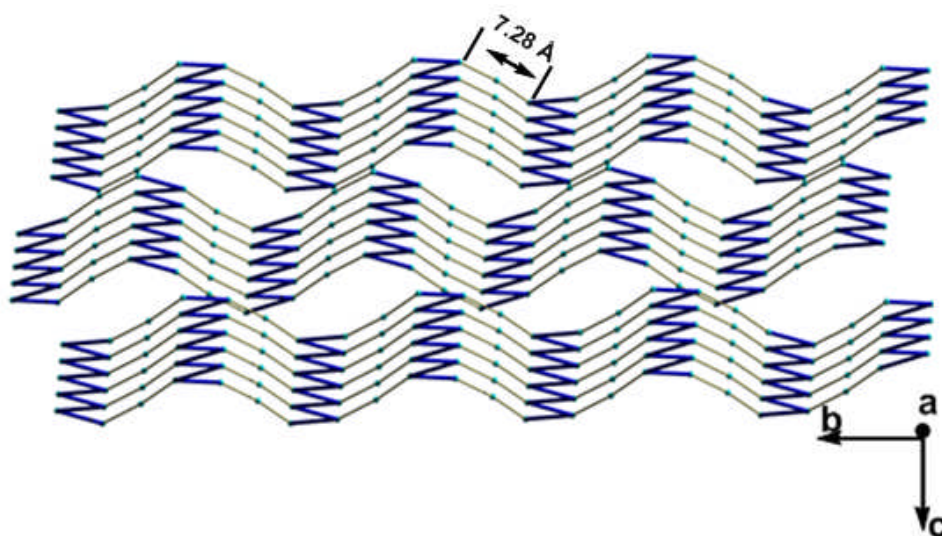


Figure 3.18: The wave-like mat arrangement of chains (dark blue lines) cross-linked by $\text{Cu}(\text{sal})_2$ units.

3.4.4 Magnetism of CuL^8_2 complexes

$[\text{CuL}^8_2]_n \cdot 2\text{THF}$ and $[\text{CuL}^8_2]_n \cdot \text{MeOH}$

The magnetic properties of all materials were studied using SQUID magnetometry. Compounds $[\text{CuL}^8_2]_n \cdot 2\text{THF}$ and $[\text{CuL}^8_2]_n \cdot \text{MeOH}$ behaved similarly. The plot of $\chi_M T$ vs. T for $[\text{CuL}^8_2]_n \cdot 2\text{THF}$ and $[\text{CuL}^8_2]_n \cdot \text{MeOH}$ are shown in Figure 3.19 and 3.22, where χ_M is the molar magnetic susceptibility. At 300 K, in the paramagnetic regime, the $\chi_M T$ values are 0.395 and 0.464 $\text{cm}^3 \text{K mol}^{-1}$, for compounds $[\text{CuL}^8_2]_n \cdot 2\text{THF}$ and $[\text{CuL}^8_2]_n \cdot \text{MeOH}$, respectively. These values correlate well to what is expected for $S=1/2$ spin with $g=2.17$ and 2.22, as calculated below. From 300 K to 25 K, $\chi_M T$ remains essentially constant. The high temperature data (> 50 K) obey the Curie-Weiss law (Figure 3.20 and 3.21) with small positive Weiss

constants (0.19 K for $[\text{CuL}^8_2]_n \cdot 2\text{THF}$ and 0.05 K for $[\text{CuL}^8_2]_n \cdot \text{MeOH}$), which imply that the short range intrachain coupling is ferromagnetic. The Curie constants agree well with $S=1/2$ spin per Cu centre. It is noteworthy that compound $[\text{CuL}^8_2]_n \cdot \text{MeOH}$ has a smaller Weiss constant than compound $[\text{CuL}^8_2]_n \cdot 2\text{THF}$ which perhaps reflects the difference in ligand geometry about the paramagnetic centres. Compound $[\text{CuL}^8_2]_n \cdot 2\text{THF}$ has Cu(II) in an environment closer to square pyramidal, where the unpaired electrons reside in $d_{x^2-y^2}$ orbitals, whereas in compound $[\text{CuL}^8_2]_n \cdot \text{MeOH}$ they reside in d_z^2 orbitals in a geometry closer to trigonal pyramidal. This translates to weaker short range coupling.

At lower temperature (20 K to 2 K) however the $\chi_M T$ values rise to *ca* $0.5 \text{ cm}^3 \text{ K mol}^{-1}$. This clearly confirms weak ferromagnetic interactions but we note that it does not imply that this 1 D Cu(II) system shows long-range magnetic order, which is not feasible above absolute zero.⁸ As we noted above, other Cu(II) complexes with a 1 D zigzag chain structure have been reported.³⁴⁻³⁸ Based on EPR spectra, Ohkubo suggested that when the unpaired electron in a square-pyramidal Cu(II) system occupies the $d_{x^2-y^2}$ orbital lying in the plane, and a bridging ligand links these equatorial sites, antiferromagnetic interactions are expected due to a σ - σ superexchange mechanism. On the other hand, when the bridging ligand links an equatorial site with an axial site (*i.e.* the complex units are orthogonal), a small ferromagnetic coupling is expected.³⁶ While our structures are rather distorted, and the orbital picture is perhaps not so clear, the near orthogonality of coordination planes in $[\text{CuL}^8_2]_n \cdot 2\text{THF}$ and $[\text{CuL}^8_2]_n \cdot \text{MeOH}$ corresponds well with the observation of ferromagnetic coupling.

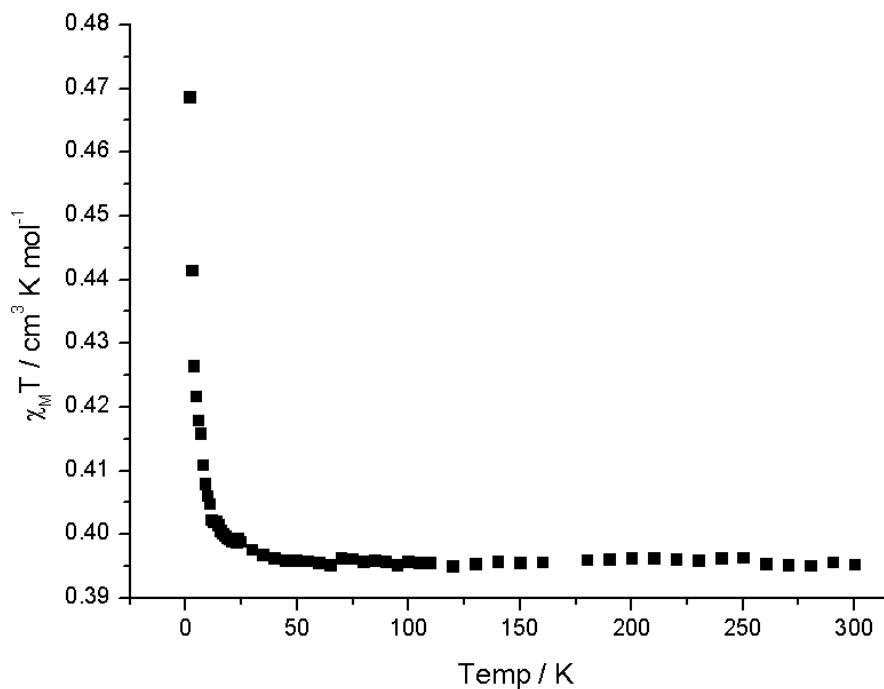


Figure 3.19: $\chi_M T$ vs. T for $[\text{CuL}^8_2]_n \cdot 2\text{THF}$ measured at 1000 Oe

In order to interpret the magnetic data of compounds $[\text{CuL}^8_2]_n \cdot 2\text{THF}$ and $[\text{CuL}^8_2]_n \cdot \text{MeOH}$ we have assumed an isolated 1 D chain structure. The data could be fitted to a high-temperature ($> 50 \text{ K}$) Heisenberg chain model ($H = 2JS_i S_j$)³³ (eqn. 1) for an $S = 1/2$ system. The least squares fit gives $g = 2.05$ and 2.22 , $J = 0.18$ and 0.10 K , $R = 1.6 \times 10^{-4}$ and 5.0×10^{-4} (standard error), for $[\text{CuL}^8_2]_n \cdot 2\text{THF}$ and $[\text{CuL}^8_2]_n \cdot \text{MeOH}$ respectively (Figure 3.20 and 3.21). These values confirm the weak intrachain ferromagnetic coupling.

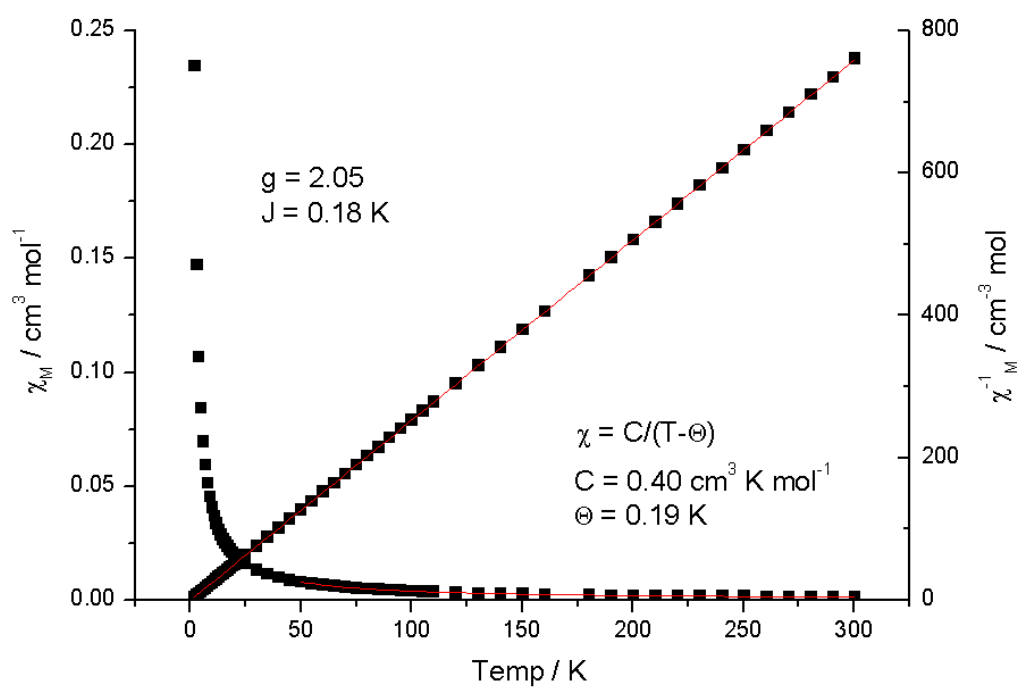


Figure 3.20: χ_M, χ_M^{-1} vs. T for $[\text{CuL}^8_2]_n \cdot 2\text{THF}$ with fitting to the Bonner-Fisher equation

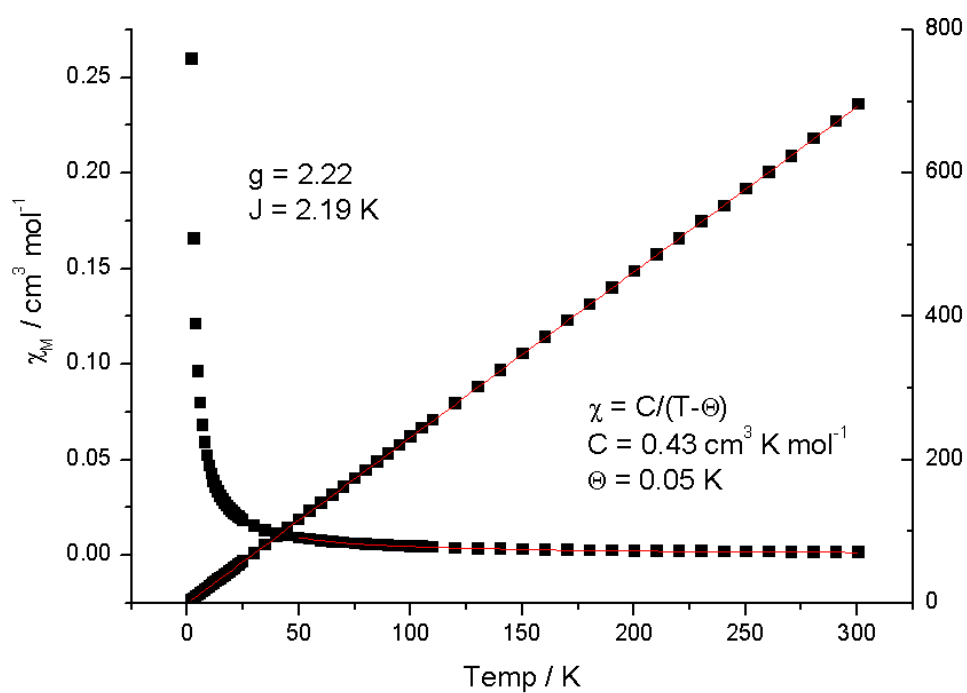


Figure 3.21: χ_M, χ_M^{-1} vs. T for $[\text{CuL}^8_2]_n \cdot \text{MeOH}$ with fitting to the Bonner-Fisher equation.

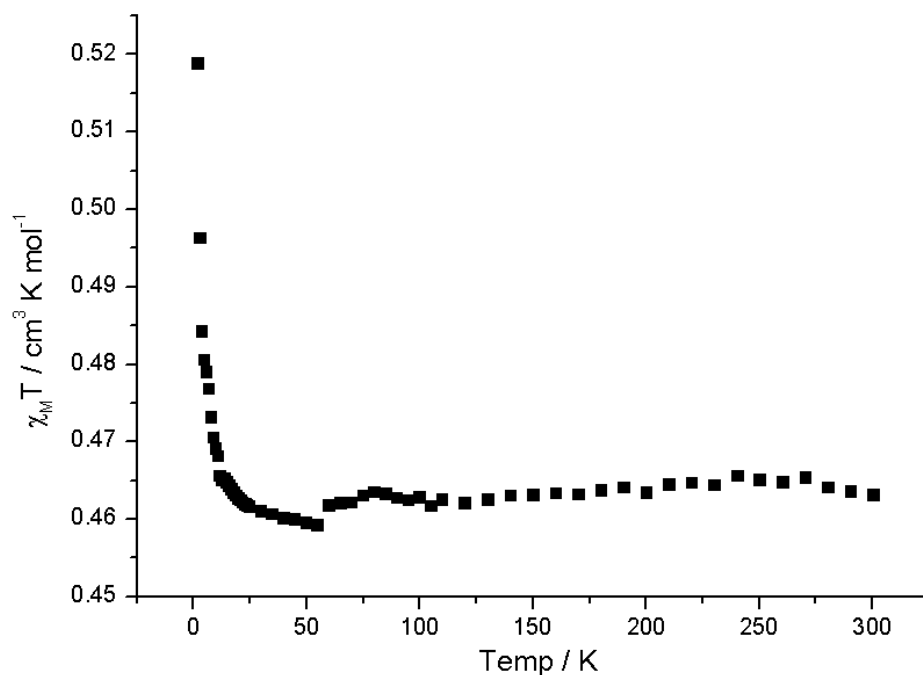


Figure 3.22: $\chi_M T$ vs. T for $[\text{CuL}^8_2]_n \cdot \text{MeOH}$ measured at 1000 Oe

$[\text{Cu}_3\text{L}^8_4(\text{sal})_2]_n$

For complex $[\text{Cu}_3\text{L}^8_4(\text{sal})_2]_n$, $\chi_M T$ decreases slightly from 300 K to 50 K (Figure 3.23) indicating that the overall short range coupling is antiferromagnetic. There is a minimum in the curve at about 25 K, below which $\chi_M T$ rises, indicating a dominant ferromagnetic-like interaction. This general form is typical of ferrimagnetic behaviour.

On the basis of the very similar structures of the CuL^8_2 chains in $[\text{Cu}_3\text{L}^8_4(\text{sal})_2]$ and (particularly) $[\text{CuL}^8_2]_n \cdot 2\text{THF}$, it is reasonable to assume that intrachain interactions are weakly ferromagnetic in $[\text{Cu}_3\text{L}^8_4(\text{sal})_2]$. While the presence of at least four different magnetic couplings between pyramidal Cu(1)/Cu(2) [ground state 2B_1] and octahedral Cu(3) [2A_1] makes a full interpretation intractable we have attempted an implementation of a mean-field

correction⁴⁰ to the high temperature Heisenberg model (Eqn. 3.2 and Figure 3.24) giving $J = 1.12$ K and $g = 1.85$. Perhaps more informatively, fitting to a modified Curie-Weiss law (Figure 12) gives $C = 0.329$ cm³ K mol⁻¹ and $\Theta = -2.39$ K, consistent with the short range antiferromagnetic behaviour which is dominant at higher temperatures.

$$\chi_{corr} = \frac{\chi_M}{1 - \left(\frac{2zJ_2}{Ng^2\beta^2} \chi_M \right)} \quad \dots\dots\dots \text{Eqn. 3.2}$$

Generally, ferrimagnetism is associated with ordered heterospin systems⁴¹⁻⁴⁴ and homospin systems are possible but much rarer⁴⁵⁻⁴⁹ since the condition for noncompensation of the individual spin moments is difficult to achieve. According to Coronado,⁵⁰ ferrimagnetism could occur in homometallic chains, provided the metals have different environments within the chains or when there is an odd number of interacting ions per unit cell. Ferrimagnetism can also appear when there are competing interactions. The complex [Cu₃L⁸₄(sal)₂] has these features, with competing ferro and antiferromagnetic interactions.

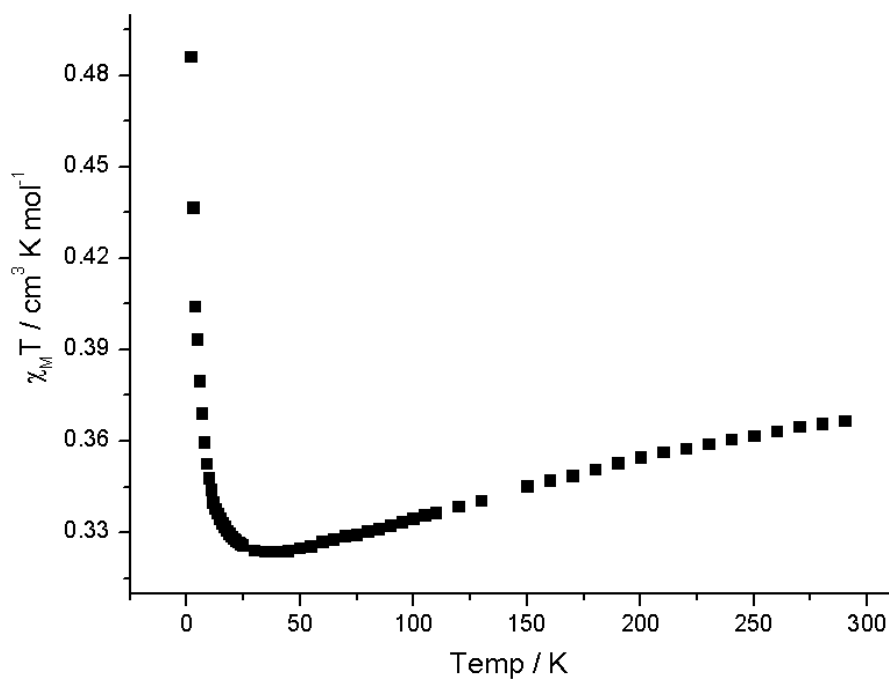


Figure 3.23: $\chi_M T$ vs. T for $[\text{Cu}_3\text{L}^8_4(\text{sal})_2]$.

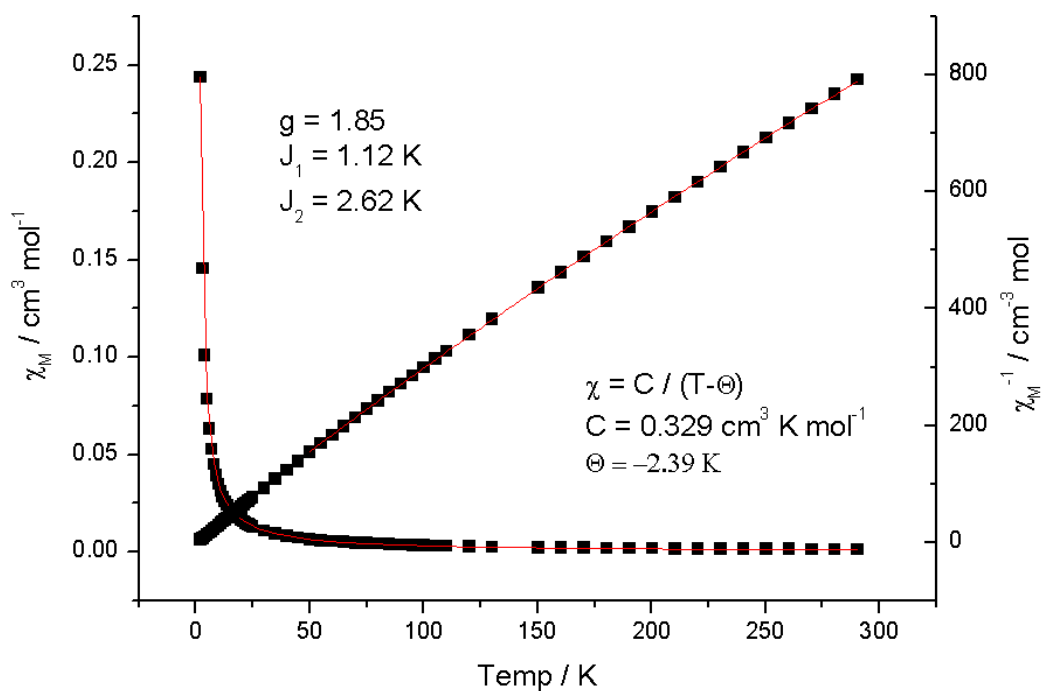


Figure 3.24: $\chi_M T$ vs. T for $[\text{Cu}_3\text{L}^8_4(\text{sal})_2]$ with fitting to a mean-field corrected high temperature Heisenberg model and modifies Curie-Weiss law ($\chi = C/(T - \Theta) + \chi_{\text{TIP}}$)

Magnetization curves of powdered samples of compounds $[\text{CuL}^8_2]_n \cdot 2\text{THF}$, $[\text{CuL}^8_2]_n \cdot \text{MeOH}$ and $[\text{Cu}_3\text{L}^8_4(\text{sal})_2]$ at 1.8 K are shown in Figure 3.25. At a field of 50000 Oe all three complexes tend to magnetically saturate at *ca.* $1 \mu_B \text{ mol}^{-1}$ in agreement with $S=1/2$ per asymmetric unit. The magnetization behaviours are slightly different with resistance to magnetization increasing in the order $[\text{Cu}_3\text{L}^8_4(\text{sal})_2] > [\text{CuL}^8_2]_n \cdot 2\text{THF} > [\text{CuL}^8_2]_n \cdot \text{MeOH}$. This most likely reflects the strength of the internal exchange interactions, where the 2 D compound is more easily magnetised than the 1 D compounds and compound $[\text{CuL}^8_2]_n \cdot \text{MeOH}$ has weaker interactions than compound $[\text{CuL}^8_2]_n \cdot 2\text{THF}$, as described above. The magnetization curves do not follow $S=1/2$ Brillouin curves with generally larger gradients which reflect the ferromagnetic coupling.

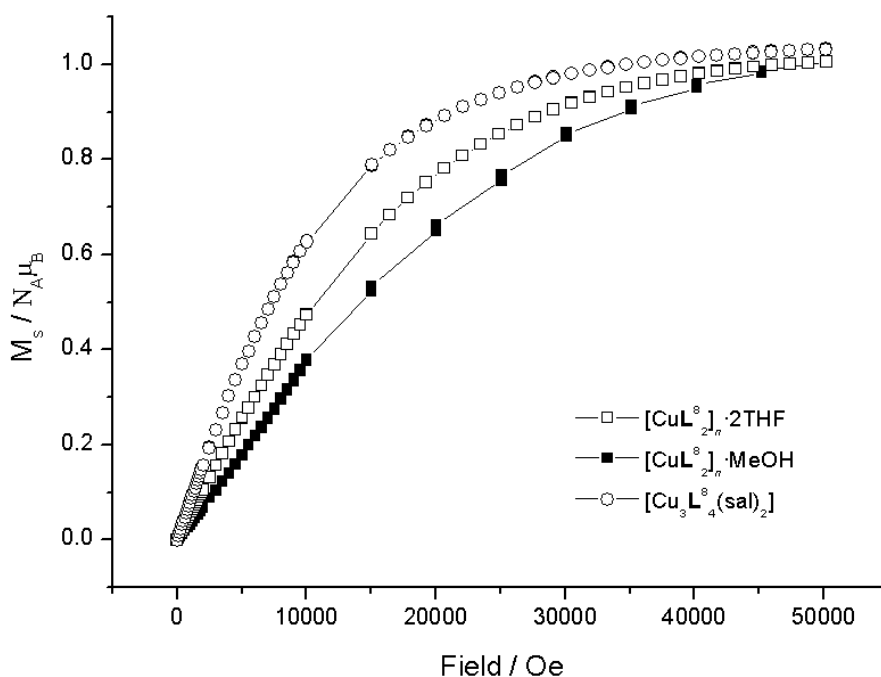


Figure 3.25: Magnetization of complex $[\text{CuL}^8_2]_n \cdot 2\text{THF}$, $[\text{CuL}^8_2]_n \cdot \text{MeOH}$ and $[\text{Cu}_3\text{L}^8_4(\text{sal})_2]$ at 1.8 K

3.5 Conclusions

Two isomeric ligands HL^n ($n = 7$ or 8) were used in this chapter. The ligand HL^8 synthesised in high yield in our hands, is particularly appealing since it can be used to form extended structures with built-in orthogonal arrangement of adjacent complex units. The treatment of NaL^n ($n = 7$ or 8) with FeCl_2 produced the isomeric framework solids $[\text{FeL}^n_2]$ ($n = 7$ or 8). The more flexible L^7 system gives a diamond-like 3 D network exhibiting a gradual spin-crossover while L^8 gives a 2 D framework which is a rare molecular example of a hard ferromagnet.

The strategy using L^8 was applied to CuCl_2 , giving two zigzag chain complexes $\text{CuL}^8_2(\text{solvent})$. In the zig-zag Cu(II) system, ferromagnetic interactions were observed along the chain of mutually orthogonal spin-carrying centres. The remaining pyridine ligand sites in chains $[\text{CuL}^8_2]$ have been exploited in crosslinking the chains to form a 2 D mat structure $[\text{Cu}_3\text{L}^8_4(\text{sal})_2]$, thereby adding weak antiferromagnetic inter-chain interactions. The competing interactions lead to observation of ferrimagnet-like behaviour in the homo-spin system, which is rather unusual. The properties of this system are ideally suited for stepwise synthesis of homo- and heterometallic magnetic materials. For example, soluble ML^8_2 chains may be treated with further metal sources to give less soluble networks. Furthermore, using paramagnetic centres with a single-ion anisotropy, unlike Cu(II) , could lead to new single chain magnets, which display slow magnetization relaxation times for applications in memory devices.⁵¹

3.6 References

1. G. Leibel, S. Demeshko, S. Dechert and F. Meyer, *Angew. Chem. Int. Ed.*, 2005, **44**, 7111-7114.
2. S. Venkataramani, U. Jana, M. Dommaschk, F. D. Sönnichsen, F. Tucek and R. Herges, *Science*, 2011, **331**, 445-448.
3. S. Heutz, C. Mitra, W. Wu, A. J. Fisher, A. Kerridge, M. Stoneham, A. H. Harker, J. Gardener, H. H. Tseng, T. S. Jones, C. Renner and G. Aeppli, *Adv. Mater.*, 2007, **19**, 3618-3622.
4. G. Karotsis, S. Kennedy, S. J. Teat, C. M. Beavers, D. A. Fowler, J. J. Morales, M. Evangelisti, S. J. Dalgarno and E. K. Brechin, *J. Am. Chem. Soc.*, 2010, **132**, 12983-12990.
5. G. Karotsis, M. Evangelisti, S. J. Dalgarno and E. K. Brechin, *Angew. Chem. Int. Ed.*, 2009, **48**, 9928-9931.
6. O. Tegus, E. Bruck, K. H. J. Buschow and F. R. de Boer, *Nature*, 2002, **415**, 150-152.
7. C. Chappert, A. Fert and F. N. Van Dau, *Nat. Mater.*, 2007, **6**, 813-823.
8. O. Kahn, *Molecular Magnetism*, WILEY-VCH, New York, 1993.
9. P. Gütlich and H. A. Goodwin, in *Spin Crossover in Transition Metal Compounds*, Springer-Verlag, Berlin Heidelberg, 2004, vol. 233,234,235.
10. L. D. Barron, *Nat. Mater.*, 2008, **7**, 691-692.
11. C. Train, R. Gheorghe, V. Krstic, L.-M. Chamoreau, N. S. Ovanesyan, G. L. J. A. Rikken, M. Gruselle and M. Verdaguer, *Nature Mater.*, 2008, **7**, 729-734.
12. E. Coronado, J. R. Galan-Mascaros, C. J. Gomez-Garcia and V. Laukhin, *Nature*, 2000, **408**, 447-449.
13. E. Coronado and P. Day, *Chem. Rev.*, 2004, **104**, 5419-5448.
14. H. Tanaka, H. Kobayashi and A. Kobayashi, *J. Am. Chem. Soc.*, 2002, **124**, 10002-10003.
15. A. Alberola, E. Coronado, J. R. Galán-Mascarós, C. Giménez-Saiz and C. J. Gómez-García, *J. Am. Chem. Soc.*, 2003, **125**, 10774-10775.
16. F. Robert, A. D. Naik, B. Tinant, R. Robiette and Y. Garcia, *Chem. Eur. J.*, 2009, **15**, 4327-4342.
17. H. Ö. Demir, İ. Kaya and M. Saçak, *Polym. Bull.*, 2008, **60**, 37-48.
18. B. Yalçın, P. A. Fatullayeva, O. Büyükgüngör, B. Koşar, S. Taşcıoğlu, A. I. Israfilov, Z. D. Ibayev, A. A. Medjidov and A. Aydın, *Polyhedron*, 2007, **26**, 3301-3309.
19. E. W. Dean and D. D. Stark, *J. Ind. Eng. Chem.*, 2002, **12**, 486-490.
20. J. M. Becker, J. Barker, G. J. Clarkson, R. v. Gorkum, G. K. Johal, R. I. Walton and P. Scott, *Dalton Trans.*, 2010, **39**, 2309-2326.
21. V. Mishra, H. Mishra, R. Mukherjee, E. Codjovi, J. Linares, J.-F. Letard, C. Desplanches, C. Balde, C. Enachescu and F. Varret, *Dalton Trans.*, 2009, 7462-7472.

-
22. C. Rajadurai, O. Fuhr, R. Kruk, M. Ghafari, H. Hahn and M. Ruben, *Chem Commun*, 2007, 2636-2638.
 23. F.-N. Shi, F. A. Almeida Paz, P. Girginova, J. Rocha, V. S. Amaral, J. Klinowski and T. Trindade, *J. Mol. Struct.*, 2006, **789**, 200-208.
 24. M. Sato, T. Ohya and I. Morishima, *Mol. Phys.*, 1981, **42**, 475-492.
 25. G. Villeneuve, J. L. Pizarro, J. M. Dance, M. I. Arriortua, T. Rojo and R. Kuentzler, *J. Magn. Magn. Mater.*, 1990, **83**, 478-480.
 26. L. Robertson, M. Duttine, M. Gaudon and A. Demourgues, *Chem. Mater.*, 2011, **23**, 2419-2427.
 27. O. Kahn and C. J. Martinez, *Science*, 1998, **279**, 44-48.
 28. G. S. Matouzenko, M. Perrin, B. Le Guennic, C. Genre, G. Molnar, A. Bousseksou and S. A. Borshch, *Dalton. Tran.*, 2007, 934-942.
 29. J. Fidler, T. Schrefl, S. Hoefinger and M. Hajduga, *J. Phys.: Condens. Matter.*, 2004, **16**, S455-S470.
 30. J. S. Miller, A. J. Epstein and W. M. Reiff, *Science*, 1988, **240**, 40-47.
 31. N. Ishii, Y. Okamura, S. Chiba, T. Nogami and T. Ishida, *J. Am. Chem. Soc.*, 2007, **130**, 24-25.
 32. D. K. Rittenberg, K. Sugiura, Y. Sakata, S. Mikami, A. J. Epstein and J. S. Miller, *Adv. Mater.*, 2000, **12**, 126-130.
 33. G. A. Baker, G. S. Rushbrooke and H. E. Gilbert, *Phys. Rev.*, 1964, **135**, A1272.
 34. H.-Z. Kou, Y.-T. Wang, W.-X. Luo, Q.-W. Xie, J. Tao, A.-L. Cui and D.-Z. Shen, *Cryst. Growth Des.*, 2008, **8**, 3908-3910.
 35. S. Ohkubo, *Bull. Chem. Soc. Jpn*, 1992, **65**, 1603-1707.
 36. M. T. T. Yoshida, T. Sato, N. Matsumoto, N. Re and J. Mrozinski, *Bull. Chem. Soc. Jpn.*, 2009, **82**, 467-471.
 37. C. S. Hong, J. H. Yoon and Y. S. You, *Inorg. Chem. Commun.*, 2005, **8**, 310-313.
 38. N. Matsumoto, T. Nozaki, H. Ushio, K.-i. Motoda, M. Ohba, G. Mago and H. Okawa, *J. Chem. Soc., Dalton Trans.*, 1993, 2157-2162.
 39. A. W. Addison, T. N. Rao, J. Reedijk, J. van Rijn and G. C. Verschoor, *J. Chem Soc., Dalton Trans.*, 1984, 1349-1356.
 40. G. Lazari, T. C. Stamatatos, C. P. Raptopoulou, V. Psycharis, M. Pissas, S. P. Perlepes and A. K. Boudalis, *Dalton. Tran.*, 2009, 3215-3221.
 41. M. Drillon, E. Coronado, M. Belaiche and R. L. Carlin, *J. Appl. Phys.*, 1988, **63**, 3551-3553.
 42. K. Inoue, K. Kikuchi, M. Ohba and H. Ōkawa, *Angew. Chem. Int. Ed.*, 2003, **42**, 4810-4813.
 43. M. Ohba, N. Usuki, N. Fukita and H. Ōkawa, *Angew. Chem. Int. Ed.*, 1999, **38**, 1795-1798.
 44. E. Pardo, D. Cangussu, M.-C. Dul, R. Lescouëzec, P. Herson, Y. Journaux, E. F. Pedroso, C. L. M. Pereira, M. C. Muñoz, R. Ruiz-García, J. Cano, P. Amorós, M. Julve and F. Lloret, *Angew. Chem. Int. Ed.*, 2008, **47**, 4211-4216.
 45. M. A. M. Abu-Youssef, A. Escuer, M. A. S. Goher, F. A. Mautner, G. J. Reiß and R. Vicente, *Angew. Chem. Int. Ed.*, 2000, **39**, 1624-1626.
-

- 46. A. Escuer, F. A. Mautner, M. A. S. Goher, M. A. M. Abu-Youssef and R. Vicente, *Chem. Comm.*, 2005, 605-607.
- 47. C. P. Landee, A. Djili, H. Place, B. Scott, R. D. Willett, D. F. Mudgett and M. Newhall, *Inorg. Chem.*, 1988, **27**, 620-627.
- 48. M. S. Reis, M. d. S. A. and V. S. Amaral, *Phys. Rev. B*, 2006, **73**, 214415.
- 49. K. Yoneda, Y. Hori, M. Ohba and S. Kitagawa, *Chem. Lett.*, 2008, **37**, 64-65.
- 50. E. Coronado, C. J. Gomez-Garcia and J. J. Borrás-Almenar, *J. Appl. Phys.*, 1990, **67**, 6009-6010.
- 51. L. Bogani, A. Vindigni, R. Sessoli and D. Gatteschi, *J. Mater. Chem.*, 2008, **18**, 4750-4758.

4. A family of transition metal complexes containing pyrrole-2-ketone derivatives

4.1 Introduction

In Chapter 2, we investigated substituent effects on the magnetic properties of a family of chiral 1 D chain Fe(II) complexes based on salicylaldimines HL^n ($n = 1 - 6$). In Chapter 3 we developed a related achiral system based on two isomeric salicylaldimines HL^n ($n = 7$ and 8), successfully extending the 1 D chain system to 2 or 3 D MOF structures more likely to give interesting and useful properties.¹ In particular, HL^8 promotes orthogonal arrangement of neighbouring units and thus promotes ferromagnetic exchange,² leading to a very rare example of a molecule-based hard magnet.³

In this chapter, we will apply this design principle to the essentially unexplored pyrrole-2-ketone bidentate ligands⁴ (Chart 4.1) and in particular the new pyridine derivative HL^9 . Our reasons for investigating this system were that: (i) it is functionally comparable with HL^8 but should produce a stronger field ligand, thus potentially introducing SCO phenomena; and (ii) a large number of synthetically accessible proligands are available in principle so that structure/property relations of complexes can be probed. Given the paucity of the coordination chemistry of pyrrole-2-ketones we also set out in parallel to

investigate the “parent” **HL**¹⁰ and the related (more electron-releasing) amide **HL**¹¹ which is readily available.⁵

Along with these three ligands (**HL**ⁿ n = 9 - 11), three transition metal ions Mn^{2+} , Fe^{2+} and Co^{2+} were studied, based on which twelve complexes have been made. The system is structurally diverse, with 1 D, 2 D, monometallic and trimetallic “sandwich” structures as well as a high nuclearity cluster being observed depending on the choice of cations and solvents. Unusual magnetic phenomena are discovered, including a system in which SCO and ferromagnetic coupling coexist.

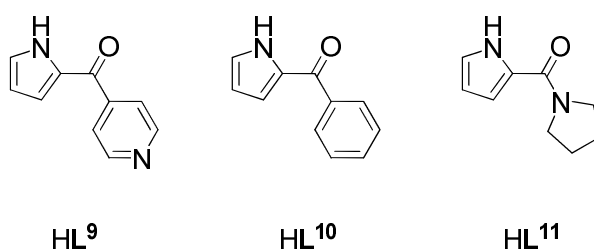


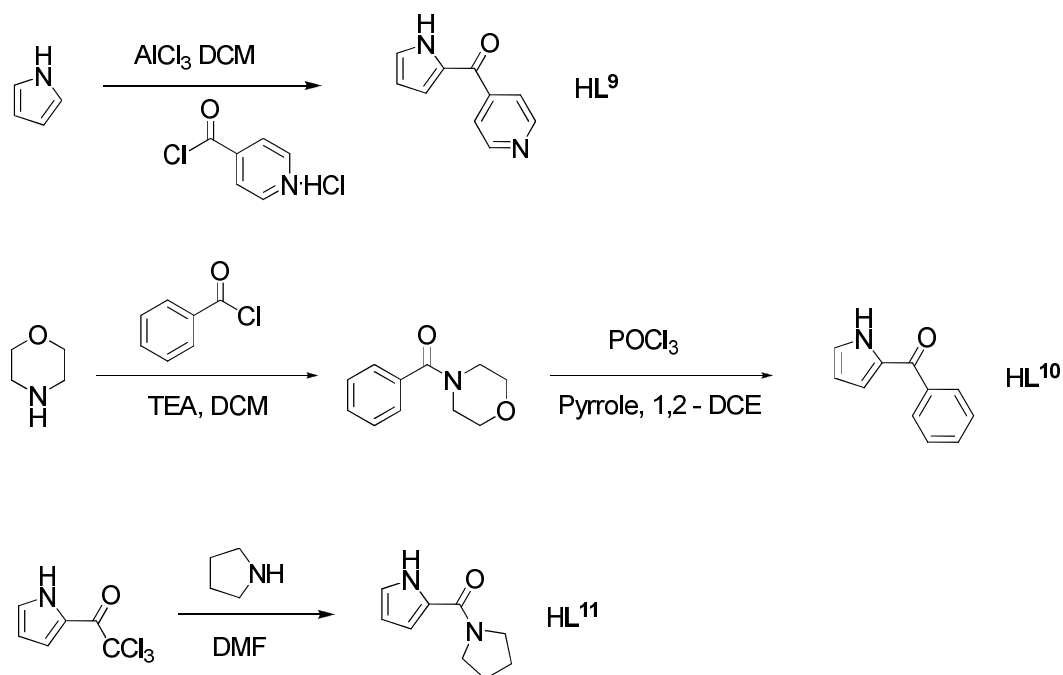
Chart **4.1**: Pyrrolyl ketone and amide ligands used in this chapter

4.2 Synthesis of proligands **HL**ⁿ (n = 9 - 11)

The pyrrolylketone **HL**⁹ was synthesized by a Friedel-Crafts reaction between isonicotinoyl chloride and pyrrole using AlCl_3 .

Phenyl substituted **HL**¹⁰ was made from morpholine in two high yielding steps.⁴ First, acylation of morpholine by benzyl chloride produced 1-benzoylmorpholine. This was stirred with fresh POCl_3 to prepare Vilsmeier reagent and then treated with pyrrole to yield the target pyridine.

The preparation of pyrrolylamide **HL¹¹** was conducted by a literature route from commercially available 2-trichloroacetylpyrrole treated with pyrrolidine.⁵



Scheme 4.1: Synthesis of proligands **HL⁹⁻¹¹**.

4.3 Complexes of **HL⁹**

4.3.1 **[FeL⁹₂]_n**

Synthesis of **FeL⁹₂**

A mixture of **HL⁹** and LiOMe in dry methanol was stirred for 15 min. Addition of FeCl_2 in methanol caused an immediate colour change to blue then more slowly to purple. After 4 h a purple solid was present in a colourless solution. The air stable

solid was collected by filtration while single crystals suitable for X-ray diffraction were grown by a similar reaction in THF/MeOH at room temperature for one week.

As shown in Figure 4.1 the repeat unit contains one Fe centre which is coordinated by two bidentate N-O ligands \mathbf{L}^9 and two pyridines from adjacent units. Overall the structure is very similar to that of the Schiff-base complex $[\text{Fe}\mathbf{L}^8]_n$ in chapter 3, and parameters are included in square brackets [thus] for comparison in the following description.

The geometry of the Fe unit is very close to octahedral with two chelate O(1)-Fe(1)-N(1) and O(1')-Fe(1)-N(1') lying in a plane. The angle of N(2)-Fe(1)-O(1) is however slightly deviated from 90°, at 87.45(6)° [85.24(14)°]. These molecular units are assembled *via* pyridine coordination to give a planar rhombic array of Fe atoms (Figure 4.2) with Fe-Fe-Fe angles of 83.41 and 96.59° [83.93 and 97.07°] and nearest neighbour coordination units are arranged almost orthogonally at 84.22° [86.0°] with Fe...Fe distances of 9.135 Å [7.44 Å]. These *xy* planes all form an angle of ca. 81.24° [72.0°] to the Fe atom plane. Figure 4.3 depicts the mutual arrangement of the layers, with the overall effect of reflecting and off-setting alternate layers in the stack. The undulations of the organic ligands are accommodated efficiently by interdigitation and no solvent is included as confirmed by microanalysis.

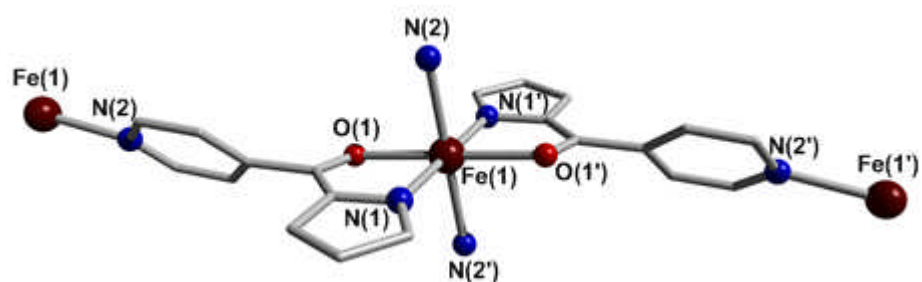


Figure 4.1: Repeat unit of complex $[\text{FeL}^9_2]_n$, Selected bond lengths (\AA) and angles ($^\circ$): Fe(1)-N(1) 2.082(2), Fe(1)-O(1) 2.1585(15), Fe(1)-N(2) 2.1991(19), N(1)-Fe(1)-N(1') 180.0, O(1)-Fe(1)-O(1') 180.0, N(2)-Fe(1)-N(2') 180.0, N(2)-Fe(1)-N(1') 89.36(7), N(2)-Fe(1)-O(1) 87.45(6).

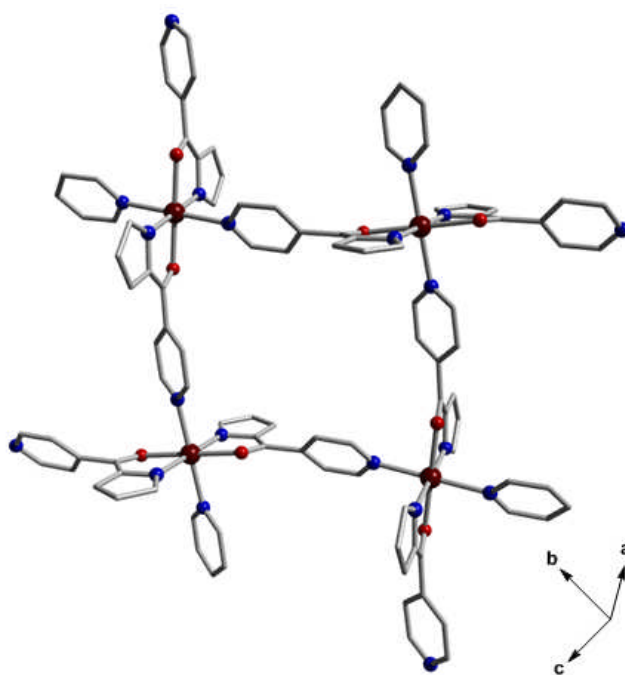


Figure 4.2: 2 D array of orthogonal complexes.

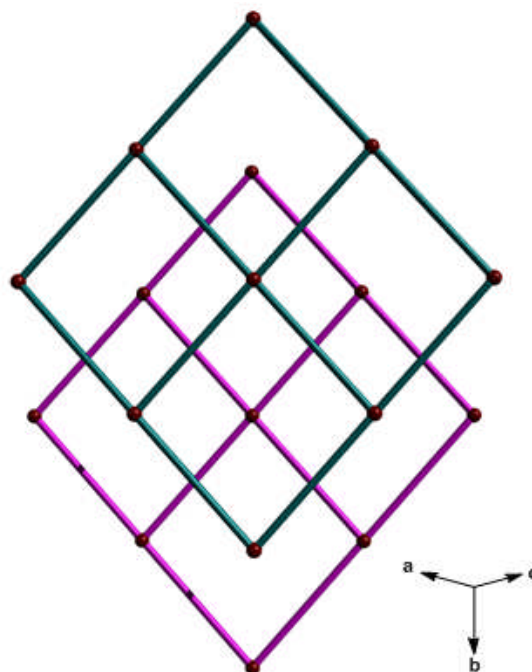


Figure 4.3: Two adjacent layers in $[\text{FeL}^9_2]_n$.

Magnetism of $[\text{FeL}^9_2]_n$

The magnetic properties of $[\text{FeL}^9_2]_n$ are very unusual. As shown in the plots of χ_M vs. T (Figure 4.4) the magnetic susceptibility data obey the Curie-Weiss law in the high temperature regime (150 K – 300 K). But as the temperature decreases, there are two thermal transitions, distinguished by two inflection points at *ca.* 120 K and 25 K respectively. These are also reflected in the form of the plot of $\chi_M T$ vs. T (Figure 4.5), where $\chi_M T$ drops sharply from $3.610 \text{ cm}^3 \text{ K mol}^{-1}$ (150 K) to $0.678 \text{ cm}^3 \text{ K mol}^{-1}$ at 50 K, while at *ca.* 25 K another maximum ($2.350 \text{ cm}^3 \text{ K mol}^{-1}$) is observed. Both transitions are reversible.

The first thermal transition (125 K) could result from a SCO while the second thermal transition suggests that $[\text{FeL}^9_2]_n$ undergoes a magnetic ordering at that temperature (25 K). This was confirmed by measurements on warming the

sample after cooling in zero field (ZFCW), followed by measuring on cooling in a field (FCC) from 2 - 50 K using a field of 100 Oe. These two curves starts to diverge at *ca.* 50 K (Figure 4.6).

The ferromagnetic hysteresis curve of $[\text{FeL}^9_2]$ at 2 K and 10 K are shown in Figure 4.7. Magnetization was not saturated at either temperature but a large coercive field (480 Oe) was observed.

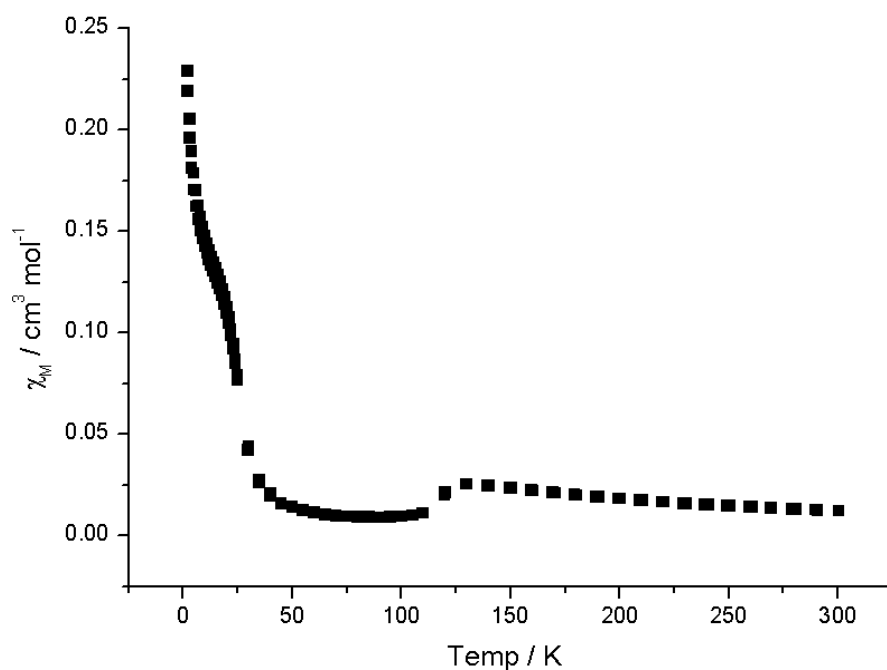


Figure 4.4: χ_M vs T curve of $[\text{FeL}^9_2]_n$ measured at 1000 Oe.

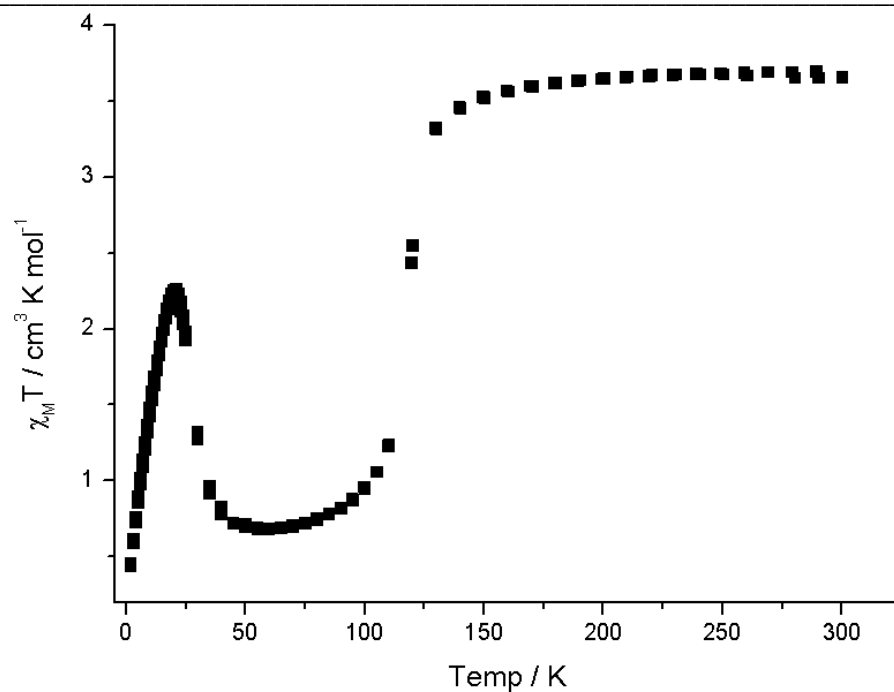


Figure 4.5: $\chi_M T$ vs T of $[\text{FeL}^9_2]_n$ measured at 1000 Oe.

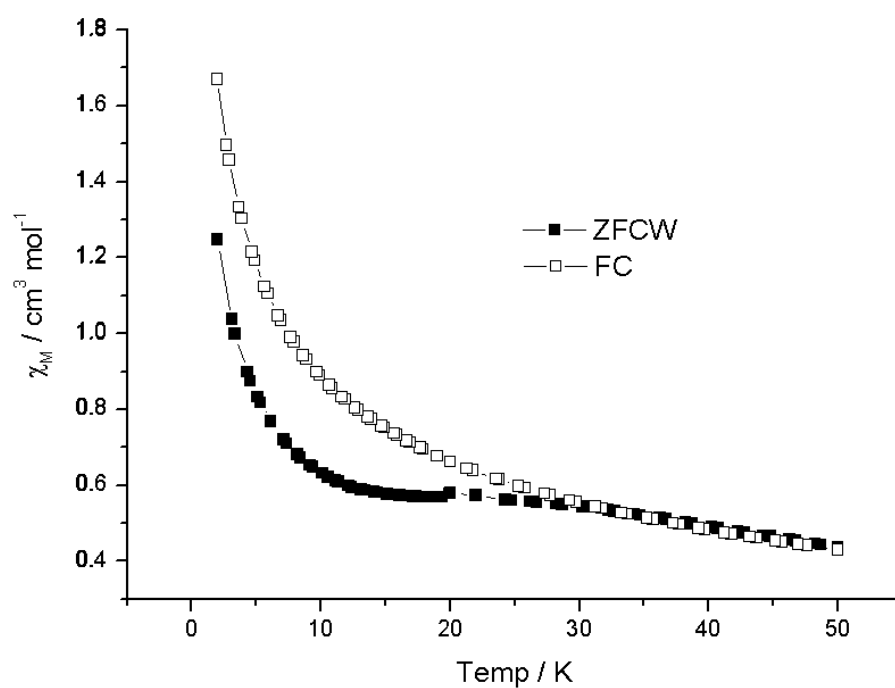


Figure 4.6: ZFCW and FCC M vs. T curves for $[\text{FeL}^9_2]_n$ measured at 100 Oe.

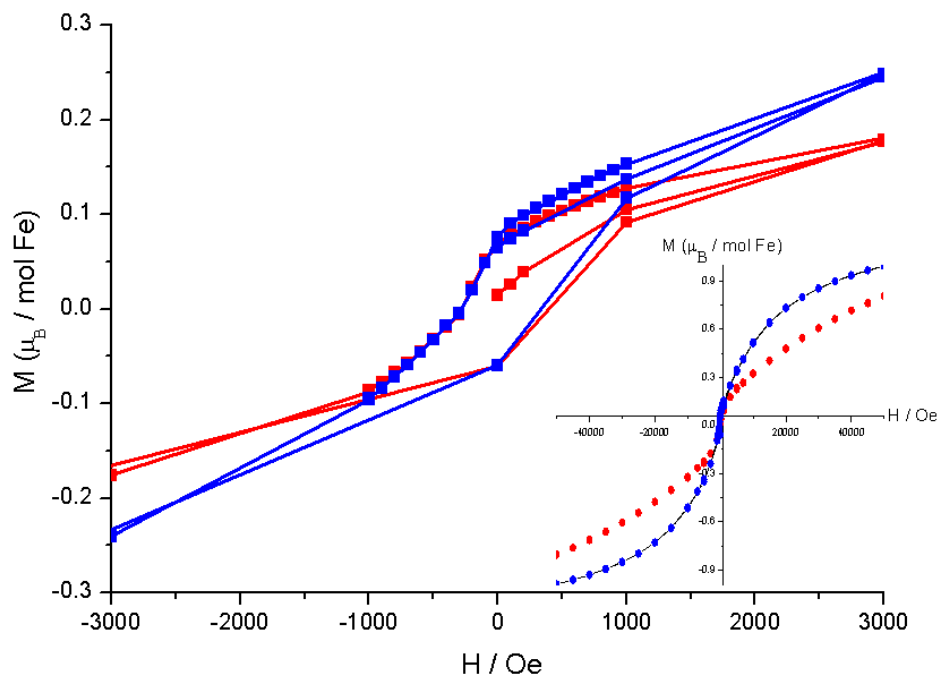


Figure 4.7: Magnetization of material $[\text{FeL}^9_2]_n$ measured at 2 K (---) and 10 K (---).

Powder XRD of $[\text{FeL}^9_2]_n$

Variable temperature powder XRD measurements were conducted on bulk samples of $[\text{FeL}^9_2]_n$. While the peaks are relatively broad, the features are readily recognisable. At 250 K, three clear peaks at $2\theta = 19.4^\circ$, 30.0° and 41.5° (Figure 4.8) shift to 20.0° , 31.2° and 42.0° respectively at 50 K. By 30 K they have moved back to 2θ positions indistinguishable from those at 250 K (Figure 4.9); in other words the patterns at 30 K (ferromagnetically coupled system) and 250 K (high spin Curie-Weiss system) are very similar (Figure 4.10). These data are consistent with the onset of magnetic ordering being coupled with the phase change back to the high temperature structure.

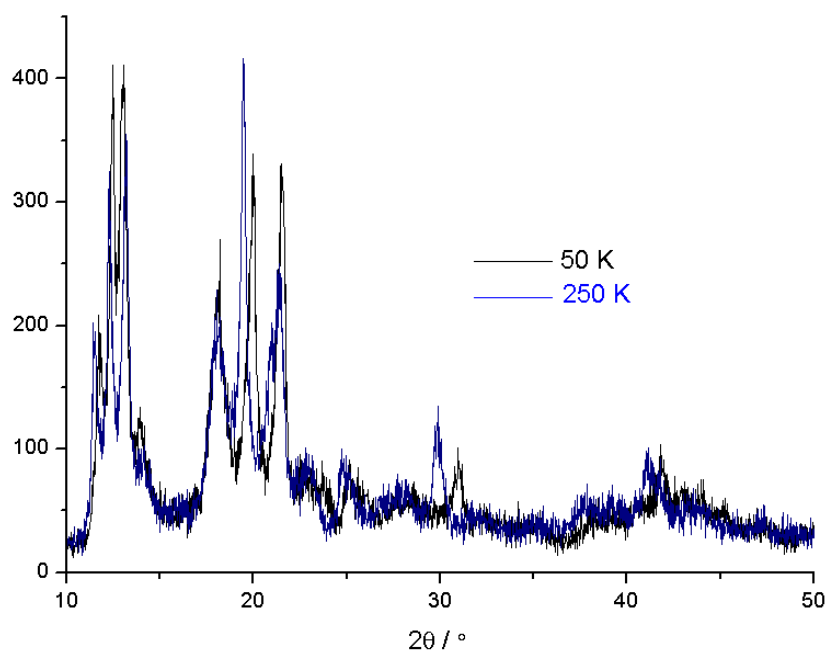


Figure 4.8: Powder XRD pattern of $[\text{FeL}^9_2]_n$ at 50 K, 250 K.

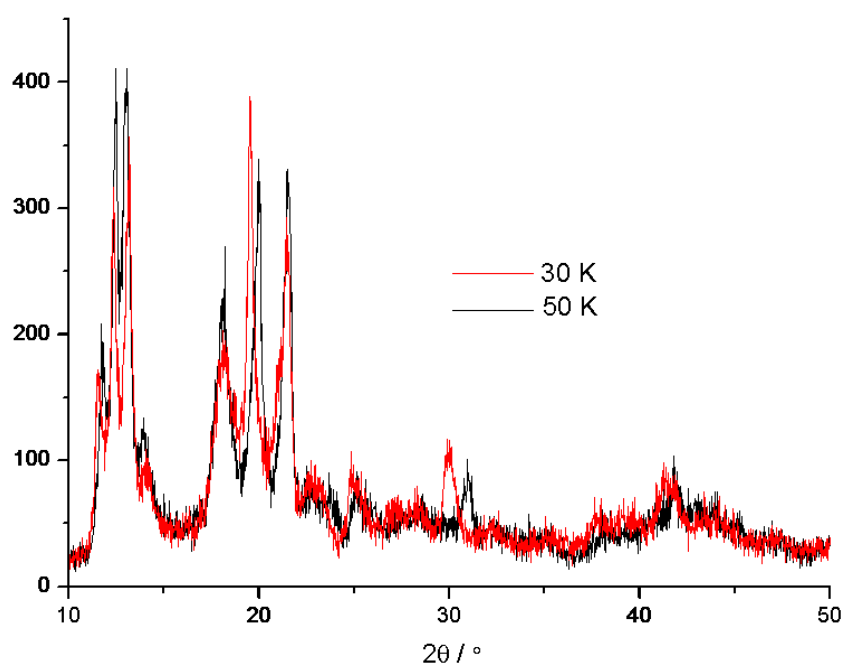


Figure 4.9: Powder XRD pattern of $[\text{FeL}^9_2]_n$ at 30 K, 50 K

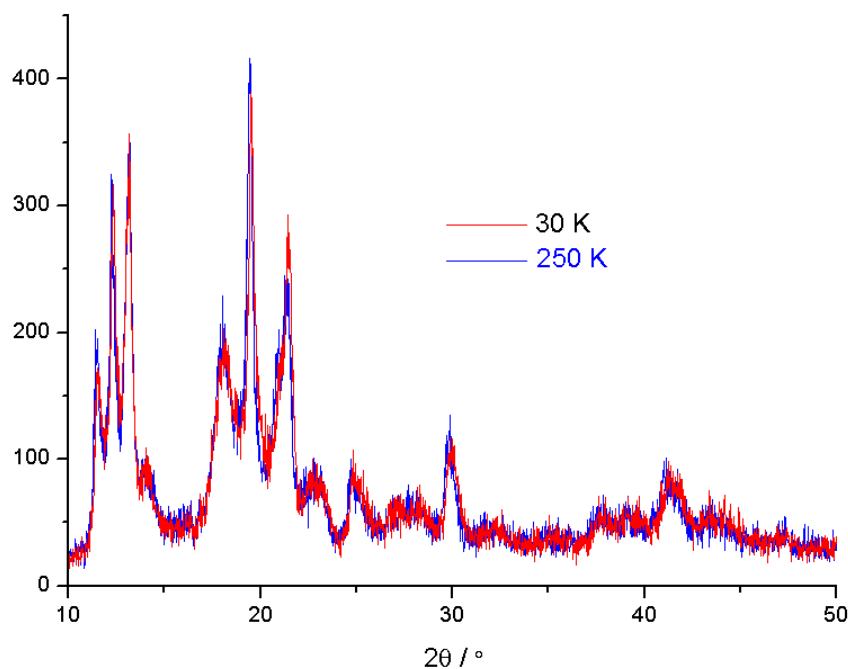


Figure 4.10: Powder XRD pattern of $[\text{FeL}^9_2]_n$ at 30 K, 250 K

SCO complexes have been studied extensively, and detailed reviews can be found elsewhere.^{1, 6} For Fe(II) SCO complexes with a regular octahedral geometry, there are two spin states: low spin ($S = 0$) and high spin ($S = 2$) and in an appropriate ligand field a reversible change from paramagnetism at high temperature to diamagnetism at low temperature is observed. This transition can also be triggered by external stimuli, such as light irradiation,⁷⁻⁸ and pressure.⁹ Recently the Fe(II) SCO complex, $\text{Fe}_2[\text{Nb}(\text{CN})_8] \cdot (4\text{-pyridinealdoxime})_8 \cdot 2\text{H}_2\text{O}$ ¹⁰ was shown to undergo conversion of its low spin state to high spin following irradiation, and, most excitingly, spontaneous magnetization was observed at 20 K.

In some very rare cases, SCO phenomena result from structural phase transitions *e.g.* $[\text{Co}(\text{C}_{16}\text{-terpy})_2](\text{BF}_4)_2$ ¹¹. In comparison, $[\text{FeL}^9_2]_n$ undergoes H.S. \rightarrow L.S. SCO *via* a more conventional thermal process followed by

spontaneous magnetization ($T_c = 25$ K) coupled with a phase change to the high spin status. In other words, this is the first example of H.S. \rightarrow L.S. \rightarrow H.S. SCO ferromagnet.

In essence, our proposal that the use of \mathbf{L}^9 as a stronger-field ligand than \mathbf{L}^8 may lead to the observation of SCO phenomena has been borne out, but in rather unexpected circumstances leading to a tristable para- dia- ferro-magnetic system.

4.3.2 CoL^9_2

In a similar manner to the above synthesis of $[\text{FeL}^9_2]_n$ a mixture of HL^9 and LiOMe in dry methanol was treated with CoCl_2 yielding a slightly air-sensitive insoluble yellow solid. Elemental analysis was consistent with a $[\text{CoL}^9_2]$ stoichiometry and although we were unable to grow single crystals, for the purposes of the following discussion we assume the material is a 2 D framework like $[\text{FeL}^8_2]_n$ and $[\text{FeL}^9_2]_n$.

The curve of $\chi_M T$ vs. T for complex $[\text{CoL}^9_2]_n$ is shown in Figure 4.11. From 200 K to 300 K, $\chi_M T$ is nearly a constant, with a value of $2.34 \text{ cm}^3 \text{ K mol}^{-1}$, rather higher than the $1.876 \text{ cm}^3 \text{ K mol}^{-1}$ calculated for high spin Co^{2+} ($g = 2.00$) presumably as a result of strong spin-orbital coupling.¹²⁻¹⁴

On decreasing the temperature apparent SCO was observed with a transition temperature of *ca.* 120 K, rather similar to that for $[\text{FeL}^9_2]_n$. After 50 K, $\chi_M T$ was found to be *ca.* $0.56 \text{ cm}^3 \text{ K mol}^{-1}$, indicating that the material is nearly all in the low spin state ($0.375 \text{ cm}^3 \text{ K mol}^{-1}$ for a free low spin Co^{2+} , assuming $g = 2.00$). This is confirmed by magnetization experiment (Figure 4.12) at 2 K where

the material is magnetically saturated at 7 T with $M = 1.17$ B.M. No SCO hysteresis was observed for this material.

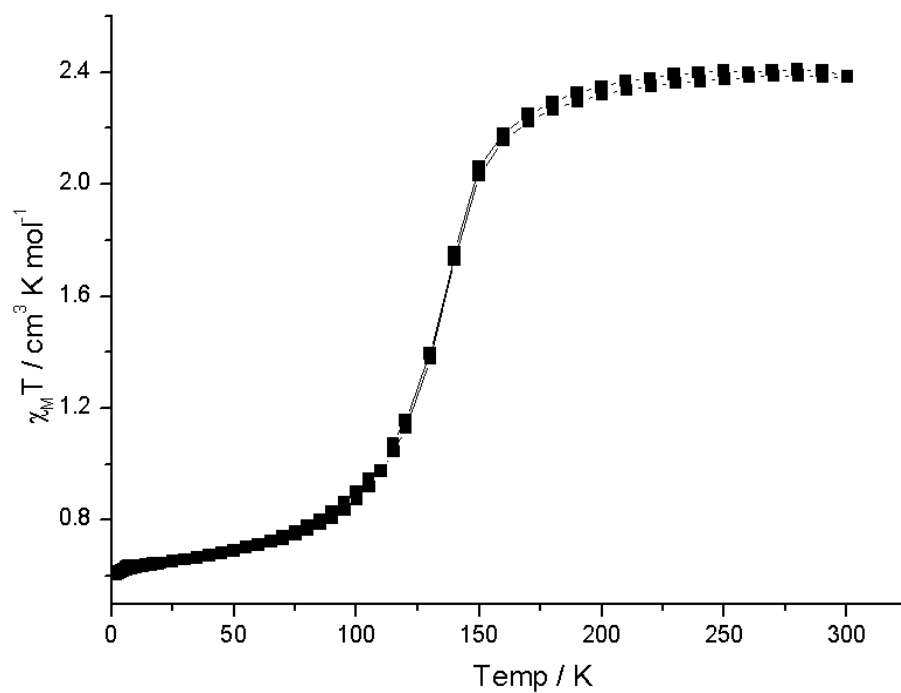


Figure 4.11: $\chi_M T$ vs. T for material $[\text{CoL}_2]_n$ measured at 1000 Oe

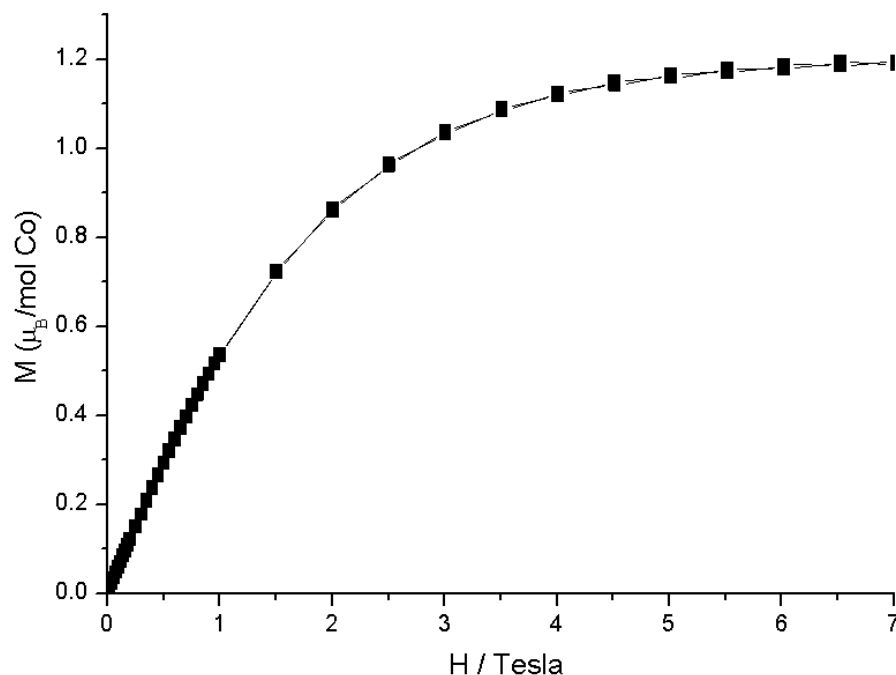


Figure 4.12: M vs. H for material $[\text{CoL}^9_2]_n$ measured at 2 K

4.3.3 Mn(II) complexes



The treatment of HL^9 with sodium hydride in THF, followed by MnCl_2 yielded a yellow suspension. The isolated solid was recrystallised from boiling THF, and crystals of $[\{\text{Na}_2\text{Mn}_2\text{L}^9_6(\text{THF})_4\} \cdot 3\text{THF}]_\infty$ suitable for X-ray diffraction were grown slowly from THF/ Et_2O .

The repeat unit contains the trimetallic sandwich-like anions $[(\text{fac-MnL}^9_3)_2-\mu-\text{Na}]^-$ (Figure 4.13), the ligating O atoms at each six-coordinate Mn(II) centre being further engaged in bridging to the central Na(1) ion. Charge balance is maintained with Na(2) coordinated *via* pyridine units to form a 1 D zigzag chain complex as shown in Figure 4.14; the four remaining pyridine units are

uncoordinated. The Mn(II) and Na(1) ions have approximate trigonal prismatic geometry while Na(2) is essentially octahedral with two *trans* oriented pyridines and four further THF ligands.

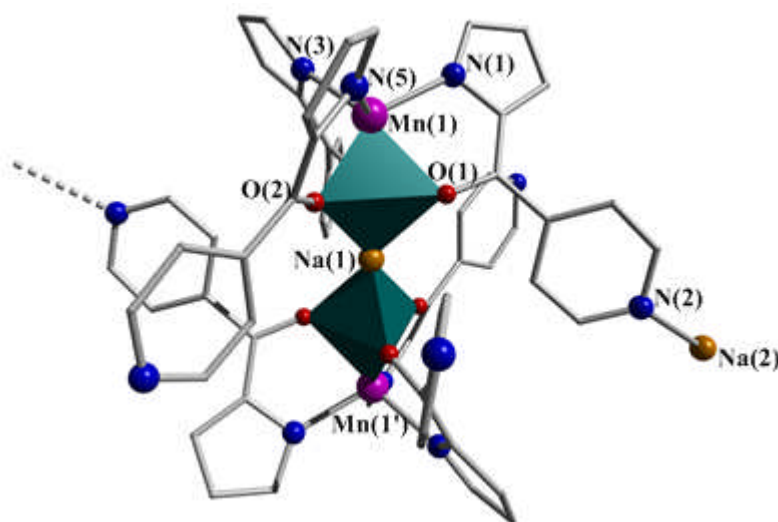


Figure 4.13: Repeat unit of chain complex $[\{\text{Na}_2\text{Mn}_2\text{L}_9(\text{THF})_4\} \cdot 3\text{THF}]_\infty$; Selected bond length (Å): Mn(1)-N(1) 2.162(2), Mn(1)-N(3) 2.151(2), Mn(1)-N(5) 2.168(2), Mn(1)-O(1) 2.3405(16), Mn(1)-O(2) 2.2791(17), Mn(1)-Na(1) 3.2409(4), Na(1)-O(1) 2.3468(16), Na(1)-O(2) 2.3793(16), Na(2)-N(2) and angles (°) Mn(1)-Na(1)-Mn(1') 180; Purple: Mn, Light yellow: Na, Red: O, Blue: N; Solvents and Hydrogen atoms are removed for clarity.

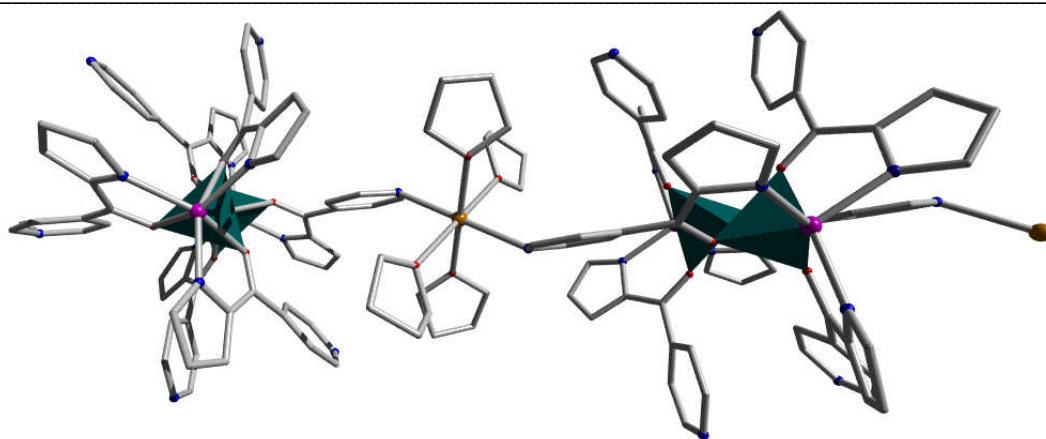


Figure 4.14: Zigzag chain structure of $[\{\text{Na}_2\text{Mn}_2\text{L}^9(\text{THF})_4\} \cdot 3\text{THF}]_\infty$.

Magnetism of $[\{\text{Na}_2\text{Mn}_2\text{L}^9(\text{THF})_4\} \cdot 3\text{THF}]_\infty$

The curve of $\chi_M T$ vs. T for $[\{\text{Na}_2\text{Mn}_2\text{L}^9(\text{THF})_4\} \cdot 3\text{THF}]_\infty$ is shown in Figure 4.15.

The value of $\chi_M T$ at 301 K is *ca* $4.597 \text{ cm}^3 \text{ K mol}^{-1}$, slightly higher than $4.377 \text{ cm}^3 \text{ K mol}^{-1}$ for a free high spin Mn^{2+} ion ($g = 2$) due to spin-orbit contributions. As temperature decreases, the value of $\chi_M T$ is nearly constant until *ca* 50 K where it begins to fall slightly, possibly due to ZFS.

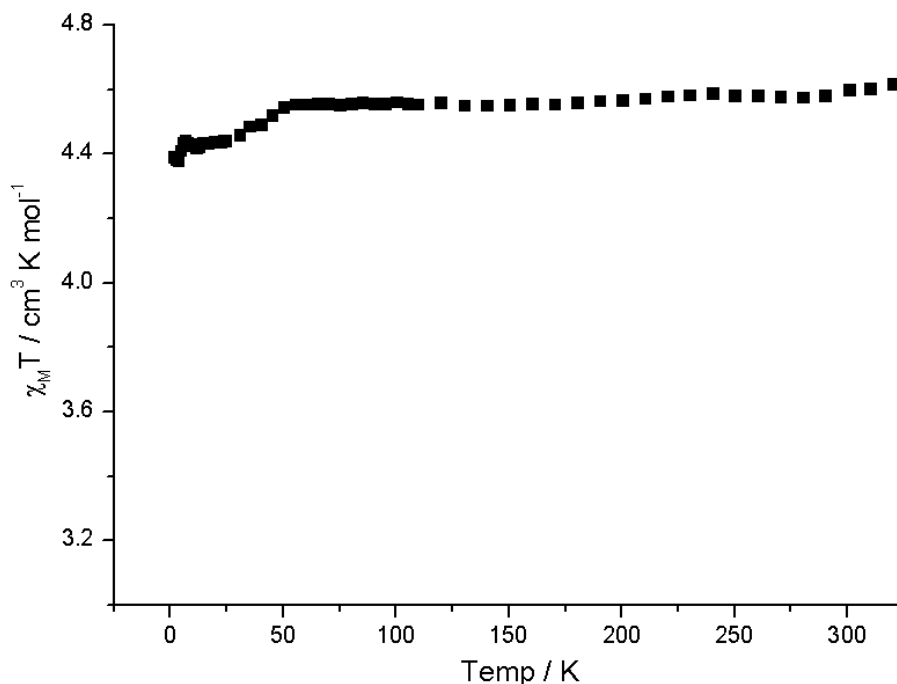


Figure 4.15: $\chi_M T$ vs. T for material $[\{\text{Na}_2\text{Mn}_2\text{L}^9(\text{THF})_4\} \cdot 3\text{THF}]_\infty$ measured at 1000 Oe

Considering that the repeat unit contains two paramagnetic Mn(II) ions linked through a diamagnetic Na^+ , the magnetic exchanges are mainly from electrostatic interactions, and therefore an isotropic Heisenberg magnetic model (HDVV)¹ was used to describe the magnetism of the material.

$$\mathbf{H} = -J \mathbf{S}_A \cdot \mathbf{S}_B + \beta (\mathbf{S}_A \cdot \mathbf{g}_A + \mathbf{S}_B \cdot \mathbf{g}_B) \cdot \mathbf{H}$$

$$\mathbf{S} = \mathbf{S}_A + \mathbf{S}_B$$

$\mathbf{S}_A, \mathbf{S}_B$ are the local spin operators, J is the isotropic magnetic coupling parameter.

From this,

$$\chi_M = \frac{2Ng^2\beta^2}{kT} \frac{e^x + 5e^{3x} + 14e^{6x} + 30e^{10x} + 55e^{15x}}{1 + 3e^x + 5e^{3x} + 7e^{6x} + 9e^{10x} + 11e^{15x}}$$

With $x = J/kT$ for local spins $S_A = S_B = 5/2$ Eqn. 4.1

As shown in Figure 4.16, a least squares fit to the equation (Eqn. 4.1) gives $J = -0.23$ K, $R = 0.02$ and $g = 1.80$, confirming that the material is very weakly antiferromagnetic. A fit to Curie-Weiss law extracts a $C = 4.765$ cm³ K mol⁻¹ and a negative $\Theta = -0.25$ K, $R = 0.07$.

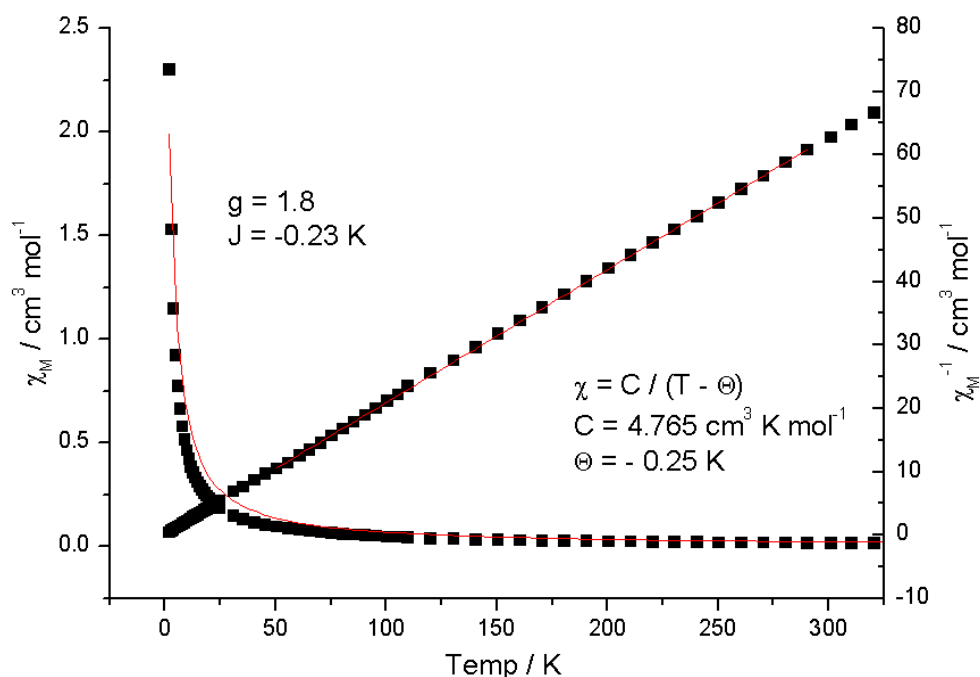


Figure 4.16: χ_M, χ_M^{-1} vs. T for material $[\{\text{Na}_2\text{Mn}_2\text{L}^9(\text{THF})_4\} \cdot 3\text{THF}]_\infty$ measured at 1000 Oe



The yellow solid $[\{\text{Na}_2\text{Mn}_2\text{L}^9(\text{THF})_4\} \cdot 3\text{THF}]_\infty$ was very soluble in hot MeCN, and recrystallization at 4 °C isolated orange single crystals of $[\{\text{Na}_2\text{Mn}_2\text{L}^9(\text{MeCN})_2\} \cdot \text{MeCN}]_\infty$ (Figure 4.17).

Similar to the THF solvate above the complex contains $[(\text{fac-}\text{L}^9_3\text{Mn})_2-\mu\text{-Na}]$ units (Figure 4.17) although the distance between Mn atoms is lower at 6.260 Å (*c.f.* 6.482 Å). Four out of the six pyridine units in each anion are

coordinated to the equatorial plane of bridging Na^+ ions, with the coordination sphere of the latter made up by two additional MeCN ligands. The Na^+ cations and $[(fac\text{-}\mathbf{L}^9_3\text{Mn})_2-\mu\text{-Na}]^-$ units are thus alternate nodes in a 2 D network (Figure 4.18).

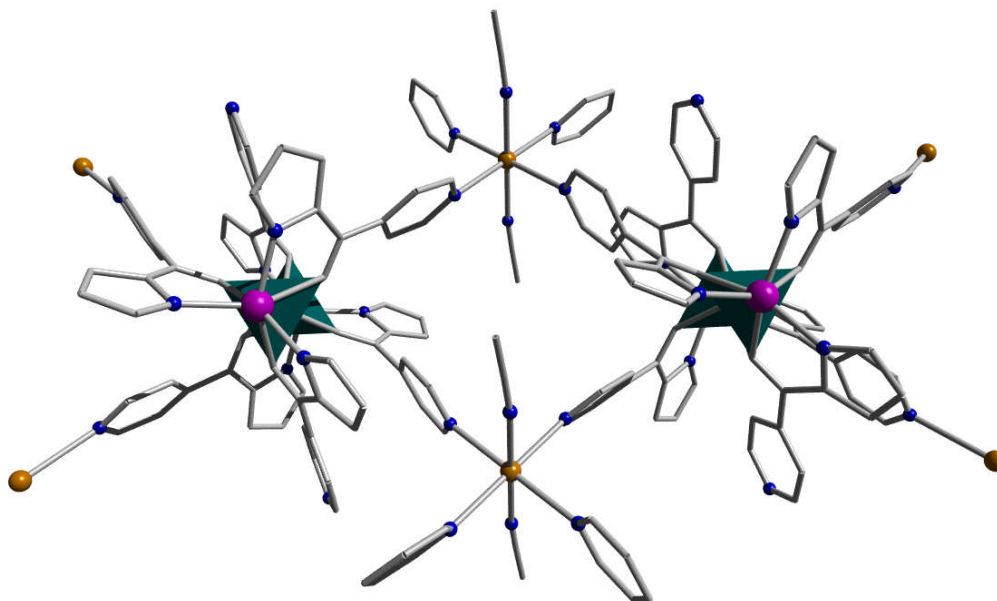


Figure 4.17: the repeat unit for complex $[\{\text{Na}_2\text{Mn}_2\mathbf{L}^9_6(\text{MeCN})_2\}\cdot\text{MeCN}]_\infty$;

Solvents and hydrogen atoms are removed for clarity

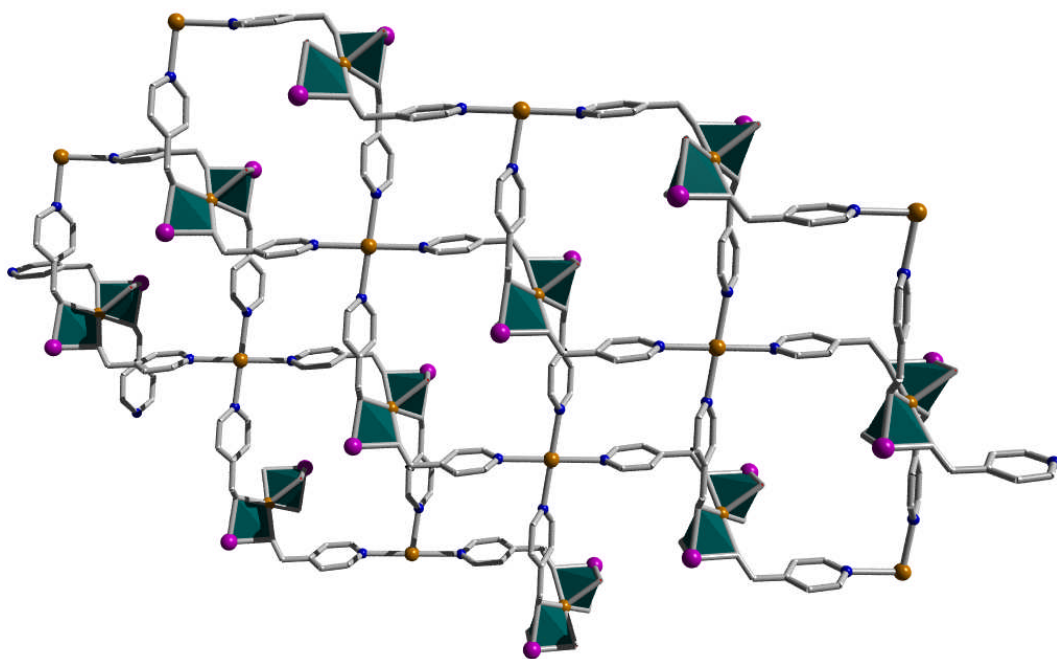


Figure 4.18: 2 D grid topology of $[\{\text{Na}_2\text{Mn}_2\text{L}^9(\text{MeCN})_2\} \cdot \text{MeCN}]_\infty$; Ligand, solvents and hydrogen atoms are removed for clarity.

Magnetism of $[\{\text{Na}_2\text{Mn}_2\text{L}^9(\text{MeCN})_2\} \cdot \text{MeCN}]_\infty$

The curve of $\chi_M T$ vs. T for $[\{\text{Na}_2\text{Mn}_2\text{L}^9(\text{MeCN})_2\} \cdot \text{MeCN}]_\infty$ is shown in Figure 4.19. The value of $\chi_M T$ is *ca.* $4.461 \text{ cm}^3 \text{ K mol}^{-1}$ at 300 K, slightly higher than $4.377 \text{ cm}^3 \text{ K mol}^{-1}$ for a free high spin Mn^{2+} ion ($g = 2.00$). On decreasing the temperature, the value of $\chi_M T$ reduces gradually, indicating antiferromagnetic exchange. Below 25 K, the value of $\chi_M T$ drops dramatically to $3.918 \text{ cm}^3 \text{ K mol}^{-1}$ at 2 K.

The curves of χ_M and χ_M^{-1} vs. T for $[\{\text{Na}_2\text{Mn}_2\text{L}^9(\text{MeCN})_2\} \cdot \text{MeCN}]_\infty$ are shown in Figure 4.20. A least squares fit to the Heisenberg magnetic model (eqn. 4.1) gives $J = -0.31 \text{ K}$. The magnetic data obeys a Curie-Weiss law (50 to

300 K) and values of $C = 4.506 \text{ cm}^3 \text{ K mol}^{-1}$ and $\Theta = -2.97$ were extracted, confirming the presence of antiferromagnetic interactions.

The curve of M vs. H (Figure 4.21) shows saturation at 5 T with M of *ca* 5 B.M., confirming that the complex $[\{\text{Na}_2\text{Mn}_2\text{L}^9(\text{MeCN})_2\} \cdot \text{MeCN}]_\infty$ contains high spin Mn(II).

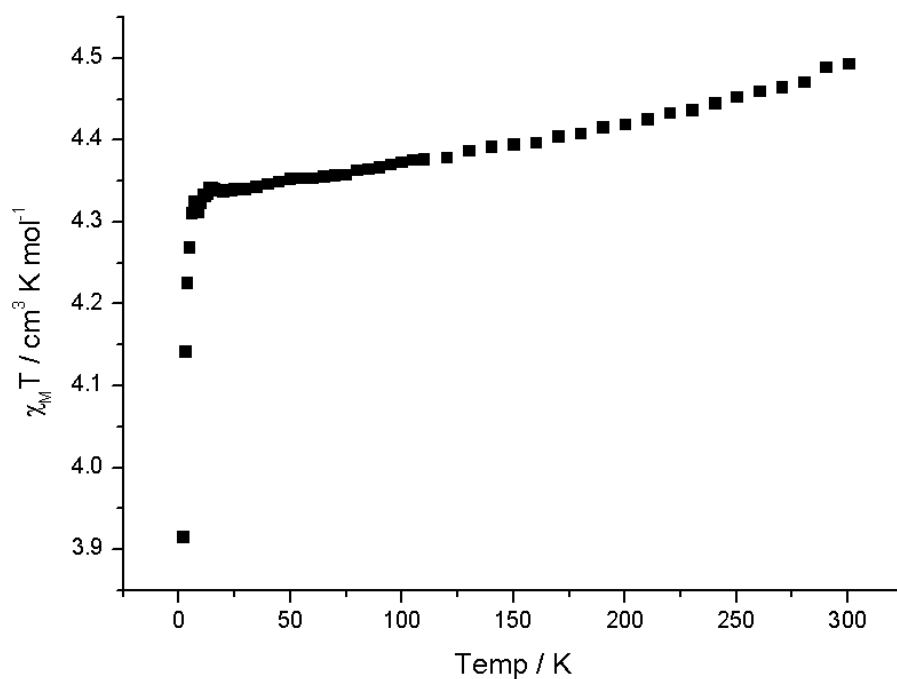


Figure 4.19: $\chi_M T$ vs. T for material $[\{\text{Na}_2\text{Mn}_2\text{L}^9(\text{MeCN})_2\} \cdot \text{MeCN}]_\infty$ measured at 1000 Oe

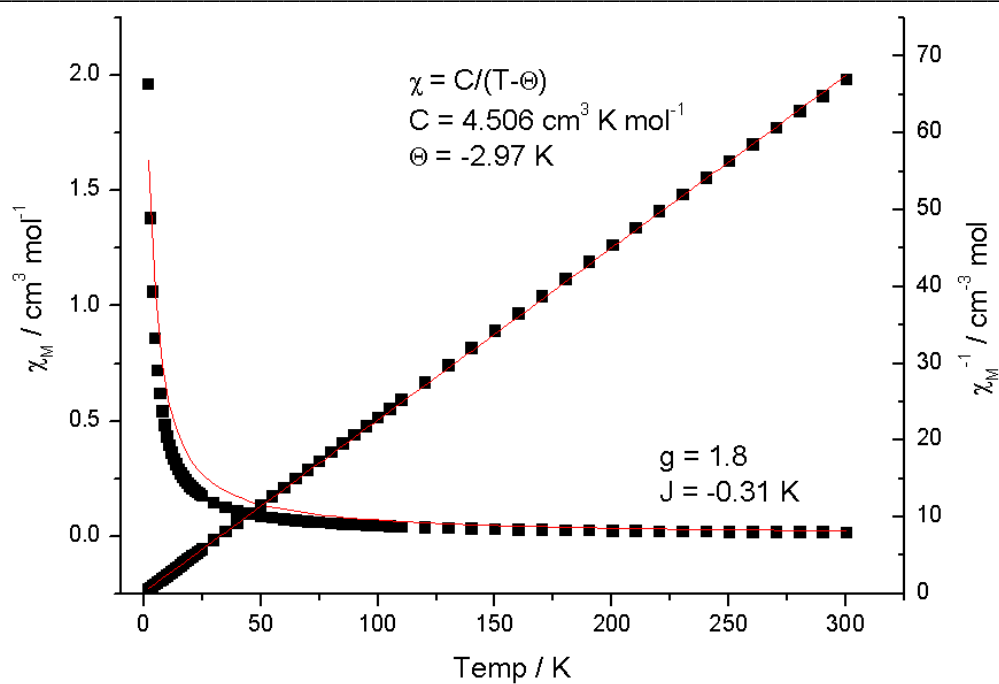


Figure 4.20: χ_M, χ_M^{-1} vs. T for material $[\{\text{Na}_2\text{Mn}_2\text{L}^9(\text{MeCN})_2\} \cdot \text{MeCN}]_\infty$
measured at 1000 Oe

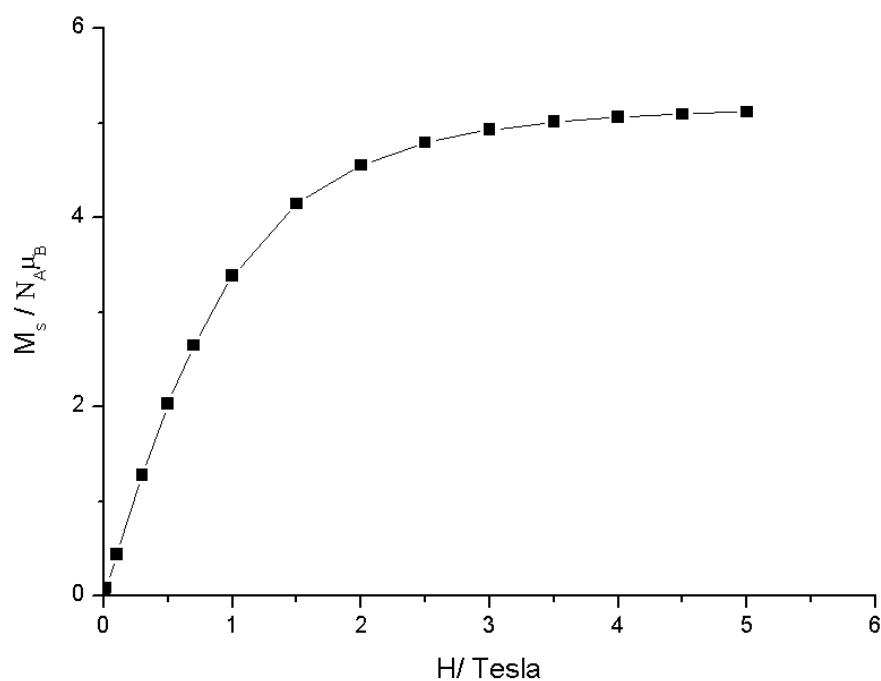


Figure 4.21: M vs. H for $[\{\text{Na}_2\text{Mn}_2\text{L}^9(\text{MeCN})_2\} \cdot \text{MeCN}]_\infty$ measured at 2 K

Attempt to synthesise complex Mn_3L^9_6

The sandwich-like anion structure present in these materials suggested to us that it may be possible to synthesise neutral systems containing three transition metal ions as shown in Figure 4.22. These might have interesting magnetic properties. We thus set out to perform salt metathesis with other alkali metal ions to see if this would facilitate formation of a transition metal bridged system.

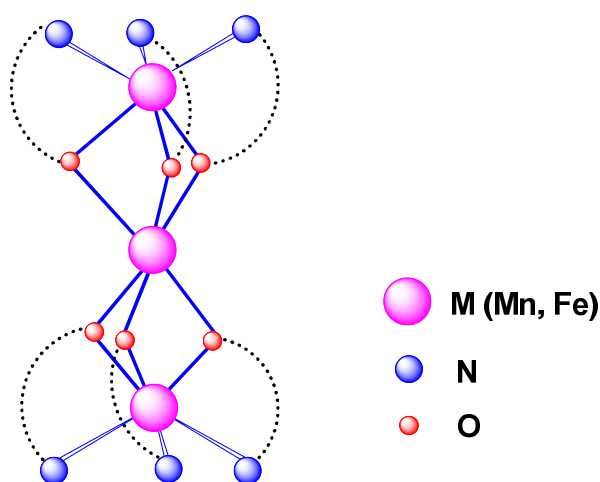


Figure 4.22: Representation of a ideal sandwich-like model

A: LiOMe method

The reaction of in situ generated LiL^9 with MnCl_2 in dry MeOH gave an analytically pure and air stable yellow solid in high yield, the LiCl remaining dissolved. The product was insoluble in common organic solvents and we were unable to form single crystals. Based on its poor solubility, we speculated that this material is more likely to be a 2 D complex $[\text{MnL}^9_2]_n$ (Figure 4.23, *c.f.* $[\text{FeL}^9_2]_n$ described in 4.3.1.) than the target Mn_3L^9_6 trimer (Figure 4.22). Elemental

analysis confirmed a stoichiometric composition MnL^9_2 , and ICP-MS analysis found no lithium in the sample.

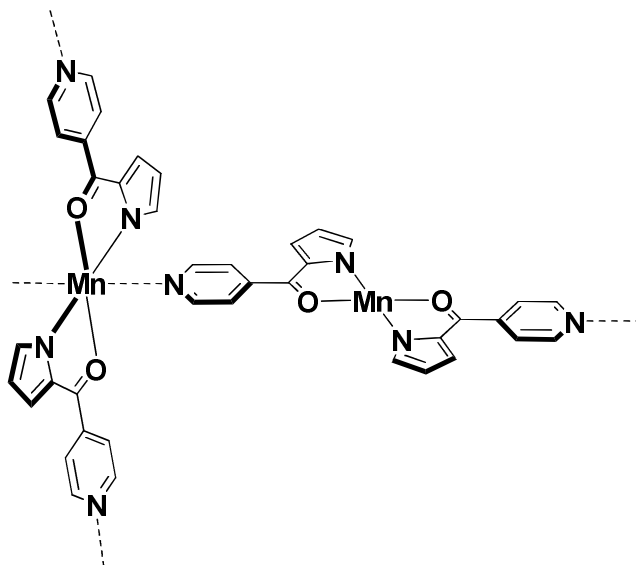


Figure 4.23: a possible 2 D molecular structure of MnL^9_2

Magnetism of MnL^9_2

The curves of χ_M^{-1} and $\chi_M T$ vs. T are shown in Figure 4.24. From 300 K to 125 K, the value of $\chi_M T$ is nearly a constant, with a value of $4.83 \text{ cm}^3 \text{ K mol}^{-1}$ is slightly higher than that expected for a free high spin Mn^{2+} ($4.377 \text{ cm}^3 \text{ K mol}^{-1}$, $g = 2.00$) but in agreement with the value for C of $4.84 \text{ cm}^3 \text{ K mol}^{-1}$ extracted from the Curie-Weiss law fit. On decreasing the temperature the value of $\chi_M T$ dropped sharply (*ca* 50 K) indicating dominant antiferromagnetic interactions ($\Theta = -1.50 \text{ K}$).

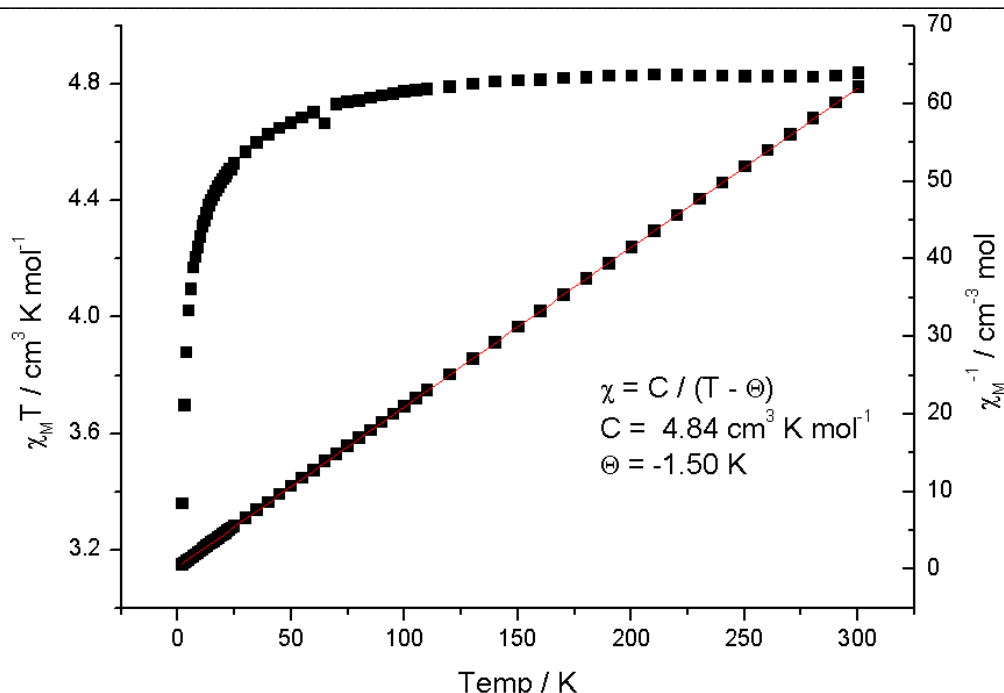


Figure 4.24: χ_M^{-1} , $\chi_M T$ vs. T for $[\text{MnL}^9_2]_n$ measured at 1000 Oe

B: KH method

The reaction mixture of in situ generated KL^9 and MnCl_2 in THF produced an orange solution. THF was removed under reduced pressure and the product was extracted into MeCN. Addition of Et_2O and cooling to $-30\text{ }^\circ\text{C}$ slowly gave a few crystals of $[\{\text{K}_4\text{Mn}_2\text{L}^9_4(\text{HL}^9)_2(\text{OH})_2(\text{MeCN})_2\}]_\infty \cdot x\text{MeCN} \cdot y\text{Et}_2\text{O}$, presumably following a reaction with adventitious water.

Due to the poor quality and disorder in the crystal, the structure was not fully refined. As shown in Figure 4.25, the asymmetric unit contains four K^+ ions and two $\text{Mn}(\text{II})$. Each $\text{Mn}(\text{II})$ is coordinated to two ligands L^9 , and *via* two μ -hydroxy bridges is connected to another $\text{Mn}(\text{II})$ ion [Figure 4.26 (a)]. The geometry about Mn is distorted octahedral [angle $\text{N}(3)\text{-Mn}(1)\text{-O}(4) = 169.45\text{ }^\circ$]. The angle of $\text{Mn}(1)\text{-O}(4)\text{-Mn}(1')$ was nearly orthogonal with an angle of 96.58 ° .

Each K ion [Figure 4.26(b)] is coordinated to two ligands HL^9 [via O(3) and O(5')], two donor atoms N(4) and N(6) of pyridyl groups from the two nearest units, as well as another three oxygen atoms O(1'), O(2') and O(4'), two from ligands L^9 and one μ -oxo [O(4')] between two Mn(II) ions. There are altogether eight K – N dashed bridges as shown in Figure 4.25 [with N(4), N(4'), N(6) and N(6') with K ions] and are linked to another four neighbouring repeat units (A, B, C and D) to form as a porous supramolecular structure shown as in Figure 4.27. Solvents (MeCN and Et₂O) are disordered within the cavities of the material.

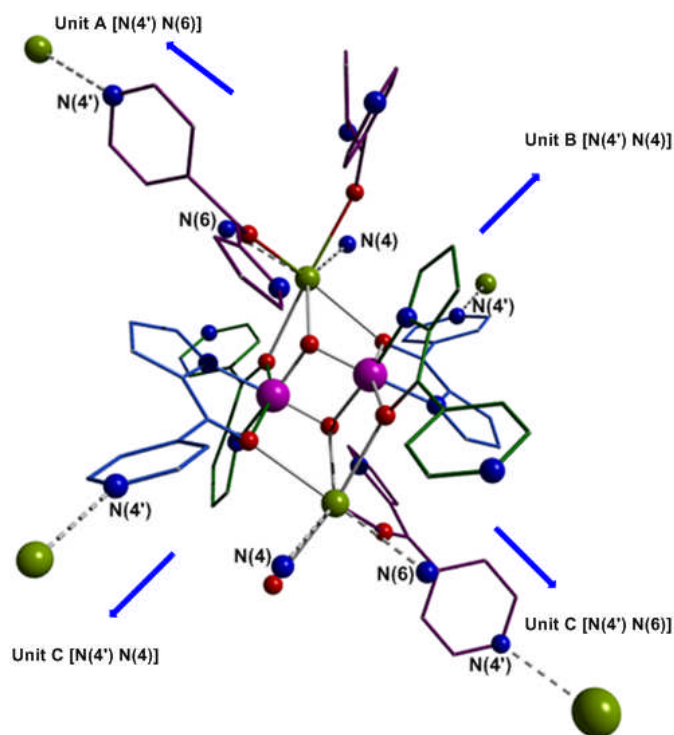


Figure 4.25: The asymmetric unit of complex $[\{ \text{K}_4\text{Mn}_2\text{L}^9_4(\text{HL}^9)_2(\text{OH})_2(\text{MeCN})_2 \}]_\infty \cdot x\text{MeCN} \cdot y\text{Et}_2\text{O}$; pink Mn, lime K, blue N, red O, light blue and green ligand L^9 , violet HL^9 ; Hydrogen atoms and solvents are removed for clarity.

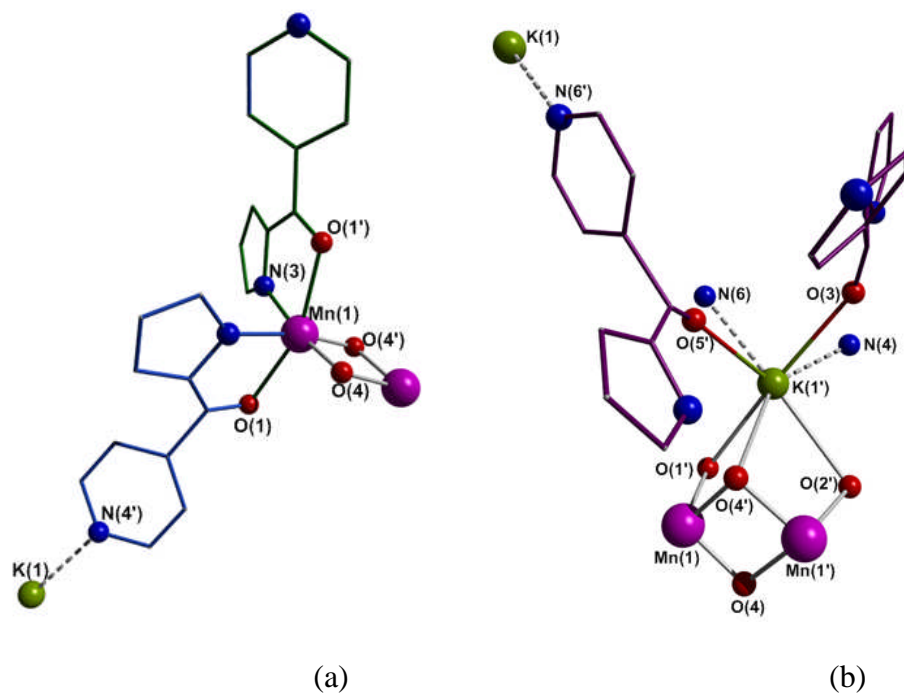


Figure 4.26: The coordination environment of Mn^{2+} and K^+ ion in the asymmetric unit of $[\{\text{K}_4\text{Mn}_2\text{L}^9_4(\text{HL}^9)_2(\text{OH})_2(\text{MeCN})_2\}]_\infty \cdot x\text{MeCN} \cdot y\text{Et}_2\text{O}$

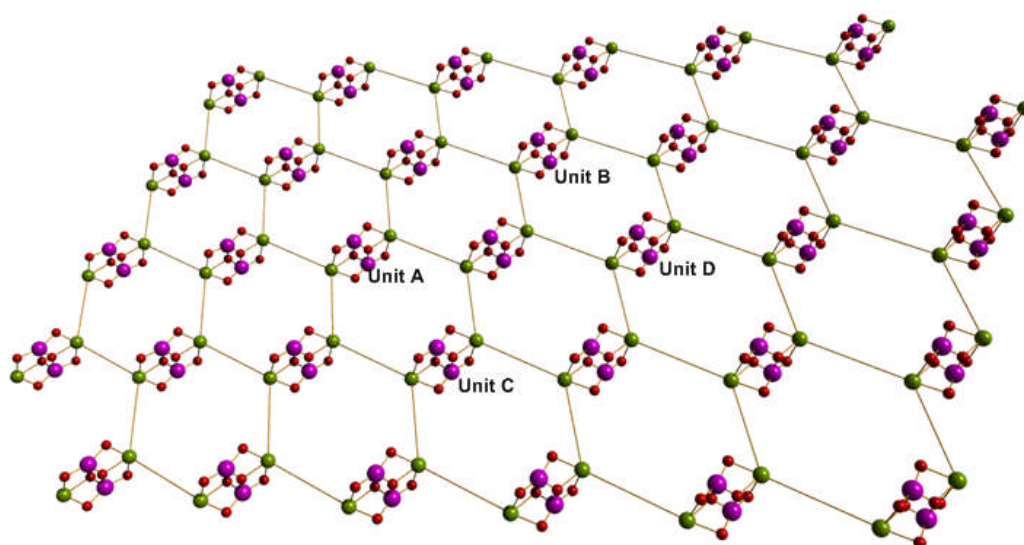


Figure 4.27: The topology of complex $[\{\text{K}_4\text{Mn}_2\text{L}^9_4(\text{HL}^9)_2(\text{OH})_2(\text{MeCN})_2\}]_\infty \cdot x\text{MeCN} \cdot y\text{Et}_2\text{O}$, Unit A, B, C and D are highlighted for comparison with Figure 4.25.

4.4 Complexes made from proligand **HL**¹⁰

In addition to the desire to explore the coordination chemistry of more simple versions of **L**⁹ we considered that replacement of the pyridinyl unit with phenyl may preclude charge balance *via* network or chain formation and thus potentially lead to the trimetallic structures sought in section 4.3.

4.4.1 [Na₂Fe₂**L**¹⁰(THF)₆]

Reaction of FeCl₂·1.5THF with in situ generated ligand salt Na**L**¹⁰ afforded a dark solution which filtered *via* a cannula and allowed to stand at 4 °C for one week. Dark single crystals of [Na₂Fe₂**L**¹⁰(THF)₆] were collected.

The asymmetric unit of [Na₂Fe₂**L**¹⁰(THF)₆] contains 1/3 of a complex cation [Na(THF)₆]⁺ and a trimetallic [(*fac*-Fe**L**¹⁰₃)₂-μ-Na]⁻ anion familiar from the Mn chemistry above. Both ions which lie on a three-fold inversion axis (Figure 4.28).

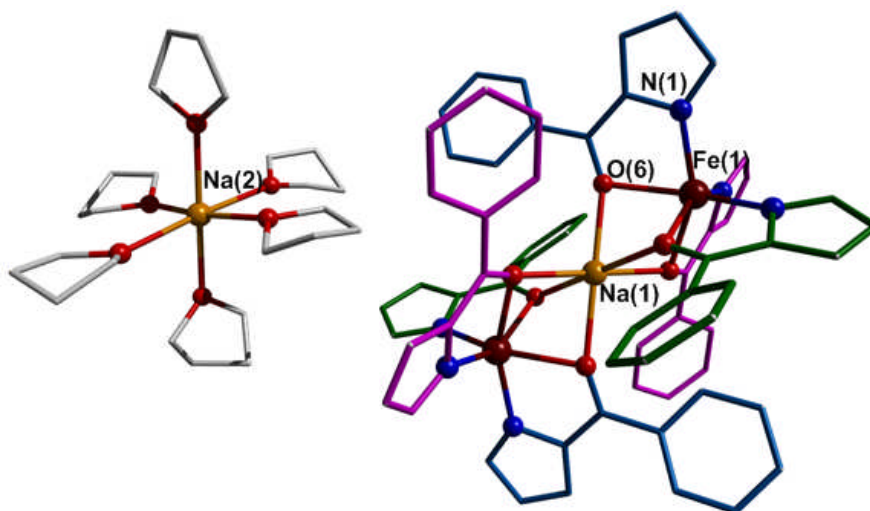


Figure 4.28: Crystal structure of $[\text{Na}_2\text{Fe}_2\text{L}^{10}(\text{THF})_6]$ showing the complex cation and anion with minor disorder removed for clarity. Selected bond lengths (\AA): Fe(1)-N(1) 2.094(4), Fe(1)-O(6) 2.277(4), Na(1)-O(6) 2.323(4) and angles ($^\circ$): Fe(1)-Na(1)-Fe(1') 180.

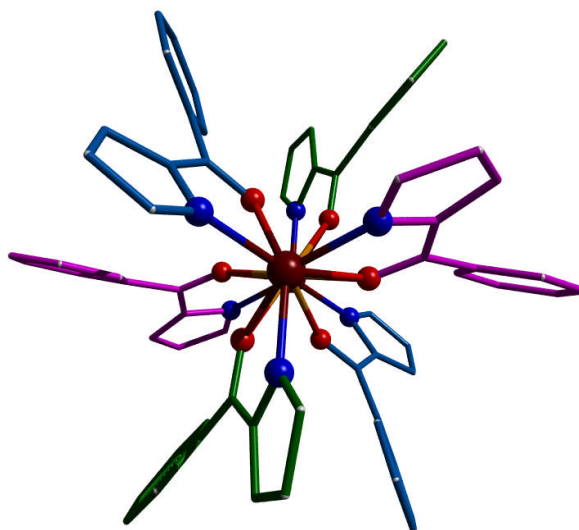


Figure 4.29: The arrangement of ligands L^{10} in complex $[\text{Na}_2\text{Fe}_2\text{L}^{10}(\text{THF})_6]$ seen from the top of view.

In the anion, the Fe-Fe distance is *ca.* 6.255 Å *c.f.* 6.482 Å in $[\{\text{Na}_2\text{Mn}_2\text{L}^9(\text{THF})_4\}_\infty] \cdot 3\text{THF}$ and 6.260 Å in $[\{\text{Na}_2\text{Mn}_2\text{L}^9(\text{MeCN})_2\}_\infty] \cdot \text{MeCN}$. One of the ligands is disordered over two positions related by a twist (58:42) about the three fold axis as shown in Figure 4.30 and 4.31, where Fe(1), Na(1) and N(1) are common to both orientations of the ligand. In addition the THF ligands in the complex cation are disordered over three positions, roughly related by rotation about the Na-O bond as shown in Figure 4.32.

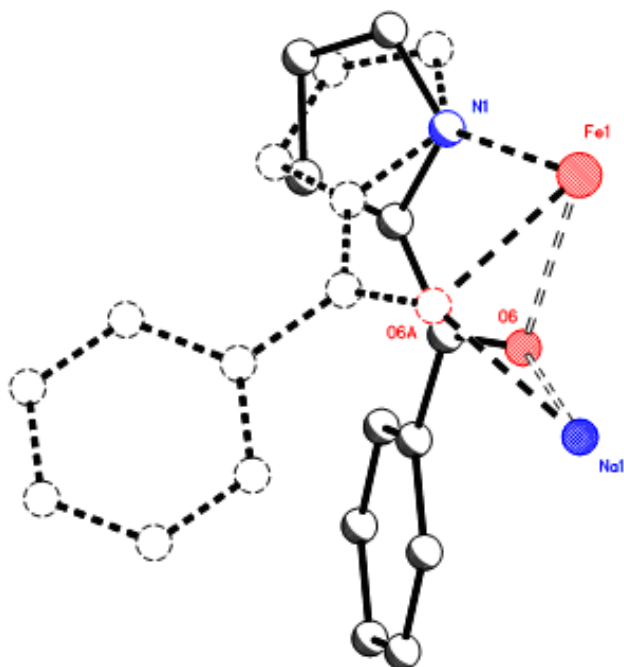


Figure 4.30: A picture showing the two disordered orientations of the ligand L^{10} about Fe(1) and Na(1). N1 is common to both orientations of the ligand.

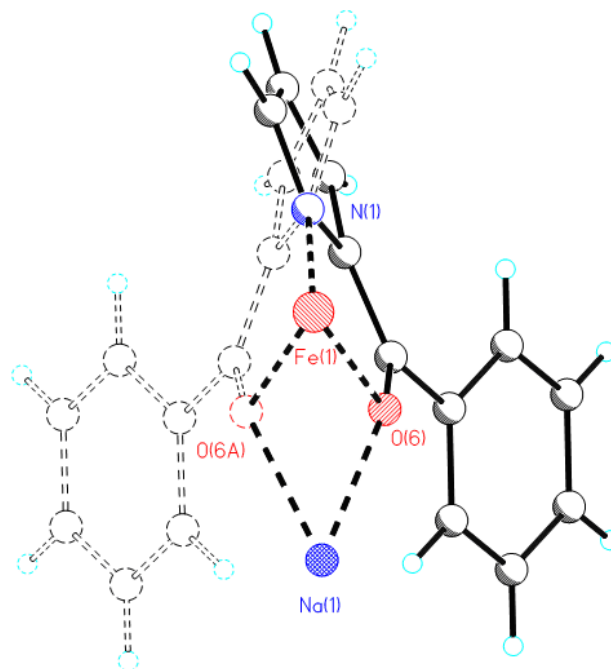


Figure **4.31**: Another view looking out from the three fold inversion axis at the two orientations of the ligand in the asymmetric unit of $[\text{Na}_2\text{Fe}_2\text{L}^{10}(\text{THF})_6]$ (54:46 major:minor). The nitrogen is common to both ligands.

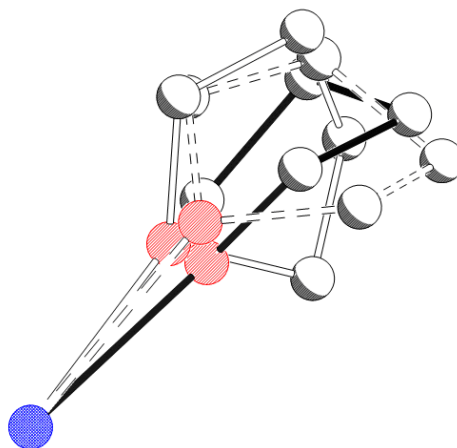


Figure **4.32**: The three different orientations of the THF coordinated to the sodium in the complex cation. (these are in the ratio 40:35:25).

There are six (disordered) THF molecules about the sodium atom.

Magnetism of [Na₂Fe₂L¹⁰(THF)₆]

The magnetic data for [Na₂Fe₂L¹⁰(THF)₆] are shown in Figures 4.33 and 4.34. From 300 K to 100 K, the $\chi_M T$ is nearly constant at 3.67 cm³ K mol⁻¹, higher than that expected for free high spin Fe(II) (3.001 cm³ K mol⁻¹, $g = 2.00$) as a result of spin-orbit contributions (generally $g > 2.00$)³ but in agreement with the value of $C = 3.761$ cm³ K mol⁻¹ from Curie-Weiss fitting (Figure 4.32) *via* which a value $g = 2.20$ was derived. On lowering the temperature $\chi_M T$ gradually falls due to ZFS. Considering that the repeat unit of the material contains two paramagnetic centres Fe(II) ions linked through a diamagnetic Na ion, the magnetic exchanges will be mainly from electrostatic interactions, and therefore isotropic Heisenberg magnetic model (HDVV) was used to describe the magnetism of the material (Eqn. 4.2).

$$\mathbf{H} = -J \mathbf{S}_A \cdot \mathbf{S}_B + \beta (\mathbf{S}_A \cdot \mathbf{g}_A + \mathbf{S}_B \cdot \mathbf{g}_B) \cdot \mathbf{H}$$

$$\mathbf{S} = \mathbf{S}_A + \mathbf{S}_B$$

$\mathbf{S}_A, \mathbf{S}_B$ are the local spin operators

From this,

$$\chi_M = \frac{2Ng^2\beta^2}{kT} \frac{e^x + 5e^{3x} + 14e^{6x} + 30e^{10x}}{1 + 3e^x + 5e^{3x} + 7e^{6x} + 9e^{10x}}$$

$$\text{With } x = J/kT \text{ for } S_A = S_B = 2 \quad \dots\dots\dots \text{Eqn. 4.2}$$

As shown in Figure 4.34, a least squares fit to the equation gives $J = -1.34$ cm⁻¹ and $g = 1.80$, suggesting that the material is antiferromagnetic. However, possibly due to the fact that the magnetic model does not count magnetic anisotropy of Fe(II) ion and is too simple to represent the real mechanism of magnetic

interactions of the material, the fits was not very good and a small *g-factor* was obtained.

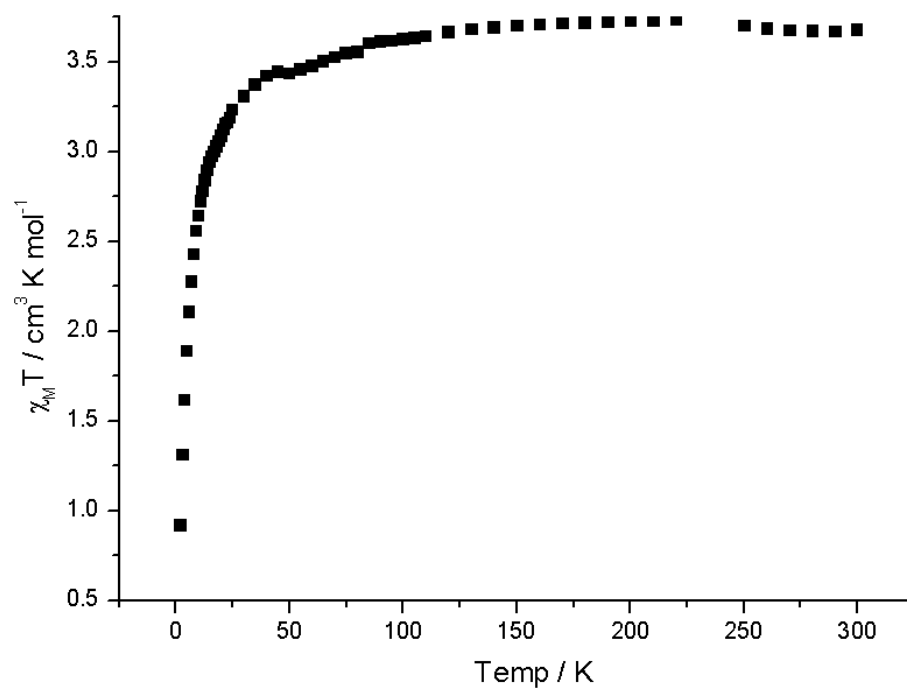


Figure 4.33: $\chi_M T$ vs T for complex $[\text{Na}_2\text{Fe}_2\text{L}^{10}(\text{THF})_6]$ measured at 1000 Oe

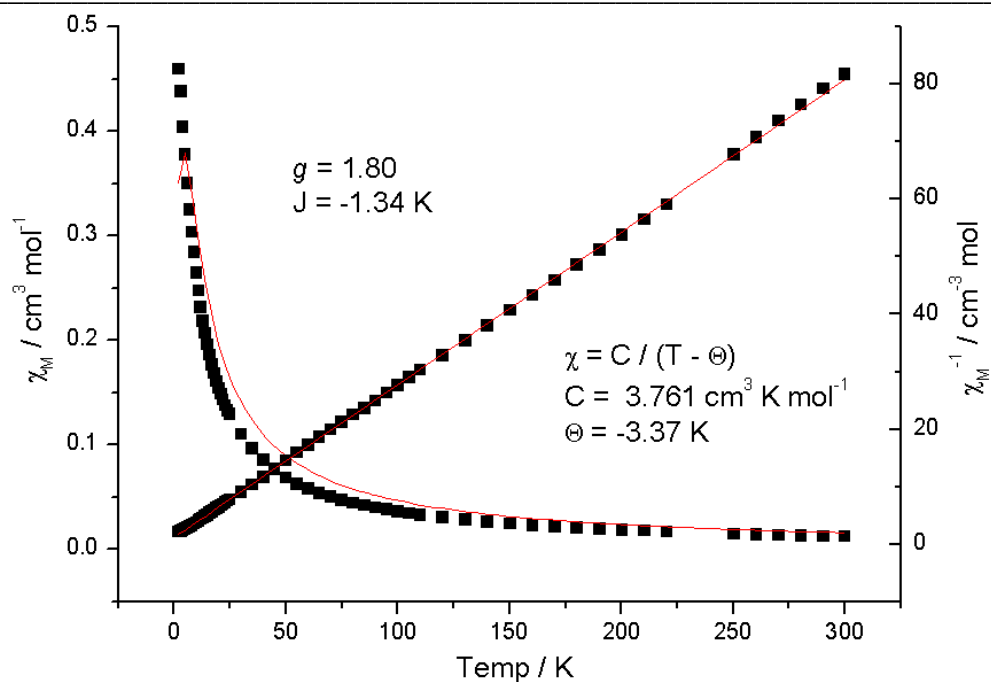


Figure 4.34: χ_M , χ_M^{-1} vs T for complex $[\text{Na}_2\text{Fe}_2\text{L}^{10}_6(\text{THF})_6]$ measured at 1000 Oe

4.4.2 $[\text{Na}_2\text{Mn}_2\text{L}^{10}_6(\text{THF})_6]_{12}$

Reaction of MnCl_2 with in situ generated ligand salt NaL^{10} yielded a yellow solution. The THF was removed under reduced pressure and the residue recrystallised from Et_2O at room temperature overnight yielding yellow block single crystals.

The unit cell of the material contains six $[(fac\text{-MnL}^{10}_3)_2\text{-}\mu\text{-Na}]^-$ anions and six sodium complex cations $[\text{Na}(\text{THF})_6]^+$, but due to the heavy disorder of benzene rings and THF molecules, we were unable to fully refine the crystal structure.

Attempt to solving the structure in P_{3C1} , the crystal cell appears hexagonal ($a = 22.8773 \text{ \AA}$, $b = 22.8773 \text{ \AA}$ and $c = 28.4825 \text{ \AA}$; $\alpha = 90^\circ$, $\beta = 90^\circ$ and $\gamma = 120^\circ$; $V = 12909.76 \text{ \AA}^3$). Only a few of the benzene rings of the ligands L^{10} about the NaMn_2 complex are discernible and several appear disordered with

rings lying within rings. The sodium complex $[\text{Na}(\text{THF})_6]^+$ is also disordered with only three of the THF rings visible. Solving the structure in lower symmetry, a larger orthorhombic C-centred cell (solving in C2) ($a = 39.6246 \text{ \AA}$, $b = 22.8773$ and $c = 28.4825 \text{ \AA}$; $\alpha = 90$, $\beta = 90^\circ$ and $\gamma = 90$; $V = 25819.49 \text{ \AA}^3$) is obtained; more of the rings of the ligands L^{10} can now be located but are still very disordered with unusual thermal parameters. This appears to be a type of disorder where both hands of the trimetallic sandwich-like Mn-Na-Mn complex lie on the same position. The pyrrole rings and phenyl rings that could be located are associated with two orientations of the benzoylpyrrole ligand with up to six different carbonyl positions disordered around the Mn-Na-Mn axis. Not all atoms could be located in the structure with all the pyrrole and phenyl rings constrained to pentagonal or hexagonals during refinement. The THF rings were either disordered or not located during the refinement. However, there is enough detail in the solution to define the cell contents which has $12 \times [\text{NaMn}_2\text{L}^{10}_6]$ anions and $12 \times [\text{Na}(\text{THF})_6]$ counter ions.

No better approaches were found trying to solve the structure in lower symmetry primitive cell settings, a repeat part of the complex is shown in Figure 4.35

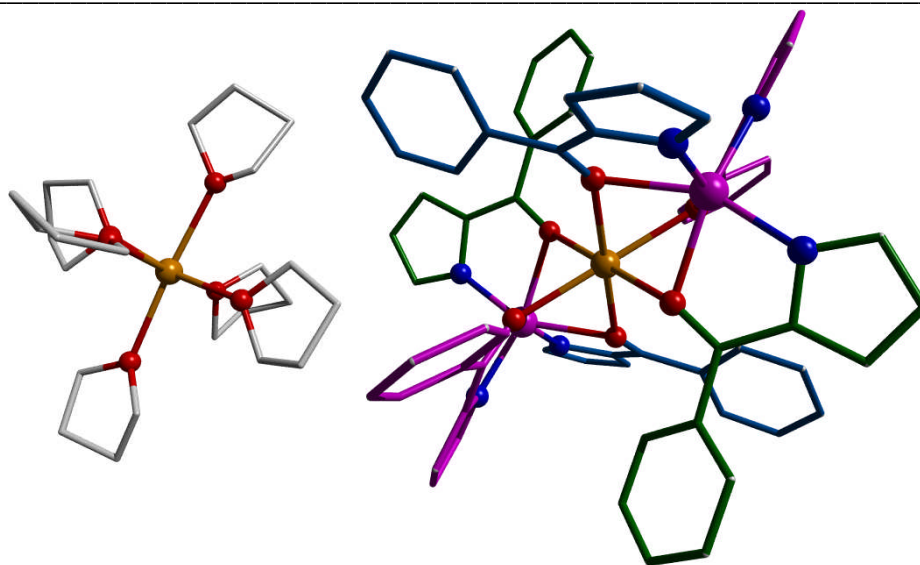


Figure 4.35: The repeat unit of complex $[\text{Na}_2\text{Mn}_2\text{L}^{10}_6(\text{THF})_6]_{12}$; Purple: Mn, Light yellow: Na, Red: O, Blue: N

Magnetism of $[\text{Na}_2\text{Mn}_2\text{L}^{10}_6(\text{THF})_6]_{12}$

Figure 4.36 shows curves of $\chi_M T$ vs. T for complex $[\text{Na}_2\text{Mn}_2\text{L}^{10}_6(\text{THF})_6]_{12}$. $\chi_M T$ falls from $4.493 \text{ cm}^3 \text{ K mol}^{-1}$ at room temperature to $4.330 \text{ cm}^3 \text{ K mol}^{-1}$ at 14 K indicating weak antiferromagnetic exchange between Mn(II) ions in the anion as we observed for other Mn(II) complexes of L^9 . The value then increases rapidly to a maximum of *ca* $5.103 \text{ cm}^3 \text{ K mol}^{-1}$ at 5 K indicating ferromagnetic coupling. This was confirmed by measurements on warming the sample after cooling in zero field (ZFCW), followed by measuring on cooling in a field (FCC) from 2 - 25 K using a field of 1000 Oe. These two curves diverge at a T_c of 5 K (Figure 4.37). At lower temperatures still, $\chi_M T$ falls rapidly again to $3.915 \text{ cm}^3 \text{ K mol}^{-1}$ at the base temperature.

Curves of χ_M and χ_M^{-1} vs. T for complex $[\text{Na}_2\text{Mn}_2\text{L}^{10}_6(\text{THF})_6]_{12}$ are shown in Figure 4.38. A fit to experimental data by using a Curie-Weiss law gave

$C = 4.496 \text{ cm}^3 \text{ K mol}^{-1}$ and $\Theta = -4.70 \text{ K}$. Magnetic data were modeled using an isotropic HDVV dinuclear magnetic model, and a least squares fit to equation (1) gave $J = -0.37 \text{ cm}^{-1}$ and $g = 1.8$ ($R = 0.002$). As with other Mn(II) complexes in this Chapter, the intra-anion magnetic exchange process between Mn(II) ions are antiferromagnetic. The ferromagnetic behavior at lower temperature could result from magnetic exchange between neighboring trimetallic anion units. However, due to the fact that the crystal structure is not fully refined, we are not able to speculate further. At 2 K, the material is magnetically saturated at 5 T with a value $M = 5 \text{ B. M.}$

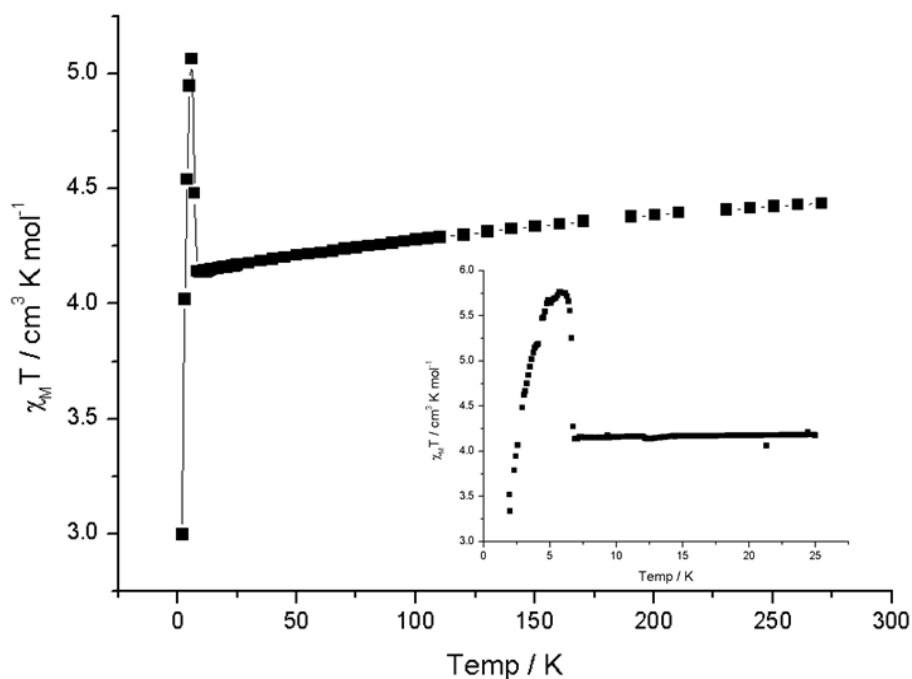


Figure 4.36: $\chi_M T$ vs. T curves for complex $[\text{Na}_2\text{Mn}_2\text{L}^{10}(\text{THF})_6]_{12}$ measured at 1000 Oe.

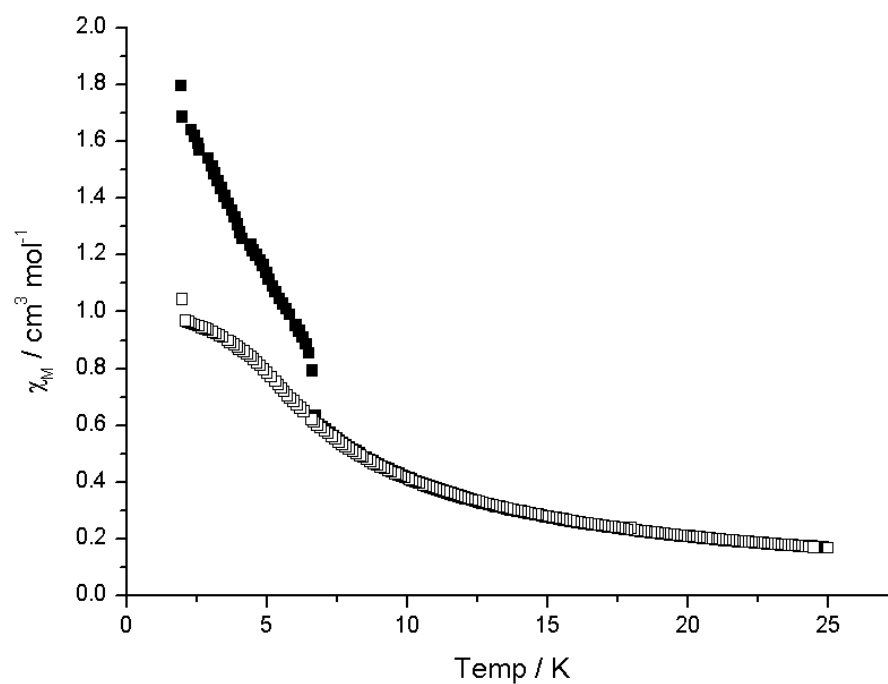


Figure 4.37: ZFCW and FCC M vs. T curves for complex $[\text{Na}_2\text{Mn}_2\text{L}^{10}_6(\text{THF})_6]_{12}$ measured at 1000 Oe.

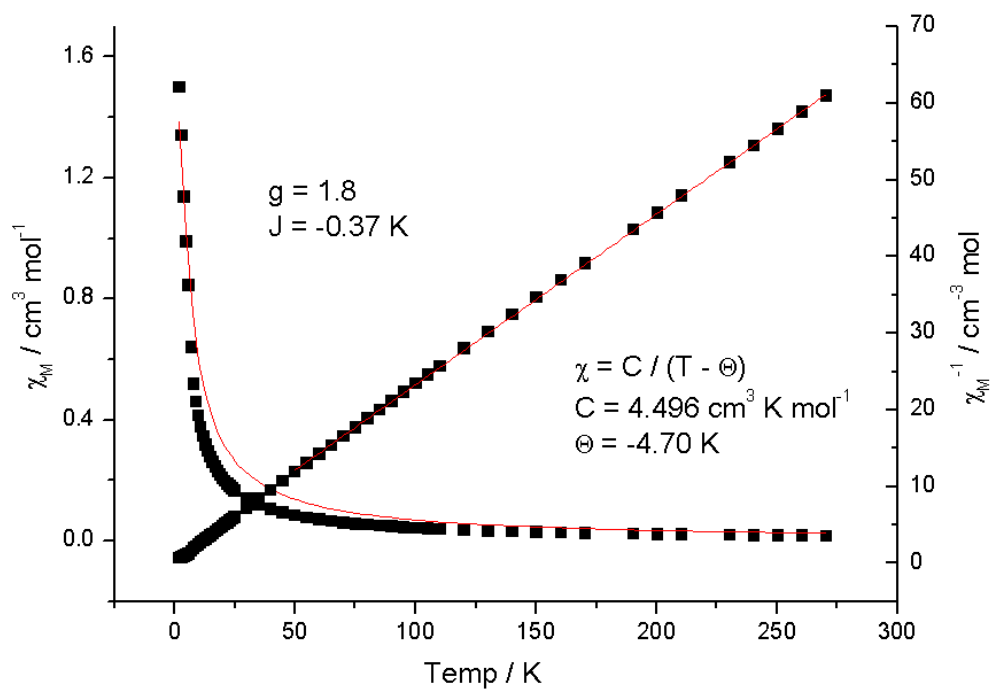


Figure 4.38: χ_M , χ_M^{-1} vs. T curves for complex $[\text{Na}_2\text{Mn}_2\text{L}^{10}_6(\text{THF})_6]_{12}$

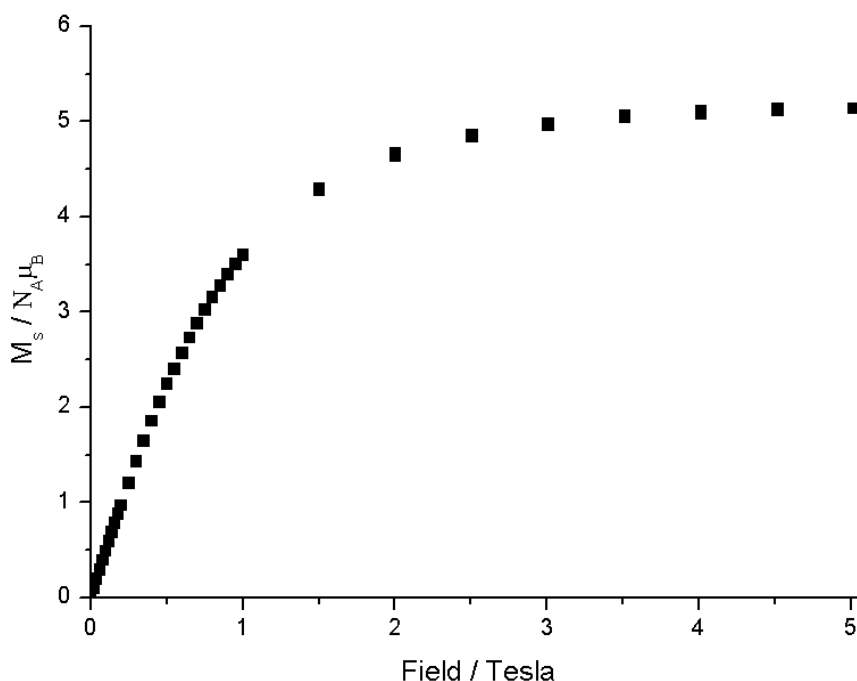


Figure 4.39: M vs. H curve for complex $[\text{Na}_2\text{Mn}_2\text{L}^{10}(\text{THF})_6]_{12}$ measured at 2 K.

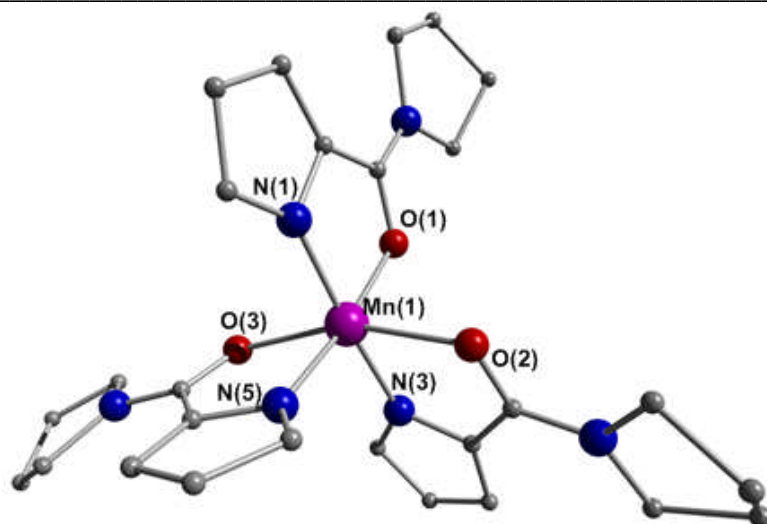
4.5 Complexes made from proligand HL^{11}

The coordination chemistry of the amide L^{11} has thus far proved rather more conventional and unproductive than that of the ketones L^9 or L^{10} . Reactions of NaL^{10} with MCl_2 ($\text{M} = \text{Mn}, \text{Fe}, \text{Co}$) under various conditions led to complexes of Mn(III) and Fe(III) (Figure 4.40) but no isolable Co system. The reactions were reproducible and gave single crystals of monometallic complexes $[\text{ML}^{11}_3]$ ($\text{M} = [\text{Fe(III)}, \text{Mn(III)}]$).

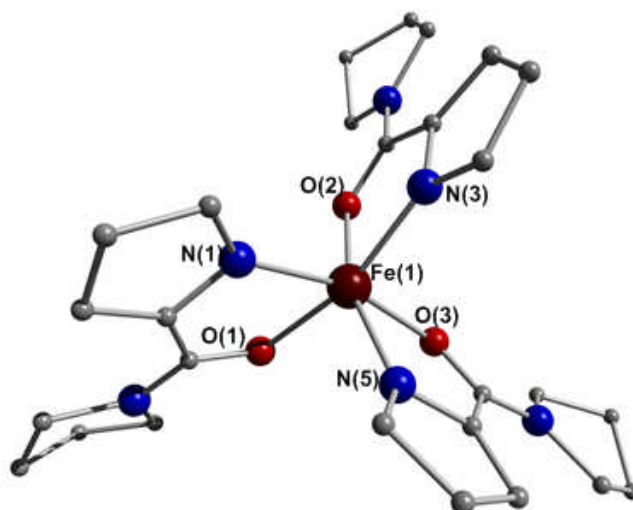
As shown in Figure 4.40(a), the asymmetric unit of complex MnL^{11}_3 contains one Mn(III) ion which is coordinated to three ligands L^{11} . The angles of N(1)-Mn(1)-N(3), O(1)-Mn(1)-N(5) and O(2)-Mn(1)-O(3) are $174.5(2)^\circ$, $171.01(18)^\circ$, and $160.27(14)^\circ$ respectively, therefore, the complex MnL^{11}_3 can be

best described as having distorted octahedral geometry. The repeat unit of the crystal structure of FeL^{II}_3 is shown in Figure 4.40(b). In the similar manner, each Fe(III) ion is coordinated with three ligands L^{II} , with an octahedral coordination geometry. The angle of N(5)-Fe(1)-O(2) , N(1)-Fe(1)-O(3) and N(3)-Fe(1)-O(1) are $161.05(7)$, $163.51(7)$ and $164.72(7)$. In contrast, the configuration of complex MnL^{II}_3 is *mer*, but the complex FeL^{II}_3 has a *fac* configuration.

On the basis of evidence presented later, we do not consider that the formation of trimetallic anions is precluded by steric factors. The electron-releasing amido units are probably responsible for the stabilisation of the higher-valent complexes as has been previously noted.¹⁵⁻¹⁶



(a)



(b)

Figure 4.40: Crystal structure of Mn(III) complex (a) and Fe(III) complex (b) made from Ligand HL¹¹; Purple: Mn, Deep red: Fe, Red: O, Blue, N; Hydrogen atoms and solvents were removed for clarity.

MnL^{II}_3		FeL^{II}_3	
Bonds / Angles	Å / °	Bonds / Angles	Å / °
Mn(1)-O(1)	1.959(4)	Fe(1)-N(3)	2.0404(19)
Mn(1)-N(1)	1.960(5)	Fe(1)-N(5)	2.0436(18)
Mn(1)-N(5)	1.972(5)	Fe(1)-N(1)	2.0489(18)
Mn(1)-N(3)	1.991(5)	Fe(1)-O(2)	2.0520(14)
Mn(1)-O(2)	2.206(4)	Fe(1)-O(3)	2.0686(14)
Mn(1)-O(3)	2.214(4)	Fe(1)-O(1)	2.0850(14)
O(1)-Mn(1)-N(5)	171.01(18)	N(5)-Fe(1)-O(2)	161.05(7)
O(2)-Mn(1)-O(3)	160.27(14)	N(1)-Fe(1)-O(3)	163.51(7)
N(1)-Mn(1)-N(3)	174.5(2)	N(3)-Fe(1)-O(1)	164.72(7)

Table **4.1**: Selected bond length and angles of crystal structure of MnL^{II}_3 and FeL^{II}_3

Accidentally, in one reaction we used wet CoCl_2 and purple solid precipitated immediately. The reaction was stirred overnight before the product was recrystallised from hot THF, yielding single crystals of a giant cluster **Co₁₆**, consisting of a trimer complex anion and large cluster cation (2 + 14) with the formula of $\{[\text{NaCo}_2\text{L}^{\text{II}}_6]^- [\text{Na}_9\text{Co}_{14}\text{L}^{\text{II}}_{18}(\text{OH})_{18}]^+ \cdot 3\text{THF}\}$ (Figure 4.41).

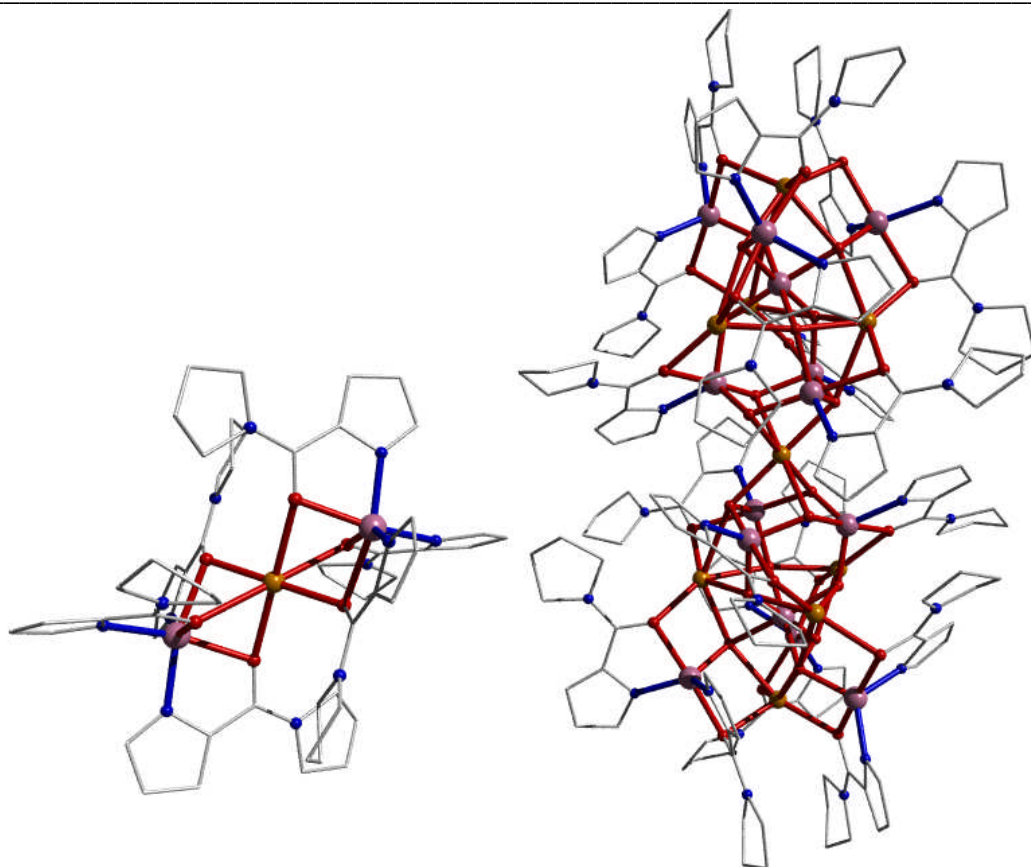


Figure 4.41: Crystal structure of complex $\{[\text{Na}_{10}\text{Co}_{16}\text{L}^{\text{II}}_{24}(\text{OH})_{18}]\cdot 3\text{THF}\}$; Pink: Co, Blue: N, Red: O; Hydrogen atoms and solvents were removed for clarity.

The complex Co_{16} crystallizes in the triclinic space group $P\bar{1}$, and the asymmetric unit contains a trimetallic sandwich-like anion $[(\text{fac-CoL}^{\text{II}}_3)_2]^-$ and a cluster cation $[\text{Na}_9\text{Co}_{14}\text{L}^{\text{II}}_{18}(\text{OH})_{18}]^+$. It is difficult to differentiate between the presence of $\text{Co(II)} - \mu\text{OH}$ or $\text{Co(III)} - \mu\text{O}^{2-}$ moieties here, but the bond distances are consistent with the former, with $\text{Co} - \text{O}$ in the range $1.962(11) - 2.041(12)$ Å [the bond lengths $\text{Co(2A)}-\text{O(21)}$, $\text{Co(2B)}-\text{O(23)}$, $\text{Co(2C)}-\text{O(11)}$, $\text{Co(3A)}-\text{O(20)}$, $\text{Co(3B)}-\text{O(22)}$, $\text{Co(3C)}-\text{O(22)}$ and $\text{Co(4)}-\text{O(24)}$ are $1.998(11)$, $1.999(11)$, $1.962(11)$, $1.996(11)$, $2.041(12)$, $2.018(12)$ and $2.095(11)$ respectively]. Typical

Co(II)-O bond lengths range from 1.998(9) to 2.456(9) while Co(III)-O lie between 1.893(8) and 1.959(9).¹⁷

The trimetallic anion contains two Co(II) metal ions and one Na ion. Each Co(II) is coordinated to three ligands \mathbf{L}^{11} , thus forming an octahedral coordination geometry. There are overall six ligands \mathbf{L}^{11} of which each oxygen atom is coordinated to Na^+ ion in the middle of the anion (Figure 4.42). The formation of the familiar trimetallic sandwich-like anions $[(fac\text{-Co}\mathbf{L}^{11}_3)_2]^-$ ion indicate that steric hindrance was not the reason for the absence of trimetallic complexes in the Fe and Mn systems (Sections 4.3 and 4.4).

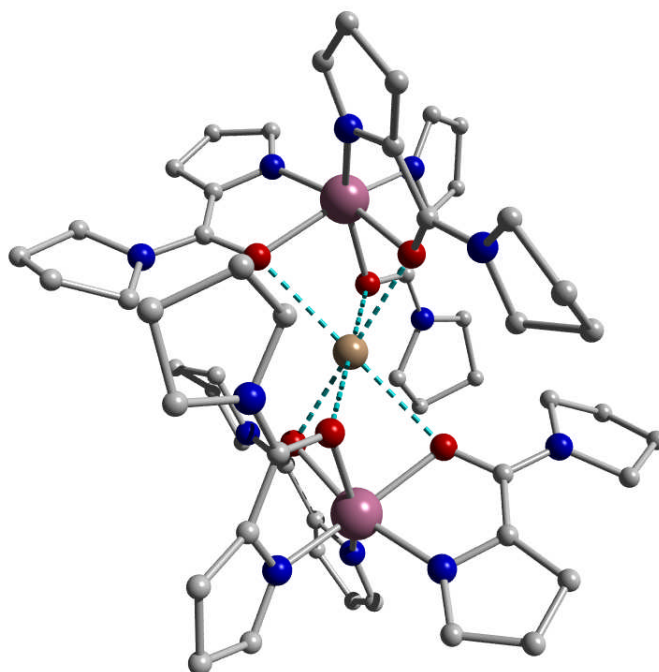


Figure 4.42: The complex anion of $\{[\text{Na}_{10}\text{Co}_{16}\mathbf{L}^{11}_{24}(\text{OH})_{18}]\cdot 3\text{THF}\}$. Hydrogen atoms and solvents were removed for clarity

The anion as shown in Figure 4.42 has 1- charge. In order to maintain charge balance, the reaction had to produce a 1+ charge cation.

As shown in Figure 4.43 (a), the cluster cation contains 14 Co(II) ions, 9 sodium ions, 18 ligands and 18 μ -OH, and is best described as a large dimer, where one Na^+ ion [Na(4)] sits in the middle as a bridge. Given that two parts of the cation ($2 \times \text{Co}_7$), which are connected by Na(4), are symmetry related and have the same geometry, only one of them is discussed here. As shown in Figure 4.43 (b), all the Co(II) ions and Na^+ ions in the cation are linked to each other through μ -OHs to form a composite architecture, where a triangular pyramid sits on a crown-shaped skeleton: each side of triangular faces of the pyramid is slightly bent, with angles ($^\circ$) of Na(3)-O(23)-Na(2B), Na(3)-(O21)-Na(2A) and Na(2B)-O(26)-Na(2A) 158.52, 159.40 and 163.19 respectively. Each μ -OH on the six sides of the triangular pyramid are coordinated to one Co(II), and three Co(II) [Co(3A), Co(3B), Co(3A)] forms the crown-shaped skeleton. All of the Na^+ ions occupy apexes, either of the pyramid or the crown.

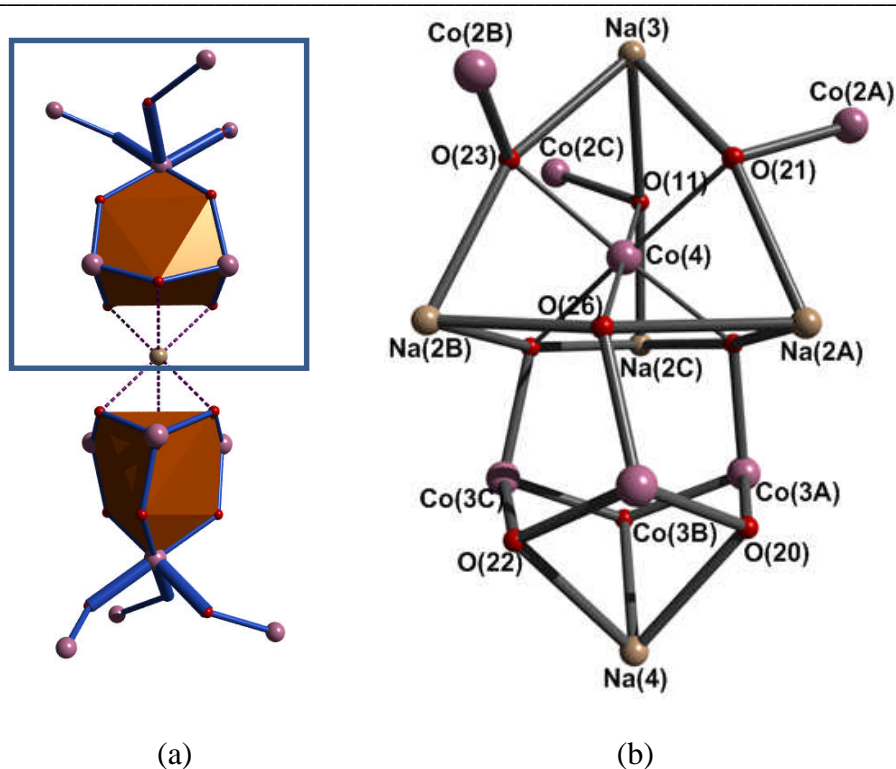


Figure **4.43**: (a) Representation of orientation of oxygen atoms and Co(II) ion in the dimer cation; (b) Representation of the top part of the dimer cation, with a triangular pyramid sitting on a crown, ligands were removed for clarity. Pink: cobalt; Red: oxygen; Tan: Sodium. Hydrogen atoms and solvents were removed for clarity

In respect of coordination chemistry of Co(II) ions, Co(4) ion is centred in the pyramid and coordinated to six μ -OH from six sides of the pyramid. Other than this, all the other Co(II) ions are five-coordinated, with trigonal bipyramid geometry. Co(2A), Co(2B) and Co(2C) are coordinated to another two ligand **L**¹¹ respectively (Figure 4.41) while Co(3A), Co(3B), Co(3C) are coordinated only to one ligand with another three μ -OHs as shown in Figure 4.43. As for Na ions, both Na(3) and Na(4) are six-coordinated, but Na(4) is coordinated to six μ -OHs

while for Na(3), in addition to three μ -OHs as shown in Figure 4.43, it is also coordinated to another three ligand \mathbf{L}^{11} . Na(2A), Na(2B) and Na(2C), however, are all five-coordinated to two ligands \mathbf{L}^{11} and three μ -OHs. Close-ups of the orientation of Co(II) ions in the cation is shown in Figure 4.44, where six Co(II) ions are linked to Co(4) through μ -OHs, forming as a stool-like Co(II) metal skeleton. Two stools are head-to-head piled up, and a Na^+ ion sits in the centre [Figure 4.43(a)].

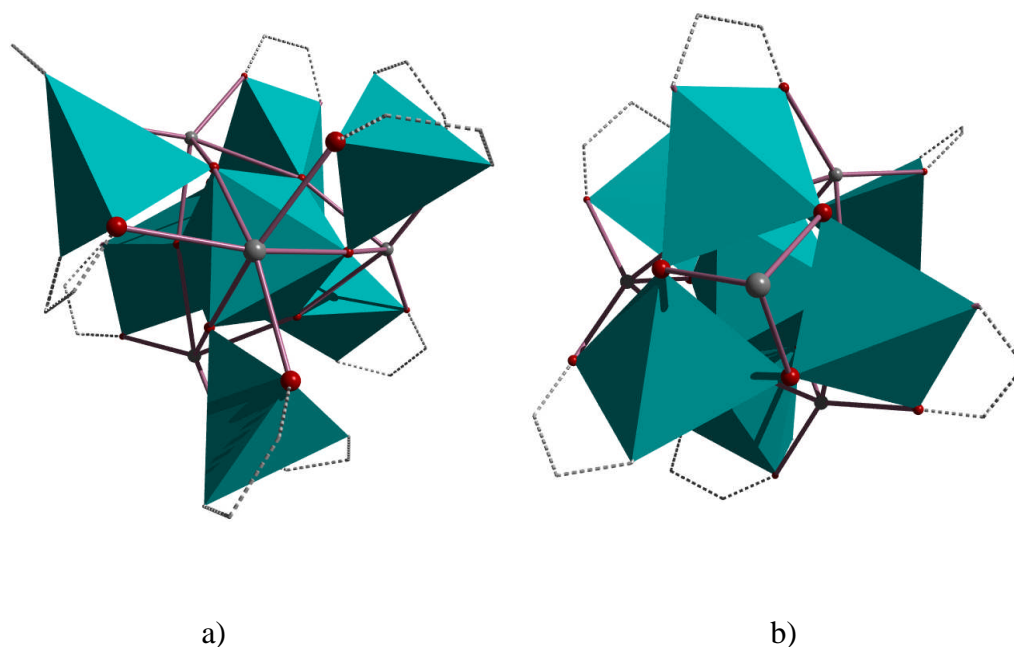


Figure 4.44: Top (a) and bottom (b) view of half part of cation cluster; Grey: Na; Red: O; each polyhedral contains a Co(II) metal centre, dashed line represent a bidentate ligand.

Magnetism of $\{[\text{Na}_{10}\text{Co}_{16}\text{L}^{11}_{24}(\text{OH})_{18}]\cdot 3\text{THF}\}$

The plot of $\chi_{\text{M}}T$ vs. T for $\{[\text{Na}_{10}\text{Co}_{16}\text{L}^{11}_{24}(\text{OH})_{18}]\cdot 3\text{THF}\}$ is shown in Figure 4.45. $\chi_{\text{M}}T$ gradually decreases from 300 K to 25 K, possibly due to antiferromagnetic exchanges. The average $\chi_{\text{M}}T$ value of *ca* $1.80 \text{ cm}^3 \text{ K mol}^{-1}$ is slightly lower than $1.876 \text{ cm}^3 \text{ K mol}^{-1}$ for a high spin Co(II) ion perhaps due to the presence of some Co(III)- $\mu\text{-O}^{2-}$ units. The anionic component is likely to be a simple paramagnet with negligible magnetic couplings since the distance between two Co(II) 6.305 \AA . In the cluster cation there are at least three types of Co(II) ions which interact to each other *via* $\mu\text{-OH}$. The complexity of the structure makes modelling this behaviour impossible at present. Interestingly, this is a quite rare magnetic salt system with two different magnetic behaviours. This is of some interest. On the other hand, magnetic exchange could be facilitated by electrostatic field interactions between magnetic cation and anion.

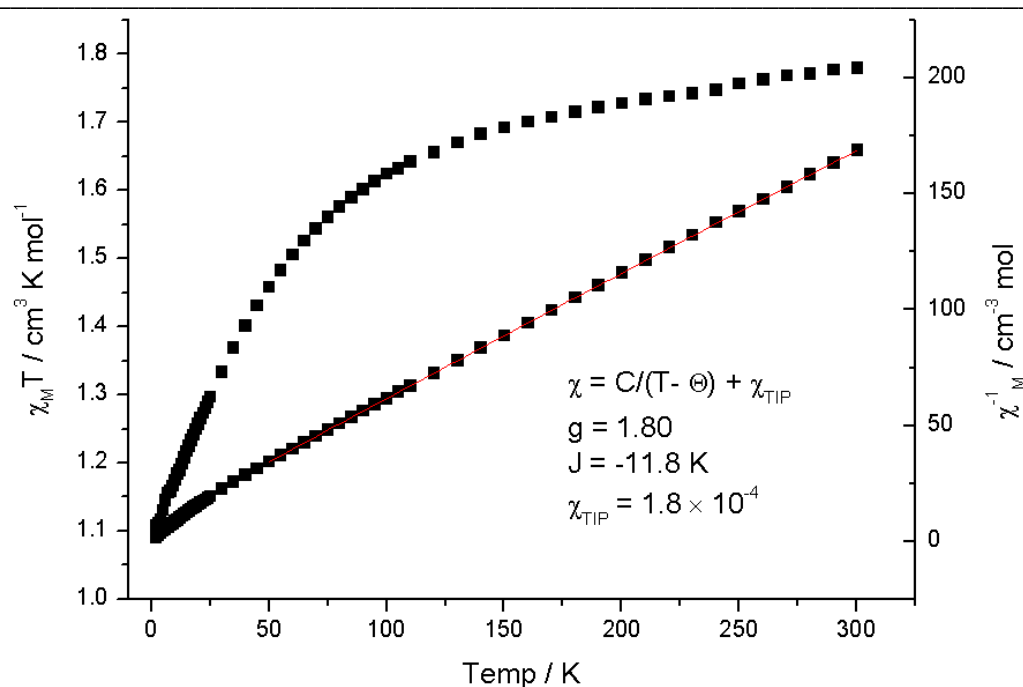


Figure 4.45: $\chi_M T$ vs. T for complex $\{[\text{Na}_{10}\text{Co}_{16}\text{L}^{\text{II}}_{24}(\text{OH})_{18}] \cdot 3\text{THF}\}$, measured at 1000 Oe.

4.6 Conclusions

The pyrrolylketone proligands HL^n ($n = 9 - 11$) are shown to be a new and exciting class for synthesis of a wide variety of complexes with interesting properties.

The $[\text{FeL}^9_2]_n$ system has a 2 D layer rhombic structure and exhibits the H.S. \rightarrow L.S. \rightarrow H.S. (ferromagnetic ordering at L.S. \rightarrow H.S) unique behaviour. It is interesting to note that this is essentially the behaviour of $[\text{FeL}^9_2]_n$ with the addition of SCO which results from L^9 being higher field than L^8 .

The trimetallic system, $[(fac\text{-M}_A\text{L}^n_3)_2\text{-}\mu\text{-M}_B]\text{M}_B^+$ [$\text{M}_A = \text{Mn(II)}$ and Fe(II) , $\text{M}_B = \text{Na, K}$; $n = 9$ and 10] are a new structure type that seems to be quite

prevalent in this ligand class. In the case of L^9 , 1 D and 2 D structures are obtained while L^{10} gave molecular trimetallic anions.

L^{11} seems to be a interesting system, giving rise to higher valent structures for Fe and Mn, although an interesting Co(14) cluster cation observed.

4.7 References:

1. O. Kahn, *Molecular Magnetism*, WILEY-VCH, New York, 1993.
2. O. Kahn, Y. Pei and Y. Journaux, *Mol. Cryst. Liq. Cryst.*, 1989, **176**, 163.
3. L. Li, G. J. Clarkson, D. J. Evans, M. R. Lees, S. S. Turner and P. Scott, *Chem. Commun.*, 2011.
4. S. Rubino, S. Petruso, R. Pierattelli, G. Bruno, G. C. Stocco, L. Steardo, M. Motta, M. Passerotto, E. D. Giudice and G. Guli, *J. Inorg. Biochem.*, 2004, **98**, 2071-2079.
5. T. J. Donohoe, P. M. Guyo, R. L. Beddoes and M. Helliwell, *J. Chem Soc., Perkin Trans.*, 1 1998, 667-676.
6. P. Gütllich and H. A. Goodwin, in *Spin Crossover in Transition Metal Compounds*, Springer-Verlag, Berlin Heidelberg, 2004, vol. 233,234,235.
7. S. Hayami, T. Kawahara, Y. Maeda, K. Inoue and O. Sato, *J. Radioanal. Nucl. Chem.*, 2005, **266**, 521-525.
8. S. Bonhommeau, T. Guillon, L. M. Lawson Daku, P. Demont, J. Sanchez Costa, J.-F. Létard, G. Molnár and A. Bousseksou, *Angew. Chem. Int. Ed.*, 2006, **45**, 1625-1629.
9. P. Gütllich, V. Ksenofontov and A. B. Gaspar, *Coord. Chem. Rev.*, 2005, **249**, 1811-1829.
10. S.-i. Ohkoshi, K. Imoto, Y. Tsunobuchi, S. Takano and H. Tokoro, *Nat. Chem.*, 2011, **3**, 564-569.
11. S. Hayami, Y. Shigeyoshi, M. Akita, K. Inoue, K. Kato, K. Osaka, M. Takata, R. Kawajiri, T. Mitani and Y. Maeda, *Angew. Chem. Int. Ed.*, 2005, **44**, 4899-4903.
12. M. Moragues-Canovás, C. E. Talbot-Eeckelaers, L. Catala, F. Lloret, W. Wernsdorfer, E. K. Brechin and T. Mallah, *Inorg. Chem.*, 2006, **45**, 7038-7040.
13. D. Wu, D. Guo, Y. Song, W. Huang, C. Duan, Q. Meng and O. Sato, *Inorg. Chem.*, 2009, **48**, 854-860.
14. K. W. Galloway, A. M. Whyte, W. Wernsdorfer, J. Sanchez-Benitez, K. V. Kamenev, A. Parkin, R. D. Peacock and M. Murrie, *Inorg. Chem.*, 2008, **47**, 7438-7442.
15. J. M. Becker, J. Barker, G. J. Clarkson, R. v. Gorkum, G. K. Johal, R. I. Walton and P. Scott, *Dalton Trans.*, 2010, **39**, 2309-2326.
16. N. P. Chmel, L. E. N. Allan, J. M. Becker, G. J. Clarkson, S. S. Turner and P. Scott, *J. Chem Soc., Dalton Trans.*, 2011, **40**, 1722-1731.

-
17. E. Rentschler and P. Alborés, *Angew. Chem. Int. Ed.*, 2009, **48**, 9366-9370.

5. Experimental Details

5.1 General Considerations

Solvents and chemicals were purchased from commercial sources (Sigma-Aldrich, Acros, Lancaster, Fisher Scientific, Alfa Aesar or Strem) and used without further purification unless otherwise stated. Deuterated solvents were purchased from Sigma-Aldrich and Cambridge Isotope Laboratories. Where necessary, deuterated solvents were freeze-thaw degassed and dried by heating to their normal boiling points *in vacuo* over potassium (or calcium hydride for d²-dichloromethane) for 3 d before vacuum distilling (trap-to-trap) to a clean, dry ampoule and stored in a dry box. Sodium hydride dispersion in mineral oil was placed in a Schlenk vessel under argon and washed three times with diethyl ether to remove the oil. The solid was then dried and stored in the glove box. Pyrazine was purchased from Aldrich and stored in the glove box. Paraformaldehyde was dried in a vacuum dessiccator over P₂O₅ for 3 d. Magnesium chloride was dried in a vacuum oven at 70 °C for 2 d prior to use.

Where appropriate, procedures were carried out under argon by using a dual manifold vacuum/argon line and standard Schlenk techniques, or MBraun dry box. Dried solvents were made by refluxing for 3 d under dinitrogen over the appropriate drying agents (potassium for THF; sodium-potassium alloy for diethyl ether, pentane; magnesium methoxide for methanol; calcium hydride for acetonitrile, dichloromethane, triethylamine) and degassed before use. THF and

diethyl ether were additionally pre-dried over sodium wire. Solvents were stored in glass ampoules under argon. All glassware and cannulae were stored in an oven (>373 K).

NMR spectra were recorded on Bruker DPX-300, DPX-400 spectrometers and the spectra were referenced internally using residual proton solvent resonances relative to tetramethylsilane ($\delta = 0$ ppm). ESI mass spectra were recorded on Bruker Esquire2000. Infrared spectra were obtained either as Nujol mulls using a Perkin-Elmer 100 FTIR spectrometer, or directly using a Nicolet FTIR instrument. Elemental analyses were performed by Warwick Analytical Services or Medac Analytical Ltd., Surrey, UK. Ultraviolet/visible spectra were obtained as appropriate solution in a quartz cell of path length 1 cm, using a Jasco V-660 spectrometer.

Single crystal X-ray diffraction data were collected on an Oxford Diffraction Gemini four-circle system with Ruby CCD area detector at Warwick or on a Bruker Nonius KappaCCD diffractometer system at the UK National Crystallography Service (NCS). Crystals were coated in inert oil prior to transfer to a cold nitrogen gas stream on the machine. The temperature of crystals was controlled using an Oxford Cryosystem Cobra. Structures were refined by direct method using SHELX (TREF)¹⁻² with additional light atoms found by Fourier methods. Crystal refinement was performed using SHELX97.²

Powder diffraction data were recorded using a Bruker D5005 (low temperature data) and D5000 diffractometer (room temperature data) with $\text{CuK}\alpha$ ($\lambda = 1.54218 \text{ \AA}$) radiation sources, step $0.02^\circ 2\theta$ and step interval 1 s. Patterns were simulated from single crystal data using the Diamond software.³

The Mössbauer spectrum was recorded in zero magnetic field at 80 K on an ES-Technology MS-105 Mössbauer spectrometer with a 100 MBq ^{57}Co source in a rhodium matrix at ambient temperature. The spectrum was referenced against a 25 μm iron foil at 298 K and spectrum parameters were obtained by fitting with Lorentzian curves.⁴ The sample was prepared under a dry nitrogen atmosphere by grinding with boron nitride powder prior to mounting in the sample holder.

Magnetisation measurements were made as a function of temperature (T) and applied magnetic field (H) using a Quantum Design MPMS-5 SQuID magnetometer. Samples were randomly orientated powders placed in Kel-F capsules. The capsule was centred using a pure Ni sample. The data were corrected for the measured diamagnetism of the capsule and the diamagnetic contributions of the sample using Pascal's constants.⁵

5.2 Experimental details for Chapter TWO

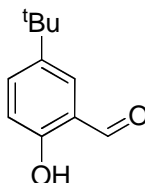
5.2.1 $\text{Fe}_2\text{Cl}_4 \cdot 3\text{THF}$

A dry glass fibre Soxhlet thimble was charged with anhydrous iron(II) chloride (5.0 g, 39.4 mmol) (STREM Chemicals) inside an inert gas glove box and connected to a round-bottomed Schlenk flask filled with anhydrous THF (200 cm^3). The apparatus was purged thoroughly with argon and the solvent heated under reflux for 4 d by which time all the metal chloride had been extracted. The compound had already begun to separate as a white microcrystalline solid. The solution was left to cool to ambient temperature and concentrated to *ca.* 50 cm^3

before the solid was collected by cannula filtration and dried *in vacuo* for 3 h. (8.5 g, 92 %).

Anal. Found (Calcd. For $C_{12}H_{24}Cl_4Fe_2O_3$): C 30.58 (30.68); H 5.16 (5.15) %.

5.2.2 5-*tert*-butyl-2-hydroxybenzaldehyde⁶



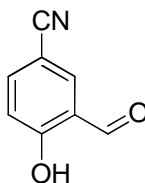
A 500 mL side arm round bottom flask with a stirrer bar was placed under argon and charged with 4-*tert*-butylphenol (3.00 g, 20.0 mmol) and dry acetonitrile (100 mL). To this was added dry Et_3N (10.4 mL 75.0 mmol), anhydrous $MgCl_2$ (2.86 g, 30.0 mmol) and the solution was stirred for 30 min. Dry paraformaldehyde (4.05 g 135.0 mmol) was added and a Schlenk condenser fitted to the round bottom flask. The mixture was heated to reflux under argon for *ca* 3h. The resulting yellow solution was allowed to cool to room temperature and was added to 5 % $HCl_{(aq)}$ (200 mL) followed by stirring for 30 min. This was followed by extraction with diethyl ether (7×25 mL). The ether fractions were combined, washed with saturated $NaCl_{(aq)}$ (3×20 mL) and the organic layer dried over anhydrous $NaSO_4$ followed by filtration. All volatiles were removed under reduced pressure to yield a yellow oil which 1H NMR spectra showed to be 5-*tert*-butyl-2-hydroxybenzaldehyde (2.97 g, 83 %).

1H NMR (300 MHz, $CDCl_3$): δ ppm 10.86 (s, 1H, $ArOH$), 9.87 (s, 1H, $HC=O$), 7.57 (dd, 1H, ArH) 7.50 (d, 1H, ArH), 6.92 (d, 1H, ArH), 1.31 (s, 9H, CMe_3).

$^{13}\text{C}\{^1\text{H}\}$ NMR 75 MHz (CDCl_3) δ ppm 190.7 (CHO), 159.3 ($\text{Ar-C}_q\text{-OH}$), 142.6 ($\text{Ar-C}_q\text{-}^t\text{Butyl}$), 134.6 (Ar-CH), 129.6 (Ar-CH), 119.8 (Ar-CH), 117.0 (Ar-CH), 33.9 (CMe_3), 31.1 (CMe_3).

MS (ESI): m/z 178 $[\text{M}]^+$, 163 $[\text{M-CH}_3]^+$, 161 $[\text{M-OH}]^+$, 148 $[\text{M-(CH}_3)_2]^+$, 133 $[\text{M-(CH}_3)_3]^+$

5.2.3 3-formyl-4-hydroxybenzonitrile⁷



A 25 mL round bottom flask with a stirrer bar was charged with salicylaldehyde (1.22 g, 10.0 mmol) and TFA (8 mL). To the reaction mixture was added hexamethylenetetramine (2.8 g, 20 mmol) all at once while stirring. After the heat evolution had ceased, the reaction mixture was heated to 90 °C and kept stirring for 8 h. TFA and other volatiles were removed on a rotary evaporator. The mixture was then cooled in an ice bath, and 50 % sulfuric acid (5 mL) and water (30 mL) were added. The reaction mixture was kept stirring for 30 min at room temperature. This was followed by extraction with diethyl ether (4×25 mL). The ether fractions were combined, washed with water (5×25 mL), saturated NaCl (aq.) (3×20 mL) and the organic layer dried over anhydrous NaSO_4 followed by filtration. All volatiles were removed under reduced pressure to yield a pale solid.

The pure product was isolated as white solid by flash column (EtOAc : hexane = 5 : 1 then 2 :1). (0.97 g, 33 %).

^1H NMR (300 MHz, CDCl_3): δ ppm 11.40 (s, 1H, ArOH), 9.88 (s, 1H, HC=O), 7.90 (d, 1H, Ar-CH), 7.73 (dd, 1H, Ar-CH), 7.07 (d, 1H, Ar-CH).

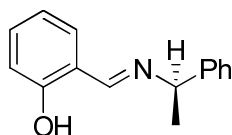
The data were found to be in excellent agreement with literature.

MS (EI): m/z 147 $[\text{M}+\text{H}]^+$.

5.2.4 General procedure for HL^n ($n = 1-6$) ligand precursors

A 100 mL round bottom flask with a stirrer bar was charged with 2-hydroxybenzaldehyde (1.0 eq.) and (*R*)-1-phenylethylamine (1.0 eq.). The reactants were dissolved in ethanol, and heated to reflux for 2-8 h (monitored by TLC). The volume of solvent was reduced by half to induce crystallization of the Schiff base product. Or alternatively, the volatiles were removed under reduced pressure and the remaining solid was washed by cold ethanol (5 mL).

(*R*)-2-[(1-phenylethylimino)methyl]phenol (HL^1)



Yield = (1.91 g, 85 %).

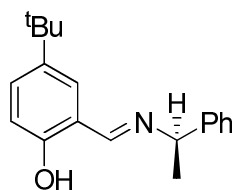
^1H NMR (400 MHz, CDCl_3): δ 13.46 (s, 1H, OH), 8.30 (s, 1H, CH=N), 7.21 (m, 5H, ArH), 7.13 (dd, $^3J = 7.7$ Hz, $^4J = 1.7$ Hz, 1H, ArH), 6.88 (d, $^3J = 8.3$ Hz, 1H,

ArH), 6.78 (dt, $^3J = 7.7$ Hz, $^4J = 1.7$ Hz, 1H, ArH), 4.46 (q, $^3J = 6.7$ Hz, 1H, CHMePh), 1.55 (d, $^3J = 6.7$ Hz, 1H, CHMePh).

$^{13}\text{C}\{^1\text{H}\}$ NMR (100 MHz, CDCl_3): 163.1 (CH=N), 161.5 (Ar- C_q), 143.7 (Ar- C_q), 132.3 (Ar-CH), 131.4 (Ar-CH), 128.7 (Ar-CH), 127.3 (Ar-CH), 126.4 (Ar-CH), 118.9 (Ar- C_q), 118.7 (Ar-CH), 117.0 (Ar-CH), 68.6 (CHMe), 24.9 (CHMe).

MS (ESI): m/z 226.2 $[\text{M}+\text{H}]^+$

(R)-2-((1-phenylethylimino)methyl)-4-tert-butylphenol (HL²)



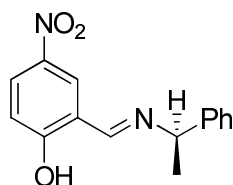
Yield = (2.52 g, 90 %).

^1H NMR (400 MHz, CDCl_3): δ 12.89 (s, 1H, OH), 8.49 (s, 1H, CH=N), 7.43 (m, 4H, ArH), 7.33 (m, 1H, ArH), 7.82 (d, 1H, $^4J = 2.5$ Hz, ArH), 6.97 (d, 1H, $^3J = 8.7$ Hz, ArH), 4.59 (q, 1H, $^3J = 6.7$ Hz, CHMePh), 1.68 (d, 3H, $^3J = 6.7$ Hz, CHMePh), 1.35 (s, 9H, ^tBu).

$^{13}\text{C}\{^1\text{H}\}$ NMR (100 MHz, CDCl_3): δ 163.7 (CH=N), 158.9 (Ar- C_q), 144.0 (Ar- C_q), 141.4 (Ar- C_q), 129.7 (Ar-CH), 128.7 (Ar-CH), 127.9 (Ar-CH), 127.0 (Ar-CH), 126.5 (Ar-CH), 118.1 (Ar- C_q), 116.6 (Ar- C_q), 68.5 (CHMePh), 34.0 (CMe_3), 31.4 (CMe_3), 24.9 (CHMe).

MS (ESI): m/z 278.2 ($M - H$)⁻.

(R)-2-((1-phenylethylimino)methyl)-4-nitrophenol (HL³)



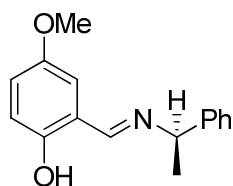
Yield = (2.35 g, 87 %).

¹H NMR (400 MHz, CDCl₃): δ 14.87 (s, 1H, OH), 8.40 (s, 1H, ArH), 8.22 (d, ⁴*J* = 2.8 Hz, ArH), 8.19 (dd, 1H, ³*J* = 9.1 Hz, ⁴*J* = 2.8 Hz, ArH), 7.36 (m, 5H, ArH), 6.99 (d, ³*J* = 9.0 Hz, ArH), 4.70 (q, 1H, ³*J* = 6.7 Hz, CHMePh), 1.70 (d, 3H, ³*J* = 6.7 Hz, CHMePh).

¹³C{¹H}NMR (100 MHz, CDCl₃): δ 168.7 (Ar-C_q), 162.4 (CH=N), 142.1 (Ar-C_q), 139.6 (Ar-C_q), 128.9 (ArH), 128.0 (ArH), 128.2 (ArH), 172.9 (ArH), 126.5 (ArH), 118.7 (ArH), 117.1 (Ar-C_q), 67.2 (CHMePh), 24.18 (CHMe).

MS (ESI): m/z 270.0 ($M + H$)⁺.

(R)-2-((1-phenylethylimino)methyl)-4-methoxyphenol (HL⁴)



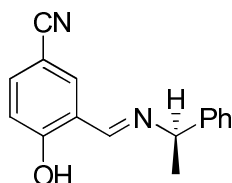
Yield = (1.91 g, 75 %).

^1H NMR (400 MHz, CDCl_3): δ 13.35 (s, 1H, OH), 8.70 (s, 1H, ArH), 7.69 (m, 4H, ArH), 7.59 (m, 1H, ArH), 7.25 (s, 1H, ArH), 7.10 (m, 1H, ArH), 4.88 (q, 1H, $^3J = 6.7$ Hz, CHMePh), 4.09 (s, 3H, OMe), 1.96 (d, $^3J = 6.7$ Hz, CHMePh).

$^{13}\text{C}\{^1\text{H}\}$ NMR (100 MHz, CDCl_3): 163.2 (CH=N), 155.2 (Ar- C_q), 152.1 (Ar- C_q), 143.9 (Ar- C_q), 128.7 (Ar-CH), 127.4 (Ar-CH), 126.6 (Ar-CH), 119.4 (Ar-CH), 118.5 (Ar- C_q), 117.4 (Ar-CH), 115.0 (Ar-CH), 68.7 (CHMePh), 55.9 (OMe), 24.9 (CHMe).

MS (ESI): m/z 256.2 ($\text{M}+\text{H}$) $^+$.

(R)-3-[(1-phenylethylimino)methyl]-4-hydroxybenzonitrile (HL⁵)



Yield = (1.21 g, 48 %).

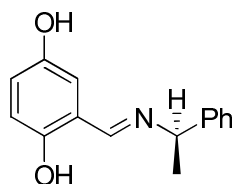
^1H NMR (400 MHz, CDCl_3): δ 14.51 (s, 1H, OH), 8.36 (s, 1H, CH=N), 7.54 (dd, 2H, $^3J = 6.7$ Hz, $^3J = 8.6$ Hz, ArH), 7.35 (m, 5H, ArH), 7.00 (d, 1H, $^3J = 8.4$ Hz, ArH), 4.64 (q, 1H, $^3J = 6.7$ Hz, CHMePh), 1.67 (d, 3H, $^3J = 6.7$ Hz, CHMePh).

$^{13}\text{C}\{^1\text{H}\}$ NMR (100 MHz, CDCl_3): 165.8 (Ar-CN), 162.0 (CH=N), 142.5 (Ar- C_q), 136.1 (Ar-CH), 135.7 (Ar-CH), 128.9 (Ar-CH), 127.8 (Ar-CH), 126.5 (Ar-CH),

118.9 (Ar-CH), 118.9 (Ar-C_q), 118.8 (Ar-C_q), 101.6 (Ar-C_q), 67.9 (CHMePh), 24.4 (CHMe).

MS (ESI): m/z 248.8 (M-H)⁻.

(R)-2-[(1-phenylethylimino)methyl]benzene-1,4-diol (HL⁶)



Yield = (1.69 g, 70 %).

¹H NMR (400 MHz, CDCl₃): 8.30 (s, 1H, CH=N), 7.35 (m, 4H, ArH), 7.26 (m, 1H, ArH), 6.83 (m, 2H, ArH), 6.72 (d, 1H, ⁴J = 2.5 Hz, ArH), 4.53 (q, 1H, ³J = 6.7 Hz, CHMePh), 1.62 (d, 3H, ³J = 6.7 Hz, CHMePh).

¹³C{¹H}NMR (100 MHz, CDCl₃): δ 162.9 (CH=N), 155.1 (Ar-C_q), 147.3 (Ar-C_q), 143.8 (Ar-C_q), 128.7 (Ar-C_q), 127.3 (Ar-CH), 126.4 (Ar-CH), 120.2 (Ar-CH), 118.7 (Ar-C_q), 117.7 (Ar-CH), 116.88 (Ar-CH), 68.6 (CHMePh), 24.9 (CHMe).

MS (ESI): m/z 242.2 (M+H)⁺.

Anal. Found (Calcd. For C₁₅H₁₅NO₂): C 74.47 (74.67), H 6.71 (6.27), N 5.98 (5.81)%.

5.2.5 General Procedure for $[\text{FeL}^n_2]$ complexes ($n = 1-5$)

The treatment of Proligand HL^n (2.0 eq.) with NaH (2.5 eq.) in THF formed a yellow solution containing NaL^n salt. A solution of $\text{Fe}_2\text{Cl}_4 \cdot 3\text{THF}$ (1.0 eq.) in THF was added *via* cannula and immediately the solution turned purple. This was stirred overnight at ambient temperature before all volatiles were removed *in vacuo*. The solid was extracted into diethyl ether or dimethyl chloride. The solution was then concentrated and red solid formed upon standing at 4 °C. The product $[\text{FeL}^n_2]$ was isolated by filtration and was found to be very air sensitive.

 $[\text{FeL}^1_2]$

Yield = (0.35 g, 78 %).

Anal. Found (Calcd. for $\text{C}_{30}\text{H}_{28}\text{FeN}_2\text{O}_2$): C 71.54 (71.44), H 5.42 (5.60), N 5.45 (5.55) %.

 $[\text{FeL}^2_2]$

Yield = (0.45 g, 46 %).

Anal. Found (Calcd. for $\text{C}_{38}\text{H}_{44}\text{FeN}_2\text{O}_2$): C 73.89 (74.02), H 7.06 (7.19), N 4.57 (4.54) %.

 $[\text{FeL}^3_2]$

Yield = (0.22 g, 42 %).

Anal. Found (Calcd. for $\text{C}_{30}\text{H}_{26}\text{FeN}_4\text{O}_6$): C 59.69 (60.62), H 4.21 (4.41), N 8.77 (9.43) %.

[FeL⁴₂]

Yield = (0.23 g, 46 %).

Anal. Found (Calcd. for C₃₂H₃₂FeN₂O₄): C 69.01 (68.69), H 5.65 (5.71), N 4.80 (4.96) %.

[FeL⁵₂]

Yield = (0.38 g, 76 %).

Anal. Found (Calcd. for C₃₂H₃₂FeN₂O₄): C 69.21 (69.32), H 4.56 (4.73), N 9.89 (10.11) %.

[FeL⁶₂]·CH₃OH

The mixture of 5-Hydroxysalicylaldehyde (0.500 g, 3.62 mmol) and KOH (0.200 g, 3.6 mmol) was stirred in methanol (20 mL) for at 0.5 h before a solution of Fe(OAc)₂ (0.320 g, 1.8 mmol) in methanol (10 mL) was added. The resulting red solution was treated with (*R*)-1-phenylethylamine (0.440 g, 3.6 mmol), precipitating an orange solid which was then filtered and dried *in vacuo* for 4 h. The complex is very air sensitive. (0.36 g, 75 %). Single crystals were grown from a saturated methanol solution upon standing at room temperature for one week.

Anal. Found (Calcd. for C₃₁H₃₂FeN₂O₅): C 65.56 (65.50), H 5.56 (5.67), N 4.89 (4.93) %.

5.2.6 $\{\text{FeL}^1_2(\mu\text{-pz})\}_\infty$

To a solution of $[\text{FeL}^1_2]$ (0.252 g, 0.5 mmol) in diethyl ether (20 mL) was added pyrazine (0.04 g, 0.5 mmol) in diethyl ether (10 mL) *via* cannula. The mixture was stirred overnight. This yielded purple solid which was then isolated by filtration. (0.19 g, 65 %). The complex is air sensitive.

IR (cm^{-1}): 1598 s, 1537 m, 1414 w, 1401 w, 1346 m, 1131, 1196, 1148, 1038, 968, 917, 885, 847, 756 w, 736 m, 697 m.

Anal. Found (calculated for $\text{C}_{34}\text{H}_{32}\text{FeN}_4\text{O}_2$): C 69.67 (69.87). H 5.48 (5.52), N 9.52 (9.59)%.

UV in MeCN (λ , nm; ϵ , $\text{M}^{-1}\text{cm}^{-1}$): 234 (54000), 260 (38000), 352 (17000), 500 (5000).

Crystallography: $[\{\text{FeL}^1_2(\mu\text{-pz})\}_\infty]$, $\text{C}_{110}\text{H}_{116}\text{Fe}_3\text{N}_{12}\text{O}_8$, $M = 1901.70$, monoclinic, $a = 28.9533(7)$ Å, $b = 13.0045(3)$ Å, $c = 26.7340(11)$ Å, $\alpha = 90.00^\circ$, $\beta = 90.526(2)^\circ$, $\gamma = 90.00^\circ$, $V = 10065.5(5)$ Å³, $T = 100(2)$ K, space group C2, $Z = 4$, 24234 reflections measured, 16354 independent reflections ($R_{\text{int}} = 0.1277$). The final R_I values were 0.0582 ($I > 2\sigma(I)$). The final $wR(F^2)$ values were 0.1476 ($I > 2\sigma(I)$). The final R_I values were 0.0790 (all data). The final $wR(F^2)$ values were 0.1542 (all data).

5.2.7 $[\{\text{FeL}^1_2(\mu\text{-bpy})\}\cdot\text{CH}_3\text{OH}]_\infty$

To a solution of $[\text{FeL}^1_2]$ (0.252 g, 0.5 mmol) in methanol (20 mL) was added 4,4'-bipyridine (0.080 g, 0.5 mmol) in methanol (10 mL). The mixture was stirred overnight. The solvent (15 mL) was removed *in vacuo* and the precipitated solid was collected by filtration. (0.26 g, 75 %). Single crystals were grown by slow cooling of a hot saturated acetonitrile solution.

IR (cm^{-1}): 1597, 1535, 1342, 1261, 1213, 1147, 1094, 1028, 799, 721, 667 w.

Anal. Found (calculated for $\text{C}_{41}\text{H}_{40}\text{FeN}_4\text{O}_3$): C 70.96 (71.10). H 5.49 (5.82), N 8.07 (8.09)%.

UV in MeCN (λ , nm; ϵ , $\text{M}^{-1}\text{cm}^{-1}$): 236 (52000), 267 (30000), 350 (16000), 500 sh (6000)

Crystallography: $[\{\text{FeL}^1_2(\mu\text{-bpy})\}\cdot\text{CH}_3\text{OH}]_\infty$, $\text{C}_{44}\text{H}_{42}\text{FeN}_6\text{O}_2$, $M = 742.69$, monoclinic, $a = 26.8700(6)$ Å, $b = 11.5749(2)$ Å, $c = 14.8955$ Å, $\alpha = 90.00^\circ$, $\beta = 121.146(3)^\circ$, $\gamma = 90.00^\circ$, $V = 3964.96(8)$ Å³, $T = 100(2)$ K, space group C2, $Z = 4$, 6483 reflections measured, 4934 independent reflections ($R_{\text{int}} = 0.1277$). The final R_I values were 0.0367 ($I > 2\sigma(I)$). The final $wR(F^2)$ values were 0.0932 ($I > 2\sigma(I)$). The final R_I values were 0.0411 (all data). The final $wR(F^2)$ values were 0.0951 (all data).

5.2.8 $\{\text{FeL}^2_2(\mu\text{-pz})\}_\infty$

To a stirred solution of $[\text{FeL}^2_2]$ (0.308 g, 0.5 mmol) in Et_2O (20 mL) was added a solution of pyrazine (0.040 g, 0.5 mmol) in Et_2O (10 mL) *via* cannula. The mixture was stirred for 15 min and concentrated to *ca* 10 mL. The precipitated solid was isolated by filtration. Single crystals were grown in acetonitrile upon standing at -5°C for one week. (0.23 g, 66 %).

IR (cm^{-1}): 1613 m, 1531 w, 1462 s, 1414 w, 1377 m, 1328, 1269, 1177, 1073, 1037, 829, 721, 697 w.

Anal. Found (Calculated for $\text{C}_{42}\text{H}_{48}\text{FeN}_4\text{O}_2$): C 72.14 (72.41), H 7.14 (6.94), N 7.85 (8.04) %.

UV in MeCN (λ , nm; ϵ , $\text{M}^{-1}\text{cm}^{-1}$): 235 (85000), 364 (20000), 488 sh (5000).

Crystallography: $\{\text{FeL}^2_2(\mu\text{-pz})\}_\infty$, $\text{C}_{130.5}\text{H}_{150.75}\text{Fe}_3\text{N}_{4.25}\text{O}_6$, $M = 2182.45$, monoclinic, $a = 25.4871(8) \text{ \AA}$, $b = 21.9537(8) \text{ \AA}$, $c = 24.8107(11) \text{ \AA}$, $\alpha = 90.00^\circ$, $\beta = 116.882(5)^\circ$, $\gamma = 90.00^\circ$, $V = 12382.3(8) \text{ \AA}^3$, $T = 100(2) \text{ K}$, space group C2, $Z = 4$, 74329 reflections measured, 40956 independent reflections ($R_{\text{int}} = 0.1277$). The final R_I values were 0.0740 ($I > 2\sigma(I)$). The final $wR(F^2)$ values were 0.1272 ($I > 2\sigma(I)$). The final R_I values were 0.3046 (all data). The final $wR(F^2)$ values were 0.1691 (all data).

5.2.9 $\{\text{FeL}^2_2(\mu\text{-bpy})\}_\infty$

To a stirred solution of $[\text{FeL}^2_2]$ (0.308 g, 0.5 mmol) in Et_2O (20 mL) was added 4,4'-bipyridine (0.080 g, 0.5 mmol) in Et_2O (10 mL) *via* cannula. The mixture was stirred for 15 min and concentrated to *ca* 10 mL. Crystals were grown in acetonitrile upon standing at -30°C for one week. (0.31 g, 80 %).

IR (cm^{-1}): 1618 m, 1527, 1329, 1267, 1250, 1212, 1177, 1143, 1055, 828, 746, 699 w.

Anal. Found (Calculated for $\text{C}_{48}\text{H}_{52}\text{FeN}_4\text{O}_2$): C 74.50 (74.60), H 6.80 (6.78), N 7.70 (7.25) %.

UV in MeCN (λ , nm; ϵ , $\text{M}^{-1}\text{cm}^{-1}$): 236 (76000), 265 (75000), 334 (20000).

5.2.10 $\{\text{FeL}^3_2(\mu\text{-C}_4\text{H}_4\text{N}_2)\}_\infty$

To a solution of $[\text{FeL}^3_2]$ (0.297 g, 0.5 mmol) in THF (10 mL) was added *via* cannula pyrazine (0.040 g, 0.5 mmol) in THF (10 mL). The mixture was stirred overnight. The solvent was removed *in vacuo* to induce crystallization. The product was isolated by filtration. Single crystals were grown by slow cooling of a hot acetonitrile solution. (0.22 g, 65 %).

IR (cm^{-1}): 1607 m (NO_2), 1539, 1335, 1261, 1192, 1149, 1126, 1079, 1040, 970, 947, 930, 807, 722, 700 w.

Anal. Found (Calculated for $C_{34}H_{30}FeN_6O_6$): C 60.31 (60.54), H 4.49 (4.48), N 12.23 (12.46) %.

UV in MeCN (λ , nm; ϵ , $M^{-1}cm^{-1}$): 233 (90000), 259 (78000), 355 (27000), 480 sh (6000).

5.2.11 $[FeL^3_2(\mu\text{-bpy})]\cdot THF]_{\infty}$

To a solution of $[FeL^3_2]$ (0.297 g, 0.5 mmol) in THF (10 mL) was added *via* cannula 4,4'-bipyridine (0.080 g, 0.5 mmol) in THF (10 mL). The mixture was stirred overnight. The solvent was removed *in vacuo* to induce crystallization. The product was isolated by filtration. (0.25 g, 61 %). Single crystals were grown in THF upon standing at $-5^{\circ}C$ for one week.

IR (cm^{-1}): 1598 m (NO_2), 1547, 1532 w, 1309 m (NO_2), 1242, 1102, 946, 805, 757, 697 w.

Anal. Found (Calculated for $C_{44}H_{42}FeN_6O_7$): C 64.38 (64.24), H 4.93 (5.15), N 10.00 (10.22) %.

UV in MeCN (λ , nm; ϵ , $M^{-1}cm^{-1}$): 234 (71000), 371 (39000), 500 sh (7000).

5.2.12 $\{FeL^4_2(\mu\text{-}C_4H_4N_2)\}_{\infty}$

To a stirred red solution of $[\text{FeL}^4_2]$ (0.282 g, 0.5 mmol) in Et_2O (20 mL) was added a colourless solution of pyrazine (0.040 g, 0.5 mmol) in Et_2O (10 mL) *via* cannula. The mixture was stirred for 30 min. and then concentrated to *ca* 10 mL. The compound crystallised as purple needles over 12 h. The crystals were isolated by filtration and dried *in vacuo* for 2 h. (0.22 g, 68 %).

IR (cm^{-1}): 1601 m, 1540, 1316, 1301, 1254, 121, 1157, 1079, 1042, 917, 815, 794, 721 w.

Anal. Found (Calculated for $\text{C}_{36}\text{H}_{36}\text{FeN}_4\text{O}_4$): C 66.90 (67.08), H 5.60 (5.63), N 8.60 (8.69) %.

UV in MeCN (λ , nm; ϵ , $\text{M}^{-1}\text{cm}^{-1}$): 236 (80000), 378 (21000), 500 sh (7000).

Crystallography: $\{\text{FeL}^4_2(\mu\text{-pz})\}_\infty$, $\text{C}_{35.5}\text{H}_{32.25}\text{Fe}_3\text{N}_{6.75}\text{O}_6$, $M = 705.28$, monoclinic, $a = 7.3694(6)$ Å, $b = 19.79738$ Å, $c = 12.1347(18)$ Å, $\alpha = 90.00^\circ$, $\beta = 102.388(12)^\circ$, $\gamma = 90.00^\circ$, $V = 1729.1(4)$ Å³, $T = 100(2)$ K, space group P2(1), $Z = 2$, 34948 reflections measured, 6087 independent reflections ($R_{\text{int}} = 0.1937$). The final R_I values were 0.0487 ($I > 2\sigma(I)$). The final $wR(F^2)$ values were 0.0833 ($I > 2\sigma(I)$). The final R_I values were 0.1659 (all data). The final $wR(F^2)$ values were 0.990 (all data).

5.2.13 $\{\text{FeL}^4_2(\mu\text{-C}_{10}\text{H}_8\text{N}_2)\}_\infty$

To a stirred red solution of $[\text{FeL}^4_2]$ (0.282 g, 0.5 mmol) in Et_2O (20 mL) was added a colourless solution of 4,4'-bipyridine (0.08 g, 0.5 mmol in Et_2O (10 mL)

via cannula. The mixture was stirred for 30 min. and then concentrated to *ca* 10 mL. The purple crystals were growing in the solution over 12 h and were isolated by filtration. (0.30 g, 83 %).

IR (cm⁻¹): 1597 m, 1537, 1320, 1256, 1215, 1156, 1041, 811, 721 w.

Anal. Found (Calculated for C₄₂H₄₀FeN₄O₄): C 69.45 (70.00), H 5.41 (5.59), N 7.73 (7.77) %.

UV in MeCN (λ , nm; ϵ , M⁻¹cm⁻¹): 236 (79000), 377 (29000), 500 sh (7000).

Crystallography: {FeL⁴(μ -C₁₀H₈N₂)}_∞, C₅₀H₅₄Cl₁₃FeN₆O_{8.50}, $M = 930.84$, monoclinic, $a = 31.3100(3)$ Å, $b = 11.6027(2)$ Å, $c = 15.9378(8)$ Å, $\alpha = 90^\circ$, $\beta = 103.807(2)^\circ$, $\gamma = 90^\circ$, $V = 2390.19(9)$ Å³, $T = 100(2)$ K, space group P2, $Z = 2$, 23230 reflections measured, 11055 independent reflections ($R_{int} = 0.0239$). The final R_I values were 0.0561 ($I > 2\sigma(I)$). The final $wR(F^2)$ values were 0.1342 ($I > 2\sigma(I)$). The final R_I values were 0.0805 (all data). The final $wR(F^2)$ values were 0.1413 (all data).

5.2.14 [{FeL⁵₂(μ -C₄H₄N₂)}·0.5CH₃OH]_∞

To a stirred red solution of [FeL⁵₂] (0.277 g, 0.5 mmol) in methanol (20 mL) was added a solution of pyrazine (0.04 g, 0.5 mmol) in methanol (10 mL) *via* cannula. The mixture was stirred for 30 min. and then concentrated to *ca* 15 mL. The

compound was precipitated over 12 h and was isolated by filtration. (0.19 g, 58 %).

IR (cm⁻¹): 2207 m (CN), 1605 m, 1524, 1482, 1349, 1261, 1210, 1156, 1041, 822, 721 w.

Anal. Found (Calculated for C_{36.5}H₃₂FeN₆O_{2.5}): C 67.36 (67.39), H 4.79 (4.96), N 12.87 (12.92) %.

UV in MeCN (λ, nm; ε, M⁻¹cm⁻¹): 244 (76000), 286 (26000), 341 (12000), 500 sh (2000).

5.2.15 [$\text{FeL}^5_2(\mu\text{-C}_{10}\text{H}_8\text{N}_2)\cdot\text{THF}$]_∞

To a stirred red solution of [FeL⁵₂] (0.277 g, 0.5 mmol) in THF (20 mL) was added a colourless solution of 4,4'-bipyridine (0.08 g, 0.5 mmol) in THF (10 mL) *via* cannula. The mixture was stirred for 2 h. and then concentrated to *ca* 15 mL. The product was precipitated immediately and collected by filtration. (0.26 g, 66 %). The single crystals were grown by slow cooling of hot CHCl₃ solution.

IR (cm⁻¹): 2214 m (CN), 1605, 1526, 1486, 1351, 1262, 1214, 1157, 1135, 1068, 827, 722 w.

Anal. Found (Calculated for C₄₆H₄₂FeN₆O₃): C 70.36 (70.59), H 5.44 (5.41), N 10.76 (10.74) %.

UV in MeCN (λ , nm; ϵ , $M^{-1}cm^{-1}$): 237 (66000) 243 (66000), 284 (20000), 336 (11000), 500 sh (1000).

Crystallography: $[\{ FeL^5(\mu-C_{10}H_8N_2) \} \cdot THF]_{\infty}$, $C_{43}H_{35}Cl_{13}FeN_6O_2$, $M = 8296.97$, orthorhombic, $a = 21.05493(13)$ Å, $b = 16.11390(10)$ Å, $c = 11.55863(8)$ Å, $\alpha = 90^\circ$, $\beta = 90^\circ$, $\gamma = 90^\circ$, $V = 3921.58(4)$ Å³, $T = 100(2)$ K, space group $P2(1)2(1)2$, $Z = 4$, 23665 reflections measured, 6066 independent reflections ($R_{int} = 0.0239$). The final R_I values were 0.0290 ($I > 2\sigma(I)$). The final $wR(F^2)$ values were 0.0775 ($I > 2\sigma(I)$). The final R_I values were 0.0319 (all data). The final $wR(F^2)$ values were 0.0784 (all data).

5.2.16 $[\{ FeL^6(\mu-C_{10}H_8N_2) \} \cdot 2THF]_{\infty}$

To a stirred red solution of $[FeL^6_2]$ (0.268 g, 0.5 mmol) in THF (20 mL) was added a solution of 4,4'-bipyridine (0.080 g, 0.5 mmol) in THF (10 mL) *via* cannula. The mixture was stirred for 30 min. and then concentrated to *ca* 15 mL. The compound precipitated as purple solid immediately. The crystals were isolated by filtration and dried *in vacuo* for 2 h. (0.30 g, 72 %). The single crystals were growing in THF solution at room temperature for one week.

IR (cm^{-1}): 3300 m (O-H), 1593, 1553, 1535, 1404, 1260, 1212, 1152, 1078, 1050, 820, 721 w.

Anal. Found (Calculated for $C_{48}H_{52}FeN_4O_6$): C 67.95 (68.90), H 6.00 (6.26), N 6.87 (6.70) %.

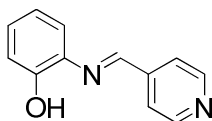
UV in MeCN (λ , nm; ϵ , M⁻¹cm⁻¹): 234 (80000), 260 (60000), 344 (27000).

Crystallography: $[\{\text{FeL}^6(\mu\text{-C}_{10}\text{H}_8\text{N}_2)\}\cdot 2\text{THF}]_\infty$, $\text{C}_{48}\text{H}_{52}\text{FeN}_4\text{O}_6$, $M = 836.79$, triclinic, $a = 8.7967(2)$ Å, $b = 8.9245(2)$ Å, $c = 14.7428(4)$ Å, $\alpha = 102.135(2)^\circ$, $\beta = 106.3342(2)^\circ$, $\gamma = 97.4319^\circ$, $V = 1063.73(4)$ Å³, $T = 100(2)$ K, space group P2, $Z = 1$, 25187 reflections measured, 13945 independent reflections ($R_{\text{int}} = 0.0239$). The final R_I values were 0.0425 ($I > 2\sigma(I)$). The final $wR(F^2)$ values were 0.1061 ($I > 2\sigma(I)$). The final R_I values were 0.0476 (all data). The final $wR(F^2)$ values were 0.1078 (all data).

5.3 Experimental details for Chapter Three

5.3.1 Synthesis of ligand precursors

2-[(pyridin-4-yl)methyleneamino]phenol (HL⁷)⁸



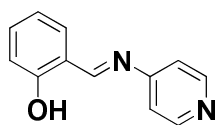
Isonicotinaldehyde (1.070 g, 10.0 mmol), 2-aminophenol (1.090 g, 10.0 mmol) were stirred in methanol (40 mL) overnight. The volume was reduced to *ca* 20 mL under reduced pressure. The resulting solid was isolated by filtration and washed with cold hexane. (1.80 g, 91 %.)

¹H NMR (300 MHz, CDCl₃): 8.77 (m, 2H, Py-CH), 8.68 (s, 1H, CH=N), 7.74 (m, 2H, Py-CH), 7.33 (dd, ³J = 8.0 Hz, ⁴J = 1.4 Hz, 1H, ArH), 7.25 (m, 1H, ArH), 7.18 (s, 1H, Ar-OH), 7.02 (dd, ¹J = 8.2 Hz, ²J = 1.3 Hz, 1H, ArH), 6.90 (m, 1H, ArH). NMR data corresponded with the literature report.

MS(ESI) m/z 196.9 [M-H]⁻

Anal. Found (Calculated for C₁₂H₁₀N₂O): C 72.50 (72.71), H 4.70 (5.08), N 14.37 (14.13) %.

N-salicylidene-4-aminopyridine (HL⁸)⁹



A 250 mL round-bottom flask fitted with a PTFE stopcock sidearm was charged with a suspension of salicylaldehyde (2.440 g, 20.0 mmol) and 4-aminopyridine (0.940 g, 10 mmol) in dry toluene (200 mL). A Soxhlet extractor equipped with a dry paper thimble charged with excess powdered CaH₂ and condenser was fitted. The condenser outlet was fitted with a T-joint allowing the reaction to be performed under an atmosphere of dry dinitrogen. The system was heated to reflux for 3 d. Toluene was removed to *ca.* 50 mL *in vacuo* under Schlenk conditions and the solution was left overnight. The resulting yellow precipitate was isolated by filtration (1.50 g, 75 %).

^1H NMR (400MHz, CD_3CN): δ 12.70 (s, 1H, Ar-OH), 8.85 (s, 1H, CH=N), 8.65 (m, 2H, Py-CH), 7.60 (dd, $^3J = 7.6$ Hz, $^4J = 1.6$ Hz, 1H, ArH), 7.49 (m, 1H, ArH), 7.30 (m, 2H, Py-CH), 7.03 (m, 2H, ArH).

$^{13}\text{C}\{^1\text{H}\}$ NMR (100 MHz, CDCl_3): δ 166.9 (CH=N), 160.8 (Ar- C_q), 155.0 (Py- C_q), 150.74 (Py-CH), 133.9 (Ar-CH), 133.1 (Ar-CH), 119.1 (Ar- C_q), 117.0 (Ar- C_q), 116.6 (Ar-CH), 115.9 (Py-CH).

MS(ESI) m/z 199.1 $[\text{M}+\text{H}]^+$

Anal. Found (Calculated for $\text{C}_{12}\text{H}_{10}\text{N}_2\text{O}$): C 72.76 (72.71), H 5.23 (5.08), N 14.13 (14.13) %.

5.3.2 Synthesis of $[\text{FeL}^n_2]$ ($n = 7, 8$) MOFs complexes

$[\text{FeL}^7_2]_n$

HL^7 (0.360 g, 1.8 mmol) was stirred with NaH (0.130 g, 5.3 mmol) in dry THF (20 mL) overnight. The resulting pink solution was filtered *via* cannula into a solution of $\text{Fe}_2\text{Cl}_4 \cdot 3\text{THF}$ (0.210 g, 0.40 mmol) in dry THF (10 mL) at room temperature. The resulting deep red solution was stirred overnight at ambient temperature and evaporated to dryness. The MeCN extracts (2×20 mL) were filtered and DCM (10 mL) was added to induce crystallization. The resulting brown solid was washed dried *in vacuo*. (0.120 g, 30 %). Single crystals $[\text{FeL}^1_2] \cdot 1\frac{1}{4}(\text{H}_2\text{O}) \cdot \frac{1}{2}(\text{MeOH})$ were grown from wet methanol.

Elemental Analysis: Found (calculated for $C_{24}H_{18}FeN_4O_2$): C 63.73 (64.02), H 4.46 (4.03), N 12.39 (12.44) %.

IR (cm^{-1}): 3050 w, 2161w, 1596 m, 1581 m, 1556 w, 1471 vs, 1444 m, 1412 m, 1282 s, 1257 vs, 1174 w, 1145 w, 1119 w, 1034 w, 1000 w, 869 m, 812 s, 799 s, 725 vs, 694 w.

UV in MeCN (λ , nm; ϵ , $M^{-1}cm^{-1}$): 221 (23991), 282 (16420), 366 (12068)

Crystallography: $[FeL^7_2] \cdot 1\frac{1}{4}(H_2O) \cdot \frac{1}{2}(MeOH)$, $C_{24.50}H_{22.50}FeN_4O_{3.75}$, $M = 488.82$, tetragonal, $a = 19.3307(2)$ Å, $b = 19.3307(2)$ Å, $c = 27.7612(8)$ Å, $\alpha = 90.00^\circ$, $\beta = 90.00^\circ$, $\gamma = 90.00^\circ$, $V = 10373.7(3)$ Å³, $T = 100(2)$ K, space group $I4_12d$, $Z = 16$, 23628 reflections measured, 3577 independent reflections ($R_{int} = 0.0795$). The final R_I values were 0.0553 ($I > 2\sigma(I)$). The final $wR(F^2)$ values were 0.1291 ($I > 2\sigma(I)$). The final R_I values were 0.1068 (all data). The final $wR(F^2)$ values were 0.1407 (all data).

$[FeL^8_2]_n$

A mixture of HL^2 (0.400 g, 2.0 mmol) and LiOMe (0.114 g, 3.0 mmol) in dry MeOH (20 mL) in a Schlenk tube was stirred for 30 min. To the mixture was added a solution of $FeCl_2$ (0.127 g, 1.0 mmol) in MeOH (10 mL) *via* a cannula. The resulting brown solution was stirred overnight at ambient temperature. The solid was collected by filtration and dried *in vacuo* for 4 h. (0.42 g, 93 %). Single

crystals were grown in an NMR tube using a small scale reaction with the starting materials having a concentration of 2.0 M.

Elemental Analysis: Found (calculated for $C_{24}H_{18}FeN_4O_2$): C 64.67 (64.02). H 4.48 (4.03), N 12.18 (12.44)%.

IR (cm^{-1}): 1580 vs, 1527 s, 1491 m, 1464 s, 1448 s, 1420 w, 1384 w, 1350 m, 1327 m, 1207 s, 1176 s, 1145 vs, 1125 w, 1089 w, 1059 w, 1027 w, 1008 m, 972 m, 922 s, 864 m, 837 s, 753 vs, 736 s, 658 w.

Crystallography: $[FeL^8_2]$, $C_{24}H_{18}FeN_4O_2$, $M = 450.27$, orthorhombic, $a = 9.9499(6)$ Å, $b = 11.0634(5)$ Å, $c = 19.3835(9)$ Å, $\alpha = 90.00^\circ$, $\beta = 90.00^\circ$, $\gamma = 90.00^\circ$, $V = 2133.73(19)$ Å³, $T = 100(2)$ K, space group $Pbca$, $Z = 4$, 11020 reflections measured, 2026 independent reflections ($R_{int} = 0.1488$). The final R_I values were 0.0830 ($I > 2\sigma(I)$). The final $wR(F^2)$ values were 0.1831 ($I > 2\sigma(I)$). The final R_I values were 0.1027 (all data). The final $wR(F^2)$ values were 0.1936 (all data).

$[CuL^7_2]_n$

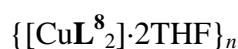
A mixture of HL^7 (0.40 g, 2.0 mmol) was stirred with NaOH (0.08 g, 2.0 mmol) in methanol (40 mL) for 1 h, yielding a yellow solution. A solution of copper(II) chloride (0.13 g, 1.0 mmol) in methanol (10 mL) was added, immediately, the solution turned red and brown solid precipitated. The reaction was stirred another

2 h at room temperature. The product was collected by filtration and dried *in vacuo*. (0.44 g, 95 %)

Elemental Analysis: Found (calculated for $C_{24}H_{18}FeN_4O_2$): C 63.03 (62.94), H 4.56 (3.96), N 12.49 (12.23) %.

IR (cm^{-1}): 1560 vs, 1530 s, 1481 m, 1460 s, 1438 s, 1380 w, 1345 w, 1327 m, 1210 s, 1170 s, 1150 vs, 1090 w, 1030 w, 1010 m, 970 m, 920 s, 864 s, 837 s, 750 vs, 746 s.

Due to insolubility of the product, UV data was not collected.



HL^8 (0.400 g, 2.0 mmol) was stirred with NaH (0.072 g, 3.0 mmol) in dry THF (20 mL) for 30 min. The resulting yellow solution was filtered *via* cannula into a solution of $CuCl_2$ (0.124 g, 1.0 mmol) in dry THF (10 mL) at room temperature. The resulting green solution was stirred overnight at ambient temperature and filtered. THF was removed to *ca.* 15 mL *in vacuo* under Schlenk conditions and the solution was stored at 5°C overnight. The resulting green precipitate was isolated by filtration (0.13 g, 22 %).

IR (cm^{-1}): 3010 w, 1608 s, 1576 vs, 1531 s, 1489 w, 1465 s, 1446 s, 1415 w, 1389 vs, 1359 m, 1337 s, 1323 w, 1184 s, 1144 s, 1123 m, 1051 w, 1004 w, 987 m, 930 s, 865 s, 835 vs, 796 w, 750 vs, 732 m.

Anal. Found (calculated for $C_{32}H_{34}CuN_4O_4$): C 63.67 (63.82). H 5.48 (5.69), N 9.52 (9.85)%.

UV in THF (λ , nm; ϵ , $M^{-1}cm^{-1}$): 246 (28,610), 275 (29,000), 396 (11,300).

Crystallography: $\{[CuL^8_2] \cdot 2THF\}_n$ $C_{32}H_{34}CuN_4O_4$, $M = 602.17$, monoclinic, $a = 10.41620(10)$ Å, $b = 28.0380(2)$ Å, $c = 10.49460(10)$ Å, $\alpha = 90.00^\circ$, $\beta = 111.6070(10)^\circ$, $\gamma = 90.00^\circ$, $V = 2849.57(4)$ Å³, $T = 100(2)$ K, space group $P2(1)/n$, $Z = 4$, 32851 reflections measured, 5472 independent reflections ($R_{int} = 0.0226$). The final R_I values were 0.0444 ($I > 2\sigma(I)$). The final $wR(F^2)$ values were 0.1158 ($I > 2\sigma(I)$). The final R_I values were 0.0456 (all data). The final $wR(F^2)$ values were 0.1169 (all data).

$\{[CuL^8_2] \cdot MeOH\}_n$

A mixture of HL^8 (0.400 g, 2.0 mmol) and LiOMe (0.114 g, 3.0 mmol) in dry MeOH (15 mL) in a Schlenk tube was stirred for 30 min. To the mixture was added a solution of $CuCl_2$ (0.124 g, 1.0 mmol) in MeOH (10 mL) *via* cannula. The resulting green solution was stirred overnight at ambient temperature. The solid was collected by filtration and dried *in vacuo*. (yield 0.41 g, 83 %).

IR ;(cm^{-1}): 3011 w, 1609 s 1577 vs, 1532 s, 1489 w, 1466 s, 1448 s, 1415 w, 1389 vs, 1359 m, 1337 m, 1323 w, 1184 s, 1144 s, 1004 w, 987 m, 931 s, 865 s, 835 vs, 750 vs, 733 m.

Anal. Found (calculated for $C_{25}H_{22}CuN_4O_3$): C 61.59 (61.28). H 4.42 (4.53), N 11.59 (11.43)%.

UV in MeOH (λ , nm; ϵ , $M^{-1}cm^{-1}$): 223 (16,400), 245 (17,000), 278 (16,500), 386 (5,550).

Crystallography: $\{[CuL^8_2] \cdot MeOH\}_n$, $C_{25}H_{22}CuN_4O_3$, $M = 490.01$, monoclinic, $a = 13.46134(12)$ Å, $b = 10.35557(8)$ Å, $c = 15.89363(14)$ Å, $\alpha = 90.00^\circ$, $\beta = 92.2134(8)^\circ$, $\gamma = 90.00^\circ$, $V = 2213.92(3)$ Å³, $T = 100(2)$ K, space group $P2(1)/n$, $Z = 4$, 36531 reflections measured, 6372 independent reflections ($R_{int} = 0.0148$). The final R_I values were 0.0250 ($I > 2\sigma(I)$). The final $wR(F^2)$ values were 0.0696 ($I > 2\sigma(I)$). The final R_I values were 0.0261 (all data). The final $wR(F^2)$ values were 0.0703 (all data).

$[Cu_3L^8_4(sal)_2]_n$

A mixture of salcylaldehyde (2.440 g, 20.0 mmol) and triethylamine (2.020 g, 20.0 mmol) in methanol (100 mL) was stirring for 10 min. To the solution was added copper chloride (1.340 g, 10.0 mmol) in methanol (10 mL). The reaction was heated to reflux for 15 min before 4-aminopyridine (1.250 g, 13.3 mmol) was added. The solution was heated to reflux for another 4 h. Methanol was removed *in vacuo* to *ca* half volume. The product thus crystallized was isolated by filtration (1.2 g, 30 %).

IR (cm^{-1}): 2118 m, 1844 m, 1602 s, 1582 s, 1527 s, 1462 m, 1433 vs, 1388 s, 1357 w, 1324 m, 1183 m, 1144 s, 1125 s, 1025 s, 930 m, 868 m, 837 m, 752 s, 658 s.

Anal. Found (calculated for $\text{C}_{64}\text{H}_{54}\text{Cu}_3\text{N}_8\text{O}_{10}$): C 60.37 (60.44). H 4.38 (4.42), N 9.32 (9.42)%.

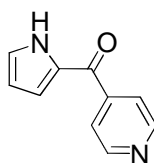
UV in MeOH (λ , nm; ϵ , $\text{M}^{-1}\text{cm}^{-1}$): 234 (54,000), 260 (38,000), 352 (17,000), 500 (5,000).

Crystallography: $[\text{Cu}_3\text{L}_4(\text{sal})_2 \cdot 2\text{MeOH}]_n$, $\text{C}_{64}\text{H}_{54}\text{Cu}_3\text{N}_8\text{O}_{10}$, $M = 1285.77$, monoclinic, $a = 11.4716(3) \text{ \AA}$, $b = 22.7485(6) \text{ \AA}$, $c = 22.5562(7) \text{ \AA}$, $\alpha = 90.00^\circ$, $\beta = 99.587(3)^\circ$, $\gamma = 90.00^\circ$, $V = 5804.1(3) \text{ \AA}^3$, $T = 100(2) \text{ K}$, space group $P2(1)/n$, $Z = 4$, 78703 reflections measured, 19804 independent reflections ($R_{\text{int}} = 0.1043$). The final R_I values were 0.0536 ($I > 2\sigma(I)$). The final $wR(F^2)$ values were 0.0930 ($I > 2\sigma(I)$). The final R_I values were 0.1518 (all data). The final $wR(F^2)$ values were 0.1078 (all data).

5.4 Experimental details for Chapter Four

5.4.1 Synthesis of ligand precursors

pyridin-4-yl(1H-pyrrol-2-yl)methanone (HL⁹)



A dry round-bottom Schlenk charged with aluminium chloride (2.848 g, 25.0 mmol) was flushed with argon and dry DCM (100 mL) was added. The mixture was stirred for 30 min before isonicotinoyl chloride (1.41 g, 10 mmol) was added. After 2 h pyrrole-2-carbaldehyde (1.9 g, 20.0 mmol) was added carefully. The reaction was stirred overnight. The flask was cooled to 0 °C using an ice-water bath before saturated NaHCO₃ solution was added slowly with stirring until the pH of the aqueous layer was *ca* 8. The aluminium by-products precipitate was removed by filtration (Celite). The product was extracted into chloroform (5 × 50 mL), dried over sodium sulfate and the solvent was removed under reduced pressure to leave the crude product. Purification by column chromatography (EA : Hex = 1:2) yielded a white crystalline solid. (1.38 g, 80 %).

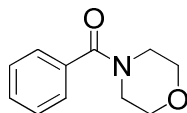
¹H NMR (400 MHz, CDCl₃): 9.42 (s, 1H, Pyr-NH), 8.35 (dd, 2H, ³*J*_{HH} = 4.38 Hz, ⁴*J*_{HH} = 1.63 Hz, py-CH), 7.25 (dd, 2H, ³*J*_{HH} = 4.38 Hz, ⁴*J*_{HH} = 1.63 Hz, py-CH), 6.78 (br, 1H, Pyr-CH), 6.45 (d, 1H, ³*J*_{HH} = 3.77 Hz, Pyr-CH), 5.93 (t, 1H, ³*J*_{HH} = 3.01 Hz, Pyr-CH).

$^{13}\text{C}\{^1\text{H}\}$ NMR (100 MHz, CDCl_3): 182.0 (CH=O), 149.7 (Py-CH), 133.3 (Py- C_q), 129.9 (Pyr- C_q), 125.9 (Pyr-CH), 121.7 (Py-CH), 119.6 (Pyr-CH), 111.0 (Pyr-CH).

MS (ESI): m/z 171.2 (M-H) $^-$

Anal. Found (calculated for $\text{C}_{10}\text{H}_8\text{N}_2\text{O}$): C 69.67 (69.76). H 4.38 (4.68), N 16.32 (16.27)%.

1-Benzoylmorpholine¹⁰



To a stirred solution of morpholine (0.958 g, 11.0 mmol) and triethylamine (1.260 g, 12.0 mmol) in dichloromethane (20 mL) at ambient temperature was carefully added benzoyl chloride (1.406 g, 10.0 mol) at a sufficiently slow rate that boiling of the solvent is minimized. The viscous dark reaction mixture was stirred for a further 1 h before water (20 mL) was added. The dichloromethane extracts (3×10 mL) were washed with water (4×15 mL) and dried over sodium sulfate. The volatiles were removed under pressured to leave an off-white product. (1.82 g, 95 %).

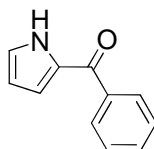
^1H NMR (300 MHz, CDCl_3): 7.21-7.40 (m, 5 H, ArH), 3.50 (br, s, 6H, CH_2), 3.29 (br, s, 2H, CH_2).

$^{13}\text{C}\{^1\text{H}\}$ NMR (75.5 MHz, CDCl_3): 169.8 (CH=O), 134.7 (Ar- C_q), 129.3 (Ar-CH), 128.0 (Ar-CH), 126.5 (Ar-CH), 76.6 (CH_2), 74.0 (CH_2), 66.3 (CH_2).

MS (ESI): m/z 191.0 ($\text{M}+\text{H}$) $^+$

Anal. Found (calculated for $\text{C}_{10}\text{H}_8\text{N}_2\text{O}$): C 69.47 (69.09). H 6.48 (6.85), N 7.02 (7.32)%.

Phenyl(1H-pyrrol-2-yl)methanone (HL^{10})¹⁰



1-Benzoylmorpholine (2.38 g, 12.5 mmol) and freshly distilled POCl_3 (2.5 mL, 26.8 mmol) were mixed under an atmosphere of dinitrogen. The suspension was heated to 35 °C until the solids were dissolved. The reaction was stirred at ambient temperature for another 5 h before pyrrole (0.55 g, 8.2 mmol) in dry 1,2-dichloroethene (*ca.* 50 mL) was added quickly. This was stirred overnight. Saturated Na_2CO_3 was slowly added to the reaction solution until the aqueous layer reached pH *ca.* 8. The separated organic layer was collected and the aqueous solution further extracted to chloroform (4×25 mL). Organic solvents were combined and washed with brine (2×20 mL) and dried over Na_2SO_4 . The solvents were removed under reduced pressure to leave an off-white product. (1.25 g, 89 %).

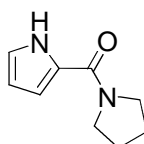
^1H NMR (400 MHz, CDCl_3): 10.15-10.25 (br, 1 H, Pyr-NH), 7.82 (d, 2H, $^3J_{\text{HH}} = 7.24$ Hz, ArH), 7.50 (t, 1 H, $^3J_{\text{HH}} = 7.30$ Hz, ArH), 7.40 (t, 2 H, $^3J_{\text{HH}} = 7.48$ Hz, ArH), 7.08 (s, 1 H, PyrH), 6.80 (s, 1 H, PyrH), 6.20 (d, 1 H, $^3J_{\text{HH}} = 3.06$ Hz, PyrH).

$^{13}\text{C}\{^1\text{H}\}$ NMR (100 MHz, CDCl_3): 185.0 (CH=O), 138.5 (Ar- C_q), 131.9 (Ar-CH), 131.2 (Pyr- C_q), 129.0 (Ar-CH), 128.4 (Ar-CH), 125.6 (Pyr-CH), 119.8 (Pyr-CH), 111.0 (Pyr-CH).

MS (ESI): m/z 172.1 ($\text{M}+\text{H}$) $^+$

Anal. Found (calculated for $\text{C}_{10}\text{H}_8\text{N}_2\text{O}$): C 76.98 (77.17). H 5.28 (5.30), N 8.02 (8.18)%.

(1H-pyrrol-2-yl)(pyrrolidin-1-yl)methanone (HL¹¹)¹¹



Freshly distilled pyrrolidine (1.421 g, 20 mmol) was added slowly into a solution of trichloroacetylpyrrole (2.125 g, 10 mmol) in DMF (15 mL). The mixture was stirred overnight before water (30 mL) was added. This was kept stirring for 10 min before dilute hydrochloride acid (2 M) was added dropwise until pH *ca* 8. The ethyl acetate extracts (5×30 mL) were dried over sodium sulfate and the solvent was removed under reduced pressure to afford a white solid. (1.38 g, 84 %).

^1H NMR (400 MHz, CDCl_3): 10.02 (s, 1H, Pyr-NH), 6.91 (m, 1H, Pyr-CH), 6.57 (m, 1H, Pyr-CH), 6.23 (dd, 1H, $^3J_{\text{HH}} = 6.38$ Hz, $^4J_{\text{HH}} = 2.66$ Hz, Pyr-CH), 3.65-3.73 (m, 4H, CH_2), 1.88-2.00 (m, 4H, CH_2).

$^{13}\text{C}\{^1\text{H}\}$ NMR (100 MHz, CDCl_3): 159.8 (CH=O), 125.7 (Pyr- C_p), 120.3 (Pyr-CH), 111.2 (Pyr-CH), 109.1 (Pyr-CH), 47.6 (CH_2), 46.2 (CH_2), 26.3 (CH_2), 23.8 (CH_2).

MS (ESI): m/z 165.0 ($\text{M}+\text{H}$) $^+$

Anal. Found (calculated for $\text{C}_{10}\text{H}_8\text{N}_2\text{O}$): C 66.27 (65.83). H 7.38 (7.37), N 17.32 (17.06)%.

5.4.2 Synthesis of complexes from proligand HL^9



HL^9 (0.516 g, 3.0 mmol) was stirred with NaH (0.086 g, 3.6 mmol, 1.2 eq.) in dry THF (20 mL) for 15 min. The resulting yellow solution was transferred *via* cannula into a solution of MnCl_2 (0.126 g, 1.0 mmol) in dry THF (20 mL) at room temperature. The reaction was stirred overnight at ambient temperature. The resulting yellow mixture was heated to reflux under reduced pressure until the yellow solid dissolved. The THF solution was filtered and the volume of the solvent was reduced by half to induce crystallization of the product. (0.25 g, 30

%). Single crystals $[\{\text{Na}_2\text{Mn}_2\text{L}^9(\text{THF})_4\} \cdot 2\text{THF} \cdot \text{Et}_2\text{O}]_\infty$ were grown from the solution of THF/Et₂O (3 : 1).

IR (cm⁻¹): 3083 w, 3062 w, 1603 w, 1561 s, 1525 vs, 1498 m, 1479 m, 1437 m, 1428 m, 1406 m, 1319 w, 1271 vs, 1214 w, 1192 s, 1071 w, 1063 w, 1045 s, 1031 vs, 985 m, 906 m, 893 s, 881 m, 837 s, 749 vs, 732 vs, 683 vs, 666 w.

Anal. Found (calculated for C₈₈H₁₀₀Mn₂N₁₂Na₂O₁₃): C 62.37 (62.55). H 5.78 (5.97), N 9.62 (9.95)%.

UV in THF (λ , nm; ϵ , M⁻¹cm⁻¹): 266 (27,000), 312 (44,000), 365 (24,000).

Crystallography: $[\{\text{Na}_2\text{Mn}_2\text{L}^9(\text{THF})_4\} \cdot 3\text{THF}]_\infty$, C₈₈H₁₀₀Mn₂N₁₂Na₂O₁₃, $M = 1689.66$, Triclinic, $a = 12.4104(6)$ Å, $b = 13.3080(6)$ Å, $c = 15.0872(6)$ Å, $\alpha = 104.434(3)^\circ$, $\beta = 102.056(4)^\circ$, $\gamma = 111.251(4)^\circ$, $V = 5804.1(3)$ Å³, $T = 100(2)$ K, space group $P-1$, $Z = 1$, 16045 reflections measured, 8012 independent reflections ($R_{\text{int}} = 0.0345$). The final R_I values were 0.0528 ($I > 2\sigma(I)$). The final $wR(F^2)$ values were 0.1380 ($I > 2\sigma(I)$). The final R_I values were 0.0583 (all data). The final $wR(F^2)$ values were 0.1432 (all data).

$[\{\text{Na}_2\text{Mn}_2\text{L}^9(\text{MeCN})_2\} \cdot \text{MeCN}]_\infty$

HL⁹ (0.516 g, 3.0 mmol) was stirred with NaH (0.086 g, 3.6 mmol, 1.2 eq.) in dry THF (20 mL) for 15 min. The resulting yellow solution was transferred *via* cannula into a solution of MnCl₂ (0.126 g, 1.0 mmol) in dry THF (20 mL). The reaction

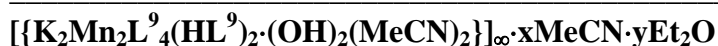
was stirred overnight at ambient temperature. The THF solvent was removed *in vacuo* and the product was extracted to MeCN (30 mL) with heating. The volume of the red MeCN solution was reduced by half to induce crystallization. (0.41 g, 63 %). Single crystals were grown from the solution upon standing at 4 °C for one week.

IR (cm⁻¹): 3065 w, 1601 w, 1560 s, 1526 vs, 1495 m, 1480 m, 1429 m, 1407 w, 1318 w, 1270 vs, 1215 w, 1194 s, 1089 w, 1071 w, 1045 m, 1030 vs, 985 m, 905 w, 894 s, 836 s, 749 vs, 732 vs, 682 vs, 666 w.

Anal. Found (calculated for C₆₆H₅₁Mn₂N₁₅Na₂O₆): C 60.47 (60.69). H 4.18 (3.94), N 16.32 (16.09)%.

UV in MeCN (λ , nm; ϵ , M⁻¹cm⁻¹): 265 (24,000), 260 (40,000), 306 (22,600).

Crystallography: [$\{\text{Na}_2\text{Mn}_2\text{L}^9_6(\text{MeCN})_2\} \cdot \text{MeCN}\}_\infty$, C₆₆H₅₁Mn₂N₁₅Na₂O₆, $M = 1306.08$, Triclinic, $a = 10.3060(4)$ Å, $b = 12.9626(4)$ Å, $c = 13.0826(6)$ Å, $\alpha = 63.489(4)^\circ$, $\beta = 80.865(4)^\circ$, $\gamma = 80.113(3)^\circ$, $V = 1534.05(11)$ Å³, $T = 100(2)$ K, space group $P-1$, $Z = 1$, 15296 reflections measured, 5867 independent reflections ($R_{\text{int}} = 0.0365$). The final R_I values were 0.0403 ($I > 2\sigma(I)$). The final $wR(F^2)$ values were 0.0992 ($I > 2\sigma(I)$). The final R_I values were 0.0433 (all data). The final $wR(F^2)$ values were 0.1020 (all data).



HL^9 (0.516 g, 3.0 mmol) was stirred with KH (0.144 g, 3.6 mmol, 1.2 eq.) in dry THF (20 mL) for 15 min. The resulting yellow solution was transferred *via* cannula into a solution of Mn_2Cl_2 (0.126 g, 1.0 mmol) in dry THF (20 mL). The reaction was stirred overnight at ambient temperature. The THF solvent was removed *in vacuo* and the product was extracted to MeCN (30 mL) with heating. The volume of the yellow MeCN solution was reduced by half and Et_2O was added, leading after two weeks at 4 °C to the deposition of a few single crystals.



HL^9 (0.344 g, 2.0 mmol) was stirred with MeOLi (0.091 g, 2.4 mmol, 1.2 eq.) in dry MeOH (20 mL) for 15 min. This resulted in a yellow solution. A solution of $MnCl_2$ (0.126 g, 1.0 mmol) in dry MeOH (15 mL) was added *via* cannula. A yellow solid precipitated immediately. The reaction was stirred for another 4 h at ambient temperature. The product was collected by filtration and dried *in vacuo* for 4 h. (0.381 g, 96 %).

IR (cm^{-1}): 3057 w, 1611 m, 1559 s, 1523 vs, 1497 m, 1437 m, 1388 vs, 1317 w, 1278.3 w, 1196 m, 1140 w, 1046 m, 991 m, 907 m, 880 m, 852 m, 748 s, 726 vs, 693.9 vs

Anal. Found (calculated for $C_{20}H_{14}MnN_4O_2$): C 60.47 (60.46). H 3.38 (3.55), N 14.32 (14.10)%.

Due to the insolubility of the material, we were unable to collect UV data.

[FeL⁹₂]_n

HL⁹ (0.344 g, 2.0 mmol) was stirred with MeOLi (0.091 g, 2.4 mmol, 1.2 eq.) in dry MeOH (20 mL) for 15 min. This resulted in a yellow solution. The solution of FeCl₂ (0.127 g, 1.0 mmol) in dry MeOH (15 mL) was added *via* canuula and immediately the solution turned blue and then purple after 1 h. The reaction was stirred overnight at ambient temperature. The purple product was collected by filtration and dried *in vacuo* for 4 h. (0.378 g, 95 %). Single crystals were grown from a slow diffusion of two diluted starting materials in MeOH solution (ca. 1.0 M).

IR (cm⁻¹): 3058 w, 1610 m, 1559 s, 1524 vs, 1497 m, 1434 m, 1415 w, 1388 vs, 1317 w, 1278 m, 1221 w, 1196 m, 1139 w, 1046 m, 993 m, 909 m, 880 m, 852 m, 748 s, 726 vs, 693 vs

Anal. Found (calculated for C₂₀H₁₄FeN₄O₂): C 60.37 (60.33). H 3.38 (3.54), N 14.32 (14.07)%.

Due to the insolubility of the material, we were unable to collect UV data.

Crystallography: [FeL⁹₂]_n, C₂₀H₁₄FeN₄O₂, *M* = 398.20, monoclinic, *a* = 7.7538(2) Å, *b* = 13.6404(4) Å, *c* = 8.2758(3) Å, *α* = 90.00°, *β* = 98.581(3)°, *γ* = 90.00°, *V* = 865.49(5) Å³, *T* = 100(2) K, space group *P*2(1)/*n*, *Z* = 2, 3844 reflections measured, 1525 independent reflections (*R*_{int} = 0.0249). The final *R*_I values were

0.0412 ($I > 2\sigma(I)$). The final $wR(F^2)$ values were 0.1147 ($I > 2\sigma(I)$). The final R_I values were 0.0441 (all data). The final $wR(F^2)$ values were 0.1189 (all data).

[CoL⁹₂]_n

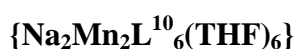
HL⁹ (0.344 g, 2.0 mmol) was stirred with MeOLi (0.091 g, 2.4 mmol, 1.2 eq.) in dry MeOH (20 mL) for 15 min. This resulted in a yellow solution. A solution of CoCl₂ (0.130 g, 1.0 mmol) in dry MeOH (15 mL) was added *via* cannula, leading immediately to precipitation of a yellow solid. The mixture was stirred for another 4 h before the product was collected by filtration and dried *in vacuo* for 4 h. (0.361 g, 90 %).

IR (cm⁻¹): 3058 w, 1607 m, 1559 s, 1525 vs, 1497 m, 1435 m, 1415 w, 1388 vs, 1318 w, 1278 m, 1221 w, 1196 m, 1149 w, 1046 m, 993 m, 910 m, 881 m, 852 m, 747 s, 725 vs, 692 vs.

Anal. Found (calculated for C₂₀H₁₄CoN₄O₂): C 60.30 (59.86). H 3.80 (3.52), N 14.02 (13.96)%.

Due to the insolubility of the material, we were unable to collect UV data.

5.4.3 Synthesis of complexes from proligand HL¹⁰



HL¹⁰ (0.513 g, 3.0 mmol) was stirred with NaH (0.086 g, 3.6 mmol, 1.2 eq.) in dry THF (20 mL) for 15 min. The resulting yellow solution was transferred *via* cannula into a solution of MnCl₂ (0.126 g, 1.0 mmol) in dry THF (20 mL) at room temperature. The reaction was stirred overnight at ambient temperature. The resulting yellow solution was filtered *via* cannula. Large yellow blocks grew at room temperature over 2 h (0.420 g, 52 %). Smaller single crystals of [Na₂Mn₂L⁹(THF)₄]_∞·2THF·Et₂O suitable for X-ray diffraction were grown from THF/Et₂O (3 : 1).

IR (cm⁻¹): 2925 vs, 2854 vs, 1602 w, 1584 m, 1464 vs, 1377 vs, 1282 m, 1196 m, 1172 w, 1095 w, 1044 m, 988 w, 905 m, 880 m, 795 w, 754 m, 730 s, 699 m, 681 w.

Anal. Found (calculated for C₉₀H₉₆Mn₂N₆Na₂O₁₂): C 66.77 (67.16). H 6.38 (6.01), N 5.32 (5.22)%.

UV in THF (λ, nm; ε, M⁻¹cm⁻¹): 244 (76,000), 302 (125,000).

{Na₂Fe₂L¹⁰(THF)₆}

HL¹⁰ (0.513 g, 3.0 mmol) was stirred with NaH (0.086 g, 3.6 mmol, 1.2 eq.) in dry THF (20 mL) for 15 min. The resulting yellow solution was transferred *via* cannula into a solution of FeCl₂ (0.127 g, 1.0 mmol) in dry THF (20 mL) at room temperature. The deep red solution was stirred overnight at ambient temperature. The resulting THF solution filtered *via* cannula. Large red blocks grew at 4 °C over one week. (0.259 g, 32 %).

IR (cm⁻¹): 2910.8 vs, 2850.2 vs, 1600.5 w, 1580.7 w, 1462.9 vs, 1377.0 vs, 1282.0 m, 1126.1 m, 1040.2 m, 905.0 m, 880.10 m, 794.3 w, 754.0 m, 730.9 s, 700.1 m.

Anal. Found (calculated for C₉₀H₉₆Fe₂N₆Na₂O₁₂): C 67.37 (67.08). H 6.38 (6.00), N 5.32 (5.22)%.

UV in THF (λ , nm; ϵ , M⁻¹cm⁻¹): 244 (30,000), 302 (48,000).

Crystallography: {Na₂Fe₂L¹⁰(THF)₆}, C₉₀H₉₆Fe₂N₆Na₂O₁₂, $M = 1611.41$, hexagonal, $a = 13.11870(10)$ Å, $b = 13.11870(10)$ Å, $c = 28.3181(5)$ Å, $\alpha = 90.00^\circ$, $\beta = 90.00^\circ$, $\gamma = 120.00^\circ$, $V = 4220.62(9)$ Å³, $T = 100(2)$ K, space group $P-3$ $1\ c$, $Z = 2$, 48829 reflections measured, 2708 independent reflections ($R_{int} = 0.0513$). The final R_I values were 0.0843 ($I > 2\sigma(I)$). The final $wR(F^2)$ values were 0.2421 ($I > 2\sigma(I)$). The final R_I values were 0.0937 (all data). The final $wR(F^2)$ values were 0.2536 (all data).

5.4.4 Synthesis of complexes from proligand HL¹¹

[Mn(III)L¹¹₃]

HL¹¹ (0.516 g, 3.0 mmol) was stirred with NaH (0.086 g, 3.6 mmol, 1.2 eq.) in dry THF (20 mL) for 15 min. The resulting yellow solution was transferred *via* cannula into a solution of MnCl₂ (0.126 g, 1.0 mmol) in dry THF (20 mL) at room

temperature and immediately the solution turned to grey. The reaction was stirred overnight at ambient temperature. The solution was filtered and volume of the solvent was reduced by half before Et₂O (5 mL) was added to induce crystallization. Yield was unoptimised. Single crystals [Mn(III)L¹¹₃] were grown from the solution of THF/Et₂O (3 : 1) over one week.

Crystallography: [Mn(III)L¹¹₃], C₂₇H₃₃MnN₆O₃, *M* = 544.53, monoclinic, *a* = 9.7037(12) Å, *b* = 17.001(2) Å, *c* = 15.6962(13) Å, *α* = 90.00°, *β* = 100.350(7)°, *γ* = 90°, *V* = 2547.4(5) Å³, *T* = 100(2) K, space group *P*2(1)/*n*, *Z* = 4, 19043 reflections measured, 4910 independent reflections (*R*_{int} = 0.0672). The final *R*_{*I*} values were 0.0907 (*I* > 2σ(*I*)). The final *wR*(*F*²) values were 0.1635 (*I* > 2σ(*I*)). The final *R*_{*I*} values were 0.1372 (all data). The final *wR*(*F*²) values were 0.1901 (all data).

[Fe(III)L¹¹₃]

HL¹¹ (0.516 g, 3.0 mmol) was stirred with NaH (0.086 g, 3.6 mmol, 1.2 eq.) in dry THF (20 mL) for 15 min. The resulting yellow solution was transferred *via* cannula into a solution of FeCl₂ (0.127 g, 1.0 mmol) in dry THF (20 mL) at room temperature and immediately the solution turned to grey. The reaction was stirred overnight at ambient temperature. The solution was filtered and volume of the solvent was reduced by half before Et₂O (5 mL) was added to induce crystallization. Yield was unoptimised. Single crystals [Fe(III)L¹¹₃] were grown from the solution of THF/Et₂O (3 : 1) over a week.

Crystallography: $[\text{Fe(III)}\mathbf{L}^{\text{II}}_3]$, $\text{C}_{27}\text{H}_{33}\text{FeN}_6\text{O}_3$, $M = 545.44$, monoclinic, $a = 9.99697(15)$ Å, $b = 31.4459(4)$ Å, $c = 16.9520(2)$ Å, $\alpha = 90.00^\circ$, $\beta = 103.4800(15)^\circ$, $\gamma = 90^\circ$, $V = 5182.28(13)$ Å³, $T = 100(2)$ K, space group $P2(1)/n$, $Z = 8$, 58787 reflections measured, 9984 independent reflections ($R_{\text{int}} = 0.0619$). The final R_I values were 0.0413 ($I > 2\sigma(I)$). The final $wR(F^2)$ values were 0.0985 ($I > 2\sigma(I)$). The final R_I values were 0.0498 (all data). The final $wR(F^2)$ values were 0.1038 (all data).



HL^{II} (0.516 g, 3.0 mmol) was stirred with NaH (0.086 g, 3.6 mmol, 1.2 eq.) in dry THF (20 mL) for 15 min. The resulting yellow solution was transferred *via* cannula into a solution of CoCl_2 (0.130 g, 1.0 mmol) in dry THF (20 mL) at room temperature and immediately the solution turned to pink. The purple solution was stirred overnight at ambient temperature. The solution was heated to reflux and filtered. The volume of the solvent was reduced by half to induce crystallization of the product. Yield was unoptimised. Single crystals $[\text{Na}_9\text{Co}_{14}\mathbf{L}^{\text{II}}_{18}(\text{OH})_{18}]^+[\text{Co}_2\text{NaL}_6]^-$ were grown from the solution of THF upon standing at room temperature over a week.

IR (cm^{-1}): 3584 w, 2925 vs, 2854 vs, 1509 m, 1460 s, 1415 w, 1377 m, 1434 w, 1298 w, 1198 w, 1058 m, 723 m.

Anal. Found (calculated for $\text{C}_{244}\text{H}_{320}\text{Co}_{16}\text{N}_{48}\text{Na}_{10}\text{O}_{49}$): C 50.27 (49.82). H 5.38 (5.48), N 11.62 (11.43)%.

UV in MeCN (λ , nm; ϵ , M⁻¹cm⁻¹): 226 (137,000), 261 (216,000), 295 (92,000)

Crystallography: [Na₉Co₁₄L¹¹₁₈(OH)₁₈]⁺[Co₂NaL₆]⁻, C₂₄₄H₃₂₀Co₁₆N₄₈Na₁₀O₄₉, M = 5882.26, triclinic, a = 17.3398(13) Å, b = 19.8891(15) Å, c = 21.4982(15) Å, α = 73.452(4)°, β = 84.288(4)°, γ = 72.314(3)°, V = 6770.5(9) Å³, T = 100(2) K, space group $P-1$, Z = 1, 49565 reflections measured, 15967 independent reflections (R_{int} = 0.1217). The final R_I values were 0.1340 ($I > 2\sigma(I)$). The final $wR(F^2)$ values were 0.2393 ($I > 2\sigma(I)$). The final R_I values were 0.2182 (all data). The final $wR(F^2)$ values were 0.2881 (all data).

5.5 Refereces

1. G. M. Sheldrick, *Acta Crystallogr., Sect. A*, 1990, **46**, 467-473.
2. G. M. Sheldrick, *Acta Crystallogr., Sect. A*, 2008, **64**, 112-122.
3. W. T. Pennington, *J. Appl. Cryst.*, 1999, **32**, 1028-1029.
4. T. C. G. N. N. Greenwood, *Mossbauer Spectroscopy*, Chapman and Hall Ltd, London, 1971.
5. G. A. Bain and J. F. Berry, *J. Chem. Educ.*, 2008, **85**, 532.
6. N. U. Hofsløkken and L. Skattebøl, *Acta Chem. Scand.*, 1999, **53**, 258-262.
7. Y. Suzuki and H. Takahashi, *Chem. Pharm. Bull.*, 1983, **31**, 1751-1753.
8. H. Ö. Demir, İ. Kaya and M. Saçak, *Polym. Bull.*, 2008, **60**, 37-48.
9. F. Robert, A. D. Naik, B. Tinant, R. Robiette and Y. Garcia, *Chem. Eur. J.*, 2009, **15**, 4327-4342.
10. S. Rubino, S. Petruso, R. Pierattelli, G. Bruno, G. C. Stocco, L. Steardo, M. Motta, M. Passerotto, E. D. Giudice and G. Gulì, *J. Inorg. Biochem.*, 2004, **98**, 2071-2079.
11. T. J. Donohoe, P. M. Guyo, R. L. Beddoes and M. Helliwell, *J. Chem. Soc. Perkin Trans.*, 1998, 667-676.